Metal-Air Batteries

Metal Deposition and Alloying in Aprotic Electrolytes for Anode Materials

Kinetic Behaviour

Dissertation

zur
Erlangung des Doktorgrades (Dr. rer. nat.)
der
Mathematisch-Naturwissenschaftlichen Fakultät
der
Rheinische Friedrich-Wilhelms-Universität Bonn

vorgelegt von

Da Xing

aus

Peking, VR China

Bonn 2021

Metal-Air Batteries

Metal Deposition and Alloying in Aprotic Electrolytes for Anode Materials

Kinetic Behaviour

Dissertation

zur
Erlangung des Doktorgrades (Dr. rer. nat.)
der
Mathematisch-Naturwissenschaftlichen Fakultät
der
Rheinische Friedrich-Wilhelms-Universität Bonn

vorgelegt von

Da Xing

aus

Peking, VR China

Bonn 2021

Angefertigt mit Genehmigung der Mathematisch-Naturwissenschaftlichen Fakultät der
Rheinischen Friedrich-Wilhelms-Universität Bonn

1. Gutachter (Betreuer): Prof. Dr. Helmut Baltruschat

2. Gutachter: Prof. Dr. Thomas Bredow

Tag der müdlichen Prüfung: 02.12.2021

Erscheinungsjahr: 2022

Selbstständigkeitserklärung gemäß Promotionsordnung der Mathematisch-Naturwissenschaftlichen Fakultät (§6, Absatz 2)

Ich versichere, dass ich die vorliegende Arbeit unter Einhaltung der Regeln guter wissenschaftlicher Praxis selbstständig verfasst, keine anderen als die angegebenen Quellen und Hilfsmittel benutzt und die Zitate kenntlich gemacht habe. Ich habe weder vor noch während meiner Promotion oder bei der Anfertigung dieser Dissertation entgeltliche oder nichtentgeltliche Beratungs- oder Vermittlungsdienstleistungen in Anspruch genommen.

Bonn, den

Acknowledgement

Foremost, I wish to express my sincere thanks to my research advisor **Prof. Dr. Helmut Baltruschat** for providing me with the opportunity and continuous support to complete the PhD study. I am grateful for his patience, motivation, enthusiasm and immense knowledge, as well as the financial support.

My appreciation is also extended to the other member of my thesis committee: Prof. Dr. Thomas Bredow, Prof. Dr. Robert Glaum, and Priv.-Doz. Dr. Elisabeth Soergel for their availability and eagerness to evaluate my thesis.

My sincere thanks also go to the former and present members of our group Abd El Aziz, Ahemd, Andreas, Christoph B., Christoph M., Ehab, Elina, Hatem, Inhee, Philip. R., Philipp H., Martina, Jan, Pawol, Sergi, and Zan for their help and support. In particular, I am grateful to Frau Rossignol for her help in administration and Frau Thome for her help in the lab.

I thank the members of mechanical, electronic and glass workshops, especially Mr. Königshoven, Mr. Paulig, and Mr. Koll for their help in designing and constructing the fine cells and repairing devices. Many thanks go to Mr. Knut Hintzen for his kind help in computer stuff.

I would like to thank my parents, my lovely daughter (ZiYi), all of my family members and my friends in Germany. They were always encouraging me and supporting me with their best wishes.

Special thanks to my beloved wife for her patience, love and motivational support that helped me reach all of my aims so far. She was always there carrying me up and stood by me through good and bad times.

Da Xing

Abstract

Electrochemical energy storage is considered to be one of the most efficient storage technologies. Metal air batteries concerning the increase in storage capacity, increase the lifetime, and reduction of weight, size and costs leads to more and more interest in battery research. In this study the metal (lithium, magnesium, and calcium) deposition and dissolution as well as alloying/de-alloying are investigated for various salts and solvents for the anode materials. The alloying-type anodes (Sb, Sn, and Bi as host material) for magnesium and calcium batteries are good choices for rechargeable metal batteries because of their high electrochemical properties.

The lithium deposition/dissolution are investigated in 1 M and 3 M LiTFSI/DMSO solution on Au and Pt electrode. The highest coulombic efficiency of Li deposition/dissolution is observed in 3 M solution on Au electrode. On Pt electrode the coulombic efficiencies are low for both concentrations. The oxidative stability of this electrolyte is found to be around 4 V. The decomposition of the specific lithium salt (LiTFSI) and of the DMSO-molecular are the main reason and demonstrated by using DEMS. Hydrogen evolution and Li-Au as well as Li-Pt alloy formation was also observed during the lithium deposition.

The magnesium deposition has been investigated in many electrolytes. MACC/TG and $Mg(BH_4)_2$/TG electrolyte systems show high reversibility and high coulombic efficiency (99 %). However, the freshly prepared MACC/TG electrolyte needs to be conditioned until it shows high reversible magnesium plating and stripping and the Al and Cl co-deposition is observed. High concentration of $Mg(BH_4)_2$/TG (1.5 M) electrolytes results in a coulombic efficiency of 70 % without addition of $MgCl_2$. With an addition of 0.5 M $MgCl_2$ the coulombic efficiency increase to 98 %. Due to the strongly reductive BH_4^- ion this electrolyte is compatible with the magnesium metal. However, the oxidative stability is quite low. (2 V vs. Mg/Mg^{2+})

Many electrolyte systems with varying Ca salts and organic solvents have been studied for Ca deposition and dissolution. Most of Ca salts are not commercially available and their solubility is quite low in the organic solvent. No reversible Ca deposition or alloying were observed in most Ca^{2+} containing electrolytes except 1.5 M $Ca(BH_4)_2$/THF (up to 98 % coulombic efficiency and 100 mV overpotential). However, the electrochemical window of these electrolytes is quite low. (3 V vs. Ca/Ca^{2+})

The electrochemical properties of Li, Mg, and Ca alloying and de-alloying with Sb, Sn, and Bi modified Au electrodes have been discussed. The cyclic voltammogram for alloying/de-alloying with Sb, Sn, and Bi modified electrode shows a positive shift of the onset potential of bulk deposition compared to that at bare Au electrode. The ratio of moles agrees with the

stoichiometry of Li_2Sb and Li_3Sb for Li alloying; Mg_3Sb_2, Mg_2Sn, and Mg_3Bi_2 for Mg alloying; and $CaSb_2$, Ca_3Sn, and $CaBi_2$ for Ca alloying. The diffusion coefficient of alloying in multi-layers has been estimated by using various electrochemical techniques. The diffusion of metal ion in a thin, bulk (massive) layer (Sb, Sn, and Bi) and the kinetic behaviours are studied by using PITT, CV, and potential step experiments.

Three completely different behaviours were observed. First, the metal alloying is controlled first by the nucleation and charge transfer after the double-layer charging and then by the diffusion; or first by the charge transfer after the double-layer charging and then by the diffusion. A plot of Q^2 vs. t is used for estimating the diffusion coefficient. Second, the other behaviour was controlled simultaneously by both charge transfer and diffusion. The current drops directly after the double-layer charge. A plot of i vs. $t^{0.5}$ is used for estimating the diffusion coefficient and, by extrapolation to t=0, the pure kinetic current. Third, the metal alloying is only diffusion-determined process. The current drops directly after the double-layer charge. A plot of Q^2 vs. t is used for estimating the diffusion coefficient.

The diffusion coefficients were estimated to be 4-7×10^{-14} cm^2/s for Mg alloying with Sb and 1-4×10^{-14} cm^2/s for Mg alloying with Bi, which are one magnitude less than the diffusion coefficient 4-8×10^{-13} cm^2/s for Mg alloying Sn. The diffusion coefficients of Ca alloying were estimated to be 0.9-1×10^{-13} cm^2/s for Ca alloying with Sb and 2-3×10^{-13} cm^2/s for Ca alloying with Bi, which is one magnitude higher than the diffusion coefficient of 3×10^{-14} cm^2/s for Ca alloying with Sn. Such diffusion coefficients, albeit still somewhat “apparent”, are much closer related to the true diffusion coefficient in the metal or alloy. Furthermore, the diffusion rate of divalent cations (Mg and Ca) is less than the diffusion rate of Li in the Sb adlayers (4-6×10^{-12} cm^2/s)

In addition, a STM measurement for the Mg alloying with Bi has been studied. The Bi bulk shows similar crystalline structure before (in aqueous solution) and after (in organic solution) transfer into the glovebox. After the Mg alloying/de-alloying the surface of Bi is smoother and the crystalline structure disappears.

Notations

Q_F	Faradaic charge	C	Concentration
C_0	Saturation concentration	E^0	Formal potential
R	The universal gas constant,	T	Temperature in Kelvin
n	Number of electron	F	Faraday constant, 96485 $C \cdot mol^{-1}$
i_0	Exchange current density	α	Trans coefficient
η	overpotential	I_0	Current density
J_0	Diffusion flux	D	Diffusion coefficient
t	Time	M	Molar mass
m	Mass	e	Electron
A	Surface area	ν	Potential scan rate
E	Potential	q	Charge density
d	Distance	I_P	Peak current
π	Pi	i_{CT}	Charge transfer current density
δ_N	Nernst diffusion layer thickness	C_s	Surface concentration
w	Width	r	Atomic radius
I_F	Faradaic current	l	Length
e	Elemental charge, 1.602×10^{-19} C	V	Voltage
f_0	Resonant Frequency	ρ_q	Density of the quartz
μ_q	Shear module of the quartz	C_f	Calibration constant
k_i	Rate constant of i-th reaction	Φ	Work function
$\hbar$	Planck's constant	Ψ	Binding energy
I_t	Tunneling current	θ	Surface coverage
$N_{surf.atoms}$	The number of surface atoms	τ	Time constant
E_{open}	Open circuit potential		

Abbreviations

LIBs	Lithium ion batteries	EVs	Electric vehicles
RMBs	Rechargeable magnesium batteries	RCBs	Rechargeable calcium batteries
GITT	Galvanostatic intermittent titration technique	PITT	Potentiostaic intermittent titration technique
RHE	Reversible hydrogen electrode	AFM	Atomic force microscopy
UPD	Underpotential deposition	OPD	Overpotential deposition
CN	Coordination number	OCP	Open circuit potential
WE	Working electrode	CE	Counter electrode
CV	Cyclic voltammetry	RE	Reference electrode
SCE	Saturated calomel electrode	Au(pc)	Polycrystalline Gold
UHV	Ultrahigh vacuum	PZC	Potential of zero charge
OER	Oxygen evolution reaction	ORR	Oxygen reduction reaction
DFT	Density functional theory	SEI	Solid electrolyte interphase
SPM	Scanning probe microscopy	STM	Scanning tunnelling microscope
OHP	Outer Helmholtz plane	IHP	Inner Helmholtz plane
IR	Infrared spectroscopy	XPS	X-ray photoelectron spectroscopy
MFM	Magnetic force microscopy	SEM	Scanning electron microscope
2D	Two-dimensional	3D	Three-dimensional
XRD	X-ray diffraction	eV	Electron volt
DM	Dipole moment	KF	Karl-Fischer
DC	Direct current	AC	Alternating current
FC	Fuel cell	bcc	Body catered cubic
fcc	Face centered cubic	CT	Charge transfer
hcp	Hexagonal close packed	rds	Rate determining step
EQCM	Electrochemical quartz microbalance	ppm	Part per million
HOPG	Highly oriented pyrolytic graphite	EIS	Electrochemical impedance spectroscopy
EDS	Energy-dispersive X-ray spectroscopy	FTIR	Fourier transform infrared spectroscopy
MACC	Magnesium-aluminum chloride complex	DEMS	Differential electrochemical mass spectrometry

List of Figures

List of Tables

Contents

Chapter 1: Introduction

1.1 Motivation

Electrochemical energy storage is considered to be one of the most efficient storage technologies. Rechargeable batteries have become essential energy storing devices, which are widely used in portable electronic devices and hybrid electric vehicles. More and better batteries have to be developed for improving our society as concerns air pollution, oil dependency, and climate change. Because Lithium-ion-batteries have several problems (limited safety, short lifetime, low energy density…) further developments are needed. The post-lithium batteries such as metal-air and multivalent batteries are starting to put pressure on the generally acknowledged Li-ion battery. The improvement in batteries concerning the increase in storage capacity, increase the lifetime, and reduction of weight, size and costs leads to more and more interest in battery research.

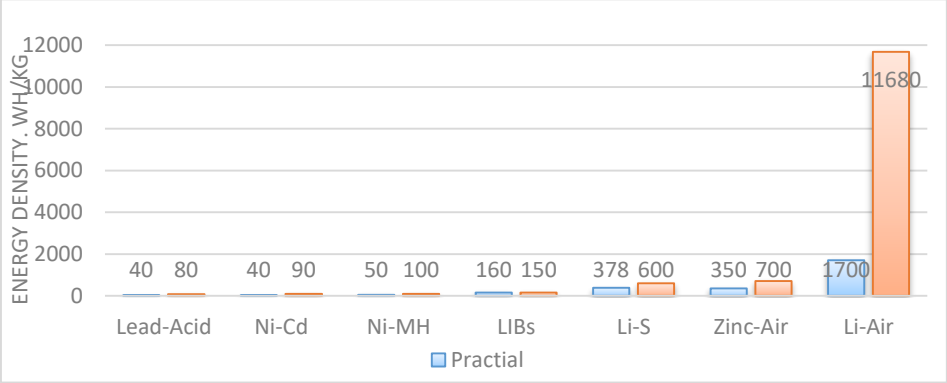

Figure 1. 1: The gravimetric energy densities (Wh/kg) for various types of rechargeable batteries. The theoretical density is shown as the red bars while the practical achievable density is indicated by the orange bars and numerical values.

Compared to conventional LIBs the Li-O_2 battery has 4-5 fold higher theoretical specific energy. [1, 2] The non-aqueous lithium-air battery therefore should be developed into a practical system because of its highest energy density. (Figure 1.1) [3] The LIB has an upper limit of the specific energy of ~ 300 Wh kg^{-1}. With the development of Li-air batteries, the electric automobiles (EVs) can be driven with long range (500 miles) on a single charge and the specific energy can be increased to 500 Wh kg^{-1}. [4-6]

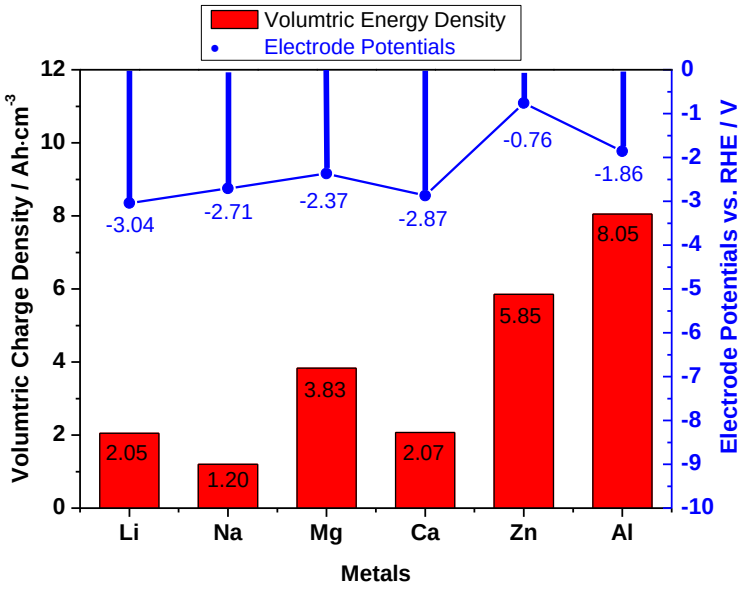

Figure 1. 2: Electrode potentials for monovalent and multivalent Metals. [4, 7]

The electrode potentials and the volumetric charge densities for monovalent and multivalent metals are shown in Figure 1.2. One of the largest problems for monovalent metals (Li and Na) used as anodes is their high reactivity; this becomes a concern for the device's safety because of the formation of dendrites grows. Magnesium is one of the most abundant elements in the Earth's crust. Due to the currently dominating market power of China, there is no issue with the abundance of Mg worldwide. Magnesium based secondary batteries have been regarded as a viable 'environmental friendly, non-toxic' alternative compared to the Li-ion systems owing to its high volumetric capacity (3833 mAh/cm^3), low equilibrium potential (-2.37 V vs. RHE), and non-dendritic growth during the deposition process. [8-12] Magnesium offers the possibility of carrying and storing more charge per ion and improve the mobility of multivalent cations in solid host structures. Furthermore, the physical properties of the magnesium should allow the building of batteries with metal anodes.

Calcium has become today more and more into public attention for metal ion batteries and metal air batteries. It has to be considered that calcium as charge carrier can achieve the same capacity with only half of the amount of ions compared to using Na^+ or Li^+. [8, 13] Calcium is the fifth most abundant element in the Earth's crust and its standard potential is -2.87 V vs. RHE and charge density of 1.34 Ah/g. Furthermore, because of less polarizing character, the Ca^{2+} ion should have more mobility than Mg^{2+}. [14]

This thesis focusses therefore on lithium, magnesium and calcium (and also their alloy type) as anode material for application in metal-air batteries. Metal deposition/dissolution (and also alloying/de-alloying) are investigated for various salts and solvents. The electrochemical

performance is studied by cyclic voltammetry and galvanostatic experiments. The stability with the respected anode is investigated by Differential Electrochemical Mass Spectrometry (DEMS), in order to check the volatile products from the electrolyte decomposition. By potential step experiments the kinetic of alloying/de-alloying is studied and the diffusion coefficient of metal ion in the solid host material can be estimated. The surface morphology (the formation of a dendrite or passivation layers) are checked by electrochemical scanning tunneling microscopy (EC-STM).

1.2 Overview of the research topics

1.2.1 Lithium Batteries

In a lithium air battery metallic lithium is used as negative electrode. The use of metallic lithium as the anode leads to a very high theoretical specific capacity (~ 3860 mAh g^{-1}) and a reduction potential of –3.040 V versus the standard hydrogen electrode. For the cathode, oxygen is the active material, which does not need to be stored in the battery but comes from the environment. The oxygen could pass through an electronically conducting porous matrix and reacts with the Li ions, which is in the electrolyte solution. At the compartment of the anode the deposition and dissolution of lithium takes place, while at the cathode the oxygen reduction reaction (ORR) and oxygen evolution reaction (OER) occurs.

During discharge the oxygen reacts with Li ions at the cathode, is reduced in the first step to LiO_2 via a one electron transfer. Then the LiO_2 will undergo a second electron transfer or a disproportionation reaction to finally form Li_2O_2 as the discharge product. The Lithium peroxide is not soluble in the aprotic solvents, [15] it deposits on the electrode and blocks the electrode. During charging the deposited Li_2O_2 is oxidized back to molecular oxygen. A cycled Li-air cell using $LiPF_6$ in tetraglyme was reported and the reaction of the Li anode with the electrolyte was studied. [16] The morphology of the Li anode is changed after several charge-discharge cycles forming dendrites at the anode due to the reaction between the electrolyte and plated Li. One of the challenges for the lithium oxygen batteries is to find a safe anode and increase the stability of a Li anode for the lithium deposition/dissolution.

The form of an artificial solid electrolyte interphase (SEI) as an anode protection film is used to increase the stability of the Li anode. [17-21] It was reported that an increase in the stability of the SEI achieved by optimizing the complex compound between the salt and solvent molecule can promote metal deposition and enhance the coulombic efficiency. Kozen et al. [22] investigated a hybrid organic/inorganic artificial SEI in order to stabilize the Li metal for the deposition. This cell can be cycled very stable for over 300 cycles at current density 1 mA/cm^2

and over 110 cycles at current density 2 mA/cm^2. Additionally the use of a super concentrated electrolyte solution can also increase the dissolving rate of the intermediates and the diffusion of ions, products and active species. For example, Liu et al. [23] demonstrated a 3 M LiTFSI in 1, 2-dimethoxyethane (DME)-based electrolytes for Li-O_2 batteries. This high-concentrated electrolyte enhanced the cycling stability in the potential range of 2.0-4.5 V vs. Li/Li$^+$ and the capacity about 1000 mAh/g. Otherwise an electrolyte based on LiTFSI in DMSO with high concentration (a molar ratio of 1:3) was investigated. [24] Another specific Li salt (4 M $LiNO_3$) in DMSO for lithium-oxygen batteries was investigated, which shows an enhancement of the cycling performance (>20 % higher coulombic efficiency than LiTFSI, LiNTF and $LiClO_4$). [25] Cells with concentrations of more than 1 M LiTFSI have a high cycling stability and coulombic efficiency.

1.2.2 Magnesium Batteries

The development of a cathode is a big challenge for Mg batteries. Gregory et al. started to investigate the transition metal oxide, sulfides and borides for Mg cathode. [26] They showed that V_2O_5 might be a suitable cathode with reasonable capacity. This kind of cathode has been later explored. It was reported by J. L. Andrews, that the V_2O_5 as a cathode material can offer low migration energies of the multivalent ions to support reversible cycling. [27] To understand how the metal oxides work for the Mg battery, theoretical calculations have been used to describe the atomic configurations and structures for the diffusion of Mg in host materials. It has been shown that the Mg^{2+}-ion coordinated by DME solvent $[Mg(DME)_x]^{2+}$ can lead to faster insertion and de-insertion in a host material. [28, 29] An alternative to cathode insertion materials is found to be an Mg-S system, which can offer high capacities and has a theoretic energy density of 3200 Wh L^{-1}, molar volume MgS: 19.9 and 24% expansion of the cathode. [30-32]
For the anodes, using a sheet of pure Mg metal is the simplest and cheapest approach. However the power density of a Mg anode is limited because of the kinetic barriers for Mg transfer on the Mg surface. Dispersed Mg particles in carbon as an anode have already been studied for Mg-S battery, it has a larger surface for the electrochemical reaction which reduces the overpotential. But this system has some disadvantage: due to the additional carbon it has a limited capacity and the dispersed magnesium can strongly react with oxygen which lead to a passivation layer. [32, 33] Further studies for the anode were done with magnesium alloys. Alloying elements have no negative effect on the electrochemical properties of Mg compared to the pure metal. Recently, antimony (Sb), tin (Sn) and bismuth (Bi) have been suggested as insertion materials, because magnesium can form intermetallic compounds with these materials.

The alloys have a high initial capacity of 298 mAh/g at 1 C rate for electrochemical magnesium deposition at Bi-Sb alloy. [34, 35] But it reduces to 215 mAh/g after 100 cycles.

The development of non-aqueous electrolytes for secondary magnesium batteries is a challenge, because the anions might be not stable with the magnesium anode or a passivation layer on the anode is formed. Furthermore the magnesium ion is doubly charged and therefore hard to pass the interphase layers on Mg surfaces. [36] The non-aqueous electrolytes, which are capable for the magnesium plating and stripping, can be classified into two categories. One is halide-ion containing electrolytes, which has several advantages. The halide-ion can react with the passivation layer, such as MgO, to allow the magnesium deposition on the surface. Otherwise using halide-ion containing electrolytes can enhance the electrochemical performance with high coulombic efficiency and low overpotential for magnesium deposition and dissolution. Finally these electrolytes have lower cost.

Some examples of the electrolytes will be shown below. There are many researchers were interested in non-aqueous electrolytes in the last 30 years. In the work by Gregory et al. [26], the synthesis of Mg electrolytes from an organomagnesium compound with aluminum chloride as a Lewis acid was published. This kind of electrolyte is enabling reversible stripping and plating of magnesium. 10 years later Aurbach et al. developed a second generation of electrolytes, the first rechargeable Mg battery with thousand stable cycles, which was formed from the reaction between Bu_2Mg and $EtAlCl_2$ in THF. [37] The active species in these electrolytes is a binuclear Mg complex with two Mg atoms which are bridged by three Cl atoms. Neson et al. reported a $PhMgCl/AlCl_3$ electrolyte which is developed from the Grignard reagents electrolytes. It shows reduced corrosion properties and an anodic stability of 5 V vs. Mg/Mg^{2+}. [38, 39] A carbonyl magnesium chloride in THF electrolyte showing high coulombic efficiency (98%) and high oxidative stability (3.2 V vs. Mg/Mg^{2+} on Pt) was reported by Carter et al. [40] In some reports, a new HMDS-based system with addition of $AlCl_3$ or $MgCl_2$ were introduced. It increased the anodic stability (3.3 V vs. Mg/Mg^{2+}) and higher coulombic efficiency (98 - 99%) compared to the HMDS-electrolytes without addition of $AlCl_3$ or $MgCl_2$. [30, 31, 41] Oxygen-based anions were also introduced as magnesium electrolytes by Liao et al. [42], such as n-butanol, tert-butanol and trimethylsilanol with addition of $AlCl_3$.Those electrolytes showed a large anodic stability (2.5 - 2.8 V vs. Mg/Mg^{2+}), but their efficiency was low and the deposition contained 2.6 atom% Al. More recently, $MgCl_2$ and $AlCl_3$ in THF solution was studied in 2005 and as it is currently known, the magnesium-aluminum chloride complex (MACC) in glymes exhibits high reversibility of deposition and dissolution , high anodic stability (-3.2 V vs. Mg/Mg^{2+}) and is compatible with some cathode.

Another class of electrolytes and salts has been investigated over the past few years that are Cl-ion free reagents. Magnesium borohydride ($Mg(BH_4)_2$) as the first inorganic salt was demonstrated to be suited, because the BH_4^- ion is a relatively strong reducing species which could probably withstand the reducing atmosphere of the Mg anode. [43] He demonstrated reversible deposition and dissolution from electorates of $Mg(BH_4)_2$ in THF. High efficient magnesium plating and stripping (94%), high current densities (25 mA/cm^2 stripping peak current) and low overpotential (-0.3 V for deposition and 0 V for dissolution) were observed. [43] However this electrolyte system had a very low current density and narrow stability window and the synthesis of such compounds is expensive and consumes long time. Based on $Mg(BH_4)_2$ a new kind of Mg salt $Mg[B(OR)_4]_2$ was developed by Zhao-Karger et al. It can be easily dissolved in several organic solvents and its ionic conductivity is in the range of 10 $mScm^{-1}$, which is comparable with Li-ion batteries. The stability window is 4.3 V vs. Mg and is stable in the air. One of the most common magnesium salt is magnesium bis(trifluoromethanesulfonyl)imide ($Mg(TFSI)_2$). It was studied in DME solution for Mg-deposition/dissolution and showed a very large overpotential (-2.0 V) and very low current densities (0.01 mA/cm^2). However the coulombic efficiency can be improved by the addition of $MgCl_2$. [44, 45] The poor performance of $Mg(TFSI)_2$ electrolytes was attributed to the instability of the TFSI-ion, instability of glymes itself and impurities in the electrolytes, such as water. [46-48] Based on the weakly coordinating anion a new simple salt $[CB_{11}H_{12}]^-$ was reported. Due to the high solubility of $Mg(CB_{11}H_{12})_2$, 1 M solution in tetraglyme was investigated and the electrolyte had a high efficiency (98%) and low overpotential. [49] In acetonitrile solvent the oxidative stability of $Mg(CB_{11}H_{12})_2$ was found to be very high (4.9 V vs. Mg/Mg^{2+}). [50]

1.2.3 Calcium Batteries

In 1964 the first calcium application for the anode in primary battery was reported, which contained high temperature melting electrolytes. [51] This cell could be discharged at 450 °C for 11 min. Later the use of a Ca-Si alloy and Ca-Y alloy as negative electrode in high temperature solid state rechargeable batteries were investigated. [52] The first investigation of Ca metal in organic electrolytes was made by Aurbach et al. [53] In their studies the electrolytes made out of solvents including acetonitrile, tetrahydrofuran, butyrolactone, and propylene carbonate with the salts $Ca(ClO_4)_2$ and $Ca(BF_4)_2$ were examined. The results have shown that due to the passivation layer formed on the Ca metal, there was no successful calcium deposition in these solvent systems.

Only a few experiments for development of the cathode for calcium batteries was studied. In 2013 a new type of Ca-S as the cathode in batteries was studied. It showed that the discharge capacity is 600 mAh/g with a discharge rate of C/3.5. (1 C rate means that a fully *charged* battery rated at 1Ah should provide 1A for one hour.) However, the reversibility is quite low. [54] Recently another concept for the rechargeable calcium batteries, for example with air, were suggested. [55] Using a DMSO-based electrolyte at room temperature the formation of a Ca superoxide was suggested. The oxygen reduction reaction and oxygen evolution reaction in Ca^{2+} containing showed high reversibility of 95 %, which could be combined with the deposition of calcium for the use of the calcium air batteries. A compatible anode is also important for the rechargeable calcium batteries. The reversible plating and striping by using Ca metal as the anode was first reported by Peled et al. The electrochemical behavior of Ca-$SOCl_2$ electrolytes was tested and it had a specific energy density of 300 Wh/kg. However, an irreversible calcium plating and stripping (with the coulombic efficiency of 5 %) due to the formation of a passivation layer ($CaCl_2$) was observed. Otherwise, alloys are considered to be an alternative anode for calcium batteries.

The development of the electrolytes for calcium batteries is challenged by the possible formation of a passivation layer, which does not allow the penetration by Ca^{2+} ion. Usually, the passivation layer on top of the Ca metal mainly composed of $CaCO_3$ and $Ca(OH)_2$. [56] In the case of cathode compatibility, most of the electrolytes have only very limited electrochemical stability windows. Furthermore, the limited solubility of the calcium salts in the organic solvents restricts the choice of the organic electrolyte.

In 2015 the reversible calcium metal deposition and dissolution at high temperature was demonstrated by Ponrouch et al. Different concentrations (0.3 M to 0.8 M) of $Ca(TFSI)_2$, $Ca(ClO_4)_2$, and $Ca(BF_4)_2$ in PC:EC electrolytes were investigated and only the $Ca(BF_4)_2$ in PC:EC shown the reversible calcium platting and stripping with coulombic efficiency of 55 % at 100 °C and exhibit a high stability window of about 4.0 V. In their studies it was been also suggested that CaF_2 is deposited on the surface at the beginning of the reduction, which could work as an SEI-layer for calcium metal deposition. In 2017 Wang et al. reported that calcium can be reversibly (95 %) plated and stripped at room temperature out of 1.5 M $Ca(BH_4)_2$ in THF. [57] It was also found in their studies that CaH_2 was formed during the deposition, which is ion conductive and could protect the surface of calcium metal. Unfortunately, the CaH_2 layer was found to grow upon cycling and is highly reactive. Recently, a chemical-electrochemical deposition mechanism for Ca plating on Pt and Au was suggested. [58] Starting with the hydrogen adsorption, the kinetics of Ca deposition is faster with Pt than with Au. More recently

the electrolyte of $Ca[B(hfip)_4]_2$ in DME for calcium plating and stripping was demonstrated by groups of Nazar [59] and Fichtner [60]. It was shown that the calcium platting and stripping out of $Ca[B(hfip)_4]_2$ in DME is reversible (80 % to 90%) at room temperature. A high oxidative stability up to 4.5 V and high ionic conductivity more than 8 mS/cm was observed. However, the CaF_2 was found to be the decomposition product.

References

[1] V. Neburchilov, H. J. Wang, J. J. Martin, W. Qu, *Journal of Power Sources* **2010**, *195*, 1271.

[2] Y. Zhang, X. Zhang, J. Wang, W. C. McKee, Y. Xu, Z. Peng, *The Journal of Physical Chemistry C* **2016**, *120*, 3690.

[3] G. Girishkumar, B. McCloskey, A. C. Luntz, S. Swanson, W. Wilcke, *Journal of Physical Chemistry Letters* **2010**, *1*, 2193.

[4] G. Zubi, R. Dufo-LÃ³pez, M. Carvalho, G. Pasaoglu, *Renewable and Sustainable Energy Reviews* **2018**, *89*, 292.

[5] K. Li, S. R. Galle Kankanamge, T. K. Weldeghiorghis, R. Jorn, D. G. Kuroda, R. Kumar, *The Journal of Physical Chemistry C* **2018**, *122*, 4747.

[6] S. Choi, G. Wang, *Advanced Materials Technologies* **2018**, *3*, 1700376.

[7] A. Ponrouch, J. Bitenc, R. Dominko, N. Lindahl, P. Johansson, M. R. Palacin, *Energy Storage Materials* **2019**, *20*, 253.

[8] J. Muldoon, C. B. Bucur, T. Gregory, *Chemical Reviews* **2014**, *114*, 11683.

[9] Z. Ma, D. R. MacFarlane, M. Kar, *Batteries & Supercaps* **2019**, *2*, 115.

[10] J. Luo, Y. Bi, L. Zhang, X. Zhang, T. L. Liu, *Angewandte Chemie International Edition*, *58*, 6967.

[11] H. Dong, Y. Liang, O. Tutusaus, R. Mohtadi, Y. Zhang, F. Hao, Y. Yao, *Joule* **2019**, *3*, 782.

[12] L. Zan, D. Xing, A. Abd-El-Latif, H. Baltruschat, *Beilstein Journal of Nanotechnology* **2019**, *10*, 2541.

[13] P. Canepa, G. Sai Gautam, D. C. Hannah, R. Malik, M. Liu, K. G. Gallagher, K. A. Persson, G. Ceder, *Chemical reviews* **2017**, *117*, 4287.

[14] M. E. Arroyo-de Dompablo, A. Ponrouch, P. Johansson, M. R. PalacÃn, *Chemical Reviews* **2019**.

[15] B. D. McCloskey, R. Scheffler, A. Speidel, G. Girishkumar, A. C. Luntz, *Journal of Physical Chemistry C* **2012**, *116*, 23897.

[16] C. O. Laoire, S. Mukerjee, E. J. Plichta, M. A. Hendrickson, K. M. Abraham, *Journal of the Electrochemical Society* **2011**, *158*, A302.

[17] M. D. Tikekar, S. Choudhury, Z. Tu, L. A. Archer, *Nature Energy* **2016**, *1*, 1.

[18] A. C. Kozen, A. J. Pearse, C.-F. Lin, M. Noked, G. W. Rubloff, *Chemistry of Materials* **2015**, *27*, 5324.

[19] F. Y. Fan, W. C. Carter, Y. M. Chiang, *Advanced Materials* **2015**, *27*, 5203.

[20] L. Porz, T. Swamy, B. W. Sheldon, D. Rettenwander, T. FrÃ¶mling, H. L. Thaman, S. Berendts, R. Uecker, W. C. Carter, Y. M. Chiang, *Advanced Energy Materials* **2017**, *7*, 1701003.

[21] A. Eftekhari, *Advanced Energy Materials* **2018**, *8*, 1801156.

[22] A. C. Kozen, C.-F. Lin, O. Zhao, S. B. Lee, G. W. Rubloff, M. Noked, *Chemistry of Materials* **2017**, *29*, 6298.

[23] Y. Liu, D. Lin, Z. Liang, J. Zhao, K. Yan, Y. Cui, *Nature communications* **2016**, *7*, 10992.

[24] B. Liu, W. Xu, P. Yan, S. T. Kim, M. H. Engelhard, X. Sun, D. Mei, J. Cho, C.-M. Wang, J.-G. C. Zhang, *Advanced Energy Materials* **2017**, *7*, 1602605.

[25] N. Togasaki, T. Momma, T. Osaka, *Journal of Power Sources* **2016**, *307*, 98.

[26] T. D. Gregory, R. J. Hoffman, R. C. Winterton, *Journal of the Electrochemical Society* **1990**, *137*, 775.

[27] J. L. Andrews, A. Mukherjee, H. D. Yoo, A. Parija, P. M. Marley, S. Fakra, D. Prendergast, J. Cabana, R. F. Klie, S. Banerjee, *Chem* **2018**, *4*, 564.

[28] M. Liu, Z. Rong, R. Malik, P. Canepa, A. Jain, G. Ceder, K. A. Persson, *Energy & Environmental Science* **2015**, *8*, 964.

[29] Z. Li, X. Mu, Z. Zhao-Karger, T. Diemant, R. J. r. Behm, C. KÃ¼bel, M. Fichtner, *Nature communications* **2018**, *9*, 1.

[30] H. S. Kim, T. S. Arthur, G. D. Allred, J. Zajicek, J. G. Newman, A. E. Rodnyansky, A. G. Oliver, W. C. Boggess, J. Muldoon, *Nature Communications* **2011**, *2*.

[31] Z. Zhao-Karger, X. Zhao, O. Fuhr, M. Fichtner, *Rsc Advances* **2013**, *3*, 16330.

[32] Z. Zhao-Karger, X. Zhao, D. Wang, T. Diemant, R. J. r. Behm, M. Fichtner, *Advanced Energy Materials* **2014**, *5*, 1401155.

[33] B. Sievert, J. Haecker, F. Bienen, N. Wagner, K. A. Friedrich, *ECS Transactions* **2017**, *77*, 413.

[34] Y. Cheng, Y. Shao, L. R. Parent, M. L. Sushko, G. Li, P. V. Sushko, N. D. Browning, C. Wang, J. Liu, *Advanced Materials* **2015**, *27*, 6598.

[35] T. S. Arthur, N. Singh, M. Matsui, *Electrochemistry Communications* **2012**, *16*, 103.

[36] S.-B. Son, T. Gao, S. P. Harvey, K. X. Steirer, A. Stokes, A. Norman, C. Wang, A. Cresce, K. Xu, C. Ban, *Nature Chemistry* **2018**, *10*, 532.

[37] D. Aurbach, Z. Lu, A. Schechter, Y. Gofer, H. Gizbar, R. Turgeman, Y. Cohen, M. Moshkovich, E. Levi, *Nature* **2000**, *407*, 724.

[38] E. G. Nelson, S. I. Brody, J. W. Kampf, B. M. Bartlett, *Journal of Materials Chemistry A* **2014**, *2*, 18194.

[39] A. J. Crowe, J. L. DiMeglio, K. K. Stringham, B. M. Bartlett, *The Journal of Physical Chemistry C* **2017**.

[40] T. J. Carter, R. Mohtadi, T. S. Arthur, F. Mizuno, R. Zhang, S. Shirai, J. W. Kampf, *Angewandte Chemie-International Edition* **2014**, *53*, 3173.

[41] L. C. Merrill, J. L. Schaefer, *Langmuir* **2017**, *33*, 9426.

[42] C. Liao, B. Guo, D.-e. Jiang, R. Custelcean, S. M. Mahurin, X.-G. Sun, S. Dai, *Journal of Materials Chemistry A* **2014**, *2*, 581.

[43] R. Mohtadi, M. Matsui, T. S. Arthur, S.-J. Hwang, *Angewandte Chemie-International Edition* **2012**, *51*, 9780.

[44] I. Shterenberg, M. Salama, H. D. Yoo, Y. Gofer, J.-B. Park, Y.-K. Sun, D. Aurbach, *Journal of the Electrochemical Society* **2015**, *162*, A7118.

[45] M. Salama, I. Shterenberg, L. Jw Shimon, K. Keinan-Adamsky, M. Afri, Y. Gofer, D. Aurbach, *The Journal of Physical Chemistry C* **2017**, *121*, 24909.

[46] J. G. Connell, B. Genorio, P. P. Lopes, D. Strmcnik, V. R. Stamenkovic, N. M. Markovic, *Chemistry of Materials* **2016**.

[47] N. N. Rajput, X. Qu, N. Sa, A. K. Burrell, K. A. Persson, *Journal of the American Chemical Society* **2015**, *137*, 3411.

[48] Y. Yu, A. Baskin, C. Valero-Vidal, N. T. Hahn, Q. Liu, K. R. Zavadil, B. W. Eichhorn, D. Prendergast, E. J. Crumlin, *Chemistry of Materials* **2017**, *29*, 8504.

[49] O. Tutusaus, R. Mohtadi, T. S. Arthur, F. Mizuno, E. G. Nelson, Y. V. Sevryugina, *Angewandte Chemie* **2015**, *127*, 8011.

[50] O. Tutusaus, R. Mohtadi, N. Singh, T. S. Arthur, F. Mizuno, *ACS Energy Letters* **2017**, *2*, 224.

[51] S. M. Selis, J. P. Wondowski, R. F. Justus, *Journal of the Electrochemical Society* **1964**, *111*, 6.

[52] J. Schoonman, A. Wolfert, *Journal of the Electrochemical Society* **1981**, *128*, 1522.

[53] D. Aurbach, R. Skaletsky, Y. Gofer, *Journal of the Electrochemical Society* **1991**, *138*, 3536.

[54] K. A. See, J. A. Gerbec, Y. S. Jun, F. Wudl, G. D. Stucky, R. Seshadri, *Advanced Energy Materials* **2013**, *3*, 1056.

[55] P. Reinsberg, C. J. Bondue, H. Baltruschat, *Journal of Physical Chemistry C* **2016**, *120*, 22179.

[56] J. S. Young, M. Smeu, *Journal of Physical Chemistry Letters* **2018**, *9*, 3295.

[57] D. Wang, X. Gao, Y. Chen, L. Jin, C. Kuss, P. G. Bruce, *Nature Materials* **2017**, *17*, 16.

[58] K. Ta, R. Zhang, M. Shin, R. T. Rooney, E. K. Neumann, A. A. Gewirth, *ACS applied materials & interfaces* **2019**, *11*, 21536.

[59] A. Shyamsunder, L. E. Blanc, A. Assoud, L. F. Nazar, *ACS Energy Letters* **2019**, *4*, 2271.

[60] Z. Li, O. Fuhr, M. Fichtner, Z. Zhao-Karger, *Energy & Environmental Science* **2019**.

Chapter 2: Fundamentals and Experimental Methods

2.1 Fundamentals

2.1.1 Electron Transfer

Electrochemical kinetics describes the evolution of mass and electron flow throughout the interface between the electrode and electrolyte. The goal is to understand the observed behavior of electrode kinetics concerning potential and concentration. An electrode reaction such as:

$$O + ne^- \leftrightarrow R \tag{2.1}$$

can be described by the Nernst equation, which shows the relationship between the electrode potential and the bulk concentrations of the participants. This equation is:

$$E = E^0 + \frac{RT}{nF} ln \frac{C_0^*}{C_R^*} \tag{2.2}$$

Where C_0^* and C_R^* are the bulk concentrations, and E^0 is the formal potential. The kinetics of reactions on the electrode is strongly affected by the applied potential.

In general, the concentration changes of the reactant close to the surface affect the potential. Thus, the overpotential at an electrode may include a term for this concentration difference which is termed concentration overpotential. Current or current density describes the overall rate of an electrode reaction. The electrode potential and overpotential affect the current density. If the pure electron (charge) transfer is considered as the rate-limiting process, the Butler-Volmer equation (Equ. 2.3) for current density in terms of overpotential is valid. [1, 2]

$$I = i_{Ox} + i_{Red} = i_0 \left(\exp\left(\frac{\alpha nF}{RT}\eta\right) - \exp\left(\frac{-(1-\alpha)nF}{RT}\eta\right)\right) \tag{2.3}$$

Where i_0 is the exchange current density; α is the transfer coefficient; z is the electron number; R is the gas constant; T is the temperature; η is the overpotential and F is the faraday constant. Figure 2.1 shows a typical current overpotential curve. The solid curve shows the total current. The symmetry is affected by the transfer coefficient α. In most cases for a reaction with an unknowns value α can be approximated with $\alpha = 0.5$. For a relative high overpotential of $z|\eta| \geq 60\ mV$ the relationship can be described by the following equations:

$$\eta = -\frac{2.3RT}{\alpha nF} log|I| + \frac{2.3RT}{\alpha nF} log I_0 \qquad for\ (\eta \leq 0) \tag{2.4}$$

$$\eta = -\frac{2.3RT}{(1-\alpha)nF} log|I| + \frac{2.3RT}{(1-\alpha)nF} log I_0 \qquad for\ (\eta \geq 0) \tag{2.5}$$

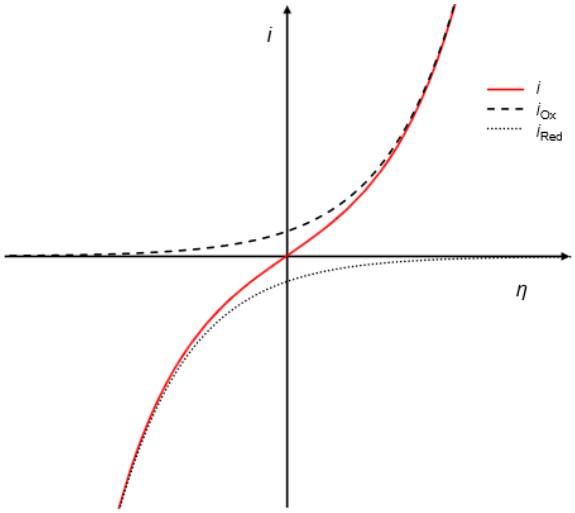

Figure 2. 1: Current-overpotential curves for the system $O + ne^- \leftrightarrow R$ with $\alpha = 0.5$, T=298 K, The dashed line show the current i_{ox} and the dotted line show the current i_{Red}.

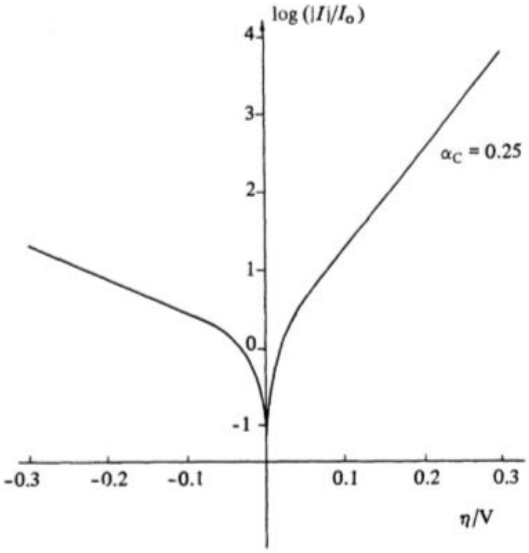

Figure 2. 2: Tafel-Plots of log $(|I|/I_0)$ versus overpotential.

The Equation 2.4 and 2.5 contains the information about the exchange current density I_0 and transfer coefficient α. The Plot of $\log|I|$ against overpotential η (Figure 2.2) is often used because the value η is usually the controlled variable. The exchange current density can be obtained by the extrapolation of the slope $\eta = 0$. The relationship between the slope and the overpotential is given by:

$$\frac{d(log|I|)}{d\eta} = -\frac{\alpha nF}{2.3RT} \tag{2.6}$$

and

$$\frac{d(log|I|)}{d\eta} = -\frac{(1-\alpha)nF}{2.3RT} \tag{2.7}$$

Usually, for a one-electron transfer process, the value of the Tafel slope is 120 mV/dec.

2.1.2 Mass Transfer

If the electron transfer is very fast, the reaction rate on the electrode will be controlled by the mass transport rate. The mass transfer can be affected by diffusion, migration, and convection. Diffusion is a process of central importance. The diffusion rate of chemical reactants is dependent on the concentration gradient and also on the diffusion coefficient. Fick's laws are often used to describe flux and the concentration as functions of time and position for diffusion. [3] Fick's first law is given by:

$$-J_O(x,t) = D_0 \frac{\partial D_0(x,t)}{\partial x} \tag{2.8}$$

Where, J_O is the diffusion flux; $\partial D_0 / \partial x$ is the concentration gradient and D_0 is the diffusion coefficient. Fick's first law shows that the flux is proportional to the concentration gradient for one-dimensional diffusion. Fick's second law as following:

$$\frac{\partial C_0(x,t)}{\partial t} = D_0\left(\frac{\partial^2 C_0(x,t)}{\partial x^2}\right) \tag{2.9}$$

It describes the change of concentration as a function of time. If the reactant is controlled by pure diffusion at the electrode, the current is related to the flux at the electrode. The solution of these equations requires a certain boundary conditions. In most cases of an alloying process in this thesis because the thickness of the alloy layer (Sb, Sn, and Bi layers) is limited and therefore the more usual boundary condition of semi-infinite diffusion is valid only for a short period of time.

2.1.3 Electrochemical Metal Deposition and Alloying

During repeatedly charging and recharging battery systems, the corresponding metal ions are consecutively deposited and redisolved into the electrolyte. The electrochemical deposition of metals involves the reduction of ions from the solution, which can be described as the following equation:

$$M^{n+} + ne^- \rightarrow M \tag{2.10}$$

The model for a detailed description of the interface is now often used as depicted in Figure 2.3. This reaction occurs at the interface between a solid-state and a solution. The charged metal ions (so called ion transfer) pass through the interface between the electrode and the electrolyte. The interface consists of a metal layer, a diffuse layer, and an inner layer. [4] Electrochemical deposition takes place in this very thin region, where there is a very high electric field (10^9 V/cm). [5]. The electric double layer can be described by a plate condenser, where one plate is the metal surface with its charge and the other is formed by the solvated ions. The nonspecifically adsorbed ions form the outer Helmholtz plane (OHP), which is also called the

diffuse layer, which extends from OHP to the bulk of the solution. The specifically adsorbed ions and their centers form the inner Helmholtz plane (IHP). The potential profile drop in this interface is also shown in Figure 2.3.

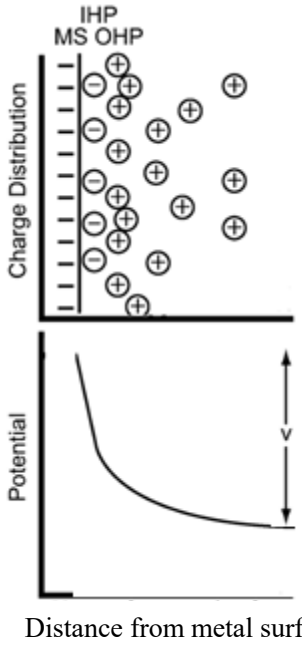

Figure 2. 3: Schematic presentation of the electrochemical interface with a negative charged metal electrode.

In comparison with bulk deposition where the crystallographic structure is not deeply changed, electrochemical alloying of the metal has a conversion process that new compounds will be created. (Equation 2.11) The substrate structure will be then formed again during the de-alloying process. (Equation 2.12)

$$M + xA^{n+} + xne^{-} \rightarrow A_xM \quad (2.11)$$

$$A_xM \rightarrow M + xA^{n+} + xne^{-} \quad (2.12)$$

The formation of a new crystalline structure during the deposition or allying from a solution starts with the transportation of metal ions to the interface and adsorption on the metal surface. Then the crystal growth starts through the nucleation process. Afterwards, the formed nuclear cluster grows to form a two-dimensional (2D) and three-dimensional phase formation (3D). [6-8].

2.2 Experimental Methods

2.2.1 Cyclic Voltammetry

Cyclic voltammetry is a very important and useful electrochemical technique that helps us to

investigate the redox mechanics and transport properties of a system in the electrolytes. In this method, the electrode potential E is changed periodically between two limits with a constant speed. The potential scan with a typical voltammogram is shown in Figure 2.4.

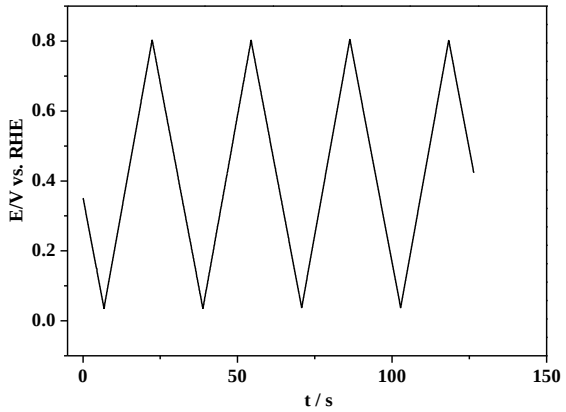

Figure 2. 4: A cyclic voltammetry potential wave form with switching potentials.

The observed faradaic current can provide information on the rate of reactions occurring at the working electrode. In the case of the multistep process, the rate is determined by the slowest step, charge transfer at the electrode surface or mass transfer. When the rate-determining process is the charge transfer reaction for the metal deposition, the current density given by the Butler-Volmer equation. The peak current is dependent on the scan rate, which is described by the Randles-Sevcik equation: [9].

For only diffusion controlled process:

$$I_p = 2.99 \times 10^5 n A C_0 D^{0.5} v^{0.5} \quad (2.13)$$

For charge transfer and diffusion controlled process:

$$I_p = 2.99 \times 10^5 n \sqrt{\alpha n_\alpha} A C_0 D^{0.5} v^{0.5} \quad (2.14)$$

Where I_p is the peak current; n is the electron number; α is the transfer coefficient; A is the electrode area; C_0 is the bulk concentration (or, in case of diffusion into a solution or alloy the maximaum or saturation concentration); D is the diffusion coefficient and v is the sweep rate. We can simply estimate the diffusion coefficient from assuming simple solid-state diffusion as rate limiting for a reversible and irreversible system from the slope of a plot of peak current versus the square root of the sweep rate. The transfer coefficient is usually assumed to be 0.5.

2.2.2 Three Electrode Cell

All experiments are carried out in a three-electrode cell. The schematic representation of a typical three-electrode cell is shown in Fig. 2.5. In a traditional three-electrode cell, three different electrodes (working, counter, and reference) are placed in the electrolyte solution. The

working electrode is placed in the central part, the reference electrode is placed in the left part and is connected to the working electrode compartment with a Luggin capillary, which is used to reduce the ohm losses. The counter electrode is placed in the right part and separated from the central part by a glass fit, in order to void the diffusion of the products formed of the counter electrode to the working electrode. During three-electrode experiments, charge flow (current) primarily occurs between the working electrode and the counter electrode while the potential of the working electrode is measured with respect to the reference electrode.

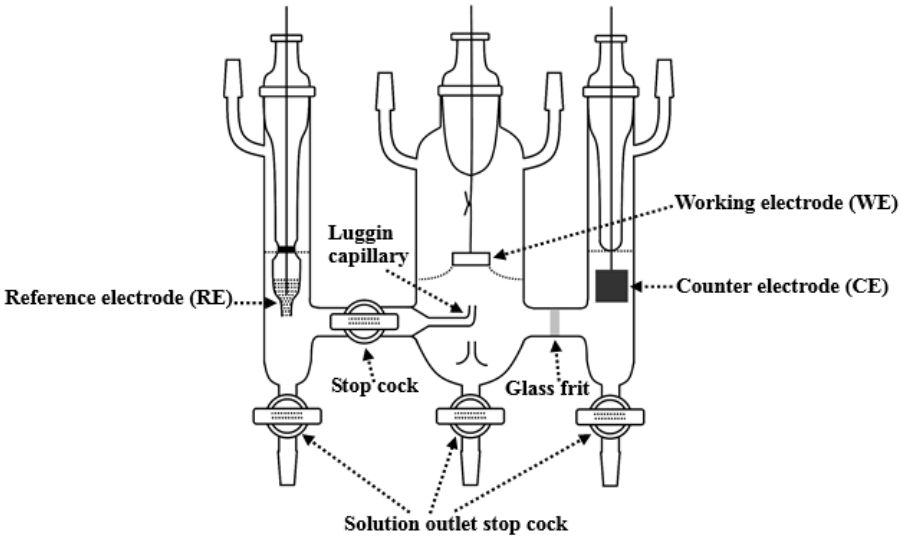

Figure 2. 5: Schematic representation of a three electrode cell for electrochemical experiments. Taken from [10]

A disk poly Au electrode with a diameter of 1 cm was used for electrochemical metal deposition and alloying. A gold single crystal electrode with a diameter of 1 cm was used for EC-STM measurement. A sputtered Au and Pt membrane was used for DEMS measurements.

The reversible hydrogen electrode (RHE) [11] was used for Sb, Sn, and Bi deposition. For Li, Mg, and Ca deposition and alloying, a lithium wire, a magnesium wire, and a calcium wire were used as the reference electrode, respectively. For some experiments of metal deposition in the glove box, an Ag wire in a 0.1 M $AgNO_3$ in MeCN solution was used for the reference electrode. Also, an Ag wire was used as the reference electrode for EC-STM measurement.

A gold wire was employed as the counter electrode in the case of Au working electrode for metal deposition in the glass cell and the EC-STM cell. For Li, Mg, and Ca deposition and alloying, a lithium wire, a magnesium wire, and a calcium wire were used as the counter electrode, respectively.

2.2.3 Potential Step Measurement

When an experiment involving an instantaneous change in potential from a value where no

electrochemical reaction occurs to a value in the mass transfer controlled region is considered, we record the current time transient to understand the kinetics of the electrolysis. A planar electrode (in this thesis a gold disk electrode with a surface area of 0.785 cm^2) and an unstirred electrolyte are used. The absolute solution of the linear diffusion equation with the initial and semi-infinite condition is known as the Cottrell-Equation: [12],

$$i = \frac{nFA\sqrt{D}C_0}{\sqrt{\pi}t} \tag{2.15}$$

In Figure 2.6 a schematic plot of current versus the time for potential step measurement is shown. Three kinds of current transients (after the initial double layer charge) correspond to three different electrochemical reaction conditions. When the reaction is diffusion-controlled, the current drops after the applied potential according to the Cottrell Equation. (Curve a in Fig 2.6) When the reaction is kinetic-controlled, the initial current stays constant. (Curve b in Fig 2.6) For reactions controlled both by kinetic and diffusion, the current drop is shown as curve c in Fig 2.5 and is given by:

$$i = i_{CT} - \frac{2i_{CT}}{nFAC_0\sqrt{\pi}\sqrt{D}} \cdot \sqrt{t} \tag{2.16}$$

Where i_{CT} is the charge transfer current density. For case a), the effect of depleting the electroactive species near the surface leads to an inverse $t^{0.5}$ function. Normally a plot of i vs. $t^{0.5}$ is needed to estimate the diffusion coefficient.

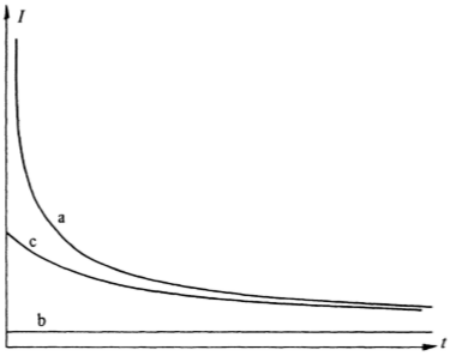

Figure 2. 6: Schematic of the Current-time dependent transients for a potential step experiment. a) diffusion-controlled reaction; b) kinetic-controlled reaction and c) both kinetic and diffusion controlled reaction.

The concentration profiles in Fig. 2.7 visualize the diffusion limitation for an electrochemical reaction. After the potential is applied, a diffusion layer is formed, and the concentration gradient of the active species appears because of the difference from bulk concentration. Then the concentration is the time-dependent falloff in the concentration at the electrode surface, which leads to the Cottrell Equation. The different behaviours are due to the different time.

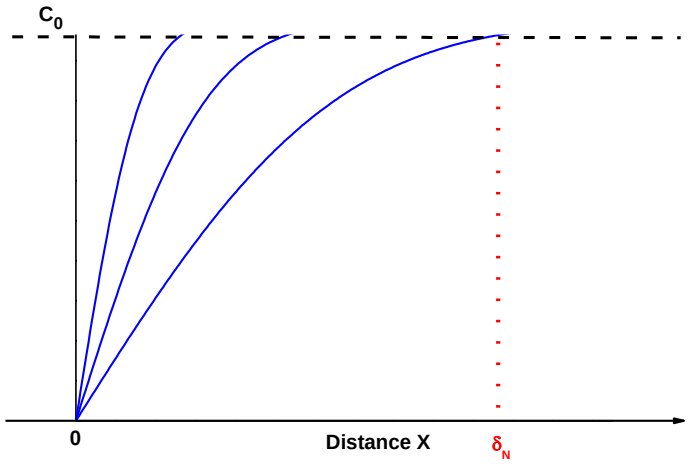

Figure 2. 7: Concentration profiles after applying potential. The diffusion layer is limited with the red dashed line.

2.2.4 Potentiostatic Intermittent Titration Technique (PITT)

The Potentiostatic Intermittent Titration Technique (PITT) is one of the most often used techniques to study the diffusion of the active electrode materials. The diffusion coefficient can be calculated from the resulting signal. In a typical PITT measurement, the open circuit potential (OCP) of the cell is recorded at the beginning. Afterwards, a negative potential at which the electrode reaction starts is applied, and the current signal is recorded for a certain period, followed by relaxation. The time for applied potential and the relaxation is usually the same. Then, a negative potential increment of 0.05 V (depending on the system) is applied to the onset potential, followed by relaxation. The same potential increment is consecutively applied, starting from the voltage resulting from the previous step and the current is recorded. The potential pulse is applied until the potential limit for the electrode reaction is reached. Each potential pulse is followed by the same relaxation time. Afterwards, a positive potential increment is consecutively applied to the voltage of the previous step. This is repeated until the positive potential limit is reached. An example of the recorded potential and current signals of PITT measurement for magnesium alloying with Sb is shown in Figure 2.8.

During both negative and positive pulse, the electrode forth and back reaction result in corresponding currents. The current signal shows the information about the diffusion coefficient of the electrode material. Depending on the reaction type the diffusion coefficient can be estimated by using the respective Equation. (Eq. 2.14 for only diffusion controlled and eq. 2.15 for charge transfer and diffusion controlled reaction) A important advantage of the PITT measurement is that the concentration of the alloyed metal ions (Li, Mg, and Ca) in the host

solid (Sb, Sn, and Bi layers) reaches often equilibrium during the relaxation period. Thus, not only the diffusion coefficient can be estimated in each step of alloying, but the equilibrium potential is determined for the concentrations reached in each step.

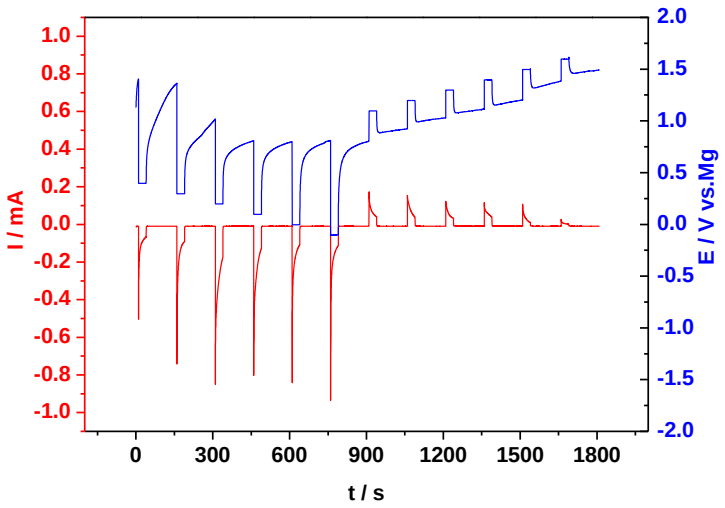

Figure 2. 8: Potential and current time curve recorded in a PITT measurement of Mg-alloying and de-alloying with Sb. Potential from 0.4 V to -0.1 V vs. Mg for the alloying and from 1.0 V to 1.5 V vs. Mg for the de-alloying. (Sb: ~105 nmol/cm^2; surface area: 0.785 cm^2)

2.2.5 Differential Electrochemical Mass Spectrometry (DEMS)

Differential Electrochemical Mass Spectrometry (DEMS) is an analytical technique that combines electrochemical cell experimentation with mass spectrometry. It allows in situ mass resolved determination of gaseous or volatile electrochemical reactants, reaction intermediates, and products in real time. The experimental setup consists of an electrochemical half-cell, the membrane interface, and a vacuum system including a quadrupole mass spectrometer.

A typical “classic” DEMS cell used in this work is shown in Fig 2.9. It consists of a cell holder made of stainless steel, which is connected to the DEMS with a KF 40 connection. A short PVC adapter is placed between the cell and DEMS to avoid the electrical connection. A Teflon membrane with an outer diameter of 25 mm is used for additional sealing. The sputtered gold coated porous Teflon membrane with 50 nm Au and d = 18 mm is placed in the central part. A good wire with a diameter of 0.05 mm is placed in a circle on the outside of the gold sputtered membrane in order to connect the working electrode with the potentiostat by touching the stainless steel cell holder. A Teflon ring with d = 40 mm, which has a hole in the centre, is placed on it. The glass cell is placed on top with a steel ring and mechanically supported by a steel frit. The reference electrode is immersed in the electrolyte via the spider. The counter electrode is separated from the working and reference electrodes by a frit.

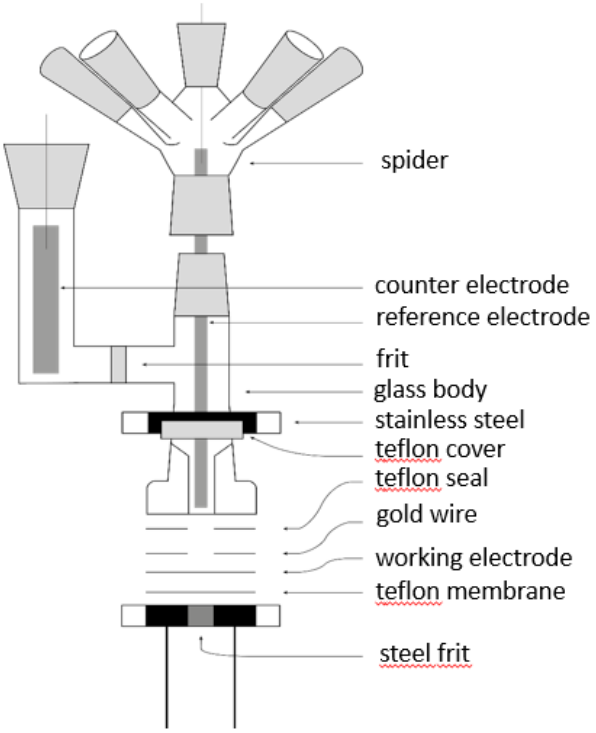

Figure 2. 9: Schematic representation of a classic DMES-cell.

The interface between the electrolytes and the vacuum is realized by a PTFE membrane. A schematic drawing of the interface between the electrolytes and the vacuum is shown in Fig. 2.10. The liquid is not allowed to pass through the membrane due to its hydrophobicity. However, the dissolved gaseous and other volatile species can pass through the pores in the membrane. The critical pore size is limited by the surface tension of the liquid and the contact angle between the liquid and Teflon.

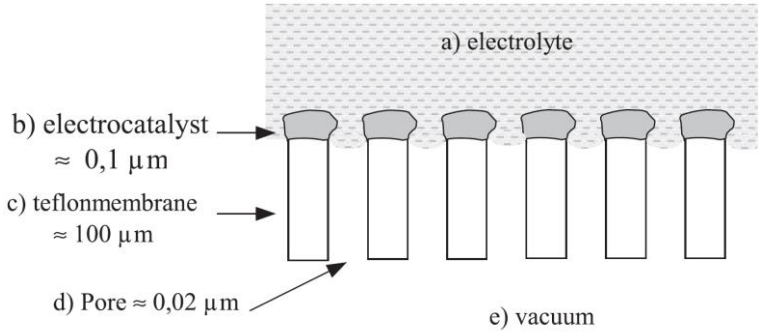

Figure 2. 10: Schematic representation of the interface between the electrolytes and the vacuum. a) Electrolytes; b) catalyst sputter deposited; c) Teflon; d) the pores in the membrane and e) the vacuum. Taken from [13].

A schematic representation of the experimental setup is shown in Figure 2.11. The electrochemical cell is connected to the first vacuum chamber. Due to the special construction of the vacuum system with two turbo pumps the partial pressure of the product and thus the ion

current of the MS is proportional to the product formation rate. Ions are created through electron bombardment ionization in the ion source. Only ions with a selected mass-to-charge ratio will reach the detector.

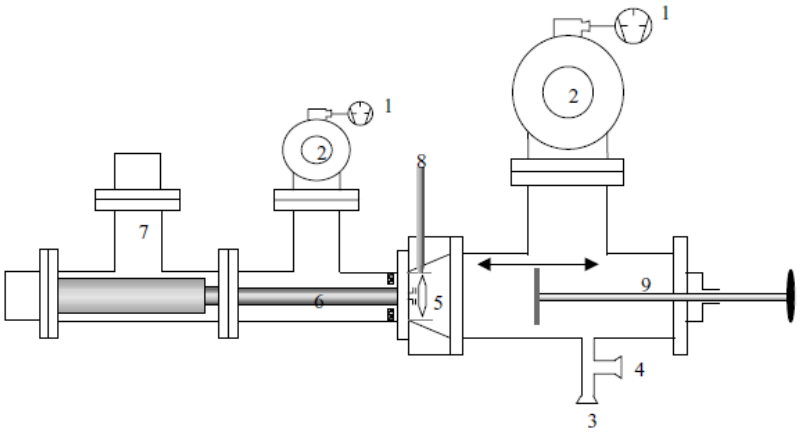

Figure 2. 11: Schematic representation of the vacuum system (1) rotary pumps, (2) turbo-molecular pumps, (3) connection to the electrochemical cell, (4) connection to the calibration leak, (5) ion source, (6) quadrupole rods, (7) secondary electron multiplier, (8) direct inlet, (9) linear drive. Taken from [13].

2.2.6 Electrochemical Quartz Crystal Microbalance (eQCM)

The Quartz Crystal Microbalance is a standard technique to detect small changes in mass by help of the piezoelectric effect. The mechanical deformation of certain crystals occurs by electrical charges on the surface of the solid phase if the crystal unit cell does not have a symmetry center. When a potential with a suitable frequency is applied, the crystal consequently oscillates. Because the frequency of this oscillator decreases with increasing mass, the changes of the frequency on the quartz crystal reflects the change of mass. The relationship between the frequency change of the quartz crystal Δf and the mass change Δm is given by Sauerbrey-Equation: [14]

$$\Delta f = -\frac{2f_0^2}{\sqrt{\rho_q \mu_q}} \cdot \frac{\Delta m}{A} = C_f \Delta m \tag{2.17}$$

Where f_0 is frequency of the quartz; ρ_q is the density of the quartz; μ_q is the shear module of the quartz and A is the electrode surface area. All the constants can be written into C_f which is called calibration constant. It is assumed that the deposited layers have a uniform thickness over the active area of the quartz crystal because the calibration constant for the quartz is not uniform. It has been shown that the calibration constant is highest in the center of the electrode. It decreases monotonically to the edge of the electrode and can almost be neglected at and outside the electrode boundary. Because the frequency changes of the quartz crystal can be detected, a

very small change in mass can be measured by QCM. The eQCM was first used to investigate the electrochemical deposition of metals on electrode surfaces. Shay and Bruckenstein reported about the galvanic deposition of about 10 layers of silver on the working electrode of a 10 MHz quartz crystal. [15] The in situ eQCM measurements for electrochemical metal deposition provides an easy way to study fundamental processes such as underpotential- and bulk deposition.

The schematic representation of the experimental setup for the eQCM is shown in Figure 2.12. By using a three-electrode cell, the shift of frequency, the changes of current and potential can be observed. The mass changes can be determined with the Sauerbrey equation. An AT quartz is usually used in the eQCM experiments.

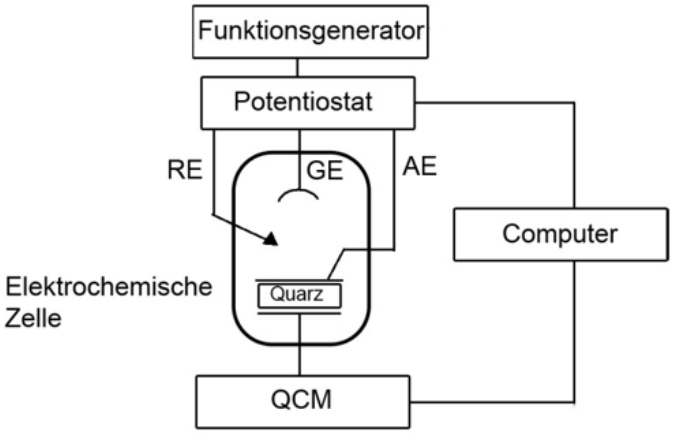

Figure 2. 12: Schematic representation of experiment setup for an eQCM mesurament.

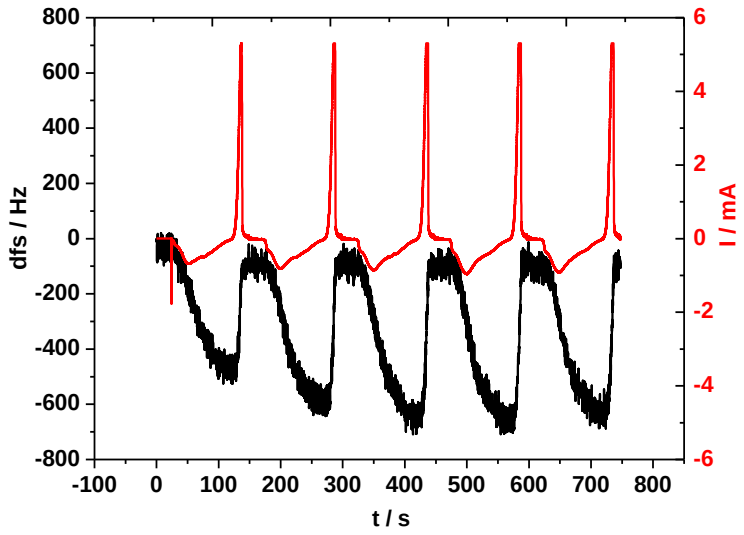

Figure 2. 13: Calibration of the quartz crystal in 5 mM CuSO4 in 1M H2SO4 with a sweep rate of 10 mV/s. black line: frequency change; red line: current transient.

The calibration of the quartz crystal was determined in a saturated 5 mM $CuSO_4$ in 1 M H_2SO_4 solution. The counter electrode is a gold wire and the reference electrode is RHE. Figure 2.13 shows the frequency change and the current transient during the calibration. In the cathodic sweep, the Cu is deposited on the surface of the quartz crystal and is dissolved in the electrolytes in the anodic sweep. The calibration constant can be calculated by the following equation:

$$C_f = \frac{Slope_{dfs/dt} \cdot F \cdot n}{M_{Cu}} \tag{2.18}$$

2.2.7 Scanning Tunneling Microscope (STM)

Scanning tunneling microscope (STM) is a classic instrument to investigate the surface morphology at the atomic level. [16] The first STM was created by Gerd Binnig and Heinrich Rohrer in 1981 at IBM in Zürich. [17] With STM, a sharp metal tip is placed close to the surface and a small bias voltage is applied between the tip and the sample. This causes a current and the electron can flow through the vacuum gap between the tip and the sample. This process is a quantum mechanical phenomenon and is called the tunnel effect. In Figure 2.14 the mechanism of the tunneling process schematically is shown.

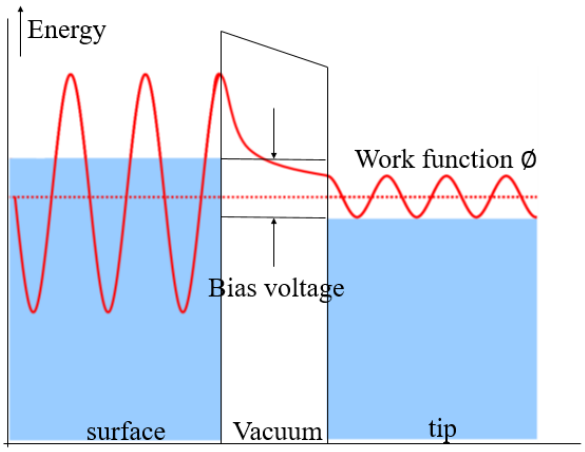

Figure 2. 14: Schematic diagram of the tunneling effect based on quantum mechanics.

The electrons tunnel under the applied voltage (V) through the vacuum gap between the STM tip and the sample surface, which result in measurable tunneling current I_T. This is described by:

$$I_t = I_0 \cdot e^{(-2k_t d)} \quad k_t = \frac{\sqrt{2m\Phi}}{\hbar} \tag{2.19}$$

Where I_0 is the function of the bias voltage and density of states in both tip and sample, m is the mass of the electron, d is the distance between the tip and sample, Φ is the work function

and ħ is the Planck's constant. [18] An STM setup is divided to four parts, a metal tip, a scanner, tunneling current amplifier, and a feedback loop. A schematic overview of the STM setup is shown in Figure 2.15.

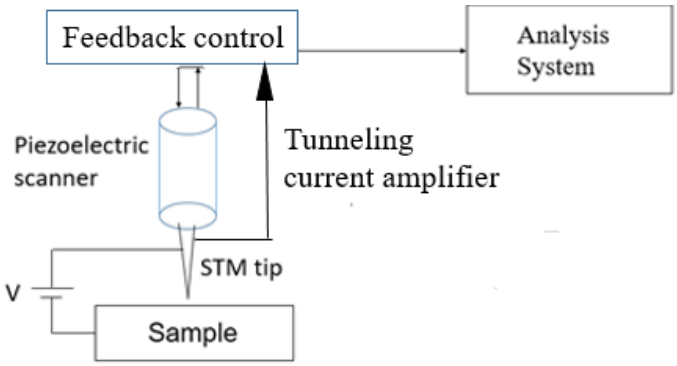

Figure 2. 15: Schematic representation of STM setup.

The STM image is realized by scanning the tip over the sample surface. There are two different operation modes. In the constant current mode, the tip move over the surface and the tip position is continuously changed to keep the tunneling current constant. On the very smooth surface under ideal conditions, the constant tunneling current refers to the constant distance between the sample surface and the tip. The tip moves automatically up and down to adjust the tunneling current with a constant value by the feedback voltage. This mode is usually used to test a relatively rough surface.

In the constant height mode, the feedback is very slow and the tip height position is kept constant. So, the changes of tunneling current are recorded for the STM image. The scan of the tip can be performed, when the feedback system is switched off or the scan rate is higher than the feedback response rate. The STM works therefore with a high sampling rate and a fast image recording so that the changes on the surface can be observed in real time. The constant height mode is usually used to probe a relatively smooth surface.

An ideal STM tip should be in atomic size, have good electrical conductivity, and be mechanically stable. Also, the tip should allow the tunneling current through the atoms at the tip. To avoid the reaction between the tip and the electrolyte, the tip must be well isolated except for a small area at the top of the tip. The STM tips were prepared by electrochemical etching [19] of Pt/Ir (90:10) wire with a diameter of 0.25 mm in 2 M KOH + 4 M KSCN solution. With this method the tips are produced routinely with similar sharpness and the time of the production is reduced. Then, they are coated with hot melt glue containing different types of polymer to minimize the Faradic current.

The preparation of the tips is carried out in a small beaker with a ring anode made by Pt wire.

A DC signal of 1.6 V with an AC square wave signal of 6.5 V at 1 kHz is applied while the tip is being manufactured. The lower part of the wire is covered with a Teflon tube and then placed in the solution. As soon as the exposed part of the wire comes into contact with the solution, the process begins immediately. The wire is then pulled back a little to create a hanging meniscus configuration. (see Fig. 2.16) The etching of the tip continues around the meniscus until there is an atomic sharp on the top of the tip. After a certain time, the lower half part of the wire is dropped into the beaker together with the Teflon tube and then thrown away. The top is rinsed thoroughly with Mili-Q water and then is inserted into the hot melt glue stick for short time and then retracted quickly.

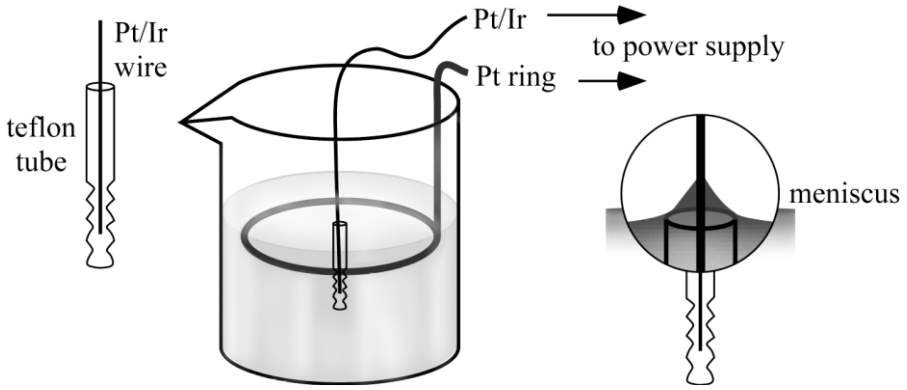

Figure 2. 16: Schematic representation of preparation of the STM tips. Taken from [20].

The Electrochemical Scanning Tunneling Microscopy (EC-STM) is an advanced method based on the principles of STM measurements for studying the interface between the electrode and the electrolyte. The fundamental theory for STM and EC-STM is generally the same. But two additional parts are used in order to introduce the STM as an EC-STM. First, a three-electrode cell (STM cell see. Fig. 2.17) consisting of a working electrode, a reference electrode, and a counter electrode is used. It was made of Kel-F material. The main chamber was made for containing electrolyte solution. The contact of the working electrode and electrolyte was through a hole with a diameter of 0.8/0.6 cm made at the bottom of the main chamber. An additional small chamber was made for placing the reference electrode, which can be connected to the main chamber via a small hole. The counter electrode was a wire placed around the inner main chamber. This configuration is similar to a normal three-electrode system with a potentiostat, in which the potential of the working electrode can be controlled by the high impedance reference electrode while the current flow between the working and counter electrodes.

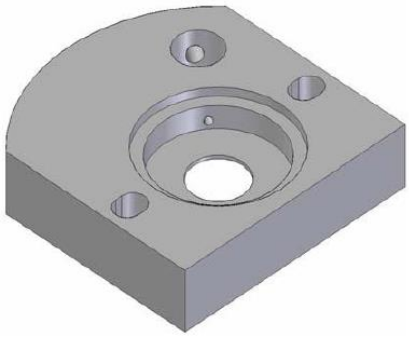

Figure 2. 17: Schematic view of STM cell.

2.2.8 Chemicals

All the chemicals and gases used in this work are summarized in table 2.1. In addition, the Li, Mg, and Ca deposition (also their alloying) are carried out in the glove box. The glass devices required for the measurements were placed in KOH solution in order to clean them from organic impurities and anions. Then the glass device had to be washed with Mili-Q water and dried in the oven for over two hours. All aqueous electrolytes were also made with Mili-Q water. All nonaqueous solutions were prepared in an MBraun glove box filled with Ar.

Table 2. 1: List of chemicals and gases.

Name	**Formula**	**Company**	**Purity (degree)**
Tetraglyme	$C_{10}H_{22}O_5$	Acros organics	99%
Acetonitrile	CH_3CN	Acros organics	99.9%
Tetrahydrofuran	C_4H_8O	Sigma-Aldrich	≥ 99.9%
Acetone	C_3H_6O	Sigma-Aldrich	99.5%
Dimethyl sulfoxide	C_2H_6OS	Acros Organics	99.7%
Propylen Carbonat	$C_4H_6O_3$	Sigma-Aldrich	anhydrous 99,7 %
Ethylen Carbonate	$C_3H_4O_3$	Sigma-Aldrich	98 %,
Sulphuric acid	H_2SO_4	Merck	95-97%, Supra pure
Perchlorat acid	$HClO_4$	VWR Chemicals	37%
Potassium hydroxide	KOH	Sigma Aldrich	85%
Copper Sulfate	$CuSO_4$	Sigma-Aldrich	≥99%
Tinn(II) sulphate	$SnSO_4$	Acros Organics	99%
Bismuth(III) oxide	Bi_2O_3	Sigma-Aldrich	≥ 98%, pure
Antimony(III) oxide	Sb_2O_3	Aldrich	99.999%

Silver nitrate	$AgNO_3$	Sigma-Aldrich	99%
Bis(trifluoromethane)sulfonimide lithium	$(CF_3SO_2)_2NLi$	Sigma-Aldrich	≥ 99%
Lithium aluminium hydride	$LiAlH_4$	Sigma-Aldrich	95%
Magnesium borohydride	$Mg(BH_4)_2$	Sigma-Aldrich	95%
Bis(trifluoromethane)sulfonimide magnesium	$Mg(TFSI)_2$	Solvionic	99.5%
Magnsium trifluoromethanesulfonate	$Mg(OTf)_2$	Merck	97%
Magnesium chloride	$MgCl_2$	Sigma	98%
Aluminium chloride	$AlCl_3$	Fluka	99%
Magnesium perchlorate	$Mg(ClO_4)_2$	Sigma-Aldrich	≥ 99%
Magnesium hydride	MgH_2	Sigma-Aldrich	Hydrogen storage grade
Calcium borohydride	$Ca(BH_4)_2$	Sigma-Aldrich	95%
Calcium borohydride bis(tetrhydrofuran)	$Ca(BH_4)_2 \cdot 2THF$	Merck	99%
Bis(trifluoromethane)sulfonimide calcium	$Ca(TFSI)_2$	Merck	95%
Calcium perchorate	$Ca(ClO_4)_2$	Sigma-Aldrich	99%
Calcium tetrafluoroborate	$Ca(BF_4)_2$	Alfa-Aesar	anhydrous 95%
Calcium trifluoromethanesulfonate	$Ca(OTf)_2$	Merck	99.9%
Calcium chloride	$CaCl_2$	Sigma-Aldrich	anhydrous ≥93%
Argon	Ar	Air Liquide	99.999%

References

[1] J. A. V. Butler, *Transactions of the Faraday Society* **1924**, *19*, 729.

[2] S. Fletcher, *Journal of Solid State Electrochemistry* **2009**, *13*, 537.

[3] A. Fick, *Ann. Phys.* **1855**, *170*, 59.

[4] S. Srinivasan, *Fuel Cells: From Fundamentals to Applications*, Springer Science & Business Media, New York, **2006**.

[5] W. Schmickler, E. Santos, *Interfacial Electrochemistry*, Springer-Verlag Berlin Heidelberg, Berlin, Heidelberg, **2010**.

[6] W. J. Lorenz, G. Staikov, *Surface Science* **1995**, *335*, 32.

[7] E. B. Budevski, G. T. Staikov, W. J. Lorenz, *Electrochemical Phase Fomation and Growth: An Introduction to the Initial Stages of Metal Deposition*, Wiley-VCH, Weinheim, **1996**.

[8] M. Paunovic, M. Schlesinger, *Fundamentals of Electrochemical Deposition, 2nd Edition*, John Wiley & Sons, Inc.,, Hoboken, **2006**.

[9] N. G. Tsierkezos, *Journal of Solution Chemistry* **2007**, *36*, 289.

[10] L. Zan, (Bonn), **2017**.

[11] F. G. Will, *Journal of the Electrochemical Society* **1986**, *133*, 454.

[12] A. J. Bard, L. R. Faulkner, *Electrochemical Methods: Fundamentals and Applications, 2nd Edition*, Wiley, New York, **2001**.

[13] H. Baltruschat, *Journal of the American Society for Mass Spectrometry* **2004**, *15*, 1693.

[14] G. Sauerbrey, *Zeitschrift für Physik* **1959**, *155*, 206.

[15] S. Bruckenstein, M. Shay, *Electrochimica Acta* **1985**, *30*, 1295.

[16] R. H. Fowler, L. Nordheim, *Physical and Engineering Sciences* **1928**, *119*, 173.

[17] G. Binnig, H. Rohrer, C. Gerber, E. Weibel, *Physical Review Letters* **1982**, *49*, 57.

[18] F. J. Giessibl, *Reviews of Modern Physics* **2003**, *75*, 949.

[19] J. Lindahl, T. Takanen, L. Montelius, *Journal of Vacuum Science & Technology B* **1998**, *16*, 3077.

[20] S. Iqbal, C. BonduÌˆ, H. Baltruschat, *The Journal of Physical Chemistry C* **2015**, *119*, 20515.

Chapter 3: Investigation of Metal (Li, Mg, and Ca) Deposition and Dissolution

3.1. Introduction

The rechargeable Metal-Air-Batteries require a reversible metal deposition during discharge and dissolution during charge. In the case of Li deposition, an artificial solid electrolyte interphase (SEI) is usually formed, which enhances the deposition and the coulombic efficiency. [1] The electrodeposit ion of divalent cations (Mg and Ca) is difficult due to the high activity of the metals. The anions are not stable and a passivation layer ($Mg(OH)_2$ and MgO for Mg deposition and $CaCO_3$ and $Ca(OH)_2$ for Ca deposition) is formed instead of SEI on the anode. [2]

Recently, a study with 3 different concentrated electrolytes (1 M, 2 M and 3 M LiTFSI in DMSO) for Li-O_2 battery was reported. [3] It shows the cells with a concentration of more than 1 M LiTFSI have a high cycling stability and coulombic efficiency. However, there is no formation of a stable SEI on the surface of the metallic lithium and the solvent molecule is not stable in contact with lithium metal. During the deposition the Li-metal can react with DMSO, resulting in electrolyte decomposition. [4] It was reported that the SEI formed without LiF in 1.0 M LiTFSI/DMSO solution, [5] the absence of a thin layer of LiF might be the reason for the decomposition of the electrolyte and for the low coulombic efficiency of the Li-deposition. The LiF layer improves the electrochemical performance of a Li-deposition in a DMSO containing electrolyte. In a Field Emission Scanning Electron Microscope (FE-SEM) experiment whisker-like dendrites were observed during the lithium deposition from the 1 M LiTFSI/DMSO [5], which could results a low current density and low coulombic efficiency.

The electrodeposition of magnesium for rechargeable battery applications has been studied for the past few years. Grignard reagents based on organomagnesium compounds were first studied by Gregory et al. [6] The magnesium-aluminium chloride complex (MACC) in glymes has been tested and shows high reversibility of deposition and dissolution, high anodic stability (-3.2 V vs. Mg/Mg^{2+}) and is compatible with some cathodes. [7] Later, new electrolyte solutions such as, $Mg(BH_4)_2$ in THF or TG, [8] $Mg(TFSI)_2$ in DME, [9] were demonstrated for Mg deposition. In addition, many theoretical and analytical studies have been reformed to understand the mechanism of magnesium deposition and dissolution.

Wang et al. reported a electrolyte containing 1.5 M $Ca(BH_4)_2$ in THF for calcium deposition and dissolution. [10] It shows a high reversibility (up to 95 %) at room temperature. However, CaH_2 was formed during the deposition and the CaH_2 layer was found to grow upon cycling

and is highly reactive. Furthermore, this electrolyte has a low electrochemical window (3.0 V vs. Ca/Ca^{2+}) and very limited stability. In addition, most of the calcium salts are not soluble or less soluble in organic solvents. Also, not all of the Ca salts are commercially available.

In this work, the Li, Mg, and Ca deposition and dissolution was investigated with various non-aqueous electrolytes. The suitability for Li-O_2 batteries of electrolytes with two different concentrations (1 M and 3 M LiTFSI in DMSO) was studied with CV and DEMS, in order to understand the mechanisms of the decompositions reaction. The non-aqueous electrolytes (MACC in TG, $Mg(BH_4)_2$ in TG, and $Mg(TFSI)_2$ in TG) were studied for the Mg deposition/dissolution. Different Ca salt types, different concentrations in several organic solvents were investigated for Ca deposition and dissolution. The target was to find out the suitable electrolyte systems for reversible metal (Li, Mg, and Ca) plating and stripping at room temperature. The fundamental physicochemical electrolyte properties such as ion conductivity, cation solvation by solvent, and anions need to be understood.

3.2 Experimental

Chemical reagents

A polycrystalline Au electrode and Pt electrode was used as working electrodes for lithium deposition measurements. LiTFSI (95%, Sigma-Aldrich) was dried under reduced pressure before use. All the Mg salts is from Sigma-Aldrich. 1.5 M $Ca(BH_4)_2 \cdot 2THF$ (99%, Sigma-Aldrich) was first dissolved in THF and then filtered after stored overnight. Extra dry DMSO (99.7%, Acros Organics) was stored over molecular sieve before use. The THF (under 5 ppm H_2O) was distilled by inorganic institute from university of Bonn and stored over molecular sieves (3 Å). Extreme dry solvents (TG and DMSO) were stored over molecular sieves (3 Å). All the metal electrochemical deposition measurements were carried out in the MBraun glovebox (H_2O < 0.5 ppm, O_2 < 0.5 ppm).

Preparation of MACC

The Tetraglyme was distilled over sodium and stored over molecular sieves (3 Å) until the water content reaches to an amount less than 5 ppm. The water content has been determined by Coulometric Karl Fischer titration (Mettler Toledo). $MgCl_2$ was heated overnight under vacuum at 290°C and then stored under thionyl chloride for 1 week. At low pressure the thionyl chlorid was removed completely. All materials were handled in an Argon filled glovebox. The MACC electrolyte was prepared by adding tetraglyme (20.5ml) to $MgCl_2$ (0.966g). While stirring the

$AlCl_3$ (1.368g) was then added stepwise. The whole mixture was stirred overnight after addition of an equivalent (H_2O: 63 ppm) amount of MgH_2 to reduce the water content (to below 10 ppm).

Cyclic Voltammogram (CV)

Electrochemical measurements for metal deposition (Li, Mg, and Ca) were carried out in a conventional three-electrode glass H-cell consisting of three compartments for fixing the working electrode, reference electrode, and counter electrode. The working electrode is placed in the central compartment and contacted with a solution in a hanging meniscus configuration. The reference electrode is placed in the compartment where it is connected to the central compartment with a Luggin capillary. The counter electrode is placed in the compartment, separated from the central compartment by a glass frit. A polycrystalline Au electrode was used as working electrodes for Mg and Ca deposition measurements. A good polished Li wire was then used as a counter electrode and an Ag wire in a solution of 0.1 M $AgNO_3$ in DMSO was used as a quasi-reference electrode. Magnesium foil was then used as a counter electrode and another one as a quasi-reference electrode. Calcium foil was then used as a counter electrode and another one as a quasi-reference electrode.

All electrochemical measurements were carried out using a potentiostat purchased from Pine Instruments, Inc. (model AFBPC1) in combination with home-made LabVIEW program (National Instruments GmbH, Munich, Germany) for recording the cyclic voltammograms (CVs)

DEMS Experiments

The electrolytes were investigated by mass spectrometry using the classical DEMS cell in the glovebox in order to determine the decomposition products. The cell was already described before in details in previous chapter 2. A porous spotterd Au and Pt membrane was used as a working electrode. A Li wire was used as a counter electrode and a 1.0 M $AgNO_3$ solution in acetonitrile as a quasi-reference electrode. The working electrode compartment was separated from the counter electrode by a frit to avoid the diffusion of the products formed on the counter electrode into the working electrode compartment.

3.3 Results and Discussion

3.3.1 Lithium Deposition and Dissolution

Figure 3.1 shows the electrochemical deposition of lithium at Au sputtered Gore-Tex Teflon membrane electrode using 1 M and 3 M LiTFSI/DMSO electrolyte. The peak current for the Li deposition in 1 M solution drops fast with increment of the cycle number. Comparatively, only small changes of the current in 3M solution were observed during cycling. The molar ratio in 1 M is 11.80 with a Li-solvent coordination number of 4.4, whereas in 3 M the un-coordinated DMSO solvent is 0, explaining that the 3 M electrolytes has a stronger electrochemical performance. [3] In dilute solution the coordination number was reported as 4, [11] which results in poor cycling behavior of lithium deposition. In 1 M solution more side reactions take place between the un-coordinated DMSO and fresh Li-metal. Otherwise in Figure 3.1b two significant shoulders at -2.8 V and -3.5 V vs. Ag/Ag^+ could be observed in 3 M solution. Considering the phase diagram of Li-Au those shoulders shows that, the Li-Au alloy is formed during the deposition of lithium. But in 1 M solution the formation of Li-Au is not clearly seen because of too many side reactions. This Li-Au alloy, which was reported before as Li_3Au. [12] was deposited on the Au surface during the deposition.

A DEMS measurement for Li-deposition at Au sputtered Gore-Tex Teflon membrane electrode from an 1 M and 3 M LiTFSI/DMSO electrolyte system is shown in Figure 3.2a and 3.2b. The experiment was starting from 0.0 V vs. Ag^+/Ag for 1 M electrolyte and from -2.0 V vs. Ag^+/Ag for 3 M electrolyte with a sweep rate of 10 mV/s so that there is no Li-deposition taking place. Then the cycles are performed in the range of -4.0 V to 0.5 V for 1 M and -4.0 V to -2.0 V for 3 M with constant sweep rate. In fig. 3.2 the cycle number 2 (H_2), 18 (H_2O), 32 (O_2), 44 (CO_2), 45 (CH_3-CH_2-NH_2), 58 (CH_3-N-N-CH_3), 62 (CH_3-S-CH_3) and 78 (DMSO) are shown. CH_3-CH_2-NH_2 and CH_3-N-N-CH_3 could be formed by the reaction of the decomposition product Li_3N of the LITFSI with DMSO solvent molecule. CH_3-S-CH_3 is a decomposition product from DMSO molecule. A high signal for m/z = 2 in the MSCVs in cathodic direction starting at -3.0 V for both 1 M and 3 M solution is observed. Hydrogen is detected during the Li_3Au alloy formation and Li-deposition. The amount of the Hydrogen for 3 M solution is higher than 1 M solution. This hydrogen evolution could be the result of a small amount of water (20 ppm) in the electrolyte. The MSCVs for m/z = 18, 32, 44, 58, 62 and 78 all have the same shape. The m/z = 45 increase slightly negative of -3.5 V in the cathode sweep for 1 M electrolyte, where the Li-deposition occurs. It is not observed for the 3 M electrolyte. That indicates that the decomposition of the DMSO-molecule take place more in the 1 M solution than in 3M solution.

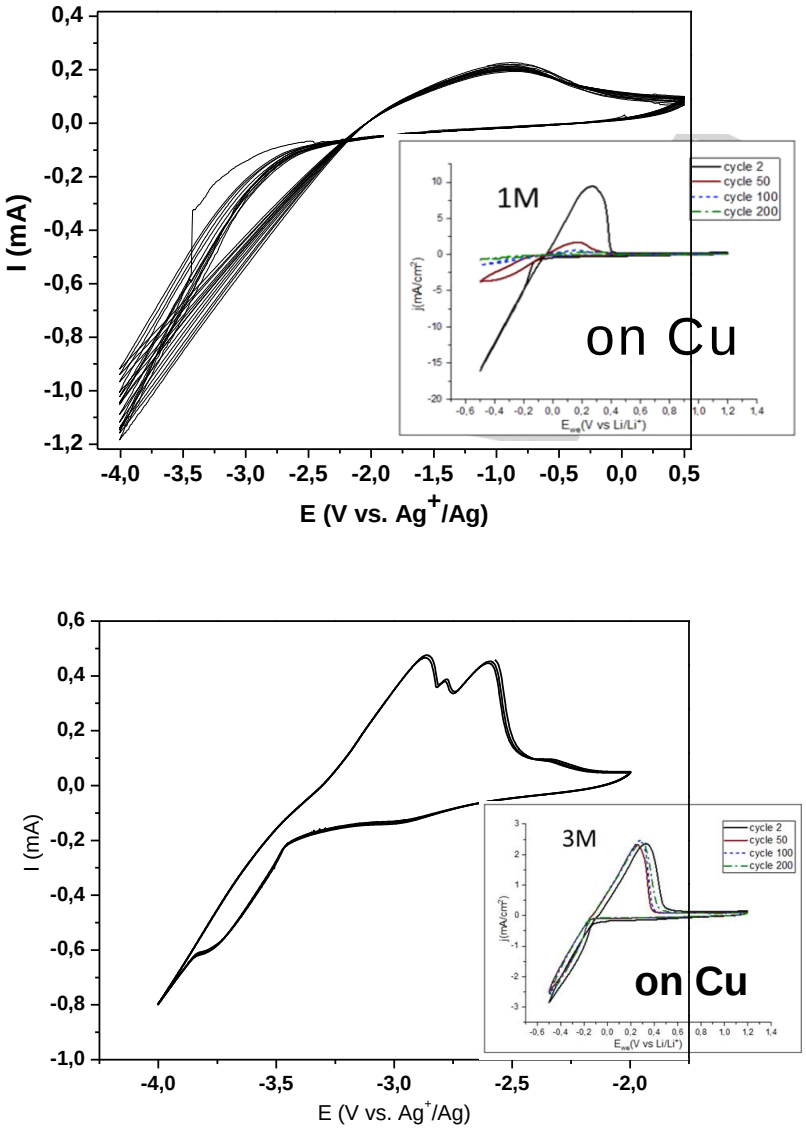

Figure 3. 1: Cyclo voltagramms of the Lithium deposition at Au sputtered Goretex teflon membrane electrode in a) 1 M LiTFSI/DMSO; b) 3 M LiTFSI/DMSO solution. Sweep rate: 10 mV/s. WE: Au; RE: Ag/Ag^+; CE: Au. Inset: lithium deposition in 1 M and 3 M LiTFSI/DMSO on a copper working electrode respectively (taken from [3]).

Figure 3.3 shows the electrochemical deposition of lithium at Pt sputtered Gore-Tex Teflon membrane electrode using 1 M and 3 M LiTFSI/DMSO electrolyte. The experiments started 0.5 V vs. Ag/Ag^+ in the cathodic direction with a sweep rate of 10 mV/s. At the open circuit voltage about 1.1 V there is no negative current when the working electrode contact with the electrolyte. After the potential reaching -2.2 V vs. Ag/Ag^+ the current increases slowly to negative values, this is attributed to an initial overpotential to form the nucleation on the Au electrode surface. (Figure 3.4 a) The current increases continuously during the negative sweep until -4.0 V, which indicate the Li-deposition on Pt surface. During the stripping reaction a small broad peak was observed in the positive sweep at -2.0 V, when -0.2 V is reached the dissolution

of lithium was complete. Considering to 3 M solution, the current drops at -2.0 V and gives rise to a shoulder, which might indicate that a Li-Pt alloy compound formed. (Figure 3.4 b) Actually there are many literature reports the platinum-lithium alloy formation. During the formation of the Pt-Li alloy the lithium plating reaction occurs on the Pt-Li alloy at such relatively low current. Once a SEI between the alloy and the solution formed, a subsequent lithium deposition could take place with high coulombic efficiency. The alloy formation at a lower negative potential than the Li-deposition is due the slower Li^+ diffusion. By using a Pt working electrode the Li-Pt alloy should occur at a lower potential near 0 V vs. Li^+/Li (-2.0 V vs. Ag/Ag^+). [13] [14]

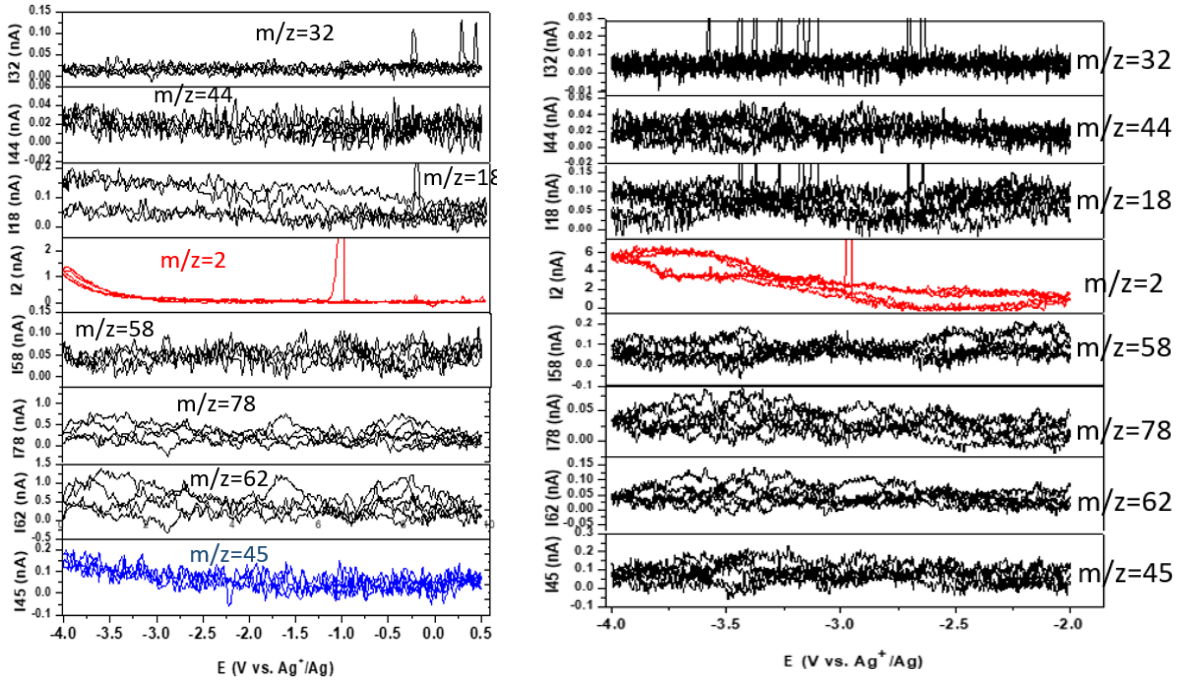

Figure 3. 2 MSCVs of Li-deposition for m/z = 2, 18, 32, 44, 45, 58, 62 and 78 on Au sputtered Goretex teflon membrane with sweep rate 10mV/s. Potentials vs. Ag^+/Ag. Left: in 1 M LiTFSI/DMSO; right: 3 M LiTFSI/DMSO.

After the potential reaches -3.5 V the fast current increase fast shows the lithium bulk deposition. In the anodic direction the lithium stripping occurs at the potential between -3.5 V and -2.0 V. Both CVs show that the efficiency of the Li-deposition and –dissolution on the Pt electrode is extremely low (~10 % for 1 M solution and ~20 % for 3 M solution) compared with the deposition on Au in 3 M solution (Figure 3.3 b) electrode. The reason for the poor efficiency of Li-deposition in DMSO containing electrolyte at Pt-electrode could be due to the formation of an unstable SEI layer, which continuously react with the electrolyte and results in a higher charge for the deposition. Another reason is the formation of a Li-Pt alloy, which is very stable after deposition on the surface and is not be dissolved into the electrolyte again during the

anodic sweep. This thin alloy layer can be react as a passivation layer. Otherwise it was reported that some decompositions products of LiTFSI, such as Li_2SO_3 and Li_2S, were formed when Li deposited. The Li_2S has a high solubility in DMSO, which means some amount of the charge is consumed during the lithium deposition on the Pt surface. It reduces the coulombic efficiency of lithium anode. Furthermore there are some other side reactions which could be take place during the deposition and dissolution such as solvent decomposition, H_2-evolution and oxygen reduction reaction.

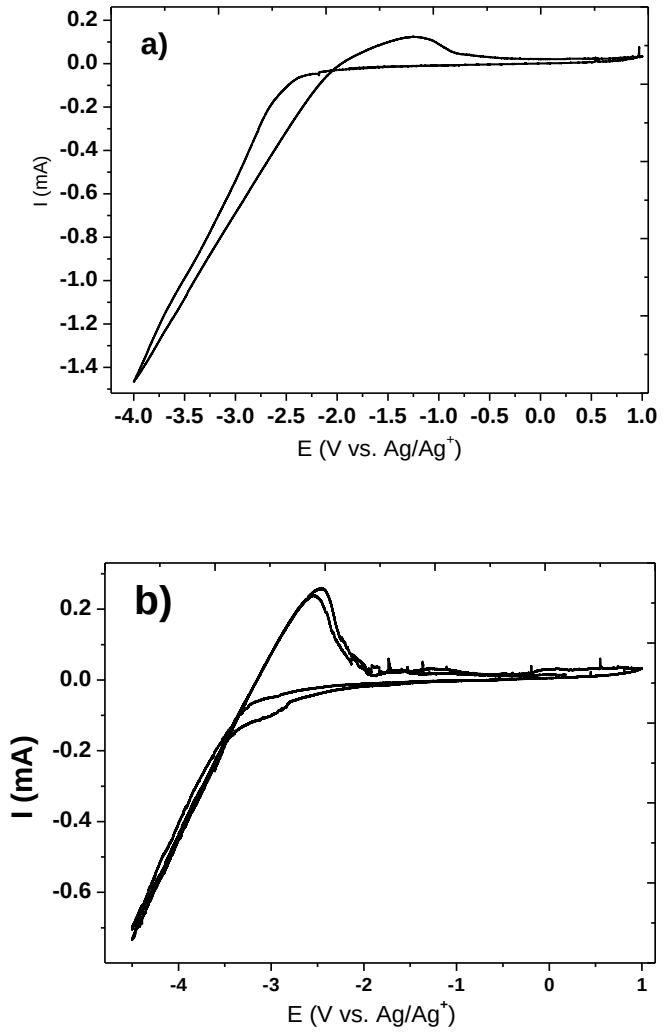

Figure 3. 3 Cyclic voltagramms of the Lithium deposition at Pt sputtered Goretex teflon membrane electrode a) 1 M LiTFSI/DMSO; b) 3 M LiTFSI/DMSO solution. Sweep rate: 10 mV/s. WE: Pt; RE: Ag/Ag+; CE: Pt. Inset: lithium deposition in 1 M and 3 M LiTFSI/DMSO on a copper working electrode respectively.

The MSCVs for the Li-deposition at Pt sputtered Goretex teflon membrane electrode from an 1 M and 3 M LiTFSI/DMSO electrolyte system are shown in Figure 3.4 a and 3.4 b. In the MSCV strong signals can be seen with m/z = 2 (H_2), 28(CO) and 62 (CH_3-S-CH_3) in the

cathodic direction, which starts with the Pt-Li alloy formation at the potential of -2.5 V vs. Ag/Ag^+. That means some small amount of hydrogen is detected in the cathodic sweep, which could be formed from reaction of Li metal with H_2O. The formation of CH_3-S-CH_3 is due to the decomposition of DMSO solvent molecule. A difference could be seen between 1 M and 3 M solution, in the anodic direction a huge signal for the CO_2 with m/z = 44 was observed when the potential reach to 0.5 V vs. Ag/Ag^+ for 1 M solution, (Figure 3.5 a) which is not observed for 3 M solution. Also, a signal for CH_4 with m/z = 16 was observed during the Li deposition. On the platinum electrode the decomposition of the electrolyte could occur more easily than on the Au electrode because of the higher reactivity of the Pt metal surface, especially for the hydrogen evolution.

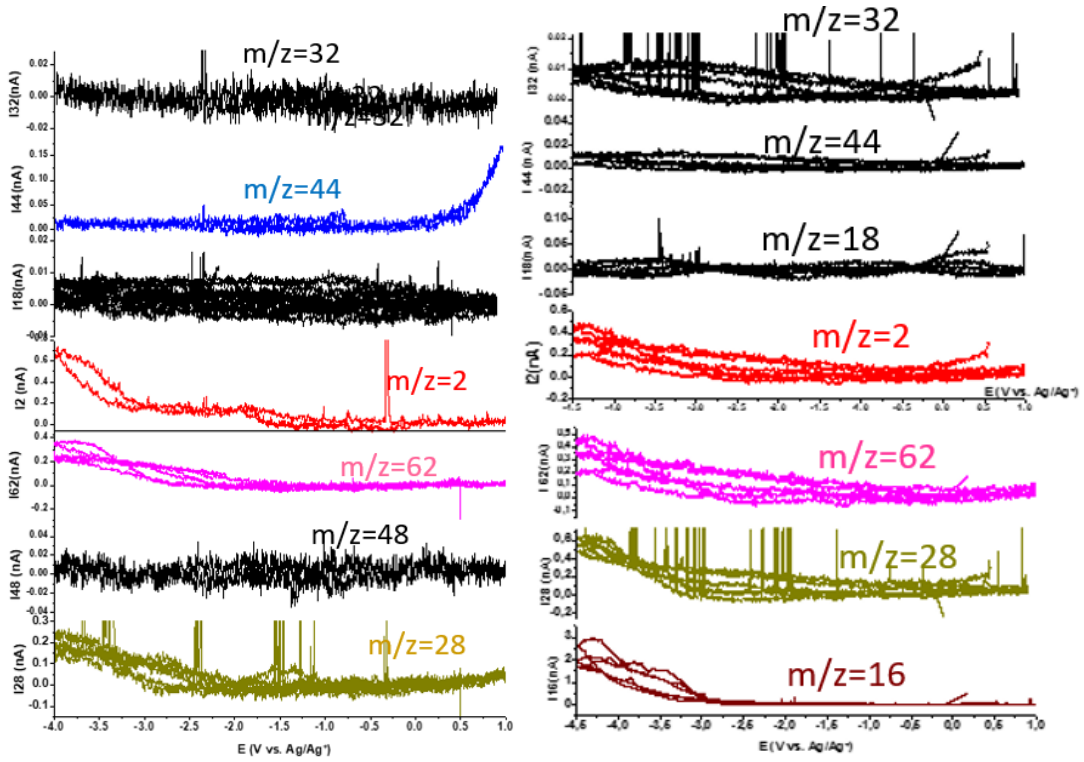

Figure 3. 4: CVs and MSCVs of Li-deposition for m/z = 2, 16, 18, 28, 32, 44, and 62 on Pt sputtered Goretex teflon membrane with sweep rate 10mV/s. Potentials vs. Ag+/Ag. Left: in 1 M LiTFSI/DMSO; right: 3 M LiTFSI/DMSO.

3.3.2 Magnesium Deposition and Dissolution

Figure 3.5 shows the electrochemical deposition of magnesium in 0.5 M MACC in TG solution with 100 mV/s. The experiment was started at 0.05 V vs. Ag/Ag+ in the cathodic direction. The open circuit potential of this electrolyte system is 0.65 V Ag/Ag^+. The black arrow in fig. 3.5 shows the direction of the sweep. It can be seen that the magnesium deposition starts at -2.85 V vs. Ag/Ag^+, and in the anodic direction a broad peak for magnesium dissolution which starts

at -2.34 V vs. Ag/Ag^+ in the first cycle. Both of these potentials shift more and more to -2.5 V vs. Ag/Ag^+ with increased cycle number i.e., the deposition process becomes more reversible (Figure 3.5) The coulombic efficiency, which was calculated from the charge of the deposition divide by the charge of dissolution, increases also from 84.3% in the first cycle to 99.9% in the stable CVs with 100 mV/s (Figure 3.6). The higher overpotential in the first cycle and the shift of this potential could be due to the freshly prepared MACC solution, which typically shows low Mg deposition and stripping reversibility at the beginning. [9, 15] The MACC solution should be first cycled until a nearly 100% reversibility of Mg-plating and stripping is observed. [15] They called this a "conditioning" of the MACC electrolytes. In the "conditioning" process some other side reactions occur, such as aluminium deposition consuming charge during the Mg-deposition. The low efficient deposition at beginning could be also due to the impurities present in reactants (water) as well as oligomers formed upon ring-opening polymerization during the initial synthesis of MACC, like in THF solvent. [15, 16]

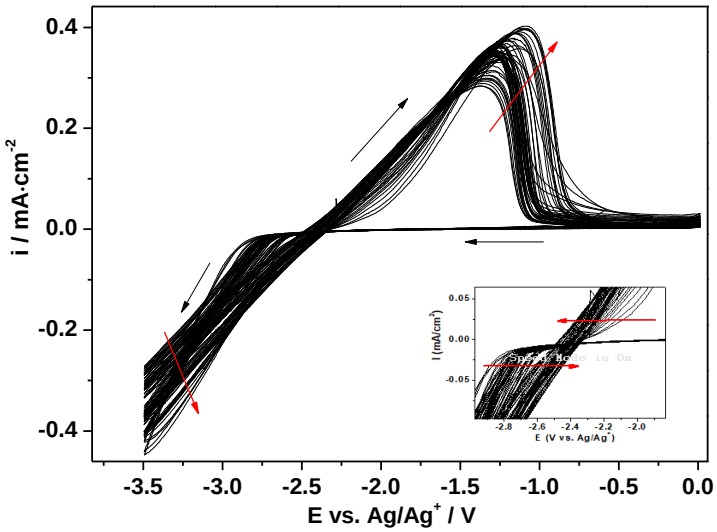

Figure 3.5: Cyclovoltammogramms for the Mg-deposition in 0.5 M MACC in TG on polycrystalline Au electrode with a sweep rate 100 mV/s. WE: Au; CE: Mg; RE: 0.1 M $AgNO_3$ in AN.

In Figure 3.7 the stable CVs for the magnesium deposition and dissolution in 0.5 M MACC in TG solution with different sweep rate from 10 mV/s to 100 mV/s are shown. This experiment was started with 100 mV/s and then switched to lower sweep rates, at the end with 100 mV/s as control. The coulombic efficiencies are all near 100 %. The oxidative stability of this electrolyte is greater than 3 V. An STM experiment has shown that no dendrites were formed in 0.5 M MACC/TG electrolyte. [17] Particles with a size of 10-30 nm and a height of 2 nm were

observed on the Au(111)-surface. A eQCM experiments shows a m.p.e value of 34 g/mol·e, which is higher than expected for pure Mg deposition (12 g/mol·e). It is due to some co-deposited compound with Al and Cl from the active species $[AlCl_4]^-$ during reversibility Mg deposition/dissolution in MACC in THF. [18] In the electrochemical deposition process of magnesium in MACC/TG system the dimer $[Mg_2(\mu\text{-}Cl)_3]^+$ cation was found to be the active species. The dimer $[Mg_2(\mu\text{-}Cl)_3]^+$ formed from the reaction between $MgCl_2$ and $[MgCl]^+$, which was formed from the aluminate-based Lewis acid reacts by transmetallation.

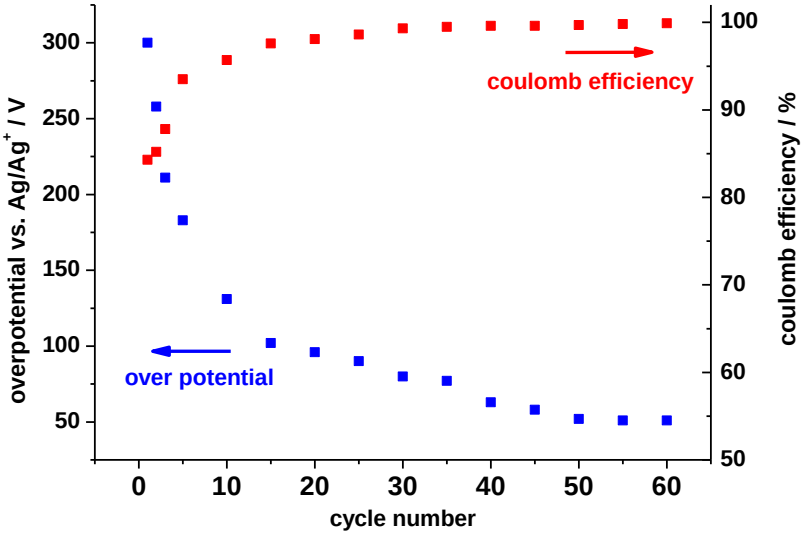

Figure 3.6: Magnesium deposition overpotential and coulombic efficiency as a function of cycle number.

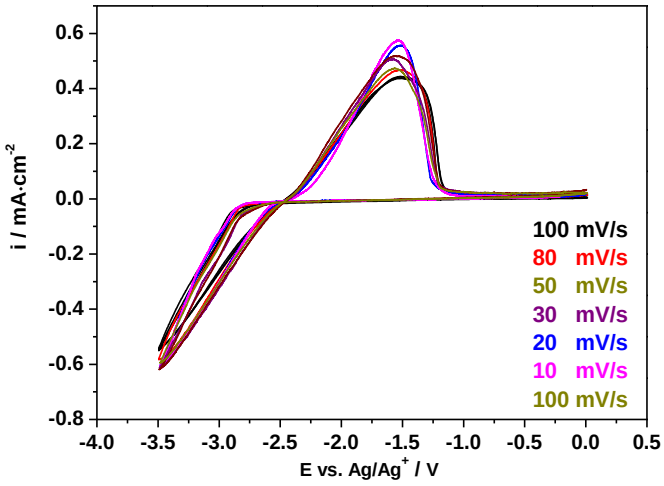

Figure 3.7: Stable CVs for Mg-plating and stripping in 0.5 M MACC in TG solution with different sweep rate.

A DEMs study has been investigated in order to check the stability of the MACC electrolyte. It has been found that ethylene formation as a decomposition product appears during the magnesium dissolution. [17] The ethylene was reductively formed by the reaction of Mg with tetraglyme.

The choice of the reference electrode is a problem. A silver wire also has been used as pseudo-reference electrode when testing the cell, but it is very dependent on the anion in the electrolytes. To avoid this issue, a calibration with a standard such as $Me_{10}Fc$ has been used. (Figure 3.8) The redox peaks appears at -0.2 V vs. Ag/Ag^+ and the Mg-deposition occurs at -2.5 V vs. $Me_{10}Fc^*$/ $Me_{10}Fc^{*+}$.

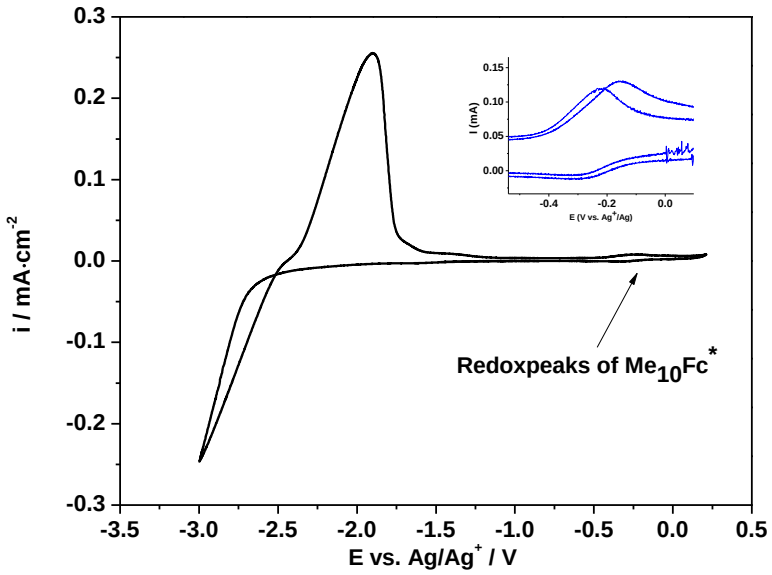

Figure 3.8: CV for Mg-plating and stripping in 0.5 M MACC + 2 mM $Me_{10}Fc$ in TG solution with 10 mV/s.

Figure 3.9 shows the electrochemical deposition of magnesium out of $Mg(BH_4)_2$-based electrolyte in TG. It is seen that the Mg-deposition from 1.5 M $Mg(BH_4)_2$/TG without $MgCl_2$ leads to a lower coulombic efficiency. (70 % without $MgCl_2$ and 95 % with $MgCl_2$) The addition of Cl^- ion also decreases both the onset potential of the Mg-deposition and dissolution. The polarization is in the electrolyte with Cl^- ion is about 200 mV lower than in pure $Mg(BH_4)_2$/TG electrolyte.

These experiments demonstrated that the electrolytes could be made compatible with magnesium metal if the anion in the salt has sufficient reductive stability. It was proposed that the chloride anion plays a big role for the formation of complexes and reduces the amount of active water in the electrolyte. From the spectroscopic analyses by Mothadi et al. was suggested that the electrochemical performance was strongly controlled by the salt dissociation. [8] In this

electrolyte the complex cation $MgBH_4^+$ works as the active species and thus improves the electrochemical performance. The presence of $MgBH_4^+$ was later proven by the theoretical calculation and was reductive stable with magnesium metal.[19] In addition to the effect of additives such as Cl^- or $LiBH_4$, which form the complex in the electrolyte completely with the BH_4^- ions, the key factor is the number of oxygen donors of the solvents. It has been found that irreversible agglomeration occurs in all glymes (from THF to tetraglyme) with borohydride salt. [20] In the long chain ether such as tetraglyme the agglomeration rate is lowest and the solvent diffuse slowly. However, the oxidative stability in all borohydride-based solution is quite low. (Here 1.7 V vs. Mg/Mg^{2+})

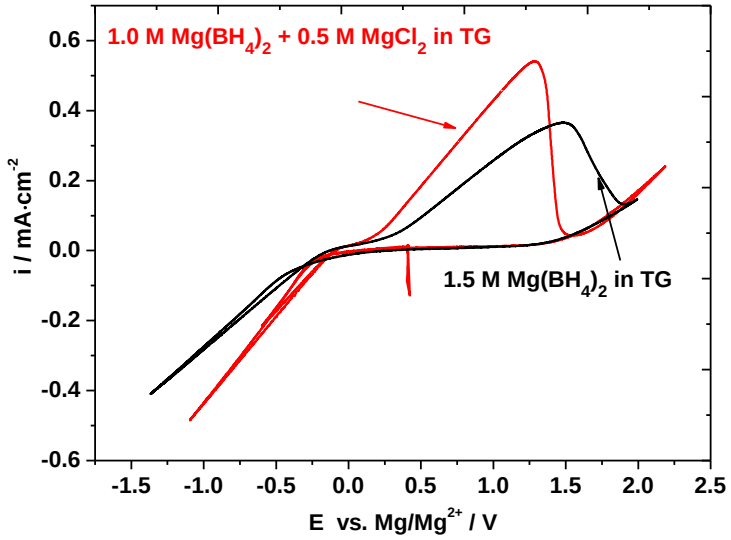

Figure 3. 9: CVs for electrochemical magnesium deposition in a three electrode cell with 10 mV/s. black: 1.5 M $Mg(BH_4)_2$ in TG; red: 1.0 M $Mg(BH_4)_2$ + 0.5 M $MgCl_2$ in TG. AE: Au; CE and RE: Mg.

It has been generally understood that a passivation layer on the magnesium surface would block the electrode. The properties of the interface plays an important role for the electrochemical performance. The formation of SEI in magnesium batteries was first reported in BH_4^- ion containing solution. It was shown that a formation of H_2 during the magnesium deposition took place, and plays a vital role in the formation of a SEI on the surface. [21] This finding obtained in this solution explains well the high coulombic efficiency and low overpontential observed for Mg deposition/dissolution.

One of the most common salts for Mg batteries is $Mg(TFSI)_2$, its anion is suitable for lithium batteries due to the high anodic stability, commercial availability and high solubility in solvent. In Figure 3.10 the CV for magnesium deposition and dissolution out of 0.5 M $Mg(TFSI)_2$/TG electrolytes is shown. A very large overpotential (2 V vs. Mg/Mg^{2+}) and low current density

(0.05 mA/cm^2) for Mg-deposition and dissolution is obvious. The coulombic efficiency was found to be below 40 %.

Oriskasa et al. have investigated the Mg plating and stripping in more details with variation of the $Mg(TFSI)_2$ concentration. (0.1 M to 1.5 M) In all solutions very larges overpotentials (2 V) and low coulombic efficiency (below 30 %) were observed, which was similar to our result. [22] It has been also found in this study that the transference number of Mg^{2+} is not very high (0.297 for 0.2 M $Mg(TFSI)_2$/DG) and is decreasing with increased concentration. That was ascribed to the strong association between the Mg^{2+} and the $TFSI^-$ anion. In the high concentration solution this association effect became more and more noticeable, thus lowering the transference number. [23] The poor performance of $Mg(TFSI)_2$ could be due to the instability of the $TFSI^-$ ion. The decomposition of the $TFSI^-$ ion can associated the presence of trace amounts of F, N, O, and C. The simulation has also proven that the instability of $TFSI^-$ ion is due to the Mg^{2+}-$TFSI^-$ complex. [19] Otherwise, the impurities in the electrolytes such as trace water could also disturb the Mg plating and stripping. Also the glyme itself is instable with the magnesium metal during the deposition. [17] Thereby, it is very difficult to achieve reversible Mg deposition and dissolution using pure simple $Mg(TFSI)_2$ electrolyte.

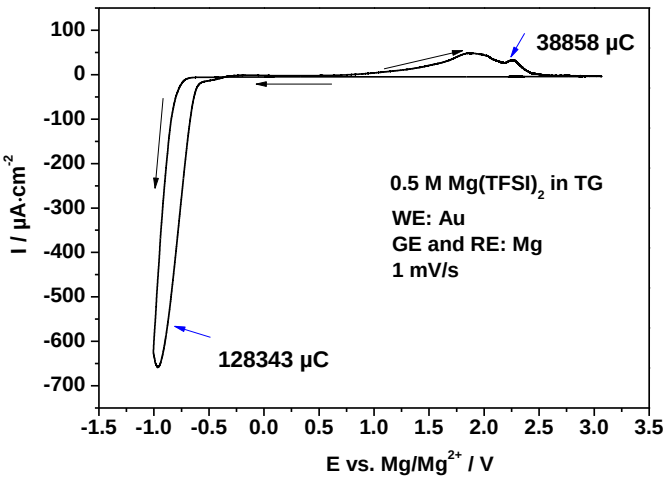

Figure 3. 10: CV for electrochemical magnesium deposition in a three electrode cell with 1 mV/s in 0.5 M $Mg(TFSI)_2$ in TG. AE: Au; CE and RE: Mg.

To avoid the instability of $[Mg\text{-}TFSI]^+$ complex and improve the electrochemical performance, a small amount of $Mg(BH_4)_2$ was added into the electrolyte. With additive of 10 mM $Mg(BH_4)_2$ the reversible Mg deposition and dissolution was observed. (Figure 3.11) This small amount of $Mg(BH_4)_2$ results in a high coulombic efficiency of 90 % and low initial deposition (-0.08 V) and (0 V) stripping potentials. In one report, this kind of electrolyte is more resistant to decomposition, as the solvation structure was changed with the reductive stable BH_4^-. A mixed

BH_4^--$TFSI^-$ solvation shell of Mg^{2+} is more stable than [MgTFSI]-. [24] Also, the BH_4^- is highly reductive, which can reduce the impurities in the electrolyte such as H_2O via following equation:

$$Ca(BH_4)_2 + 2H_2O \rightarrow Ca\,[B(OH_3)]_2 + 4H_2\uparrow$$

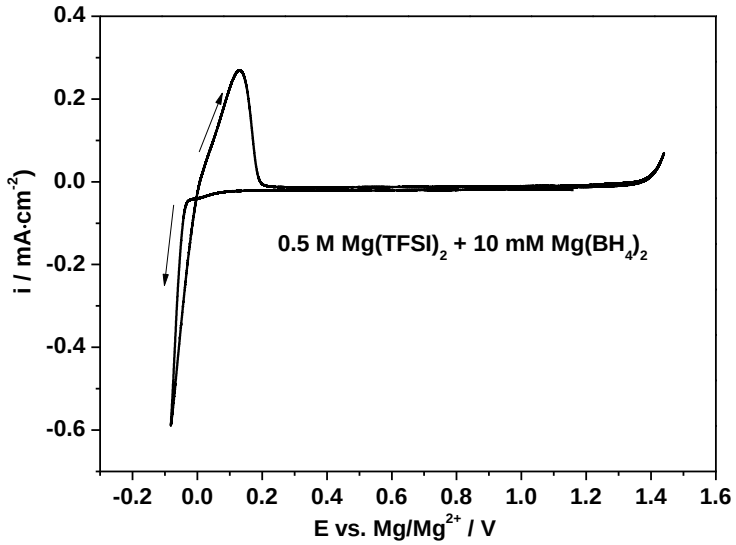

Figure 3. 11: CV for electrochemical magnesium deposition in a three electrode cell with 1 mV/s in 0.5 M $Mg(TFSI)_2$ + 10 mM $Mg(BH_4)_2$ in TG. AE: Au CE; and RE: Mg.

3.3.3 Calcium Deposition and Dissolution

As shown in Figure 3.12, the calcium deposition and dissolution was carried out by cyclic voltammetry using a three-electrode cell in 1.5 M $Ca(BH_4)_2$ in THF electrolyte at room temperature. The coulombic efficiency and the current density increase upon cycles. (Figure 3.12 left) The coulombic efficiency reach to 97 % in the stable CV (Figure 3.12 right) from 72.7 % at the first initial cycle. The variation of coulombic efficiency with the cycle number was shown in Figure 3.13. Calcium deposition was starting at about -0.2 V vs. Ca/Ca^{2+} (200 mV more negative than the thermodynamic potential of Ca/Ca^{2+}), and a high current density for calcium stripping was observed. (7 mA/cm^2) The anodic stability of this electrolyte is up to 3 V vs. Ca/Ca^{2+}.

To better understand the properties of this electrolyte, the Ca salt concentration for the calcium deposition was varied (Figure 3.14), and the ion conductivity was studied. (Figure 3.15) The current density of the calcium stripping peak and the coulombic efficiency of calcium plating and stripping was increasing with increased concentration. In the 0.3 M solution no calcium dissolution was observed. The ion conductivity also increases with increased concentration of $Ca(BH_4)_2$. From 0.5 M to 1.5 M a linear relationship between the conductivity and the concentration is observed, below 0.5 M the conductivity increases only slowly. These results

indicate that the reversible calcium plating and stripping occurs only out of the electrolyte with the concentration of $Ca(BH_4)_2$ higher than 1.2 M.

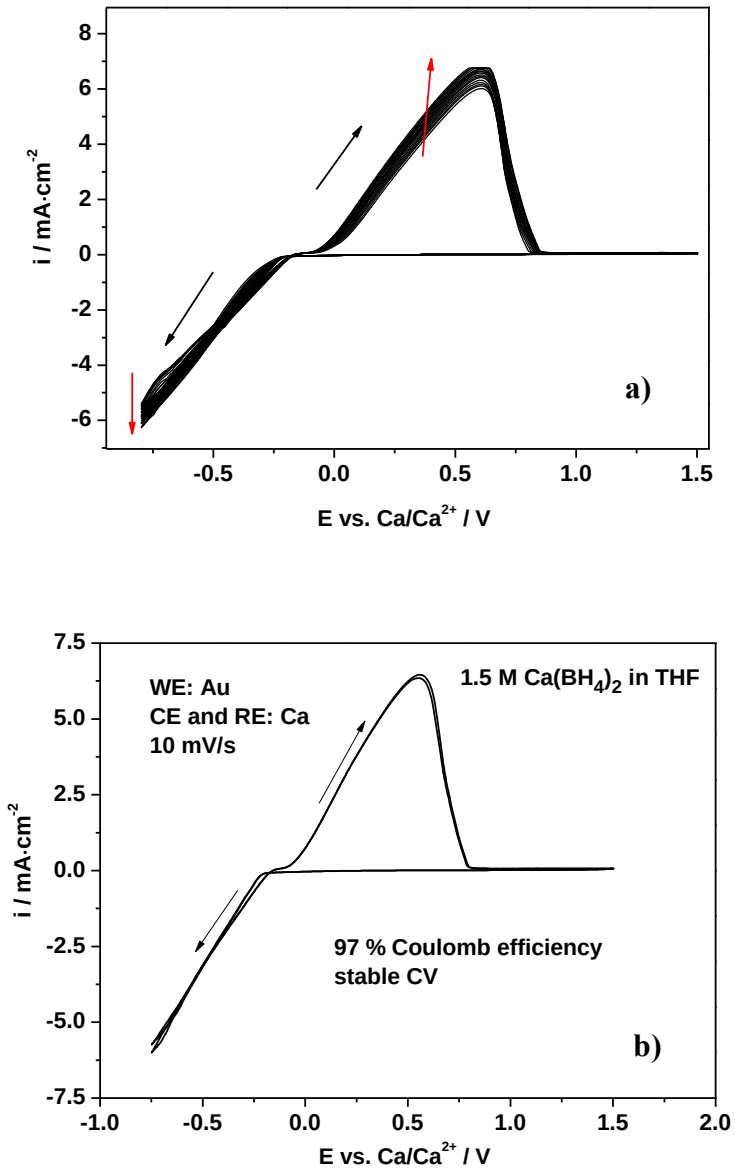

Figure 3. 12: Cyclovoltammogramms for the Ca-deposition in 1.5 M $Ca(BH_4)_2$ in THF on polycrystalline Au electrode with a sweep rate 10 mV/s. WE: Au; CE and RE: Ca. a): the first 10 cycles. The coulombic efficiency and the current density increase upon cycles. b): stable CV with the reversibility of 97 %.

At a lower concentrations of $Ca(BH_4)_2$ (e.g. 0.5 M), additional THF molecules coordinate to the Ca ion and thereby increase the solvation effect. This result was obtained from ^{43}Ca NMR spectra, which showed a chemical up field shift of the ^{43}Ca signals (ca. 2.3 ppm). [25] After introduction of $LiBH_4$ a 16.1 ppm down field shift of ^{43}Ca was observed for 1.5 M $Ca(BH_4)_2$-$LiBH_4$-THF electrolyte, which suggests a weaker solvation effect. As a result of the distribution

function, the coordination number of oxygen in the first solvation shell of Ca^{2+} is reduced by about 40 % in the $Ca(BH_4)_2$-$LiBH_4$-THF electrolyte. [25] Even at low concentration with 0.4 M $Ca(BH_4)_2$-$LiBH_4$-THF electrolyte the calcium deposition showed high reversibility and low overpotential at room temperature.

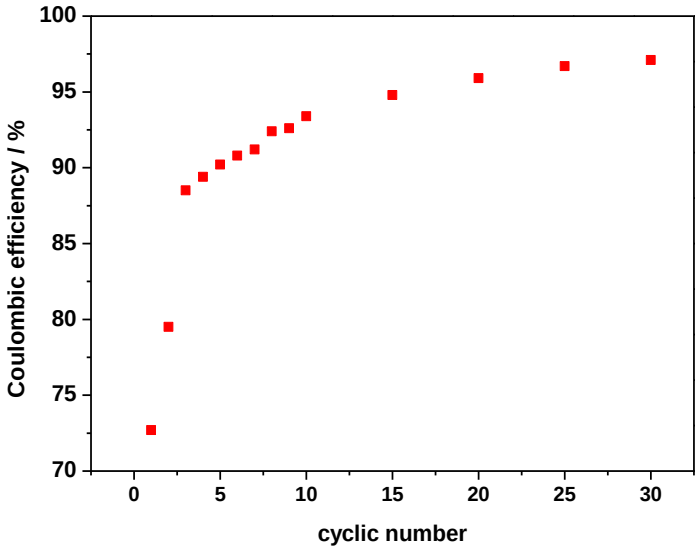

Figure 3. 13: Variation of coulombic efficiency with the cycle number. 72.7 % at the first cycle and 97 % in the stable CV.

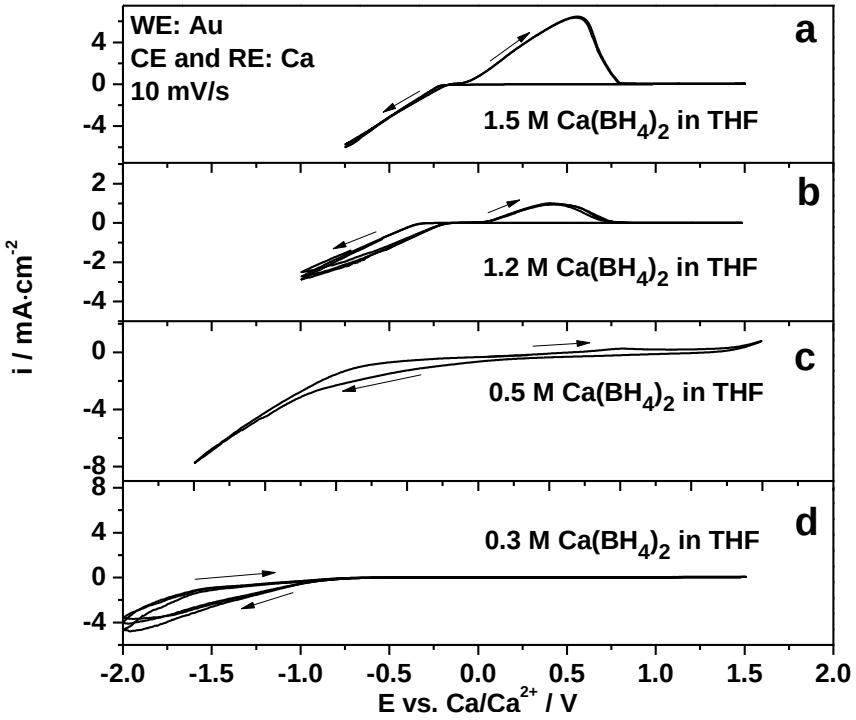

Figure 3. 14: variation of the Ca salt concentrations in THF-based electrolytes for the calcium deposition and dissolution with 10 mV/s. AE: Au; RE and CE: Ca. a) 1.5 M $Ca(BH_4)_2$; b) 1.2 M $Ca(BH_4)_2$; c) 0.5 M $Ca(BH_4)_2$; d) 0.3 M $Ca(BH_4)_2$.

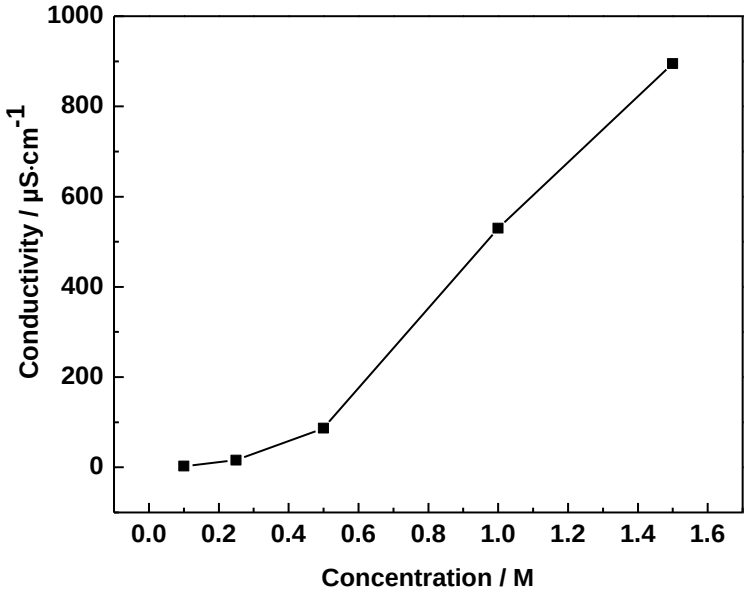

Figure 3. 15: conductivity measurements of variation the $Ca(BH_4)_2$ concentration (0.1 M to 1.5 M) in THF.

To investigate the electrochemical Ca-deposition in other organic solvents, two electrolytes with a ratio of 6: 1 between THF/DG and THF/DME were examined. The CVs are shown in Figure 3.16. The addition of DG and DME has a negative effect on the Ca-deposition, the coulombic efficiency in both electrolytes was reduced from 97 % to 80 % due to the instability of the DG and DME themselves and the lower solubility of $Ca(BH_4)_2$ in DME. After cycling some white crystals were found in the cell.

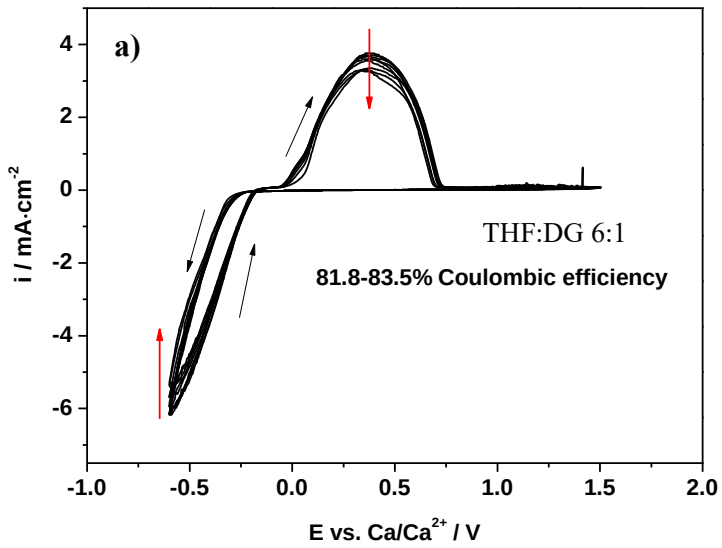

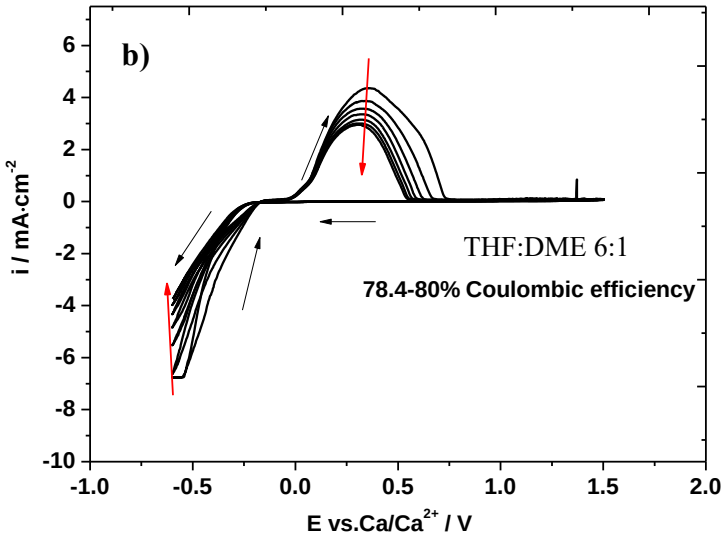

Figure 3. 16: CVs of the $Ca(BH_4)_2$-based electrolytes for the calcium deposition and dissolution with 10 mV/s. AE: Au; RE and CE: Ca. a) 1.5 M $Ca(BH_4)_2$ in THF/DG (6:1); b) 1.5 M $Ca(BH_4)_2$ in THF/DME (6:1).

Calcium bis(trifluoromethanesulfonyl)imide ($Ca(TFSI)_2$) is another commercially available simple Ca salt. No sufficient electrochemical deposition of calcium was observed in any experiments carried out with $Ca(TFSI)_2$. Due to the instability of tetraglyme itself in the presence of deposited metal [17] or trace water impurities [26] and the previous result in $Ca(BH_4)_2$/THF, THF as a solvent was suggested for investigation of calcium deposition with $Ca(TFSI)_2$. (Figure 3.17) No reversible deposition and dissolution of calcium in 0.5 M $Ca(TFSI)_2$ in THF and in 0.5 M $Ca(TFSI)_2$ + 0.5 M $Ca(BH_4)_2$ in THF electrolytes is observed. Since $LiAlH_4^-$ is a relatively strong reducing agent, which might withstand the reducing environment of the calcium anode, the addition of a small amount $LiAlH_4^-$ (0.05 M) was introduced into the electrolyte. The investigation of this mixed electrolyte with $Ca(TFSI)_2$ (0.5 M and 1.0 M) and 0.05 M $LiAlH_4^-$ in THF are shown in Figure 3.17 c and d. However, the addition of $LiAlH_4^-$ cannot enable the cycling with the observation of the $TFSI^-$ reduction and THF oxidation. In other experiments with introduction of $HMDS^-$ ion und CaH_2 the calcium deposition also was not observed. Even a small amount of $TFSI^-$ anion (0.2 M $Ca(TFSI)_2$) can influence the electrochemical performance $Ca(BH_4)_2$/THF (Figure 3.18). The reason for unsuccessfully calcium deposition with $Ca(TFSI)_2$ was in previous studies to the instability of $TFSI^-$ anion during reduction and instability of some complexes of Ca^{2+} with $TFSI^-$. [19, 26]

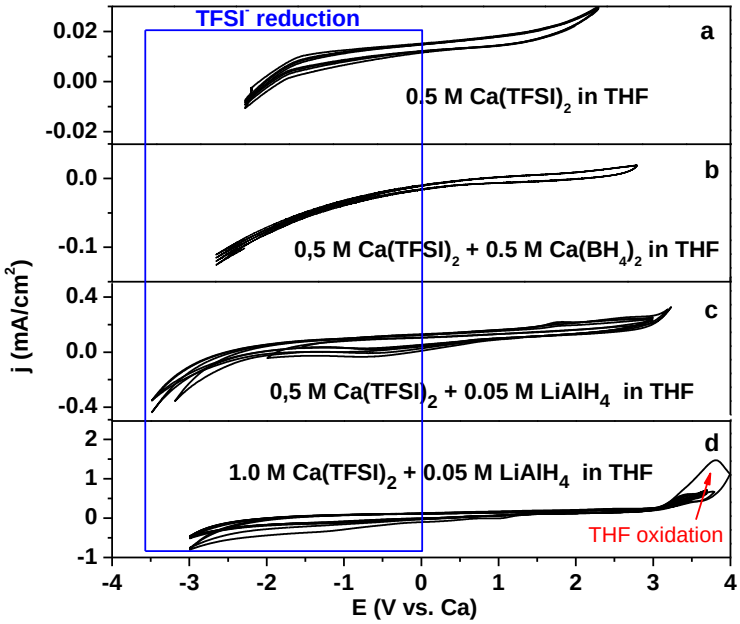

Figure 3. 17: CVs of the $Ca(TFSI)_2$-based electrolytes in THF for the calcium deposition and dissolution with 10 mV/s. AE: Au; RE and CE: Ca. a) 0.5 M $Ca(TFSI)_2$; b) 0.5 M $Ca(TFSI)_2$ + 0.5 $Ca(BH_4)_2$; c) 0.5 M $Ca(TFSI)_2$+ 0.05 M $LiAlH_4$; d) 1.0 M $Ca(TFSI)_2$+ 0.05 M $LiAlH_4$.

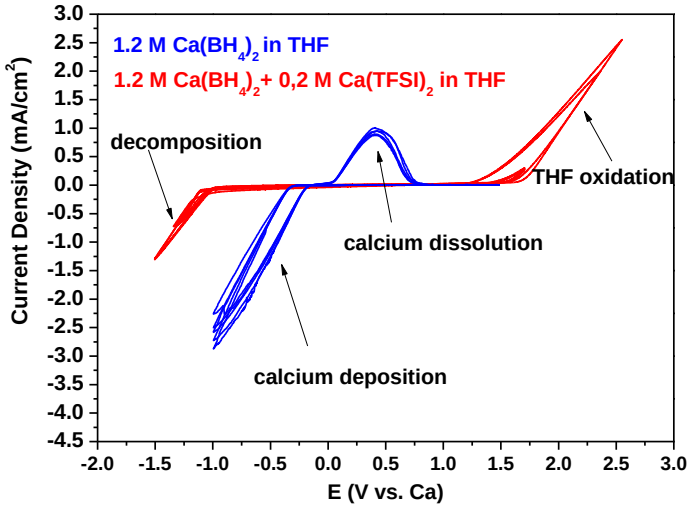

Figure 3. 18: Cyclovoltammogramms for the Ca-deposition in 1.2 M $Ca(BH_4)_2$ in THF (blue) and 1.2 M $Ca(BH_4)_2$ + 0.2 M $Ca(TFSI)_2$ in THF (red) on polycrystalline Au electrode with a sweep rate 10 mV/s. WE: Au; CE and RE: Ca. With addition of 0.2 M $Ca(TFSI)_2$ the reversible Ca plating and stripping was disturbed.

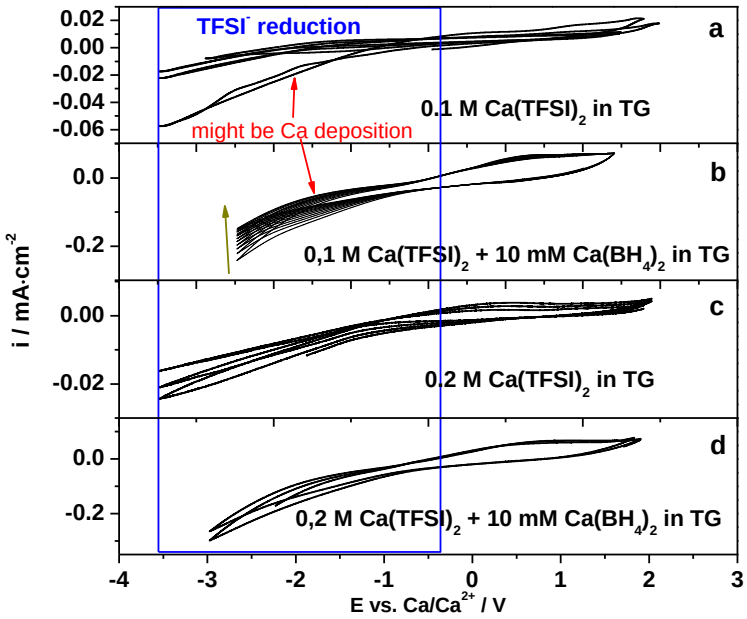

Figure 3. 19: CVs of the $Ca(TFSI)_2$-based electrolytes in TG for the calcium deposition and dissolution with 10 mV/s. AE: Au; RE and CE: Ca. a) 0.1 M $Ca(TFSI)_2$; b) 0.1 M $Ca(TFSI)_2$ + 10 mM $Ca(BH_4)_2$; c) 0) 0.2 M $Ca(TFSI)_2$; d) 0.2 M $Ca(TFSI)_2$ + 10 mM $Ca(BH_4)_2$.

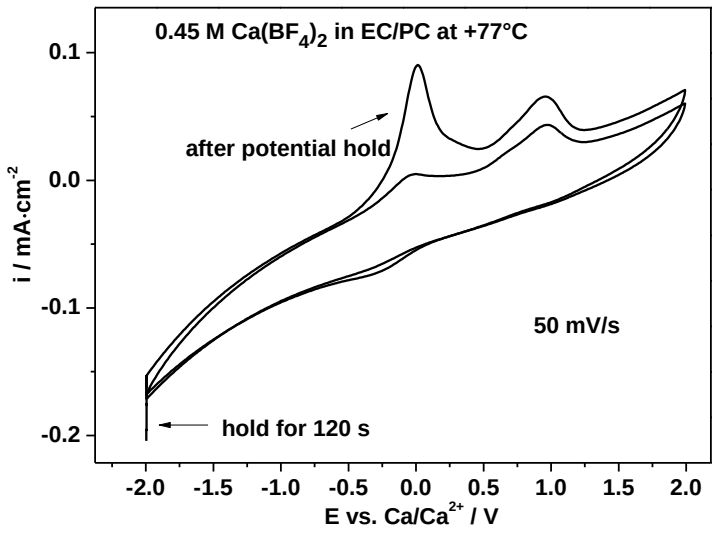

Figure 3. 20: Cyclovoltammogramms for the Ca-deposition in 0.45 M $Ca(BF_4)_2$ in PC/EC (1:1 wt%) on polycrystalline Au electrode with a sweep rate 50 mV/s. WE: Au; CE and RE: Ca. After potential hold for 120 s the Ca stripping peak was appears.

In Figure 3.19 the CVs of the measurements of $Ca(TFSI)_2$ in TG are shown. In neither 0.1 M or 0.2 M $Ca(TFSI)_2$ in TG the reversible Ca plating and stripping were observed. In the cathodic sweep the current drop at about -0.5 V vs. Ca corresponding to the decomposition of the $TFSI^-$ ion. (Figure 8.5 a and c) Because of the observation of reversible Ca plating and stripping in $Ca(BH_4)_2$/THF system, a small amount of $Ca(BH_4)_2$ (10 mM) was added in the electrolytes in order to enhance the electrochemical performance. The current density reach to -0.25 mV/cm^2

with 10 mV/s in the first cycle. (Figure 8.5 b and d) However, it was decreasing fast from the second cycle and no reversible calcium stripping has been found. In addition, the Ca deposition is also not observed in the electrolyte containing 0.8 M $Ca(BH_4)_2$ in TG.

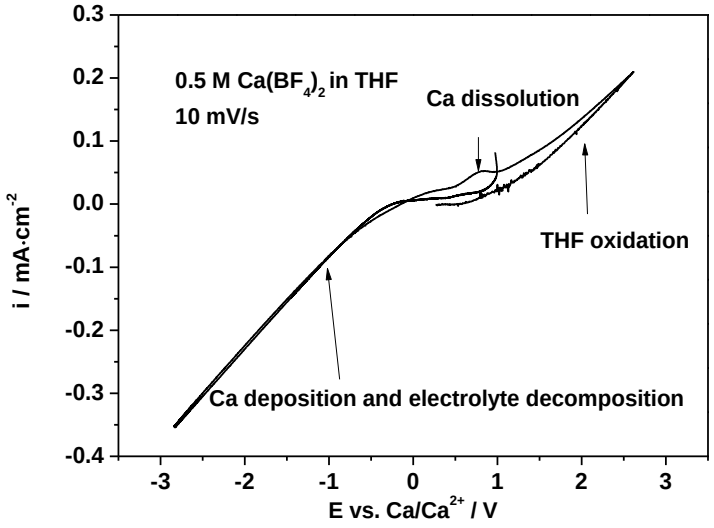

Figure 3. 21: Cyclovoltammogramm for the Ca-deposition in 0.5 M $Ca(BF_4)_2$ in THF on polycrystalline Au electrode with a sweep rate 10 mV/s. WE: Au; CE and RE: Ca.

The following experiments of Ca plating and stripping out of $Ca(BF_4)_2$ in THF and in DMSO aimed at achieving a reversible Ca-deposition at room temperature, since THF is suitable for reversible Ca-deposition with 1.5 M $Ca(BH_4)_2$ and DMSO is suitable for Li-deposition with high concentration of LiTFSI (3 M). [3, 10] In 0.5 M $Ca(BF_4)_2$ in THF solution a very small peak starting at 0.5 V vs. Ca/Ca^{2+} in the anodic sweep is seen, which is attributed it to be the Ca-dissolution. (Figure 3.21) In the cathodic sweep the current was increasing continuous at ca. 0 V vs. Ca/Ca^{2+} due to the Ca-deposition and electrolyte decomposition.

In 0.5 M $Ca(BF_4)_2$ in DMSO no reversible calcium plating and stripping was observed. (Figure 3.22 a) In the Figure 3.22 b the calcium deposition starting at -0.8 V vs. Ca/Ca^{2+} was observed with introduction of 10 mM $Ca(BH_4)_2$ in DMSO a broad peak at 0.7 V vs. Ca/Ca^{2+} in the anodic sweep has been found, which is related to the dissolution of calcium. However, the coulombic efficient is very low (10 %) and anodic stability is about 2.0 V refer to calcium compared with in PC/EC electrolyte (4.0 V).

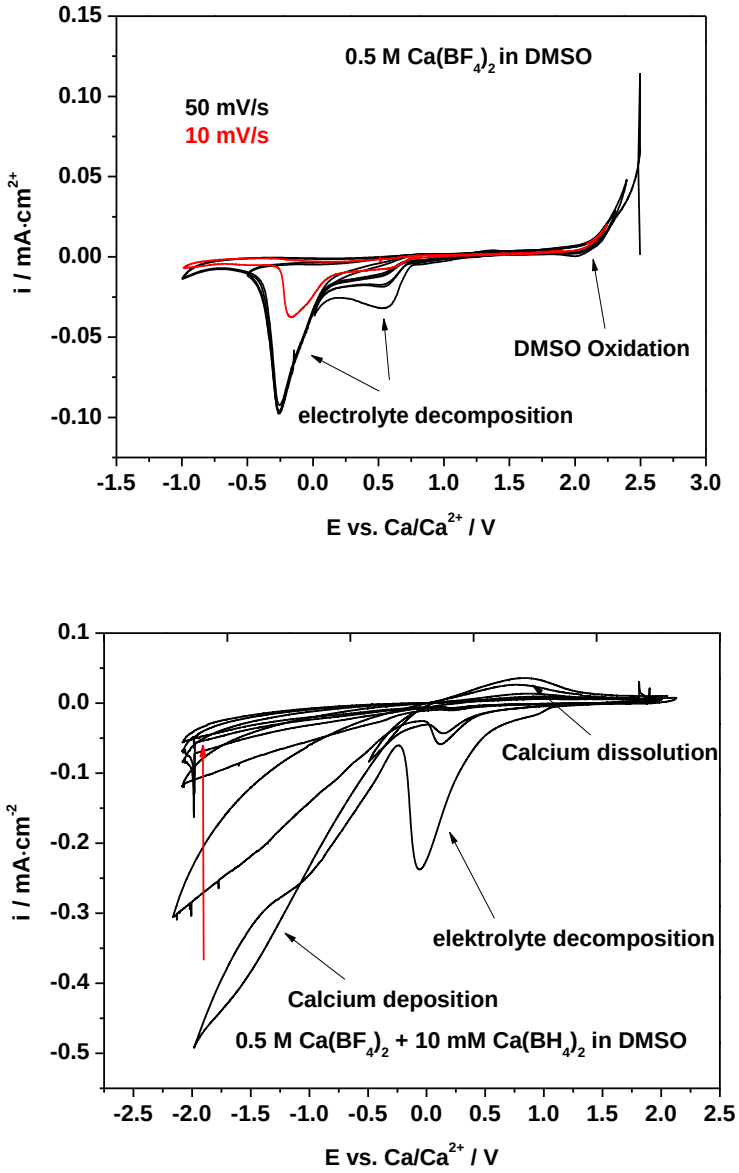

Figure 3. 22: CVs of the $Ca(BF_4)_2$-based electrolytes in DMSO for the calcium deposition and dissolution with 10 mV/s. AE: Au; RE and CE: Ca. left) 0.5 M $Ca(BF_4)_2$; b) 0.5 M $Ca(BF_4)_2$ + 10 mM $Ca(BH_4)_2$.

3.4 Conclusion

The lithium deposition and dissolution in 1 M and 3 M LiTFSI/DMSO solution on an Au and Pt sputtered Gore-Tex Teflon membrane electrode using CV and DEMS has been studied. We found that the concentration is an important factor for the Li plating/stripping. On Au electrode in 3 M DMSO-based solution the highest coulombic efficiency was observed, because there is no free DMSO molecule, all DMSO molecule are used to form the complexes with LiTFSI, which is active species for the lithium deposition. For 1 M solution on Au electrode and for 1M and 3M solution on Pt electrode the coulombic efficiencies are low. The decomposition of the specific lithium salt (LiTFSI) and of the DMSO-molecular are the main reason and demonstrated by using DEMS. We propose that an unstable SEI is formed during the lithium deposition, because the decomposition products have a high solubility in DMSO solution. Hydrogen evolution was also observed during the lithium deposition.

We discussed the electrochemical properties of magnesium deposition from MACC, $Mg(BH_4)_2$ and $Mg(TFSI)_2$ in TG solution. The 0.5 M MACC in TG solution shows a high coulombic efficiency (99.5 %), low overpotential and high oxidative stability (up to 3 V). The magnesium deposition occurs at about -2.2 V vs. $Me_{10}Fc^{*}/Me_{10}Fc^{*+}$. Freshly prepared MACC needs to be conditioned due to impurities present in solution, complex formation with solvent or Al co-deposition, until it shows high reversible magnesium plating and stripping. However, one of the most important limitations of MACC electrolytes is the incompatibility with typical current collectors due to the high concentration of Cl^- ion.

The high concentration of $Mg(BH_4)_2$/TG (1.5 M) electrolytes results in reversible magnesium deposition and stripping. The coulombic efficiency is 70 %, which is lower than the electrolyte with a small amount of $MgCl_2$ introducing into 1.0 M $Mg(BH_4)_2$/TG. This electrolyte is compatible with magnesium metal, since the BH_4^- is a strongly reductive species. The complex $Mg(BH_4)^+$ was present in the electrolyte and worked as the active species during the magnesium plating and stripping. However, the anodic stability is quite low (ca. 2 V vs. Mg/Mg^{2+}). The standard reference $Me_{10}Fc^{*}$ could not be used in this electrolyte, because it is not stable with the present of BH_4^- ion.

The 0.5 M $Mg(TFSI)_2$/TG and 0.25 M $Mg(TFSI)_2$ + 0.5 M $MgCl_2$/TG electrolytes doesn't show high reversible magnesium deposition and dissolution. A very large separation (2 V) between magnesium plating and stripping was observed in 0.5 M $Mg(TFSI)_2$/TG. The poor electrochemical performance of this electrolyte is mainly related to the instability of the $TFSI^-$ ion. This limitation of stability for $Mg(TFSI)_2$ is one of the most important factor for the magnesium plating and stripping, which include the Mg^{2+}-$TFSI^-$ association in TG and $TFSI^-$

interact with the some impurities in the solution, such as water and $Mg(OH)_2$.

The electrochemical deposition of calcium in non-aqueous solvents is summarized in the Table 8.1. It has been found that most of the calcium salt are insolvable and only a few Ca-salts are commercially available. Only very limited types of the salts could be investigated in THF, in TG and in DMSO.

In $Ca(BH_4)_2$/THF electrolytes the calcium plating and stripping can be considered only in the solution with the concentration higher than 1.2 M. The highest current density, the highest coulombic efficiency (97 %) and lower overpotential (100 mV) were detected at room temperature in 1.5 M $Ca(BH_4)_2$/THF. After continuous cycling the CV was stable. The ionic conductivity increases slightly from 0.1 M to 0.5 M and increase linearly steeply from 0.5 M to 1.5 M. The oxidation stability of the $Ca(BH_4)_2$/THF is 3 V versus Ca/Ca^{2+}, which is even low for a possible cathode. In addition, a mixture of THF with DG and DMSO was investigated. In both electrolytes the reversible Ca plating and stripping can be observed, but the coulombic efficiency were decreasing from 97 % to ca. 80 % upon cycling with initial value of 95 % in both case.

In $Ca(TFSI)_2$-based electrolytes no calcium plating and stripping was found. With 0.5 M and 1.0 M $Ca(TFSI)_2$ in THF or in TG and with electrolytes additives of $Ca(BH_4)_2$, HMDS, or CaH_2, only electrolyte decomposition and solvent oxidation were observed. The instability of $TFSI^-$ ion is the problem for reversible Ca-plating and stripping. With presence of such a small amount of $Ca(TFSI)_2$ in 1.2 M $Ca(BH_4)_2$/THF the peaks for Ca-plating and stripping were totally disappeared. The reversible Ca-plating and stripping at room temperature in $Ca(BF_4)_2$/THF or in $Ca(BF_4)_2$/DMSO were not observed.

In this chapter the problems of the calcium anode for rechargeable calcium batteries are not solved. In the electrolytes, which are suitable for reversible Ca-plating and stripping, CaH_2 or CaF_2 are formed during the reduction. It is difficult to find suitable electrolytes and anode materials, which are compatible with high voltage cathodes. In addition, the difference in plating behaviour between Mg and Ca is need to be understood for further investigations, since Mg can undergo partial reduction Mg^{2+} to Mg^+.

Table 3. 1: the electrochemical deposition of calcium in non-aqueous solvents. The electrolyte with * is the result from literature and reproduced. The electrolyte with # is the result from the project partner or from Mr. Wieland.

	THF	2.5-Dimethyl-THF	DME	TG	DMSO	NMP	EC:PC
$Ca(BH_4)_2$	1.5 M	1.0 M	0.775M#	0.8 M#			
$Ca(BH_4)_2$*2THF	1.5 M* [10]						
$CaCp_2(THF)_2$	0.75 M#				1.0 M#		
$Ca(TFSI)_2$	1.5M			1.0 M			
0.5M $Ca(TFSI)_2$+0.5M $Ca(BH_4)_2$							
0,5 M $Ca(TFSI)_2$+0,05 M $LiAlH_4$							
$Ca(TFSI)_2$ + $CaCl_2$							
$Ca(ClO_4)_2$							0.3M
$Ca(BF_4)_2$							0.45M* >75°C [27]
$Ca(BF_4)_2$ + $Ca(BH_4)_2$							
$Ca(OTf)_2$							
$CaCl_2$							
$Ca(AlH_4)_2$	0.25 M						
$Ca[Al(hfip)]_2$	0.25M#						
$Ca[B(hfip)]_2$	0.4 M#		0.3 M	Glyme			
$Ca[B(hfip)]_2$			0.25 M				
$Ca[B(hfip)]_2$+ additive $Ca(BH_4)_2$							
$Ca[B(hfip)]_2$+ additive HMDS							
$Ca[B(hfip)]_2$+ additive CaH_2							
$Ca[B(Cat)_2]_2$	0.5 M#						
$Ca[B(hfip)]_2$+ additive $Ca(BH_4)_2$	0.5M+0.14M						
$Ca(SCN)_2$							
0.5 M $CaCl_2$ + $AlCl_3$							

Suitable	Problematic	unsoluble

References

[1] A. C. Kozen, C.-F. Lin, O. Zhao, S. B. Lee, G. W. Rubloff, M. Noked, *Chemistry of Materials* **2017**, *29*, 6298.

[2] J. S. Young, M. Smeu, *Journal of Physical Chemistry Letters* **2018**, *9*, 3295.

[3] K. Pranay Reddy, P. Fischer, M. Marinaro, M. Wohlfahrt-Mehrens, *ChemElectroChem* **2018**, *5*, 2758.

[4] M. Roberts, R. Younesi, W. Richardson, J. Liu, T. r. Gustafsson, J. Zhu, K. EdstrÃ¶m, *ECS Electrochemistry Letters* **2014**, *3*, A62.

[5] N. Togasaki, T. Momma, T. Osaka, *Journal of Power Sources* **2016**, *307*, 98.

[6] T. D. Gregory, R. J. Hoffman, R. C. Winterton, *Journal of the Electrochemical Society* **1990**, *137*, 775.

[7] Y. Gofer, R. Turgeman, H. Cohen, D. Aurbach, *Langmuir* **2003**, *19*, 2344.

[8] R. Mohtadi, M. Matsui, T. S. Arthur, S.-J. Hwang, *Angewandte Chemie-International Edition* **2012**, *51*, 9780.

[9] I. Shterenberg, M. Salama, Y. Gofer, E. Levi, D. Aurbach, *Mrs Bulletin* **2014**, *39*, 453.

[10] D. Wang, X. Gao, Y. Chen, L. Jin, C. Kuss, P. G. Bruce, *Nature Materials* **2017**, *17*, 16.

[11] B. Liu, W. Xu, P. Yan, S. T. Kim, M. H. Engelhard, X. Sun, D. Mei, J. Cho, C.-M. Wang, J.-G. C. Zhang, *Advanced Energy Materials* **2017**, *7*, 1602605.

[12] T. Bach, **2017**.

[13] S. S. Zhang, K. Xu, J. Read, *Journal of Power Sources* **2011**, *196*, 3906.

[14] K. Okita, K.-i. Ikeda, H. Sano, Y. Iriyama, H. Sakaebe, *Journal of Power Sources* **2011**, *196*, 2135.

[15] C. J. Barile, E. C. Barile, K. R. Zavadil, R. G. Nuzzo, A. A. Gewirth, *Journal of Physical Chemistry C* **2014**, *118*, 27623.

[16] J. Luo, S. He, T. L. Liu, *ACS Energy Letters* **2017**, *2*, 1197.

[17] P. Hegemann, M. Hegemann, L. Zan, H. Baltruschat, *Journal of The Electrochemical Society* **2019**, *166*, A245.

[18] T. Liu, Y. Shao, G. Li, M. Gu, J. Hu, S. Xu, Z. Nie, X. Chen, C. Wang, J. Liu, *Journal of Materials Chemistry A* **2014**, *2*, 3430.

[19] N. N. Rajput, X. Qu, N. Sa, A. K. Burrell, K. A. Persson, *Journal of the American Chemical Society* **2015**, *137*, 3411.

[20] D. Samuel, C. Steinhauser, J. G. Smith, A. Kaufman, M. D. Radin, J. Naruse, H. Hiramatsu, D. J. Siegel, *Acs Applied Materials & Interfaces* **2017**, *9*, 43755.

[21] T. S. Arthur, P.-A. Glans, N. Singh, O. Tutusaus, K. Nie, Y.-S. Liu, F. Mizuno, J. Guo, D. H. Alsem, N. J. Salmon, *Chemistry of Materials* **2017**, *29*, 7183.

[22] Y. Orikasa, T. Masese, Y. Koyama, T. Mori, M. Hattori, K. Yamamoto, T. Okado, Z.-D. Huang, T. Minato, C. Tassel, J. Kim, Y. Kobayashi, T. Abe, H. Kageyama, Y. Uchimoto, *Scientific Reports* **2014**, *4*, 5622.

[23] N. Sa, B. Pan, A. Saha-Shah, A. A. Hubaud, J. T. Vaughey, L. A. Baker, C. Liao, A. K. Burrell, *ACS Applied Materials & Interfaces* **2016**, *8*, 16002.

[24] J. Z. Hu, N. N. Rajput, C. Wan, Y. Y. Shao, X. C. Deng, N. R. Jaegers, M. Hu, Y. W. Chen, Y. Shin, J. Monk, Z. Chen, Z. H. Qin, K. T. Mueller, J. Liu, K. A. Persson, *Nano Energy* **2018**, *46*, 436.

[25] Y. L. Jie, Y. S. Tan, L. M. Li, Y. H. Han, S. T. Xu, Z. C. Zhao, R. G. Cao, X. D. Ren, F. Y. Huang, Z. W. Lei, G. H. Tao, G. Q. Zhang, S. H. Jiao, *Angewandte Chemie-International Edition* **2020**, *59*, 12689.

[26] Y. Yu, A. Baskin, C. Valero-Vidal, N. T. Hahn, Q. Liu, K. R. Zavadil, B. W. Eichhorn, D. Prendergast, E. J. Crumlin, *Chemistry of Materials* **2017**, *29*, 8504.

[27] A. Ponrouch, M. R. Palacin, *Current Opinion in Electrochemistry* **2018**, *9*, 1.

Chapter 4: Insertion of Magnesium into Antimony Layers on Au Electrodes: Kinetic Behaviour

D.Xing[a], P.P. Bawol[a], A. A. Abd-El-Latif[a, b, c] L.X.Zan[a, d] and H. Baltruschat[a]*

[a] Institut für Physikalische und Theoretische Chemie, Universität Bonn, Römerstraße 164, D-53117 Bonn, Germany

[b] Current address: Accumulator Materials Research (ECM), Zentrum für Sonnenenergie- und Wasserstoff-Forschung Baden-Württemberg (ZSW), Lise-Meitner-Str. 24, 89081 Ulm

[c] Permanent address: National Research Centre, Physical Chemistry Dept., El-Bohouth St. Dokki, 12311 Cairo, Egypt

[d] Current address: Key Laboratory of Chemical reaction engineering of Shaanxi Province; College of Chemistry & Chemical engineering, Yan'an University, Yan'an, 716000,P.R. China

*Corresponding author: baltruschat@uni-bonn.de

4.1 Abstract

Magnesium based secondary batteries are regarded as a viable alternative to the immensely popular Li-ion systems. One of the largest challenges is the selection of a Mg anode material since the insertion/extraction processes are kinetically slow because the large ionic radius and high charge density of Mg^{2+}.

In an attempt to bridge the gap between insertion measurements in 3D composite electrode materials and that in an idealized pure model system, we studied the insertion and diffusion of Mg in a thin, massive layer of Sb deposited on Au by using PITT, CV and potential step experiments. Mg insertion from a MACC/tetraglyme electrolyte into a Sb starts 300 mV positive of the onset potential of Mg deposition as shown by cyclic voltammetry. The molar ratio of Mg to Sb agrees well with the stoichiometry of a Mg_3Sb_2 alloy (Zintl-phase). The diffusion coefficient of Mg-insertion into Sb – layers and the charge transfer rate have been estimated by the above techniques. Such diffusion coefficients, albeit still somewhat "apparent", are much more closely related to true diffusion coefficient in the metal or alloy. The diffusion coefficient of Mg into the Sb layers are in the range of $4\text{-}7\times10^{-14}$ cm^2s^{-1}. A very high Tafel slope of 370 mV/dec was found in potential step experiments. Mg insertion has further been investigated by XPS measurements. Besides Mg and Sb, also Al and Cl signals were detected, particularly at the outer parts of the layer.

Keywords: Magnesium, insertion, electrodeposition, alloy, diffusion coefficient, kinetics

4.2 Introduction

Rechargeable batteries have become essential energy storing devices, which are widely used in portable electronic devices and hybrid electric vehicles. Magnesium based secondary batteries have been regarded as a viable 'environmental friendly, non-toxic' alternative compared to the Li-ion systems owing to its high volumetric capacity. [1-5] Unlike lithium, magnesium has no tendency to form dendrites during recharge. [6-8] But on the other hand, Mg anode is covered by an insulation layer, differently from the formation of a solid electrolyte interface (SEI) layer. One of the main challenges in the commercialization of Mg-ion batteries is the incompatibility of magnesium anode with many electrolytes because of the formation of this passive film on the anode surface resulting from the interaction of with the electrolyte. This problem is particularly demanding when trying to combine an Mg anode with an oxygen cathode in an Mg oxygen battery. [9-11] The development of an Mg^{2+} insertion anodes compatible with the electrolyte might circumvent some of the problems.

Recently, antimony (Sb), tin (Sn) and bismuth (Bi) have been suggested as insertion materials, because magnesium can form intermetallic with these materials. Bi and Sb have rhombohedral crystal structures forming double layers. They can form alloys in a wide composition range [12, 13]. A high initial capacity of 298 mAh/g at 1C rate has been reported for electrochemical magnesiation at electrodeposited $Bi_{0.88}Sb_{0.12}$ alloy by Arthur et al. [13] However, the capacity is declining to 215 mAh/g after 100 cycles.

A powdered Sn electrode has been used by Singh et al. as an anode for Mg-ion insertion/extraction. [14] However, they found a higher capacity close to the theoretical value (903 mAh/g) and low voltage difference for Mg insertion and extraction (+0.15 vs. 0.20 V), the capacity dropped to 200 mAh/g after 10 cycles at 0.05 C rate. They attributed the low coulombic efficiency to the material pulverization after the severe volume change. The development of a Sn anode, which demonstrate reversible Mg-insertion/de-insertion at 0.2 V vs. Mg, delivering discharge capacity of 270 mAh/g with PhMgCl/THF at room temperature, was reported by Nguyen et al. [15] Another study of a in situ de-alloying of bulk Mg_2Sn for the formation of high performance Mg-Ion battery anodes was investigated in. [16] A reversible capacity of 300 mAh/g was observed over 150 cycles at the rate of C/5.

Insertion/de-insertion of Mg at electrochemically deposited Bi in $Mg(TFSI)_2$/acetonitrile solution has been also investigated. Tan et al. prepared a nanostructured Mg_3Bi_2 anode material and reported a high coulombic efficiency (99%), high reversible specific capacity (360 mAh/g) and high stability for Mg electrolytes. [17] Bi-nanotubes as an anode material for Mg

insertion/de-insertion showed a superior cycling stability and rate performance in 0.1 M $Mg(BH_4)_2$-1.5 M $LiBH_4$-diglyme. [18] The high cycle ability upon Mg insertion/extraction was attributed to effectiveness of Bi-nanotubes in resisting the volume change. At electrodeposited Bi-CNT composite materials as magnesium battery anodes in $Mg(ClO_4)_2$/MeCN electrolyte, a high initial specific capacity of 180 mAh/g, dropped to 50 mAh/g after 3 cycles.[19]

Among Ge, Si, and Sn as anode materials for Mg insertion, Si could provide the lowest insertion voltage (0.15 eV vs. Mg) and the highest specific capacity of 3827 mAh/g according to DFT calculations. However, it is hard to overcome the slow diffusion of Mg into Si and the large volume expansion (216%). On the other hand, Sn can provide a competitive volumetric energy density (7.4 Wh/cc) under 100% volume expansion. [20]

Only very few reports on diffusion coefficients are available for Mg-anode materials. Until now no diffusion coefficient for Mg insertion into Sb adlayers was reported. Zhou et al. present the data set of the dilute tracer diffusion coefficients of about 10^{-12} to 10^{-13} m^2/s depending on the temperature for Sb substitutional alloying elements in Mg calculated from calculations based on density functional theory (DFT). [21] Ramanathan reported a diffusion coefficient of 1×10^{-14} from GITT (Galvonostatic Intermittent Titration Technique) measurements for Mg into Bi particles (0.1 nm) in 0.25 M C_2H_5MgCl-$((C_2H_5)_2AlCl)_2$ in THF electrolyte. [22] Another novel Bi-based anode (Bismuth oxyfluoride, BiOF) with a stable alloying reaction shows high magnesium storage performance and high cycling stability. The D_{Mg} values estimated from CV to about $1.28\text{-}1.78\times10^{-14}$ cm^2/s. [23]

More data for diffusion coefficients in alloys and insertion compunds are available for cathode materials. E.g., a CuS cathode for a Magnesium ion battery can reversibly work at room temperature and provide a high capacity of 400 mAh/g in a MACC electrolyte. The diffusions coefficient for Mg-ion into CuS to form the Mg_xCuS was determined as 1.97×10^{-14} cm^2/s by GITT. [24]

The rate of insertion, and therefore the diffusion coefficient of metal ions in the electrode material is one of the important evaluation parameters for fast charging and discharging metal ion battery. For determining diffusion coefficient of Lithium in the solid states electrode materials, electrochemical methods such as Electrochemical Impedance Spectroscopy (EIS), [25, 26] Galvanostatic Intermittent Titration Technique (GITT), [25, 27] Potentiostatic Intermittent Titration Technique (PITT) [28-32] and Cyclic Voltammetry (CV) [33, 34] have been applied.

In this manuscript, we thus want to bridge the gap between measurements of intercalation rates and apparent diffusion coefficients in composite electrodes of intercalation compounds and true

diffusion coefficients of an anodes materials for the magnesium battery.

We describe the electrochemical deposition of Sb on Au electrode by cyclic voltammetry and eQCM techniques. We then study the insertion of Mg into multilayers of Sb using non-aqueous electrolyte (MACC in tetraglyme). In a previous publication, we have already studied the deposition of Sb on Au (111) including a characterization by STM. [5] The apparent diffusion coefficient of Mg in the solid state and the rate of charge transfer will be estimated from cyclic voltammetry and potential step experiments and the cycling reversibility of insertion/de-insertion will be demonstrated. In addition, a XPS study of Mg insertion/de-insertion is reported.

4.3 Experimental

Chemicals, materials and electrolyte

All aqueous electrolytes were prepared by 18.2 MΩ from Milli-Q water and de-aerated with high purity argon gas for at least 15 min before use. Electrochemical measurements in 0.5 M H_2SO_4 (spectro pure grade) were implemented in a conventional three electrode glass-cell. A Au sheet 1 cm^2 and RHE are used as counter electrode and a reference electrode respectively. The electrochemical deposition of antimony at an Au working electrode was done in 0.25 mM Sb_2O_3 (99.999%, Aldrich) + 0.5 M H_2SO_4 electrolyte.

A polycrystalline Au electrode and an antimony modified Au electrode was used as working electrodes for Mg deposition measurements. Magnesium foil was used as a counter electrode and another one as a quasi-reference electrode. All the magnesium electrochemical deposition measurements were carried out in the MBraun glovebox (H_2O < 0.5 ppm, O_2 < 0.5 ppm).

Au-sputtered quartz crystals (5 MHz, d = 25.4 mm) used for the electrochemical quartz crystal microbalance (eQCM) measurements were purchased from Quartztechnik Daun GmbH. The control unit was obtained from Gamry Instruments. Cu deposition from 0.1M $CuSO_4$ in 0.1 M H_2SO_4 solution has been used to calibrate the eQCM.

Preparation of MACC

All chemicals were purchased from Sigma-Aldrich. The tetraglyme was distilled over sodium and stored over molecular sieves (3 Å) until the water content reaches to an amount less than 5 ppm. The water content has been determined by Coulometric Karl Fischer titration (Mettler Toledo). $MgCl_2$ was heated overnight under vacuum at 290°C and then stored under thionyl chloride for 1 week. At low pressure the thionyl chlorid was removed completely. All materials

were handled in an Argon filled glovebox. The MACC electrolyte was prepared by adding tetraglyme (20.5ml) to $MgCl_2$ (0.966g). While stirring the $AlCl_3$ (1.368g) was then added stepwise. The whole mixture was stirred overnight after addition of an equivalent (H_2O: 63 ppm) amount of MgH_2 to reduce the water content (to below 10 ppm after). For details see Hegemann et al. [8]

Cyclic voltammetry (CV) and potential step experiments

Electrochemical measurements in 0.5 M H_2SO_4 were carried out in a conventional three electrode glass H-cell consisting of three compartments for fixing the working electrode, reference electrode and counter electrode. The working electrode is placed in the central compartment and contacted with solution in a hanging meniscus configuration. The reference electrode is placed in the compartment where it is connected to the central compartment with a Luggin capillary. The counter electrode is placed in the compartment, separated from the central compartment by a glass frit.

All electrochemical measurements were carried out using a potentiostat purchased from Pine Instruments, Inc. (model AFBPC1) in combination with homemade LabVIEW program (National Instruments GmbH, Munich, Germany) for recording the cyclic voltammograms (CVs).

XPS-Measurment

To investigate the chemical state of Sb modified electrodes by X-Ray Photoelectron Spectroscopy (XPS), a Sb layer was electrodeposited on Au electrodes (d=10 mm) during a 90 min potential hold at 0.1 V vs RHE in 0.5 m H_2SO_4 with 0.25 mM Sb_2O_3. In a further experiment, an electrode was transferred to an Ar filled glovebox. Insertion of Mg was performed at a constant potential for 820 min at ~ 0.1 V vs $Mg^{2+}|Mg$ in the MACC electrolyte. The sample electrodes are mounted on a crystal holder manufactured out of steel. After the Mg insertion, the sample is washed with dry THF and mounted into a homemade sample transfer system. This transfer system allows the transfer of a sample between the glovebox and the UHV chamber without contact to air. In the measurements in which the Sb electrode was examined without an insertion of magnesium, the electrode was first washed with a mixture gas of Ar:H_2 (9:1) after Sb deposition and then transferred to the XP spectrometer via the laboratory atmosphere. The XP Spectrometer is part of a homemade UHV chamber with a base pressure of $5 \cdot 10^{-10}$ mbar. [35, 36] The used X-Ray source is a non-monochromatized Mg K_α (1253.6 eV) source. As electron energy analyzer a hemispherical electron analyzer (Omnicron NanoTechnology EA 125) is used. Survey spectra were recorded with a pass energy of 50 eV

and an energy resolution of 0.5 eV. High-resolution spectra were recorded with different pass energies (references to this are made in the evaluation) and an energy resolution of 0.1 eV. To increase the signal to noise ratio, the high-resolution spectra are an average of 6 spectra. The binding energy was calibrated using the Au $4f_{7/2}$ peak at 83.95 eV, [37] which is present in all measurements after a certain Ar^+ etching time. The XPS measurements were accompanied by Ar^+-etching (Physical Electronics Model 04-191, 3 kV, $I_{emission}$=25 mA, I_{sample}=1 µA).

4.4 Results and discussion

4.4.1 Preparation of Sb modified Au electrode and eQCM characterization

The cyclic voltammogram of electrochemical deposition of bulk Sb at polycrystalline Au electrode is shown in Fig. 4.1a. It is similar to that observed at Au(111) electrode except for the much broader monolayer stripping peak. [5] Sb UPD (C_1 and C_2) and Sb bulk deposition at Au electrode has been also studied by eQCM. Fig.1 right shows the frequency change during the deposition and dissolution of Sb and the corresponding CVs. When the potential was held at 0 V for different periods of time (10 min and 30 min), the continuous decrease in frequency confirmed bulk Sb deposition according to:

$$Sb^{3+} + 3\ e^- \leftrightarrow Sb \qquad (4.1)$$

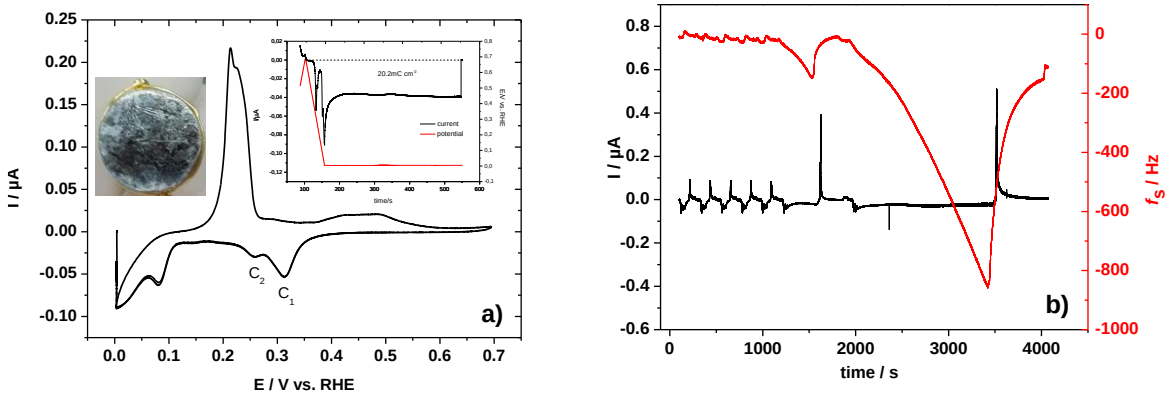

Figure 4. 1a): Cyclic voltammograms of polycrystalline Au in 0.25 mM Sb_2O_3 + 0.5M H_2SO_4 electrolyte at the sweep rate of 10 mV s^{-1}. Inset: current transient when the potential was held at 0 V for 9 min after a potential sweep as indicated in red (dotted) and photo of Au surface modified by large amount of Sb. b): eQCM measurement of Sb deposition on Au electrode, the potential was held at 0 V for 10 min and then for 30 min.

The eQCM results of bulk antimony deposition and dissolution are summarized in table 1. The experimental results of m.p.e value is in a good agreement with the theoretical value. The expected m.p.e value for antimony is 40.58 g/mol, since antimony has an atomic mass of 121.76 g/mol and three electrons are exchanged per deposited Sb-atom.

The faradaic charge of Sb deposition is higher than that of dissolution charge. This difference indicates some side reactions during deposition, e.g. reduction of residual oxygen. After deposition, the Sb-modified Au electrode was transferred to the glovebox under inert atmosphere where the electrochemical insertion of Mg from MACC electrolyte was started.

Table 4. 1: The calculated mpe values for Sb deposition and dissolution during a potential hold at 0 V.

Time of potential holding	**Sweep**	**Δf_s / Hz**	**Δm / µg**	**ΔQ / mC**	**m.p.e / g/mol**
10 min	cathodic	145	2.66	7.4	34.7
	anodic	135.2	1.95	6.1	30.7
30 min	cathodic	842.8	12.15	30.9	37.8
	anodic	797	11.5	27.4	40.4

4.4.2 Mg insertion and deposition

a) Cyclic voltammetry

Fig. 4.2 shows the comparison of electrochemical deposition and stripping behavior of Mg at a bare gold electrode and at a Sb-modified gold electrode in 0.5 M $MgCl_2$ + 0.5 M $AlCl_3$ in tetraglyme. At the bare Au-electrode (see black curve), the slight increase in the current in the potential range of 0 V to -0.3 V (vs. Mg) probably is due to the reduction of oxides or a blocking layer which inhibits nucleation of Mg. The abrupt increase in the current at the potential below -0.3 V is due to bulk deposition of Mg. In the anodic going sweep, the current remains negative in the potential range of -0.75 to 0 V due to the continuous deposition of Mg. At E > 0 V, which is the true reversible Mg potential vs the quasi-reference, as revealed by the straight crossing of the zero line, Mg is dissolved. On Sb-modified gold electrode (see red and blue curves) deposition occurs already 0.32 V more positive, giving rise to a shoulder which we attribute to the insertion of Mg into the Sb-adlayer and formation of the magnesiated binary phase of

antimony (Mg_3Sb_2) (phase diagram in Fig. S4.1 [38]), according to the following equation:

$$2Sb + 3Mg^{2+} + 6e^{-} \Rightarrow Mg_3Sb_2 \quad (4.2)$$

The formation of magnesiated binary phases of Bi and Sn (Mg_3Bi_2 and Mg_2Sn respectively) have been suggested before. [14, 38] From the thermodynamic data for Mg_3Sb_2 alloy formation [39] $\Delta_f^o H = -300193.56\,J/mol$, and $\Delta_f^o S = -52.50\,J/mol \cdot K$, the calculated potential for Mg Sb alloy formation at room temperature is ~550 mV (vs. Mg). Therefore, the experimental positive shift for the insertion of Mg into Sb adlayers of 320 mV is in agreement with the theoretical expectation. After the saturation of the host-layers, bulk deposition of Mg starts with the corresponding increase of the cathodic current. As opposed to bulk deposition on Au, bulk deposition on the Sb modified surface occurs without nucleation overpotential. In the anodic going sweep, the bulk dissolution peak and the de-insertion peak overlap into a wide anodic peak (see red curve). However, de-insertion becomes clearly visible when the potential was reversed at -0.2 V, i.e. before the bulk deposition (see blue curve). Mg de-insertion takes place at a more positive potential compared to that of bulk dissolution. The onset of the de-insertion above 0.6 V vs. Mg is also in agreement with the above mentioned value of 0.55 V for the alloy formation. A large separation between the insertion and de-insertion peaks (ΔE) become obvious of around ≈ 0.3 V for the onset potential, and it probably indicates that the electrochemical behavior is determined by the solid state diffusion step. [40]

Table 4. 2: Dependence of Mg insertion/de-insertion integrated charges on the potential sweep rate and the corresponding coulombic efficiencies. (The charge of insertion was integrated until 0.1 V for 1 mV/s, until 0 V for 5 and 10 mV/s, and until -0.1 V for 20, 50, and 100 mV/s in the cathodic sweep. The charge of de-insertion was integrated between 0.4 V and 1.4 V for all the curves in the anodic sweep.)

υ (mV/s)	**Charge (μC/cm²) (cath.)**	**Charge (μC/cm²) (anod.)**	**Col. Eff. (%)**	**Ratio of Mg:Sb of insertion**
100	2048	2043	99	0.34
50	3536	3451	97.5	0.59
20	4167	4162	99	0.69
10	5406	5284	97.7	0.90
5	6846	6837	99	1.14
1	9111	9061	99.4	1.52

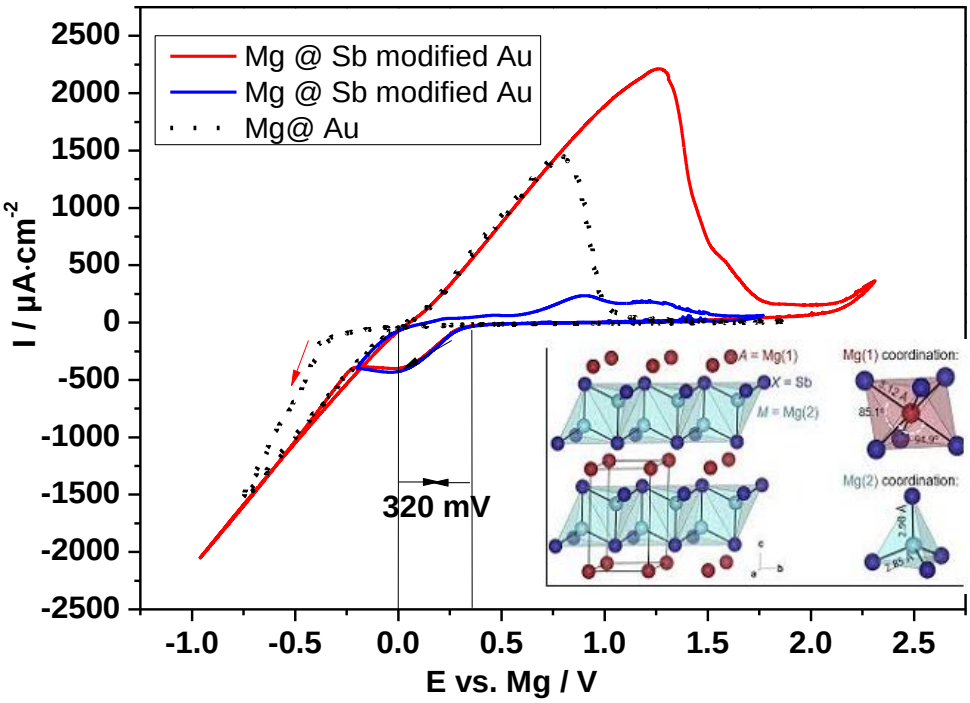

Figure 4. 2: Cyclic voltammograms of Mg deposition/dissolution at bare Au-electrode (black curve) and Sb modified Au-electrode (70 nmol/cm^2 red and blue curves) in MACC/tetraglyme at the sweep rate of 17 mV s^{-1}. (Blue curve): Mg insertion/de-insertion at Sb modified electrode in the potential range of -0.25 V to 1.75 V.

The amount of inserted Mg in Sb is calculated from the charge of the cathodic peak around 0 V to be 56 nmol/cm^2 (Fig. 4.2). The amount of Mg de-inserted in the anodic peaks is 55 nmol/cm^2. Together with the amount of deposited Sb we obtain a ratio for Mg:Sb of 0.8, whereas the theoretical value is 1.5 for the Mg_3Sb_2 phase. The structure model of Mg_3Sb_2 is shown of the insert in Fig. 4.2. [41, 42]

Fig. 4.3 shows the cyclic voltammograms of a Sb modified Au electrode (~31.5 nmol/cm^2 Sb on Au) in MACC/tetraglyme at different sweep rates from 1 to 100 mV s^{-1} in the potential range of -0.1 to 1.4 V vs. Mg. The charge for magnesation/demagnesation of antimony at different potential sweep rates is shown in table 4.2. It increases as expected with decreasing sweep rate and thus with increasing the time of insertion. (A control experiment at 50 mV/s recorded at the end of experiment the CV measurements gave an identical result as in the beginning.). Thus, there is no deactivation of the electrode surface and no noticeable change in the Sb layer in the course of these cyclic voltammograms.) The ratio between the faradaic charge of anodic (de-insertion) and cathodic (insertion) gives the apparent coulombic efficiency. So, close to 99 % of the deposited magnesium is dissolved in the subsequent anodic sweep independently of the sweep rate. The cathodic charge is slightly larger than anodic charge due to parasitic reactions

such as hydrogen evolution or reduction of organic solvent [8, 43].The ratio between Mg and Sb for the sweep rate (1 mV) of 1.52 (theoretical value 1.5 for Mg_3Sb_2), means that the Mg is saturated in the Sb layers for low sweep rates. For higher sweep rates, the time is not sufficient to achieve saturation obviously diffusion is too slow. This is also the reason for the incomplete magnesiation in the experiment of fig 4.2.

4.4.3 Determination of diffusion coefficient of Mg into Sb adlayers

From cyclic voltammetry, we can simply estimate the diffusion coefficient from the change of peak current with varying sweep rates assuming solid state diffusion as rate limiting using eq.(4.3) (Randles-Sevcik equation for an irreversible system and semi-infinite diffusion) [44]:

$$I_p = 2.99 \times 10^5 n\sqrt{\alpha n_\alpha} A C_0 D_{Mg}^{0.5} v^{0.5} \quad (4.3)$$

Here, I_p is the peak current in amps (A); n is the number of electrons transferred in the reaction ($2e^-$ for Mg^{2+}); A is the apparent surface area of the working electrode (0.785 cm^2); D_{Mg} is the diffusion coefficient of Mg ($cm^2\ s^{-1}$) in Sb; υ is the sweep rate ($V\ s^{-1}$); C_0 is the concentration of Mg (theoretically, 0.038 mol cm^{-3} since the density of Mg_3Sb_2 alloy is 4.02 g/cm^3) in the solid state. For this equation to hold, it is assumed that during deposition the concentration of Mg within the Sb layer at the surface is constant (the saturation concentration) and drops to zero within the Sb layer (semi-infinite diffusion condition). The assumption of semi-infinite diffusion is only valid for higher sweep rates where saturation of the Sb layer is largely incomplete. (On the contrary, for low sweep rates or high diffusion coefficients and fast charge transfer, the extent of insertion is determined by thermodynamics, and the current will be proportional to the sweep rate.) Thus for diffusion controlled processes, I_p should depend linearly on $\sqrt{v}$ as, e.g., was found for lithiation of graphite particle electrode. [45]

An almost linear relationship between the Mg insertion and de-insertion peak currents and square root of sweep rate was obtained as shown in the inset of Fig. 4.3. A plot of the peak potential vs. ln $v^{1/2}$ results in a slope of 120 mV/dec suggesting an irreversible charge transfer, see Fig. S4.2. From the slope of 1315 mA $V^{-1/2}$ $s^{1/2}$ in fig. 4.3, we estimate a diffusion coefficient of 1.1×10^{-14} cm^2 s^{-1} assuming $\alpha n_\alpha = 0.5$ for Mg insertion. (Since the above mentioned boundary conditions are not valid for de-insertion, the diffusion coefficient is calculated from the insertion peak only.)

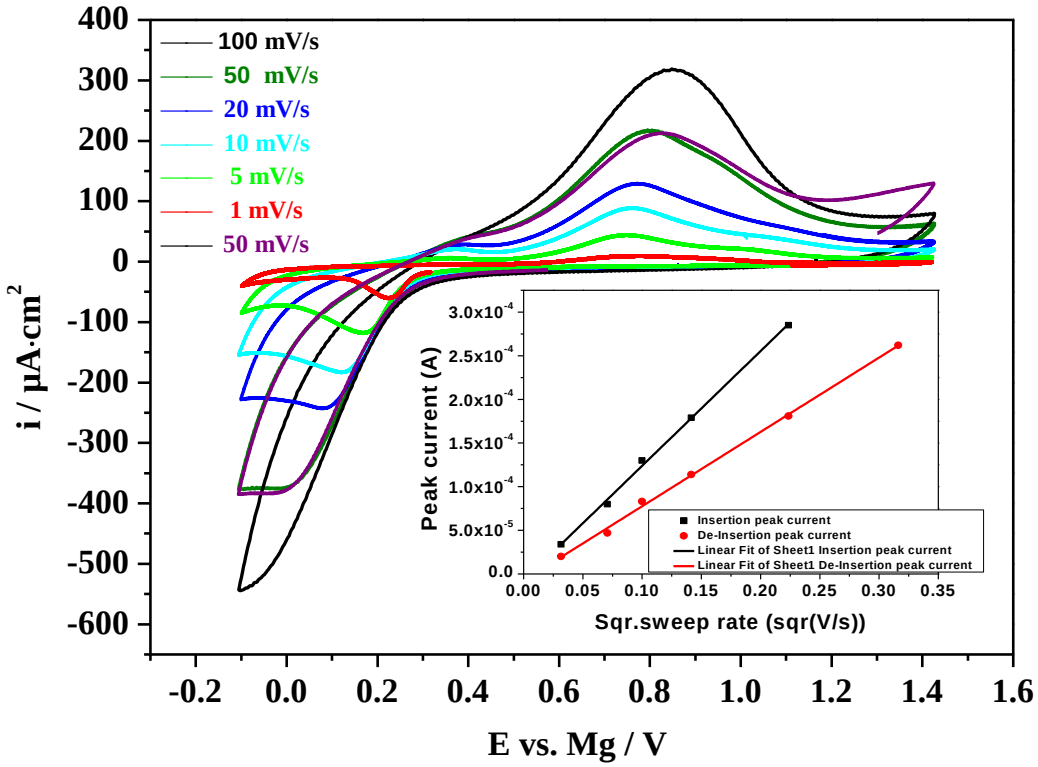

Figure 4. 3: Cyclic voltammograms of Mg insertion into Sb modified Au electrode (~31.5 nmol/cm^2) in MACC/tetraglyme at different sweep rates from 1 to 100 mV s^{-1}. Inset: Plot of I_p (peaks current) vs. $\upsilon^{1/2}$ (square root of scan rate). Here, the value of αn_α is 0.5. $I_p = 2.99 \times 10^5 n\sqrt{\alpha n_\alpha} A C_0 D_{Mg}^{0.5} v^{0.5}$

b) Potential step

A more accurate determination of the diffusion coefficient and the insertion kinetics should be possible in potential step experiments. Three different potential step experiments were performed with different Sb thicknesses. Here, thick Sb layers were used in order to achieve a long period during which the Cottrell Equation is valid. Before each step experiment a CV for Mg-insertion/de-insertion including Mg bulk deposition and dissolution was recorded (cf. Fig. S4.3). The potential was then first held at 1.5 V (where complete de-insertion of Mg takes place) in MACC electrolyte. Afterwards, the potential was stepped to a potential where magnesium is inserted into the antimony layer. Then, the potential was stepped back to 1.5 V for 10 min where the extraction of magnesium takes place, the faradaic current drops down to nearly 0 after a time depending on the insertion period and potential.

A potential step experiment to various insertion potentials is shown in Figure 4.4. The potential was stepped from 1.5 V vs. Mg to the selected potentials between -0.1 V and 0.2 V vs. Mg (each potential for 5 min and for 10 min), where magnesium is inserted into the antimony layer. (Then

the potential was stepped back to 1.5 V until the current dropped to nearly 0.) After the initial double layer charging, the current for insertion nearly stays constant or slightly increases for few seconds, indicating an initial kinetic rate limitation; the slight current increase may be due to some contribution of a nucleation and growth process. A plot of the potential versus the logarithm of the initial current (after double layer charging) is shown in S4.4. The value of Tafel slope is 370 mV/decade, much higher than the typical value of 120 mV/decade for one-electron transfer. This value of Tafel slope is equivalent to $\alpha n_\alpha = 0.16$ and therefore, for an assumed α of 0.5 to 0.3, to the transfer of olny 0.5 to 0.3 elementary changes. This is certainly related to the fact that we are dealing here with a coupled ion-electron transfer: Sb has a layered structure, and the Mg^{2+} ions are likely to initially diffuse (together with the counter ion) in between those layers before a phase transition to the Zintl phase is taking place, which is indicated by the current maxima in the transients. These effects certainly deserve more attention, but this is beyond the scope of this paper. [46] A further reason for the large Tafel slope might be the potential dependence of the equilibrium concentration of Mg in the alloy. Using the above value of $\alpha n_\alpha = 0.162$ instead of 0.5 for the calculation of the diffusions coefficient from fig 4.3 in the Randles-Sevcik equation (eq. 4.3). We obtain D = 3.4×10^{-14} cm^2/s.

The concentration profiles in Fig. 4.5 visualize the change from kinetic to diffusion limitation for the Mg insertion in Sb. The initially nearly constant current corresponds to a constant concentration gradient. This is reasonable because the reactant is the Mg ion in solution, and therefore the reaction rate of the charge transfer does not depend on the concentration in the Sb. (This is different from the usual mixed charge-transfer and diffusion control.) Or, vice versa, one can take the experimental result as a proof that the surface concentration of Mg in Sb is not influencing the rate. Concentration at the interface increases until the concentration corresponding to the equilibrium concentration at the given potential is reached. Then diffusion control sets in as described by the Cottrell equation and later the limited thickness of the Sb layer leads to further flattening.

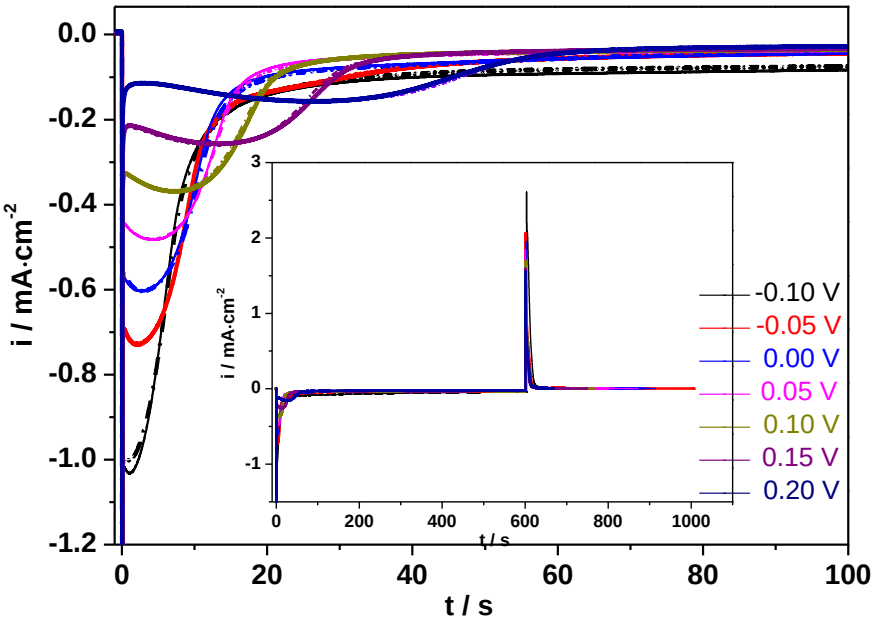

Figure 4. 4: The fisrt 300 s of Mg-insertion into Sb from MACC/tetraglyme electrolyte at different potentials respectively. Insert: Potential step experiment for Mg insertion and de-insertion. (The fresh deposited Sb-adlayers is about 82 nmol cm^{-2}. Repeated experiments for 5 min deposition are shown as broken line. (Hardly visible because superposition)

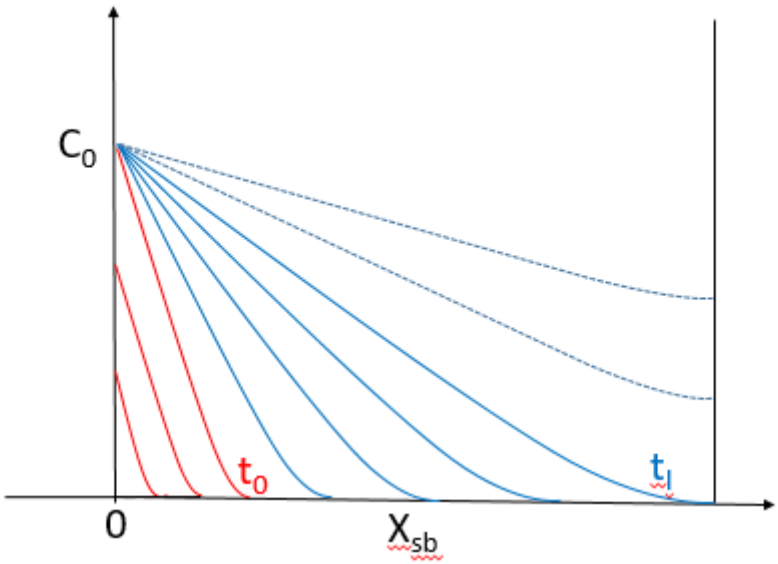

Figure 4. 5: Schematic concentration profiles for the Mg-insertion into Sb-adlayer. Red line: kinetically controlled process before the onset of the current decrease. Blue line: after the concentration reaches the maximal concentration C_0, concentration decreases as typical for diffusion limited processes. After t_l boundary condition for Cottrell behavior is no longer valid (dotted lines).

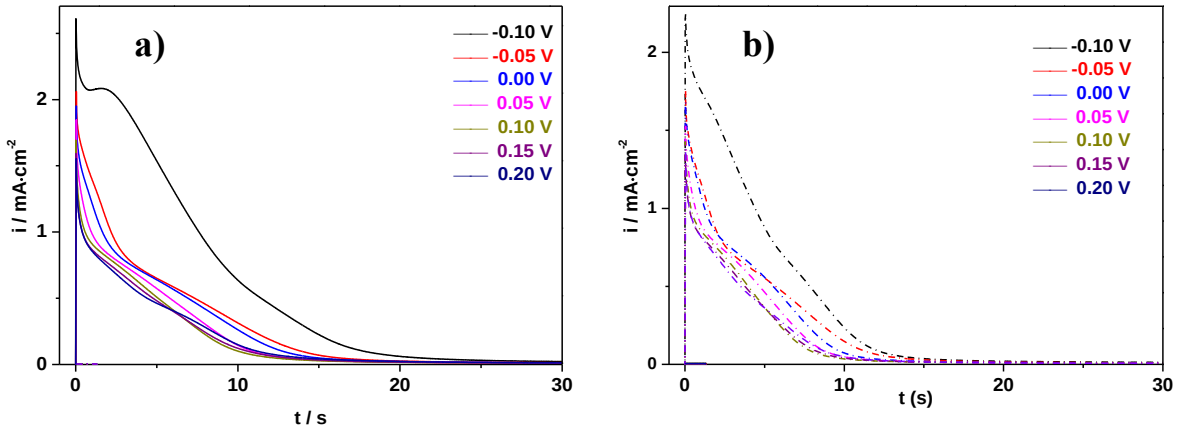

Figure 4. 6: Potential step experiment for Mg de-insertion in MACC/tetraglyme electrolyte from Sb modified Au electrode (~82 nmol cm^{-2}) at 1.5 V after insertion at the indicated potential values for a) 10 min and b) 5 min.

In order to check whether the initial current increase (indicating a nucleation phenomenon) might be due to a slow reduction of an oxide layer on the Sb formed during transfer from the aqueous preparation solution to the glove box, we also examined the lithium insertion into Sb-modified polycrystalline Au-electrode by potential step experiments, There, no indication for a nucleation is visible from the plot of current versus time and therefor an oxide layer does not seem to be the cause of the nucleation phenomenon. (More Details in supporting information S4.5-S4.8 and table S4.1.)

Fig. 4.6 shows the current transients during de-insertion of Mg. Only after insertion at the lowest potential and for the longer insertion time of 10 min. a similar transient was observed as during insertion, notably a constant initial current with a faint indication of nucleation. Qualitatively the shape of the others resembles more to that expected for a mixed charge transfer – diffusion controlled process, which is reasonable since the rate of Mg-de-insertion depends on the concentration of Mg in the Sb layer. However, since a homogeneous distribution of Mg and equilibration is not achieved during the insertion period, the transients have a more complicated shape.

Table 4. 3: Dependence of Mg insertion/de-insertion integrated charges (The steady states current at t (10 min) was subtracted) during the potential step experiments on potential of insertion, the corresponding coulombic efficiencies, the ratio between Sb and Mg and the diffusions coefficient. (~82 nmol cm^{-2} Sb on Au and Surface area was 0.785 cm^2)

E/V vs. Mg	amount of Sb / nmol cm^{-2}	Charge 10min cath. /mC cm^{-2} (corr. value)	Charge 10 min anod /mC cm^{-2}	Charge 5min cath. /mC cm^{-2} (corr. value)	Charge 5 min anod /mC cm^{-2}	Ratio of Mg:Sb for insertion [de-insertion] for 10 min	D (10 min) /10^{-14} cm^2/s Insertion [de-insertion]	D (5 min) /10^{-14} cm^2/s Insertion [de-insertion]
0.2	~82	20.8 (6.57)	7.11	14.4 (7.24)	6.05	0,41 (0.45)	1.43 [6.28]	1.45 [2.55]
0.15	~82	23.4 (8.11)	8.52	15.6 (7.33)	6.55	0.52 (0.55)	2.52 [8.11]	2.50 [5.88]
0.1	~82	24.7 (8.39)	9.05	16.0 (7.40)	8.26	0.54 (0.58)	3.45 [5.15]	3.12 [6.02]
0.05	~82	25.8 (9.15)	11.9	17.2 (8.77)	9.75	0.59 (0.76)	4.47 [10.7]	4.47 [5.59]
0	~82	28.0 (11.1)	14.3	19.1 (10.6)	11.9	0.71 (0.91)	5.31 [11.4]	6.58 [11.5]
-0.05	~82	29.8 (11.6)	16.9	20.6 (11.1)	13.7	0.73 (1.08)	7.03 [14.2]	7.88 [11.1]
-0.1	~82	35.8 (15.9)	24.7	26.7 (16.5)	15.8	1.00 (1.56)	4.82 [13.5]	5.02 [10.1]
0.1	~145	17.5 (13.1)	13.8	n.d.	n.d.	0.47 (0.62)	2.08 [4.65]	n.d.
0	~145	33.9 (22.5)	27.9	n.d.	n.d.	0.80 (1.28)	3.57 [8.32]	n.d.
-0.1	~218	80.4 (31.5)	66.9	49.2 (30.3)	43.2	1.91 (1.59)	7.71 [17.4]	6.43 [4.3]

The charges for insertion and de-insertion of magnesium are summarized in table 4.3 together with the ratio between the deposited Sb and the inserted Mg. As obvious from a comparison of the charge at 0 V with the theoretical charge for the formation of the Mg_3Sb_2 alloy (23.7 mC/cm^2), the uncorrected deposition charges are clearly too large. This is caused by the large, constant residual currents, which we attribute to side reactions: The MACC solutions are produced from the reaction between $MgCl_2$ and $AlCl_3$ in TG solvents. Usually the solutions need a "conditioning" processes [47] before a high magnesium deposition/dissolution reversibility is achieved. During this process aluminum could also be inserted into the Sb-adlayers or be deposited on the surface after the Mg-insertion, the aluminum deposition is slow and occurs over long time. [48] (Phase diagram for Al-Sb system see in S4.9) This will be further

discussed in the context of the XPS measurements below. In addition TG may decompose at the potential limits. [8] Therefore, we also corrected the cathodic charge for Mg-insertion for 5 min and 10 min by subtracting the current at t =10 min for each step. But those corrected values are far too low and lower than the charges observed during dissolution. Since during dissolution of the inserted Mg the current drops to zero, the corresponding charge values seem most reliable. In Table 4.3 it is seen that the ratio between inserted Mg and deposited Sb (calculated from the de-insertion charge) increases with decreasing insertion potential from 0.45 to 1.56 after 10 min insertion, to be compared to the theoretical value of 1.5. This latter value for -0.1 V is only slightly too large, which may be caused by some bulk deposition. It should be kept in mind, though, that some Mg might have been replaced by Al during these long deposition times, but since the only possible alloy phase of Sb and Al is AlSb, the corresponding charge for saturation with Al is the same as for saturation with Mg.

A similar potential step experiment was performed for another freshly deposited Sb-adlayer (~145 nmol cm^{-2}) (Figure S4.10) and a similar result was obtained. The corresponding CV is shown in Figure S4.10. A slight current increase at the beginning of the Mg-insertion is observed again for both potential steps (0 V and 0.1 V). After 10 min insertion the current does not drop to 0, but reached a constant value (8 µA at0.1 V and 10 µA at 0 V). The charges of Mg-insertion/de-insertion are also included in Table. 3 as well as the ratio between the deposited Sb and the inserted Mg. In a further experiment (with 218 nmol cm^{-2}) we varied the insertion time from 10 to 600 s at -0.01 V with a similar result (fig. S4.11). In particular, this experiment confirms that saturation is not achieved after 5 min.

To verify that the current decrease during insertion after the faint maximum is due to diffusion limitation, and in order to better estimate the diffusion coefficient, we evaluated the transients according to the Cottrell equation for semi-infinite diffusion:

$$i = \frac{zFA\sqrt{D}C_o}{\sqrt{\pi t}} \tag{4.4}$$

(Here, A is the surface area; C_0 is the magnesium concentration in the antimony layer at the boundary to the electrolyte during the potential step; at a potential just before bulk deposition it should correspond to the maximum Mg content in Sb, which theoretically is 0.038 mol cm^{-3} since the density of Mg_3Sb_2 alloy is 4.02 g/cm^3.) Of course, diffusion into a thin layer of Sb follows this equation only as long as the concentration at the other boundary, the Sb/Au interface, remains zero. On the other hand, because of the nucleation and kinetic hindrance at the beginning, pure diffusion behavior as described by the Cottrel Equation only starts after the

initial time t_0 (cf. fig. 4.5). Therefore it is more convenient to use the integrated Cottrell equation, where short times are at the origin of the graph of the charge Q vs. $t^{0.5}$, eq. (4.5). This way of elucidation of the data has the advantage that the exact start of validity of the Cottrell behavior does not play a role. (The plot of Q vs $t^{0.5}$ are shown in fig. S4.12.) (Of course, this relation only holds as long as the concentration of Mg at the inner boundary to Au remains zero.)

Even more instructive is a plot, which is linear in time, i.e. Q^2 vs t, allowing a better comparison with the original transients in fig.4.6. D can then be calculated from the slope as shown in Fig. 4.7. After an initial deposition of about 2 mC/cm^2, Q^2 increase linearly up to a value, which is similar value for all potential steps (about $Q^2 = 32.8$ (mC/cm)^2, Q=5.73 mC/cm^2) This charge corresponds to about 1/3 of the saturation value. At longer times the concentration at the 2nd boundary, the interface between Sb and Au, does not remain zero, and therefore the Cottrel Equation is no longer valid. (see the concentration profile in Fig. 4.5) The plots of Q^2 vs t for ~145 nmol/cm^2 and ~218 nmol/cm^2 are shown in fig.S4.13 and S4.14.

$$Q = \frac{2zFA\sqrt{D}C_o}{\sqrt{\pi}}\sqrt{t} \tag{4.5}$$

The corresponding diffusion coefficients are included in table 3. (The results of ~218 nmol/cm^2 are shown in table S4.2) It should be noted that only for the most negative deposition potential the concentration difference between the surface and the Sb bulk corresponds to C_0. At more positive potentials the concentration at the surface is lower, the highest possible value being the equilibrium concentration corresponding to the applied deposition potential. Since this equilibrium concentration is not known, we used C_0 for the concentration in eq. (4.4) and (4.5), knowing that this leads to values of D which should be corrected by $(C_0/C)^2$, where C is the concentration at the surface. Therefore, the value of 7×10^{-14} cm^2/s should represent the most reliable value. The value obtained from the evaluation of the Randles Sevcik equation (eq. 4.3) of 3.4×10^{-14} cm^2/s is close to that observed in the potential step to 0.1 V. This is reasonable since this is about the peak potential of the CVs.

When considering these diffusion coefficients, the following aspects have to be taken into account:

1. Although very thin Sb layers deposited on Au (111) are extremely smooth, [5] this is certainly not the case to the same extent for the somewhat thicker layers deposited on polycrystalline Au.
2. The incorporation of Mg into the Sb layer leads to an expansion and changing thickness.

3. The evaluation of the slope in fig. 4.7 is done at a time after the maximum in the current transient, i.e. after the phase transition. Therefore, the diffusion coefficient likely corresponds to that of Mg in Mg_3Sb_2. However, this is the phase transition close to the surface only, and therefore the experimental value of D may well be influenced by the propagation rate of the phase change.
4. The diffusion coefficients obtained from the de-insertion transients are considerably larger.

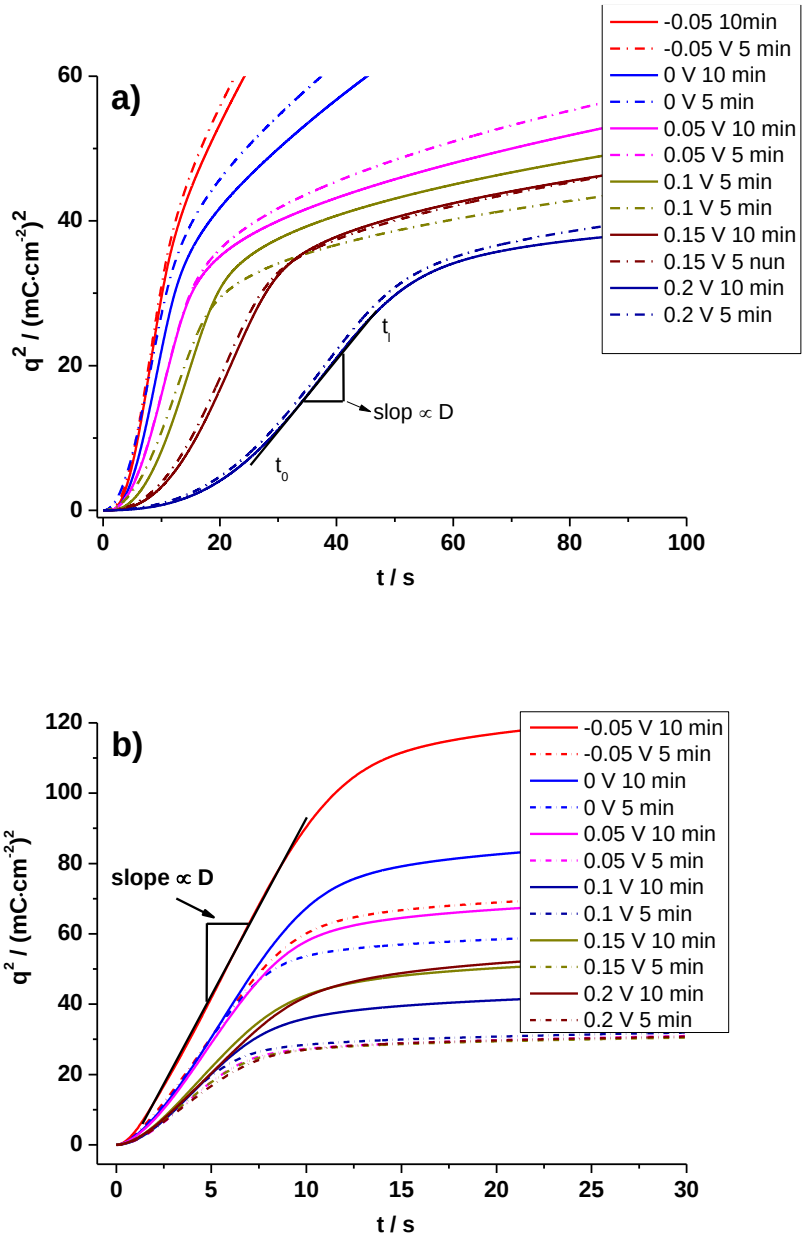

Figure 4. 7: Plot of transient Charge (Q^2 vs. t) for a) Mg insertion at different potentials (from -0.05 V to 0.2V) with the insertion time 10 min and b) Mg de-insertion at 1.5 V in Sb layers and the slope for calculation of the diffusions coefficient. (Sb: ~82 nmol/cm^2; surface area: 0.785 cm^2)

c) PITT-Measurement (Potentiostatic Intermittent Titration Technique)

The experiment starts by recording the open circuit potential (OCP at about 1.8 V vs. Mg/Mg^{2+}) of this system. Then, a step composed of 30 s pulse at the potential 0.3 V (where the insertion of Mg take place), followed by 2 minutes of relaxation with the cell switched off is applied. Afterwards, again a potential pulse to a potential increased by -0.1 V is applied, and the current signal is recorded for 30 s, followed by 2 minutes of relaxation time. The same potential increment is consecutively applied, starting from the voltage resulting from the previous step and the signal is recorded for 30 s. The potential pulses are applied until the lower limit of -0.1 V is reached, where bulk deposition of Mg starts. Each potential pulse is followed by 2 minutes of relaxation time. Afterwards, from 1.0 V positive potential increments of 0.1 V are consecutively applied to the voltage resulting from the previous step, and the signal is also recorded for 30 s. The potential pulses are repeated until the upper limit of 1.5 V is reached. Each potential pulse is followed by 2 minutes of relaxation time.

During the negative potential pulses, Mg-ions are inserted into Sb. The reverse occurs during the positive discharging potential pulses, where the Mg-ions are de-inserted from the negative electrode, and the corresponding current is recorded. (Fig. 4.8 a). During each relaxation period, the cell is switched off. Then, at the beginning of each potential pulse, a peak in the current signal is observed. Afterwards, the value of the current signal decreases in an exponential like fashion. The shape of the transient is similar to that of the previous potential step experiments. Differently from the previous potential step experiments, each new insertion is occurring into Sb already containing some Mg.

The total charge deposited in the 6 pulses amounts to 35.8 mC/cm^2, corresponding to a Mg:Sb ratio of 1.76. Theoretically, the total charge of dissolution should equal that of deposition/insertion. This, is obviously not the case. The reason is the same as for the large residual current in the potential step experiment of fig.4.4: slow decomposition of the electrolyte during the negative potential pulses and probably currentless dissolution of Mg during the potential holds. This effect will be discussed below.

Also, the rest potential during the relaxation period attains fairly positive potential values and does not remain constant suggesting that despite of the large negative charge corresponding to saturation of Sb with Mg a real saturation is not achieved. (Ideally, at the end of the relaxation period, the concentration is identical within the thin layer, and the potential corresponds to the equilibrium potential for that concentration, which is calculated from the total charge flown.)

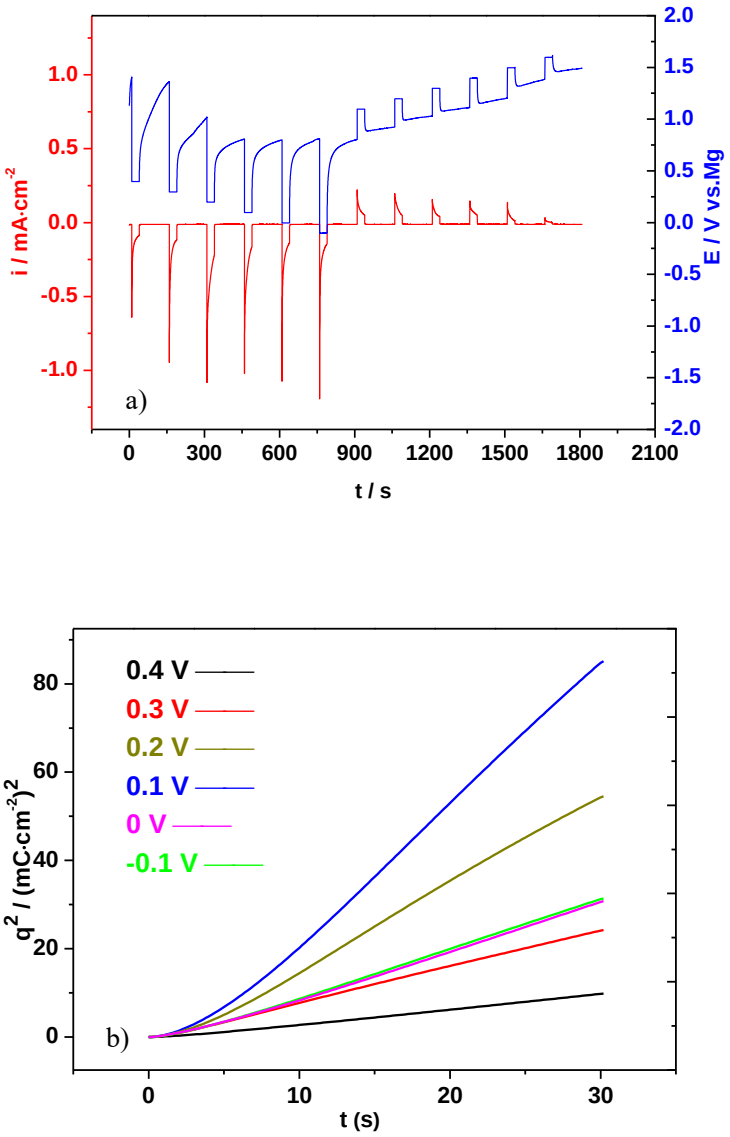

Figure 4. 8: a) Potentials and relative current Curve from the PITT-measurement to determine the diffusions coefficient of Mg-insertion and de-insertion in the Sb-adlayers. Potential from 0.4V to -0.1 V for the insertion and from 1.0 V to 1.5 V for the de-insertion. b) Plot of the Q^2 versus the time for the insertion process to calculate the diffusion coefficient. Where the signal becomes linear, the diffusion coefficient is calculated from the slope. (Sb: ~105 nmol/cm^2; surface area: 0.785 cm^2)

The value of D is again calculated from the linear slope of Q^2 vs. the time of insertion as shown in Fig. 4.8 b with the integrated Cottrell equation, here for the C_0 we used for simplicity the saturations concentration for the calculation of the diffusions coefficient. (The plot of Q vs $t^{0.5}$ are shown in Fig. S4.15.) The estimated diffusion coefficients from the PITT measurement are summarized in Table. 4.4. It should be kept in mind though that it would be more correct to use the concentration difference ΔC between the achievable equilibrium concentration at the

respective potential (C_0 in the case of the lowest potentials) and the surface concentration achieved in the preceding relaxation period; the values therefor ar off by the factor $(C_0/\Delta C)^2$. It is therefore not astonishing that the value for the lowest potential pulse ($D = 1.6\times10^{-14}$ cm^2/s is lower than that in the potential step experiment in table 4.3 ($D = 7\times10^{-14}$ cm^2/s). A further difference is that in the potential step experiment the Mg ions always first diffuse into the pure Sb layers during the insertion process, followed by the structure change from Sb to Mg_3Sb_2. But in the PITT measurement, there is a 30 s relaxation time between two alloying processes. In this relaxation period, the Sb structure can partially change to Mg_3Sb_2, which leads to a diffusion of Mg ion into a mixture of Sb and Mg_3Sb_2 phase. The mobility of Mg ions in the pure Sb layers is probably higher. But the largest value that observed at 0.1 V is close to that in the potential experiment at 0.1 V and therefore can be taken as a confirmation for the determination of the diffusion coefficients.

Table 4. 4: the calculated value of the diffusion coefficient for Mg-ions into Sb-adlayers by using PITT-measurment, (the amount of deposited Sb is ~105 nmol/cm^{-2})

Potential (V)	**D (/10^{-14} cm^2/s)**	**Ratio of Mg:Sb (sum value)**
0.4	0.5	0.15
0.3	1.1	0.39
0.2	2.8	0.67
0.1	4.6	0.95
0	1.5	1.30
-0.1	1.6	1.76

4.4.4 XPS characterization of the Sb electrode after magnesium insertion

After the electrochemical deposition/insertion of Mg into Sb, the electrode was removed from the cell and washed with 5 mL THF. (The XPS characterization of the Sb-deposit is shown in S4.16.The amount of deposited Sb is estimated from the deposition current and also the inserted Mg to be 1000 nmol/cm^2) The electrode was then transferred under Ar atmosphere to the UHV of the XP spectrometer. The recorded XPS Survey spectra are shown in Figure 4.9.

The XPS spectra could be assigned the specific core electron excitation of Mg, Al, Cl, C, Sb, O and of the substrate Au. With the help of Ar^+ etching a depth profile is also obtained. After a total duration of 270 min of Ar^+ etching the XP spectrum shows almost only the core level

excitations of the Au substrate. (This shows that the chemical composition of the total deposited Sb film, together with the modification by Mg insertion, is examined in the following.) The first spectrum after the transfer is dominated by carbon. The chemical environment of the carbon can be seen from the high resolution C 1s region. (More details about the C signal see Fig. S4.17)

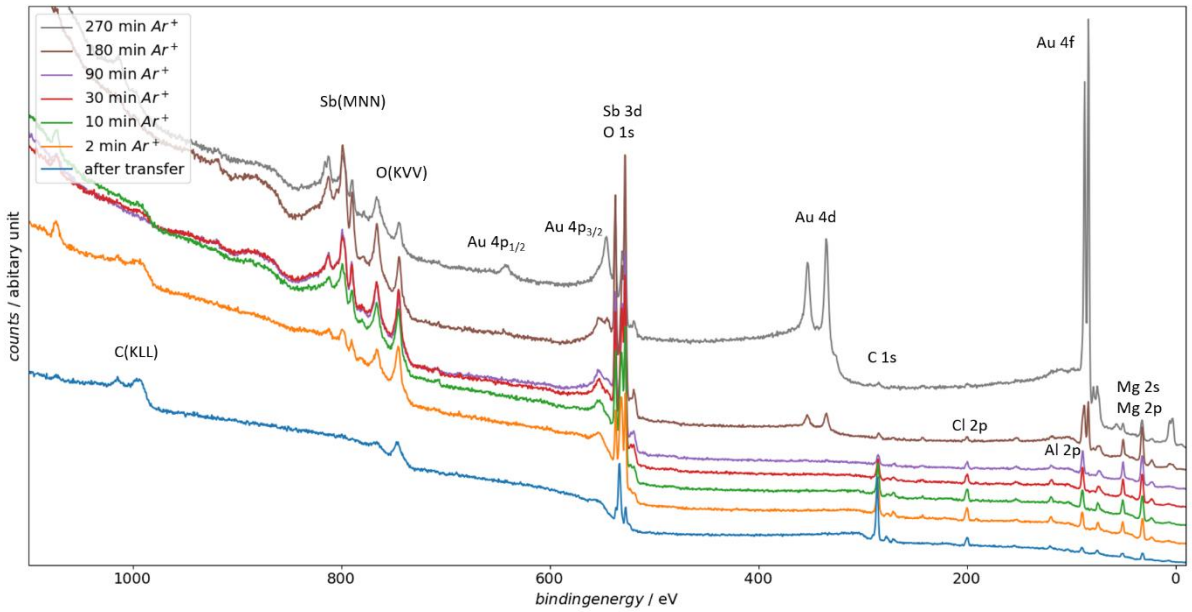

Figure 4. 9: XP survey of the Sb modified Au electrode after the Mg insertion. The XP spectra are taken after the transfer and for different Ar^+ etching times.

The high resolution spectrum of the Mg 2p core level excitation in Fig. 4.10 (a) shows a relatively broad peak, which shifts to low binding energies for longer Ar^+ etch times. A deconvolution of these peaks into different Mg species does not seem reliable. However, the width of the peak indicates that $MgCl_2$, MgOH, MgO and Mg are likely to contribute. The shift of the peak to higher binding energies indicates a higher proportion of Mg(0) in the investigated layer for longer Ar^+ etch times.

By means of the deconvolution of the Al 2p core level excitation (see Fig. 4.10 (b)) it can be shown that elemental aluminium is present within the deposited layer at a binding energy of 72.8 eV [49]. In the deconvolutions routine, Al(0) and Al(+III) were each fitted with a doublet of gaussian-lorentz peaks. The area ratio corresponds to the expected ratio for a 2p core level excitation and the peak generation was fixed at 0.42 eV [50]. Thus it can be shown that a side reaction during Mg insertion in Sb is the deposition of elemental aluminium. Most of the Al(+III) on the electrode surface is probably formed from Al(0) during the transfer of the electrode into the XP spectrometer, as discussed above.

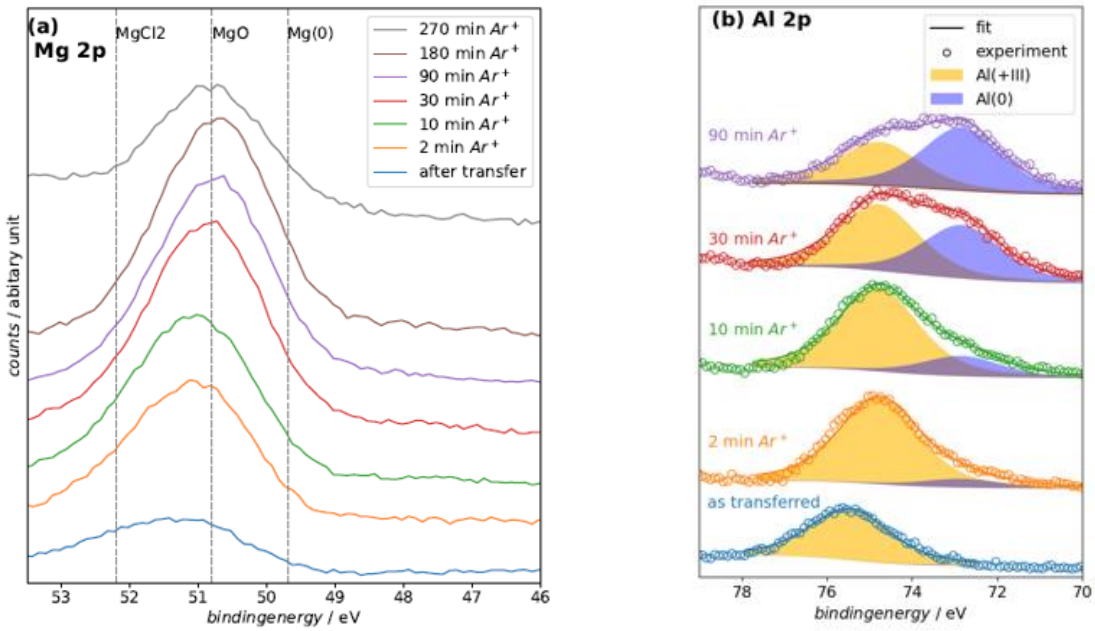

Figure 4. 10: (a) High resolution XP spectra showing the Mg 2p core level excitation. (b) High resolution XP spectra showing the Al 2p core level excitation. Here a deconvolution of the experimental data is performed. Thereby two species Al(0) and Al(+III) each with a p excitation doublet with an binding energy difference of 0.42 eV were used.[50] Both sets of spectra were recorded with a pass energy of 50 eV and a step width of 0.1 eV.

The atomic ratios were calculated from the individual XP spectra using the atomic sensitivity factors of the core level excitation of the different peaks [51]. In Figure 4.11 these are shown in a bar chart. For a better overview, the influence of carbon was not included. The values shown are the atomic proportion in relation to the sum of all elements shown. It is noticeable that the value for oxygen is very high and does not decay even after longer sputtering times. It can be assumed that the surface or large parts of the Sb layer are oxidized during the transfer into the XP spectrometer due to traces of O_2 in the Ar atmosphere. (The contamination of O_2 and H_2O in the Ar gas used is 2 ppm/mol) For a rough estimate and as an upper limit for the amount of oxygen uptake, with these concentration are calculated for the 5 min of transfer time a close of 5×10^5 langmuir, sufficient for 5×10^5 monolayers of oxygen. It is therefore conclusive that during the duration of the transfer (about 5 min), the deposited layers oxidize, which explains the high oxygen signal. The products of this oxidation reaction are hydroxides and oxides. In fact, the deconvoluted O 1s signal indicates the presence of these products. The binding energy of the deconvoluted O 1s region 1 (see red shaded area in fig. S4.18) indicates hydroxides, whereas the deconvoluted region 2 (see orange shaded area in fig. S4.18) indicates oxides in the XP spectra.

In general, this oxidation process limits the significance of the chemical shift of the binding

energies, since oxidation is an artifact of the transfer process. Nevertheless, the XP spectra unravel some important information about the electrochemical reactions during the insertion.

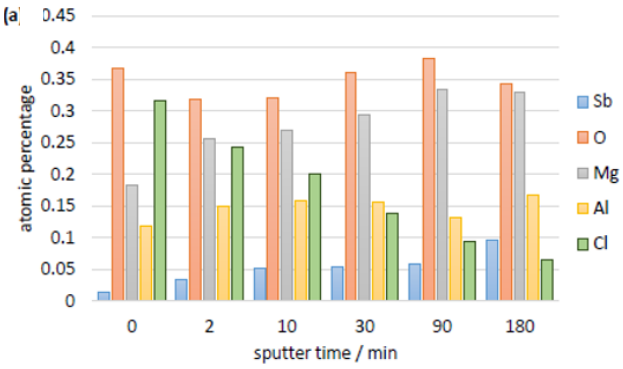

Figure 4. 11: Atomic ratios of Sb, O, Mg, Al and Cl to the sum of the displayed elements. The ratios were calculated out of the XP spectra taking the atomic sensitivity factors of the core level excitations into account (corresponding element and symmetry of the atomic orbital) [51]. Regarding the oxygen signal, this evaluation is more complex and the O 1s signal had to be deconvoluted from the overlap between the O 1s and Sb 3d signal (see Fig. S4.18).

An important observation is the dependence of the Cl signal as a function of the Ar^+ etch time. It can be seen that the Cl signal decreases with increasing Ar^+ etch time and therefore it is a species that can be found on the surface. In addition to the deposited Mg, Al is also observed in the XP spectra. In Fig. 4.11 it is shown that the ratio of Al to Mg decreases with increasing Ar^+ etch time. Thus the Al signal is also originated from the electrode surface. Similar observations were made by Gewirth and coworkers in the case of bulk magnesium deposition from MACC in THF based electrolyte. [52]

When looking at the ratio of Mg to Sb it is striking that the experimentally determined amount of Mg is greater than corresponding to the stoichiometry of Mg_3Sb_2. This finding could have several reasons. For one, it is conceivable that the antimony oxide present is chemically reduced by the inserted Mg, which would result in the formation of magnesium oxide. The spectrum after insertion shows no detectable amount of Sb in the oxidized state. (cf. Fig S4.18) Furthermore, in the presence of Cl^- ions in the electrolyte a magnesium surface decorated with Cl^- could be formed. This was postulated in the MACC/THF system and is due to the underlying exothermic process. [53] Furthermore, the formation of Al-Sb alloy is conceivable. The reasons listed above would explain the larger amount of Mg.

4.4.5 Discussion

Mechanism of the Mg insertion into Sb out of MACC

On the basis of the findings in the XPS experiments and the literature on Mg deposition from MACC a mechanism for the insertion of Mg into Sb from MACC will be formulated. Most reports in the literature have been conducted in the THF based electrolyte and report a magnesium dimer as an electroactive species for magnesium deposition with the molecular formula $[Mg_2(\mu\text{-}Cl)_3(THF)_6]^+$ [52, 54-57] If THF is exchanged by tetraglyme, the exact structure of the active species is not known, but we assume that it is a similar species (probably the dimer), because the electrochemical measurements between tetraglyme and THF do not differ in terms of electrochemically deposited species and reversibility. [55] Of course, the coordination of the dimer by tetraglyme would be different than by THF. Therefore, the coordination by tetraglyme is neglected in the following and only the structure of dimer $[Mg_2(\mu\text{-}Cl)_3]^+$ is considered. The $[Mg_2(\mu\text{-}Cl)_3]^+$ complex is forming out of $MgCl_2$ and $AlCl_3$ in solution:

$$2MgCl_2 + AlCl_3 \longrightarrow [Mg_2(\mu\text{-}Cl)_3]^+ + AlCl_4^- \qquad (4.6)$$

In a simplifyed reaction $[Mg_2(\mu\text{-}Cl)_3]^+$ is electrochemically inserted into Sb:

$$3[Mg_2(\mu\text{-}Cl)_3]^+ + 4\ Sb + 12e^- \longrightarrow 2Mg_3Sb_2 + {}^-9Cl^- \qquad (4.7)$$

The authors would like to point out that the mechanism of the charge transfer is currently discussed in the literature [58]. Due to the different electrochemical potentials of Mg_3Sb_2 ($E(Mg_3Sb_2$=550 mV vs. Mg/Mg^{2+} from calculation of the thermodynamic data) and (the standard potential of E(Al) = -1.67 V vs. RHE, so E(Al) = 0.7 vs. Mg/Mg^{2+} and E(Al) = 0.3 vs. Al/Al^{3+} (1.0 V vs. Mg/Mg^{2+}) for AlSb phase formation), there is thermodynamically driving force that the insertion compound can reduce $AlCl_4^-$ to metallic Al:

$$2Mg_3Sb_2 + 4AlCl_4^- \longrightarrow 3[Mg_2(\mu\text{-}Cl)_3]^+ + 2Sb + 4Al + 7Cl^- \qquad (4.8)$$

The free Cl^- anions generated in equations (4.7) and (4.8) can now adsorb on the electrode surface (as observed in the XPS measurement). A catalysis of a magnesium deposition by Cl^- is reasonable, as it a well-known phenomenon for different metal deposition [59, 60]. Another advantage of chloride anions is the binding properties of chloride to water, which can reduce the activity of free water. This would prevent passivation of the reactive Mg_3Sb_2 electrode by residual water in the electrolyte. In addition, reaction (4.8) would generate free Sb, allowing reaction (4.7) to take place again. These argument can be an explanation for the background current in the potential jump experiment after long periods of time (compare Fig. 4.4).

From CV, the diffusion coefficient of Mg insertion into Sb multilayers was estimated to be

1.1×10^{-14} cm^2/s with $\alpha n_\alpha = 0.5$ and 3.4×10^{-14} cm^2/s with the experimental value for $\alpha n_\alpha = 0.16$; in PITT measurements a value of 4.6×10^{-14} cm^2/s was found. From potential step experiments the most reliable value is 7.0×10^{-14} cm^2/s. These values are in good agreement, in particular when considering that the values lower than 7.0×10^{-14} cm^2/s correspond to positive potentials where saturation is not achieved. They are about three orders of magnitude lower than the value obtained for the diffusion of Li^+ ions in composite WO_3 [27, 61, 62] and $Li_{1-x}CoO_2$ [34, 63, 64]. They are one order of magnitude lower than the value obtained from CVs for Li^+ ions in $LiFePO_4$ [40] Mao el. determined the ion diffusion coefficient (1.97×10^{-14} cm^2 s^{-1}) of magnesium in the CuS-solid-solution region near the end of discharging and charging. [24] These values are higher than the estimated value from GITT measurements for Mg diffusion into porous Bi electrode (particle size of 0.1 nm) in magnesium organohaloaluminate electrolyte. [22]

The diffusion of Mg in solid host structures is more hindered than that of monovalent alkali cations such as Li^+ and Na^+. [65] Furthermore, it has to be taken into account that the above literature values of apparent diffusion coefficients correspond to the effective diffusion within a composite layer of the material and whereas we have determined the diffusion in the bulk of the homogenous material. This discrepancy on the diffusion coefficient values may be due to the difference in the time of relaxation of Mg into electrodeposited Sb. In the cyclic voltammetry, the relaxation time after the insertion is not enough to get a stable profile with homogenous distribution of Mg in the whole layers of Sb. Consequently, during the stripping process, there is a competition between the continuous distribution of Mg especially in the deep layers and the extraction of Mg from the outer layers. In potential step experiments for 10 min was enough to relax the Mg in the antimony layers and to obtain constant concentration of Mg everywhere. The incongruity of D_{Li} values obtained from different electrochemical techniques has been reported. [66-68]

The observed Tafel slope of 370 mV/decade is unexpectedly high. The corresponding value of the apparent transfer coefficient of 0.16 suggests that the Mg ion is only slightly discharged when undergoing the transfer from the liquid to the Sb phase and therefore stays in contact with the Cl^- counter ion during the rate-determining step.

4.5 Conclusions

The electrochemical deposition of antimony on Au was investigated in 0.5 M H_2SO_4 containing 0.25 mM Sb_2O_3 by cyclic voltammetry. Magnesium deposition/dissolution on Au and Sb modified Au electrodes were investigated in 0.5 M $MgCl_2$ + 0.5 M $AlCl_3$ in tetraglyme electrolyte. At the Sb modified Au electrode insertion of Mg into Sb starts at around 320 mV more positive than the onset potential of bulk deposition at Au electrode. From the ratio of the amount of the inserted Mg to that of the deposited Sb we conclude that a Mg_3Sb_2 alloy is formed in the corresponding peak. High coulombic efficiencies of Mg stripping to insertion charges have been observed in cyclic voltammetry and potential step experiments. The MACC is a complex system that during the insertion of Mg, the Al and Cl could also be inserted into the Sb-adlayers. An observation of Al and Cl signals are found on the surface from the XPS data.

Consistent data for the diffusion rate of Mg into Sb multilayers were obtained from CV, from potential step experiments and from PITT measurements. The best estimate for the diffusion coefficient is 7×10^{-14} cm^2s^{-1}, which is two orders of magnitude lower than the value for Li^+ ions from our work (see supporting information).

The mechanism for the insertion of Mg into Sb from MACC is complex. The very high Tafel slope suggests that the Mg ion is hardly discharged in the rate-determining step and therefore might initially enter the Sb layer together with its counter ion. Furthermore, Mg in the insertion compound may in part be slowly replaced by Al from the MACC electrolyte. But the exact role of Cl^- and the suggested mechanism are not yet completely clear, further studies are necessary.

References

[1] J. Muldoon, C. B. Bucur, T. Gregory, *Chemical Reviews* **2014**, *114*, 11683.

[2] Z. Ma, D. R. MacFarlane, M. Kar, *Batteries & Supercaps* **2019**, *2*, 115.

[3] J. Luo, Y. Bi, L. Zhang, X. Zhang, T. L. Liu, *Angewandte Chemie International Edition*, *58*, 6967.

[4] H. Dong, Y. Liang, O. Tutusaus, R. Mohtadi, Y. Zhang, F. Hao, Y. Yao, *Joule* **2019**, *3*, 782.

[5] L. Zan, D. Xing, A. Abd-El-Latif, H. Baltruschat, *Beilstein Journal of Nanotechnology* **2019**, *10*, 2541.

[6] **D. Aurbach**, **Y. Cohen**, **M. Moshkovich**, *Electrochemical and Solid-State Letters* **2001**, *4*, A113.

[7] D. Aurbach, A. Schechter, M. Moshkovich, Y. Cohen, *Journal of The Electrochemical Society* **2001**, *148*, A1004.

[8] P. Hegemann, M. Hegemann, L. Zan, H. Baltruschat, *Journal of The Electrochemical Society* **2019**, *166*, A245.

[9] P. Reinsberg, A. A. Abd-El-Latif, H. Baltruschat, *Electrochimica Acta* **2018**, *273*, 424.

[10] P. Fischer, P. Reinsberg, R. M. Schwarz, M. Marinaro, M. Wachtler, T. Diemant, R. J. Behm, H. Baltruschat, L. Jörissen, *Journal of The Electrochemical Society* **2018**, *165*, A2037.

[11] P. Reinsberg, C. J. Bondue, H. Baltruschat, *Journal of Physical Chemistry C* **2016**, *120*, 22179.

[12] Y. Cheng, Y. Shao, L. R. Parent, M. L. Sushko, G. Li, P. V. Sushko, N. D. Browning, C. Wang, J. Liu, *Advanced Materials* **2015**, *27*, 6598.

[13] T. S. Arthur, N. Singh, M. Matsui, *Electrochemistry Communications* **2012**, *16*, 103.

[14] N. Singh, T. S. Arthur, C. Ling, M. Matsui, F. Mizuno, *Chemical communications* **2013**, *49*, 149.

[15] D.-T. Nguyen, S.-W. Song, *Journal of Power Sources* **2017**, *368*, 11.

[16] H. Yaghoobnejad Asl, J. Fu, H. Kumar, S. S. Welborn, V. B. Shenoy, E. Detsi, *Chemistry of Materials* **2018**, *30*, 1815.

[17] Y.-H. Tan, W.-T. Yao, T. Zhang, T. Ma, L.-L. Lu, F. Zhou, H.-B. Yao, S.-H. Yu, *ACS nano* **2018**, *12*, 5856.

[18] Y. Shao, M. Gu, X. Li, Z. Nie, P. Zuo, G. Li, T. Liu, J. Xiao, Y. Cheng, C. Wang, J.-G. Zhang, J. Liu, *Nano Letters* **2014**, *14*, 255.

[19] R. A. DiLeo, Q. Zhang, A. C. Marschilok, K. J. Takeuchi, E. S. Takeuchi, *ECS Electrochemistry Letters* **2015**, *4*, A10.

[20] O. I. Malyi, T. L. Tan, S. Manzhos, *Journal of Power Sources* **2013**, *233*, 341.

[21] B.-C. Zhou, S.-L. Shang, Y. Wang, Z.-K. Liu, *Data in brief* **2015**, *5*, 900.

[22] M. Ramanathan, A. Benmayza, J. Prakash, N. Singh, F. Mizuno, *Journal of The Electrochemical Society* **2016**, *163*, A477.

[23] W. Wang, L. Liu, P.-F. Wang, T.-T. Zuo, Y.-X. Yin, N. Wu, J.-M. Zhou, Y. Wei, Y.-G. Guo, *Chemical communications* **2018**, *54*, 1714.

[24] M. Mao, T. Gao, S. Hou, F. Wang, J. Chen, Z. Wei, X. Fan, X. Ji, J. Ma, C. Wang, *Nano letters* **2019**, *19*, 6665.

[25] J. Wang, J. M. Bell, *Solar energy materials and solar cells* **1999**, *58*, 411.

[26] C. s. O. Avellaneda, L. O. S. BulhÃµes, *Solid State Ionics* **2003**, *165*, 59.

[27] M. Stromme Mattsson, *Solid State Ionics* **2000**, *131*, 261.

[28] A. V. Ivanishchev, A. V. Churikov, I. A. Ivanishcheva, A. V. Ushakov, *Ionics* **2016**, *22*, 483.

[29] J. Kaspar, M. Graczyk-Zajac, R. Riedel, *Electrochimica Acta* **2014**, *115*, 665.

[30] W. J. A. S. Gomes, D. g. M. AraulÌjo, A. J. F. Carvalho, S. P. Campana-Filho, F. Huguenin, *The Journal of Physical Chemistry C* **2013**, *117*, 16774.

[31] B. Horstmann, B. Gallant, R. Mitchell, W. G. Bessler, Y. Shao-Horn, M. Z. Bazant, *The Journal of Physical Chemistry Letters* **2013**, *4*, 4217.

[32] A. V. Churikov, V. O. Romanova, *Ionics* **2013**, *18*, 837.

[33] C. Kim, P. J. Phillips, B. Key, T. Yi, D. Nordlund, Y.-S. Yu, R. D. Bayliss, S.-D. Han, M. He, Z. Zhang, A. K. Burrell, R. F. Klie, J. Cabana, *Advanced Materials* **2015**, *27*, 3377.

[34] M. D. Levi, G. Salitra, B. Markovsky, H. Teller, D. Aurbach, U. Heider, L. Heider, *Journal of The Electrochemical Society* **1999**, *146*, 1279.

[35] A. S. Shatla, A. A. Abd-El-Latif, S. Ayata, D. Demir, H. Baltruschat, *Electrochimica Acta* **2020**, *334*, 135556.

[36] H. M. Amin, C. J. Bondue, S. Eswara, U. Kaiser, H. Baltruschat, *Electrocatalysis* **2017**, *8*, 540.

[37] C. J. Powell, *Journal of Electron Spectroscopy and Related Phenomena* **2012**, *185*, 1.

[38] T. B. Massalski, *ASM international* **1992**, *3*, 2874.

[39] A. A. Nayeb-Hashemi, J. B. Clark, *Bulletin of Alloy Phase Diagrams* **1984**, *5*.

[40] B. Kumar, J. Kumar, R. Leese, J. P. Fellner, S. J. Rodrigues, K. M. Abraham, *Journal of the Electrochemical Society* **2010**, *157*, A50.

[41] J.-i. Tani, M. Takahashi, H. Kido, *Physica B: Condensed Matter* **2010**, *405*, 4219.

[42] S. Gupta, A. K. Ganguli, J. D. Corbett, *Inorganic chemistry* **2006**, *45*, 8175.

[43] F. M. Michalak, J. R. Owen, *Solid State Ionics* **1996**, *86*, 965.

[44] A. J. Bard, L. R. Faulkner, *Electrochemical Methods: Fundamentals and Applications*, 2nd ed., John Wiley & Sons Inc., New York, Weinheim, **2001**.

[45] B. Markovsky, M. D. Levi, D. Aurbach, *Electrochimica Acta* **1998**, *43*, 2287.

[46] D. Fraggedakis, M. McEldrew, R. B. Smith, Y. Krishnan, Y. R. Zhang, P. Bai, W. C. Chueh, Y. Shao-Horn, M. Z. Bazant, *Electrochimica Acta* **2021**, *367*.

[47] C. J. Barile, R. Spatney, K. R. Zavadil, A. A. Gewirth, *Journal of Physical Chemistry C* **2014**, *118*, 10694.

[48] I. Shterenberg, M. Salama, Y. Gofer, E. Levi, D. Aurbach, *Mrs Bulletin* **2014**, *39*, 453.

[49] C. Hinnen, D. Imbert, J. M. Siffre, P. Marcus, *Applied Surface Science* **1994**, *78*, 219.

[50] A. K.-V. Alexander V. Naumkin, Stephen W. Gaarenstroom, Cedric J. Powell *X ray Photoelectron Spectroscopy Database 20, Version 4.1:* http://srdata.nist.gov/xps **2012**.

[51] C. D. Wagner, L. E. Davis, M. V. Zeller, J. A. Taylor, R. H. Raymond, L. H. Gale, *Surface and interface analysis* **1981**, *3*, 211.

[52] C. J. Barile, E. C. Barile, K. R. Zavadil, R. G. Nuzzo, A. A. Gewirth, *Journal of Physical Chemistry C* **2014**, *118*, 27623.

[53] P. Canepa, G. S. Gautam, R. Malik, S. Jayaraman, Z. Rong, K. R. Zavadil, K. Persson, G. Ceder, *Chemistry of Materials* **2015**, *27*, 3317.

[54] O. Mizrahi, N. Amir, E. Pollak, O. Chusid, V. Marks, H. Gottlieb, L. Larush, E. Zinigrad, D. Aurbach, *Journal of the Electrochemical Society* **2008**, *155*, A103.

[55] C. J. Barile, R. G. Nuzzo, A. A. Gewirth, *The Journal of Physical Chemistry C* **2015**, *119*, 13524.

[56] K. A. See, K. W. Chapman, L. Zhu, K. M. Wiaderek, O. J. Borkiewicz, C. J. Barile, P. J. Chupas, A. A. Gewirth, *Journal of the American Chemical Society* **2016**, *138*, 328.

[57] K. A. See, Y.-M. Liu, Y. Ha, C. J. Barile, A. A. Gewirth, *ACS Applied Materials & Interfaces* **2017**, *9*, 35729.

[58] K. Ta, K. A. See, A. A. Gewirth, *The Journal of Physical Chemistry C* **2018**, *122*, 13790.

[59] D. C. Johnson, E. W. Resnick, *Analytical Chemistry* **1977**, *49*, 1918.

[60] Z. Nagy, J. P. Blaudeau, N. C. Hung, L. A. Curtiss, D. J. Zurawski, *Journal of The Electrochemical Society* **1995**, *142*, L87.

[61] M. Deepa, T. K. Saxena, D. P. Singh, K. N. Sood, S. A. Agnihotry, *Electrochimica Acta* **2006**, *51*, 1974.

[62] G. Leftheriotis, S. Papaefthimiou, P. Yianoulis, *Solid State Ionics* **2007**, *178*, 259.

[63] Y.-I. Jang, B. J. Neudecker, N. J. Dudney, *Electrochemical and Solid-State Letters* **2001**, *4*, A74.

[64] H. Xia, S. Y. Meng, L. Lu, G. Ceder, **2007**.

[65] G. G. Amatucci, F. Badway, A. Singhal, B. Beaudoin, G. Skandan, T. Bowmer, I. Plitza, N. Pereira, T. Chapman, R. Jaworski, *Journal of the Electrochemical Society* **2001**, *148*, A940.

[66] K. Tang, X. Yu, J. Sun, H. Li, X. Huang, *Electrochimica Acta* **2011**, *56*, 4869.

[67] Y.-C. Chang, J.-H. Jong, G. T.-K. Fey, *Journal of The Electrochemical Society* **2000**, *147*, 2033.

[68] P. Yu, B. N. Popov, J. A. Ritter, R. E. White, *Journal of The Electrochemical Society* **1999**, *146*, 8.

Supporting Information

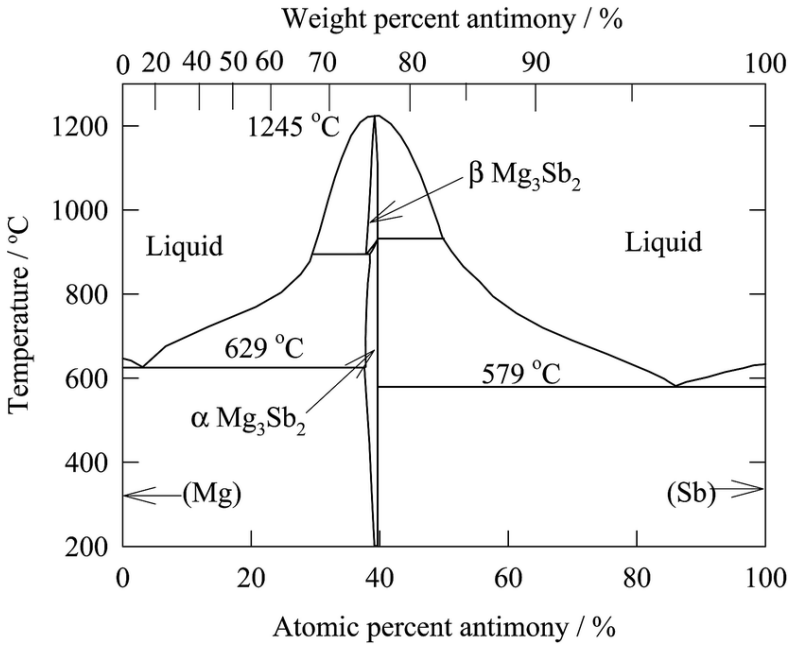

Figure S4. 1: Phase Diagrams of Mg-Sb binary systems. There is only one thermodynamic stable phase Mg_3Sb_2 for this binary system. [1]

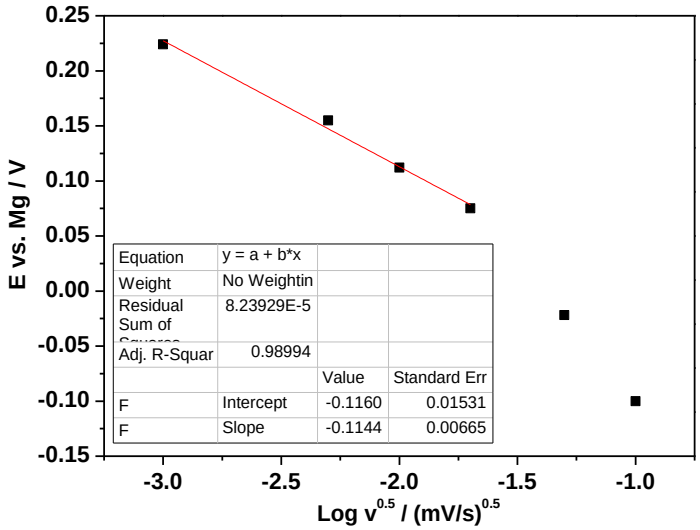

Figure S4. 2: Plot of the peak potential for Mg-insertion versus $\log(v^{0.5})$ (here, v is the sweep rate from 1 mV/s to 100 mV/s, The Sb-layer is about 82 nmol/cm^2) and the used equation is showing as follow:

$$E_p = E^0 - \frac{RT}{\propto F}[0.078 + ln\left(\frac{D_0^{0.5}}{k^0}\right) + ln(\frac{\alpha F v}{RT})^{0.5}]$$

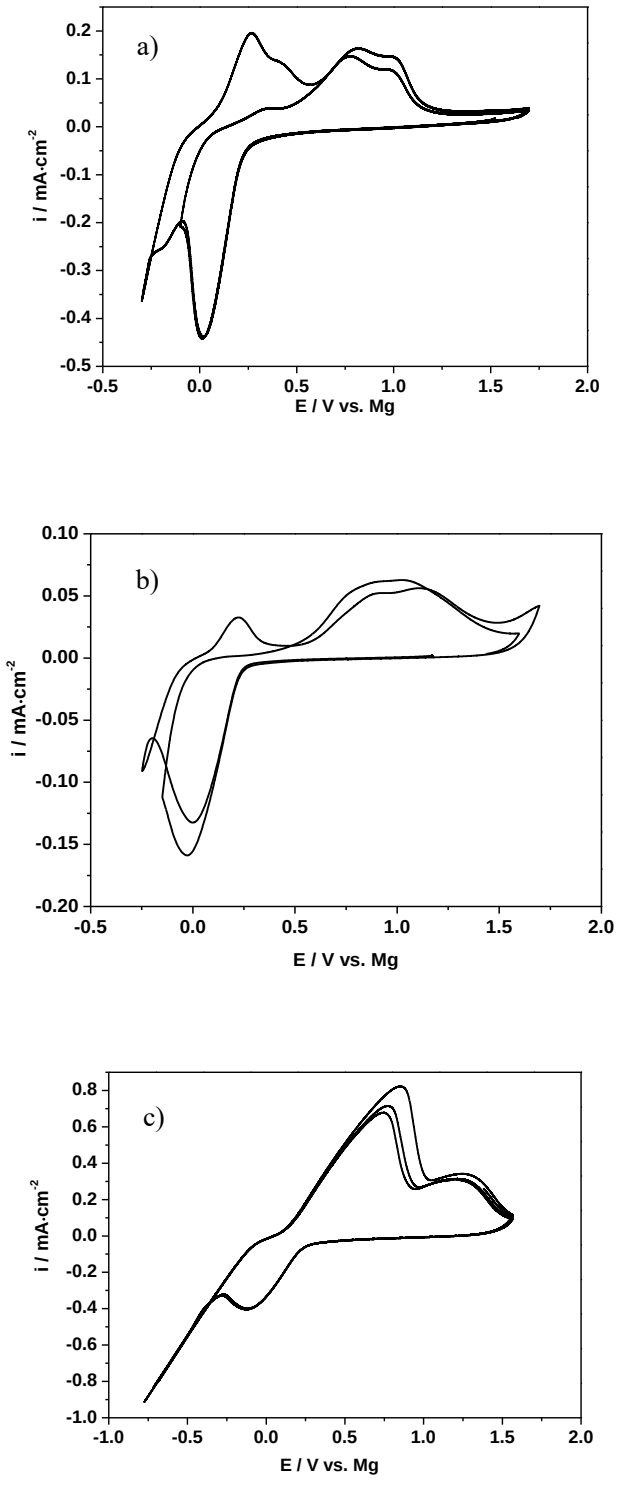

Figure S4. 3: Cyclic voltammograms of Mg insertion into Sb modified Au in MACC/tetraglyme electrode a) Sb: ~82 nmol/cm^2 at weep rates 50 mV s^{-1}; b) Sb: ~145 nmol/cm^2 at weep rates 1 mV s^{-1}; c) Sb: ~218 nmol/cm^2 at weep rates 10 mV s^{-1}.

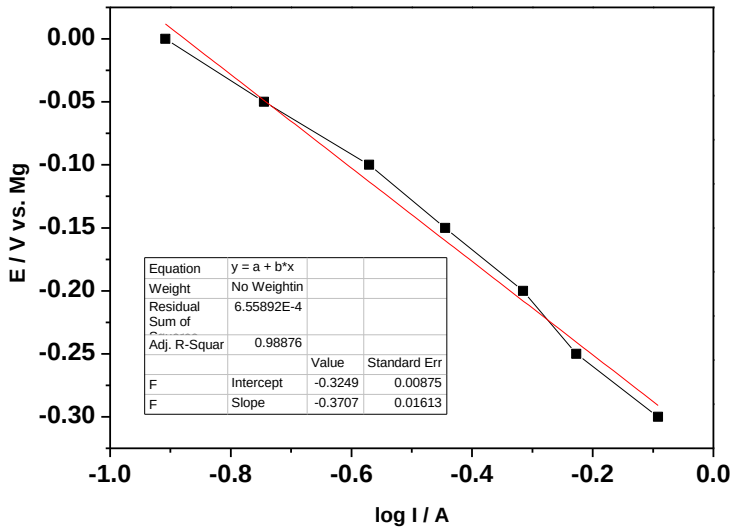

Figure S4. 4: Tafel plot of the overpotential versus the limited current for each jump potential. From the linear fitting the tafel slop could be determined to be 370 mV/disc, this value is higher than the usual value for kinetically controlled charge transfer, which is 120 mV/div. Certainly also the potential dependence of the equilibrium alloy composition plays a role.

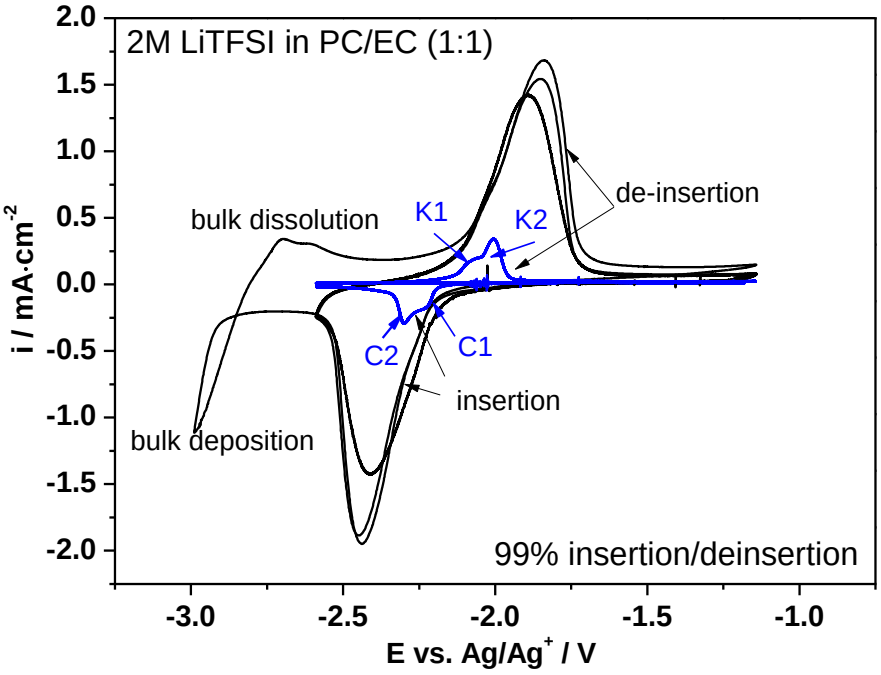

Figure S4. 5: Cyclic voltammograms of Li deposition/dissolution at Sb modified Au-electrode (183 nmol/cm²) at sweep rate 10 mV/s in the potential range of -3.0 V to -1.2 V vs. Ag/Ag^+ (-0.3 V to 1.5 V vs. Li) (black) and 1 mV/s in the potential range of -2.6 V to -1.2 V vs. Ag/Ag^+ (0.1 V to 1.5 vs. Li) (blue).

Figure S4.5 shows the electrochemical deposition/dissolution and insertion/de-insertion of Li at a Sb-modified gold electrode in 2 M LiTFSI in PC/EC (1:1) electrolyte. Both curve shows the increase in the current at potential -2.1 V due to the Li-insertion into Sb-adlayers and formation of lithium interaction binary phase of antimony. (Phase diagram is showed in Fig. S4.6) [2] The abrupt increase in the current at the potential below -2.8 V is due to bulk deposition of Li (black curve). On the anodic going sweep Li is dissolved at E > -2.8 V, which is the true reversible Li potential vs the quasi-reference. The de-insertion start in the anodic direction at -2.1 V. The insertion and de-insertion of Li into Sb-adlayers indicates a reversible system with a reversibly of 99% for insertion/de-insertion. In both direction two peaks are observed A1 and A2 for the cathodic sweep, C1 and C2 for anodic sweep. We attribute this to two different Li-Sb intermetallic compounds. The amount of the deposited Sb and the inserted Li in Sb (from the charge of the sum A1 and A2 in the cathodic going sweep with 1 mV/s) was calculated to be 183 and 433 nmol/cm^2 respectively according to the corresponding peak in the cyclic voltammograms. The charge for the insertion with the sweep rate from 10 mV/s is same as for 1 mV/s. The ratio between the amounts of the inserted Li to the deposited Sb is thus 2.36. (Li:Sb = 2 for Li_2Sb)

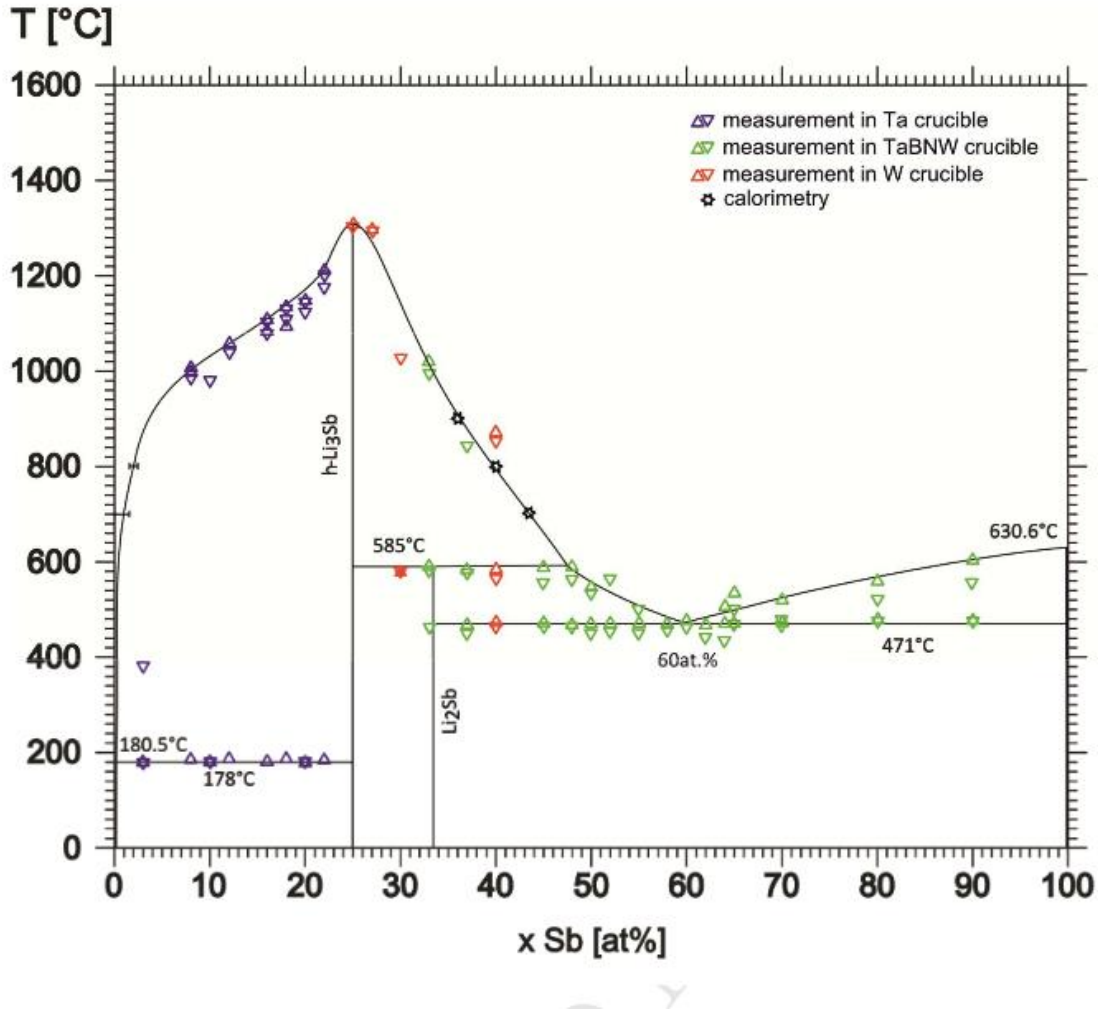

Figure S4. 6: Phase Diagrams of Li-Sb binary systems. There are two thermodynamic stable phases for this binary system, Li_3Sb and Li_2Sb.

In the potential step experiments which are shown in Fig. S4.7, the potential was first held at -0.8 V vs Ag/Ag^+ in Li^+ containing PC/EC electrolyte. Afterwards, the potential was stepped to a more negative potential (-2.6 V vs. Ag/Ag^+), at which lithium could be inserted into the antimony layer, for different time periods (60-600 s), then the potential was stepped back to -0.8 V vs. Ag/Ag^+ until the current drop to the base line. The plot of the current versus the time for lithium insertion is shown in figure S4.7. The insert shows the insertion of the first 30 s. The current transient has a different shape compared to the Mg-insertion. Here a nucleation process is not observed. The current for Li-insertion drops directly after the double layer charge and after 100 s reach the base line. Obviously, insertion is faster and less side reactions occur than during the Mg-insertion.

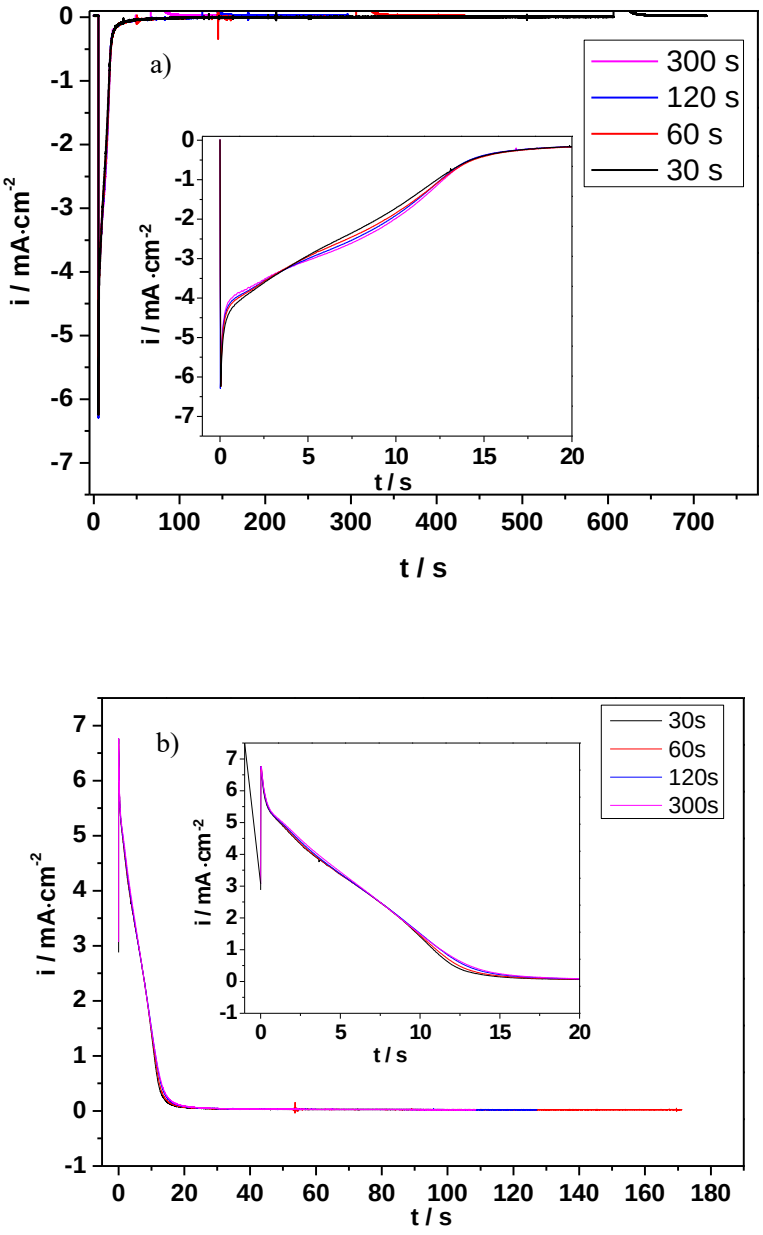

Figure S4. 7: Potential step experiment for a) Li-insertion and b) Li de-insertion from 2 M LiTFSI/TC/EC electrolyte into Sb modified Au electrode at -2.6 V vs. Ag/Ag^+ respectively. Insert: the first 30 s of the a) Li-insertion and b) Li de-insertion.

The charges of the insertion/de-insertion, the ratio between the deposited Sb and the inserted Li and the calculated diffusions coefficient are summarized in table S4.1. The charges of Li insertion and extraction only slightly increase with the time of insertion. The apparent coulombic efficiency is about 99%. The stronger current decrease after 10 s is likely to be caused by the limited thickness of the SB – layer: The diffusion layer reaches the inner boundary between Sb and the Au substrate.

Table S4. 1: Dependence of Li insertion/de-insertion integrated charges during the potential step experiments on potential of insertion, the corresponding coulombic efficiencies, the ratio between Sb and Li and the diffusions coefficient. (~183 nmol cm^{-2} Sb on Au)

Insertions time (s)	**Charge (mC/cm^2) (cath.)**	**Charge (mC/cm^2) (anod.)**	**Eff. (%)**	**Ratio of Li:Sb**	**D ($*10^{-12}$) insertion (de-insertion)**
30	37.8	37.7	99.8	2.13	4.5 (1.6)
60	38.7	38.4	99.3	2.18	5.3 (2.1)
120	39.6	39.5	99.6	2.23	6.1 (2.5)
300	39.8	39.6	99.2	2.25	6.4 (2.9)

By using the integrated Cottrell equation the diffusions coefficient could be calculated. In the figure S8 shows the plot of the charge Q versus square root of the time s. The diffusion coefficient varies within 4.5-6.4×10^{-12} cm^2 s^{-1} depending on the lithium content in the Sb modified electrode, which is two orders of magnitude higher than the value for Mg^{2+} ions, and similar to the reported value.[3, 4] (Here for the C_0 we used the saturations concentration, theoretically 0.017 mol cm^{-3} for Li_2Sb) We cannot exclude some contribution of a kinetic hindrance, more data would be necessary.

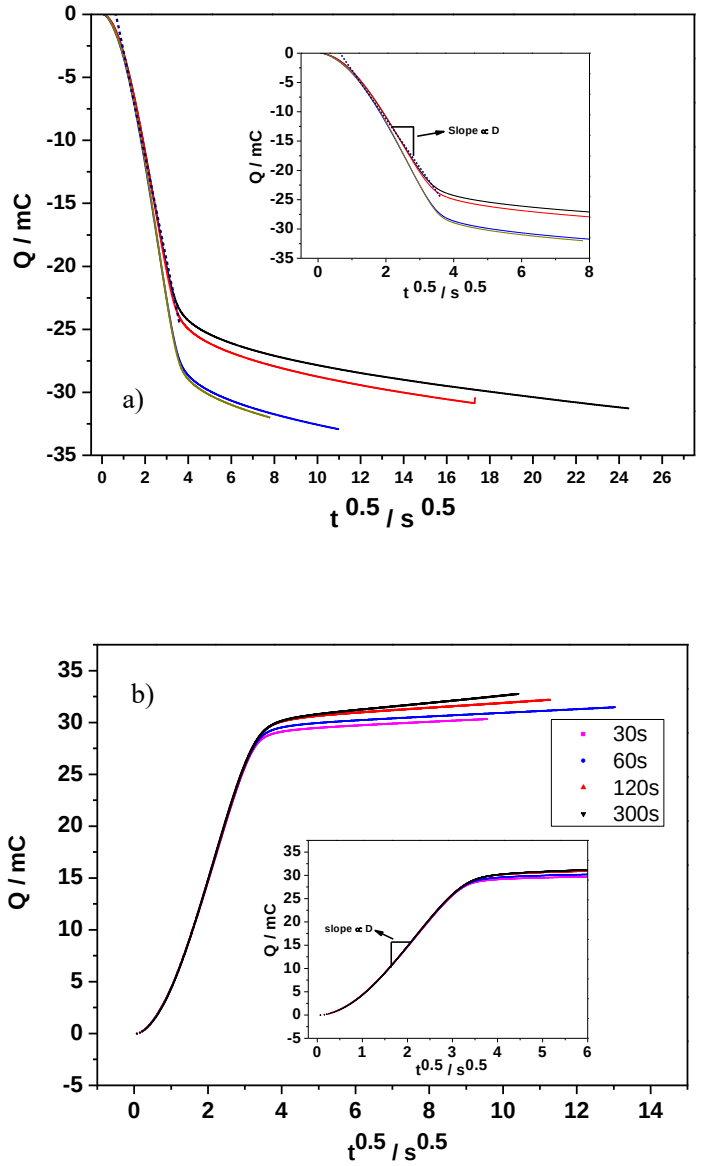

Figure S4. 8: Plot of the charge vs. square roots of the time for the a) insertion process and b) de-insertion process to calculate the diffusion coefficient. Where the signal becomes linear, the linear regression tool allows the diffusion coefficient calculation. Insert: shows one example of the linear fitting for the calculation of diffusion coefficient.

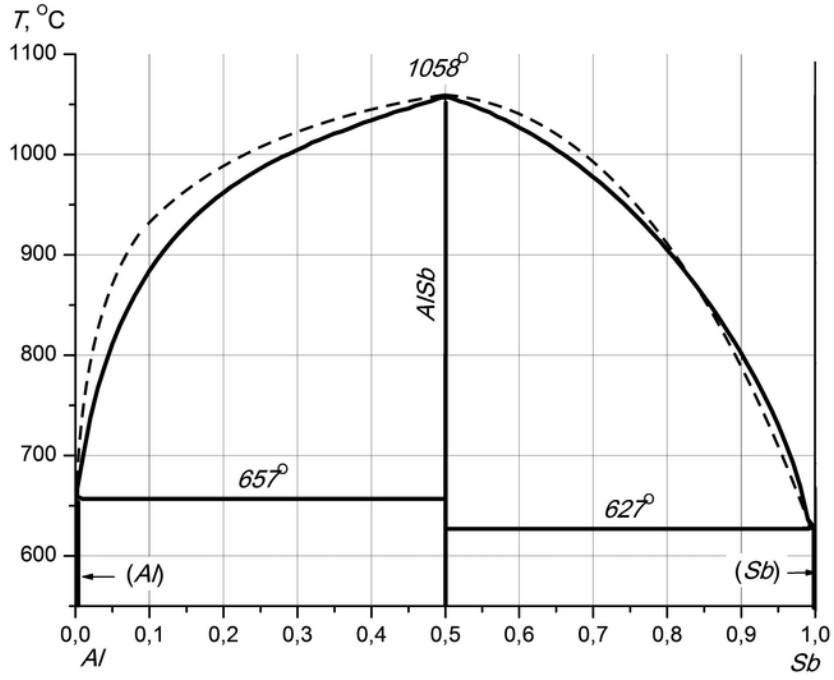

Figure S4. 9: Phase Diagrams of Al-Sb binary systems. There is only one thermodynamic stable phase AlSb for this binary system. [5]

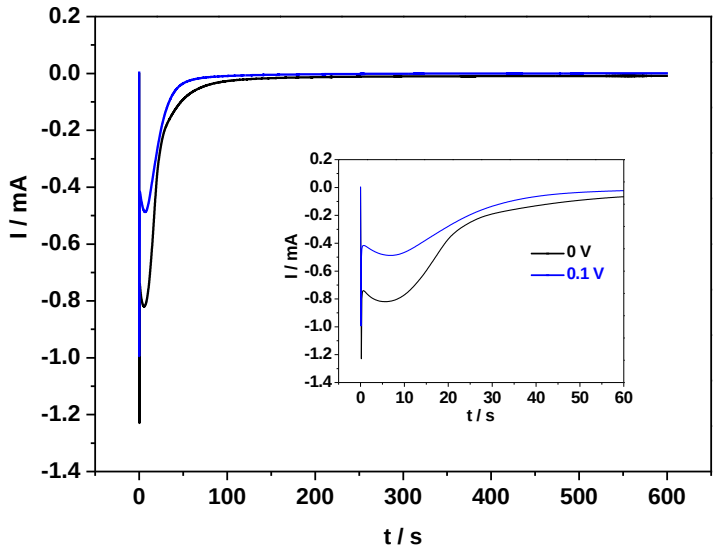

Figure S4. 10: Potential step experiment for Mg insertion from MACC/tetraglyme electrolyte into Sb (~145 nmol cm^{-2}) modified Au electrode at 0 V and 0.1 V respectively. Insert: the first 80 s of insertion. (Surface area was 0.785 cm^2)

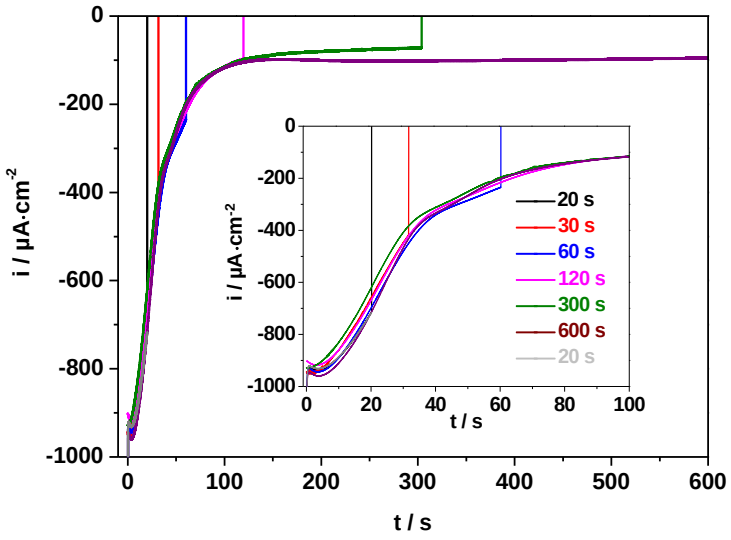

Figure S4. 11: Current transients of potential step experiment for Mg insertion from MACC/tetraglyme electrolyte into Sb modified Au electrode at -0.10 V respectively. Different insertion time from 20-600 s. Insert: the first 100 s of the insertion (Sb: ~218 nmol/cm^2; surface area: 0.785 cm^2)

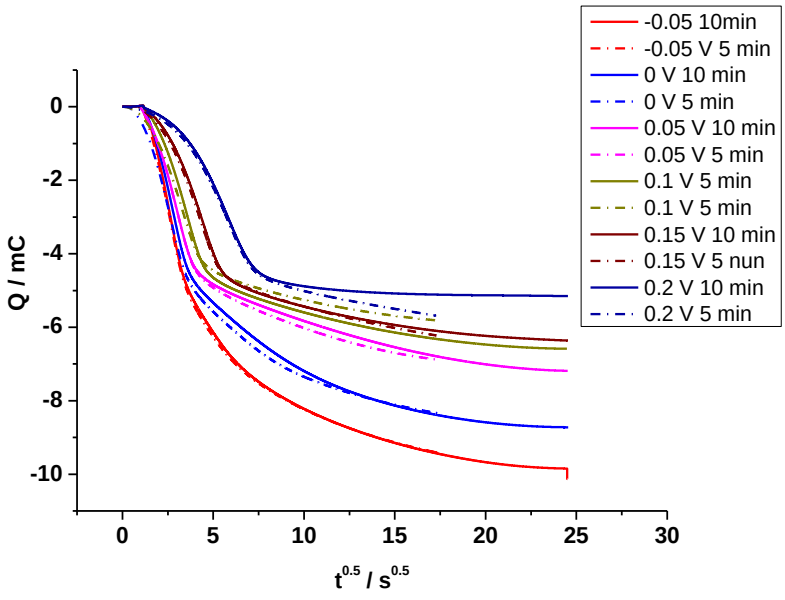

Figure S4. 12: Plot of transient Charge versus t0.5 for mg insertion at different potentials (from -0.05 V to 0.2 V) with the insertion time 10 min (solid line) and 5 min (Dash dot line). The charges are calculated from the CVs in fig.4. (Sb: ~82 nmol/cm^2; surface area: 0.785 cm^2)

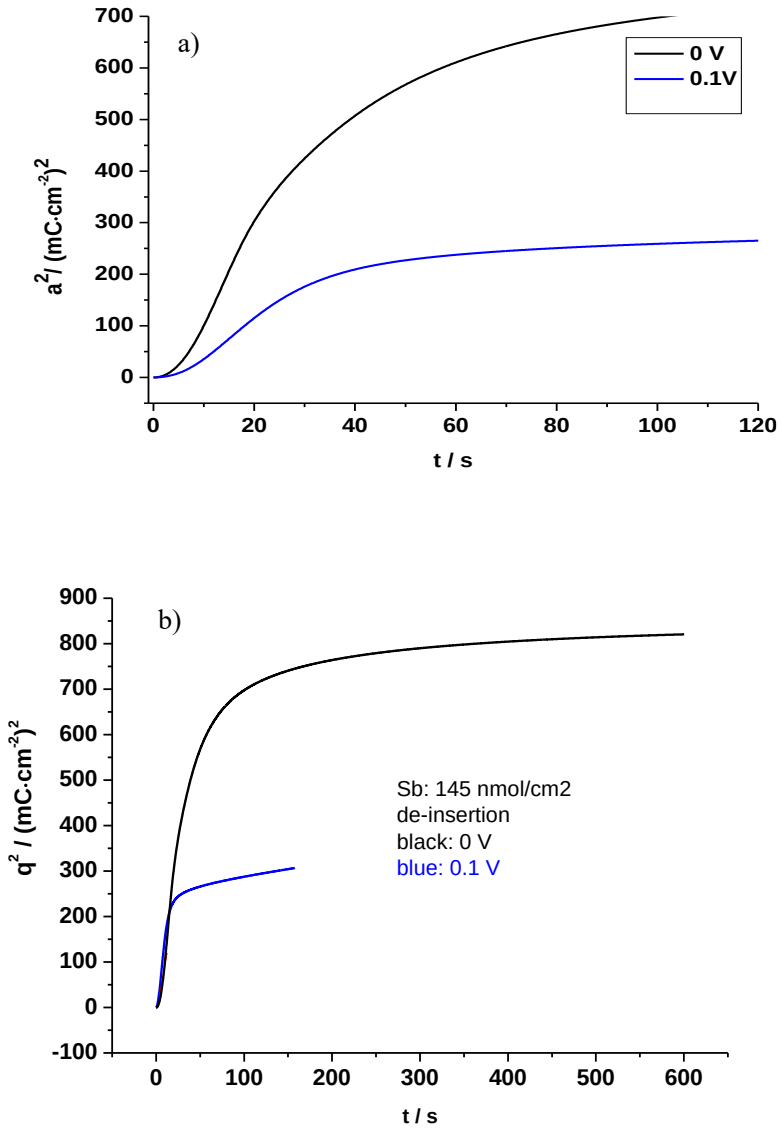

Figure S4. 13: Plot of transient Q^2 vs. t for Mg a) insertion and b) de-insertion at different potentials (0 V and 0.1 V) with the insertion time 10 min into Sb layers. (Sb: ~145 nmol/cm^2; surface area: 0.785 cm^2)

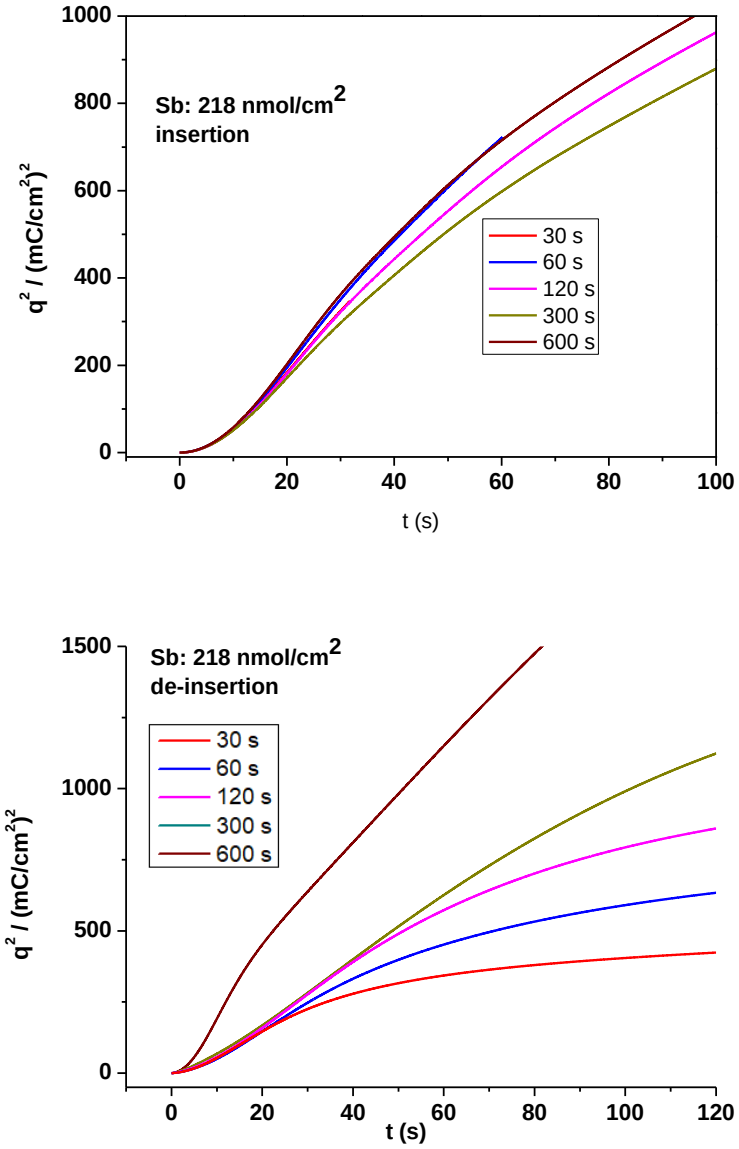

Figure S4. 14: Plot of transient Q^2 vs. t for Mg a) insertion and b) de-insertion at -0.1 V with different insertion time from 30 s to 600 s into Sb layers. (Sb: ~218 nmol/cm^2; surface area: 0.785 cm^2)

Table S4. 2: Dependence of Mg insertion/de-insertion integrated charges during the potential step experiments on time of insertion and the corresponding coulombic efficiencies. (~218 nmol cm^{-2} Sb on Au)

t (s)	cath.Charge /(mC/cm²) (corr. value)	anod. Charge /(mC/cm²)	Eff. (%)	Ratio of Mg:Sb Insertion [de-insertion]	D of Insertion /(10^{-14} cm²/s) [de-insertion]
20	17.6 (15.0)	17.1	97.4	0.36 [0.41]	5.67 [4.26]
30	21.7 (19.5)	21.4	98.9	0.46 [0.51]	5.83 [4.38]
60	32.8 (28.3)	31.5	96.0	0.67 [0.75]	7.58 [3.92]
120	38.6 (30.0)	36.7	94.9	0.71 [0.87]	7.12 [4.17]
300	49.2 (30.8)	43.2	87.8	0.73 [1.03]	6.43 [4.35]
600	80.4 (31.6)	66.9	83.2	0.75 [1.59]	7.75 [17.4]
20	18.7 (17.3)	17.7	92.5	0.41 [0.42]	5.92 [4.55]

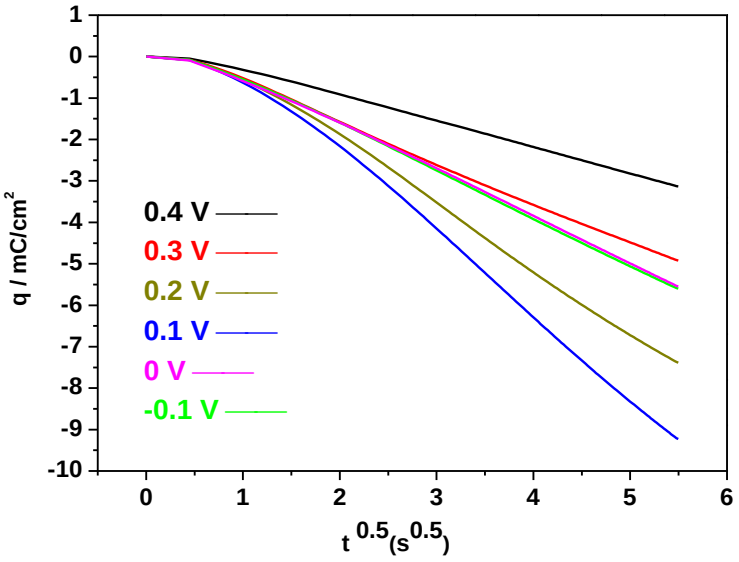

Figure S4. 15 Plot of the charge vs. squawroots of the time for the insertion process to calculate the diffusion coefficient. Where the signal becomes linear, the linear regression tool allows the diffusion coefficient calculation. (Sb: ~105 nm/cm²; surface area: 0.785 cm²)

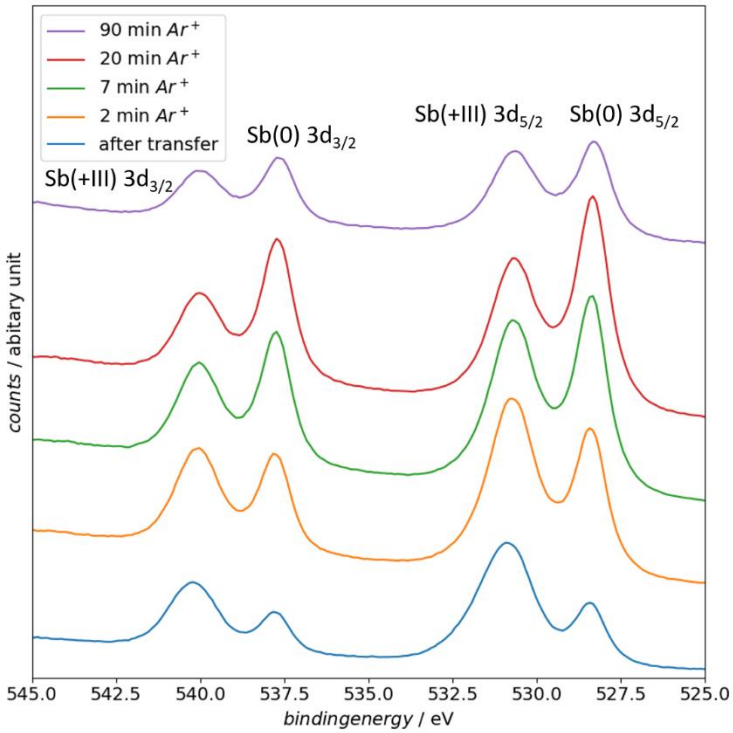

Figure S4. 16: XP spectra of the Sb 3d region for different Ar^+ etching times. Recorded with a pass energy of 15 eV and a step width of 0.1 eV.

Figure S4.16 shows the Sb 3d region for the deposited Sb layer, after transfer for different Ar^+ etch times. A total of 4 peaks can be observed. The doublet at 528.4 eV binding energy and 537.7 eV binding energy can be assigned to the elemental antimony [6]. Each of these peaks shows another one shifted to higher binding energies. Here an assignment of an antimony oxide species can be made. The O 1s peak of the antimony oxide is not directly measurable because it is hidden by the Sb 3d transitions. With the help of the Auger transition of oxygen from the survey spectrum, however, the existence of oxygen on the electrode surface could thereby verified. Furthermore the surface was etched with Ar^+ ions. The etching times are shown in Figure S16. The combination of Ar^+ etching and XPS shows that the proportion of antimony oxide to antimony decreases for longer etching times. However, we could not experimentally observe a pure Sb(0) surface. There are several possible reasons for this: The short contact of the electrochemically deposited antimony with the laboratory air is sufficient to partially oxidize the antimony even in deeper atomic layers. On the other hand, it is also conceivable that the deposited antimony surface has a high roughness, which means that the Ar^+ beam does not hit and remove the entire surface. Different etching rates of the different species of the surface are also conceivable. As a result, the elemental antimony, for example, could be removed more quickly than the antimony oxide, resulting in a distorted depth profile.

Finally, this measurement shows that the deposited antimony film is oxidized by contact with air. This is especially relevant for thin antimony films. This finding is not surprising when the different redox potentials of antimony and oxygen are considered.

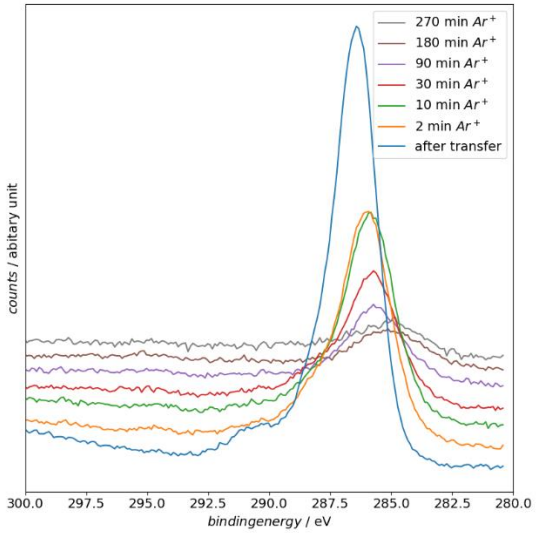

Figure S4. 17: High resolution XP spectrum of the C 1s region for different Ar^+ etching times. Recorded with a pass energy of 50 eV and a step width of 0.1 eV.

Figure S4.17 clearly shows that the detected carbon is a species on the electrode surface: During the Ar+ etching process the signal is hardly detectable. In addition, the broadening of the signal to Figure 15 clearly shows that the detected carbon is a species on the electrode surface: During the Ar+ etching process the signal is hardly detectable. In addition, the broadening of the signal to higher binding energies shows that the carbon present is oxidized in the first spectrum (after the transfer). There is a shoulder particularly noticeable at 290 eV binding energy [6]. This indicates a proportion of carbonates on the surface. In general, the oxidized state of the carbon fits well with the observed binding energy of the O1s core level excitation. It is known that the negative potentials and the reactivity of the inserted Mg can lead to side reactions at the interface electrode/electrolyte. [7] [8] [9] This can lead to the accumulation of decomposition products of the electrolyte on the electrode surface.

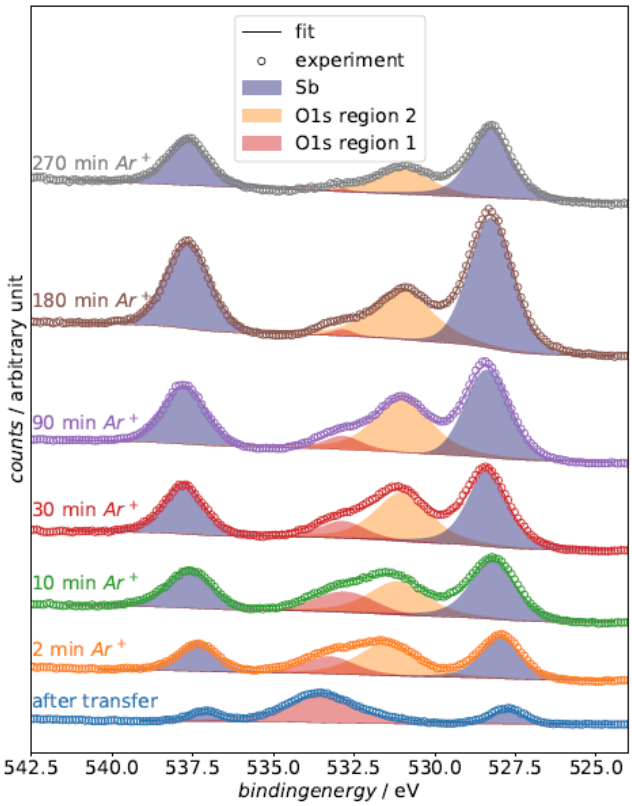

Figure S4. 18: XP spectra showing the deconvoluted Sb 3d O 1s region. The experimental data is shown as circles. The different deconvoluted species are shown as hatched areas and the resulting fit as a line. The different spectra are originated from different Ar+ etch times (see image labeling).

In general, the antimony oxide could be reduced due to the negative potential in the subsequent insertion experiment, or it could be reduced in a chemical pathway through the inserted Mg. A precise mechanism is still unknown here. However, it can be emphasized that the insertion material is elemental antimony and not antimony oxide.

Reference

[1] M. Paliwal, I. H. Jung, *Calphad-Computer Coupling of Phase Diagrams and Thermochemistry* **2009**, *33*, 744.

[2] A. Beutl, D. Cupid, H. Flandorfer, *Journal of Alloys and Compounds* **2015**, *695*, 1052.

[3] M. Stromme Mattsson, *Solid State Ionics* **2000**, *131*, 261.

[4] M. D. Levi, G. Salitra, B. Markovsky, H. Teller, D. Aurbach, U. Heider, L. Heider, *Journal of The Electrochemical Society* **1999**, *146*, 1279.

[5] G. A. Panov, M. A. Zakharov, in *Journal of Physics: Conference Series, Vol. 643*, IOP Publishing, **2015**, p. 012102.

[6] A. K.-V. Alexander V. Naumkin, Stephen W. Gaarenstroom, Cedric J. Powell *X ray Photoelectron Spectroscopy Database 20, Version 4.1:* http://srdata.nist.gov/xps **2012**.

[7] Y. Gofer, R. Turgeman, H. Cohen, D. Aurbach, *Langmuir* **2003**, *19*, 2344.

[8] H. Kuwata, M. Matsui, N. Imanishi, *Journal of The Electrochemical Society* **2017**, *164*, A3229.

[9] T. Seguin, N. Hahn, K. Zavadil, K. Persson, *Frontiers in chemistry* **2019**, *7*, 175.

Chapter 5: Magnesium Deposition and Alloying with Sn on Au Electrode

5.1 Introduction

As another intermetallic anode Mg-Sn-alloy has been investigated. A powdered Sn electrode was used by Singh et al. as an anode for Mg-ion alloying/extraction. [1] They found a high capacity close to the theoretical value (903 mAh/g) and low voltage difference for Mg alloying and extraction (+0.15 vs. 0.20 V), the capacity dropped to 200 mAh/g after 10 cycles at 0.05 C rate. They attributed the low coulombic efficiency to the material pulverization after the severe volume change. The development of a magnesium tin anode, which demonstrates reversible Mg-alloying/de-alloying at 0.2 V vs. Mg, delivering discharge capacity of 270 mAh/g with PhMgCl/THF at room temperature, was reported by Nguyen et al. [2] Another study of an in situ de-alloying of bulk Mg_2Sn for the formation of high-performance Mg-Ion battery anodes was investigated in [3]A reversible capacity of 300 mAh/g was observed over 150 cycles at the rate of C/5. However, the problem with the Mg_2Sn intermetallic anode is the rate capability and reversibility, which is probably due to the slow kinetics of the Mg^{2+} in the structure of Mg_2Sn at room temperature.

Furthermore, the Sn-Sb system has been investigated by Parent et al. for Mg storage. [4] A Sn-Sb alloy has been used as a precursor for in situ formation of Sn nanoparticles. It has been reported that the Mg atoms could replace the Sn atoms of Sn-Sb alloy during the first charge and discharge (conditioning). Inherently, only the small Sn particles (<33±20) exhibit highly reversible magnesiation after conditioning. The size of the Sn-nanostructure plays a big role, only stable Sn morphologies < 40 nm are needed for the reversible Mg alloying/de-alloying and fast kinetic. [4]

The phase diagram and the crystal structure of Mg_2Sn are shown in Figure 5.1. There is only one thermodynamic alloy stable intermetallic compound of the Mg-Sn system with a eutectic point on the Mg-rich side in Mg–Sn alloy (Mg_2Sn 63.1% Mg and 36.9% Sn). The cubic crystal structure with the point group $m\bar{3}m$ and the unit cell contains eight Mg atoms and four Sn atoms. The Mg atoms are located in the tetrahedron of the Sn atoms.

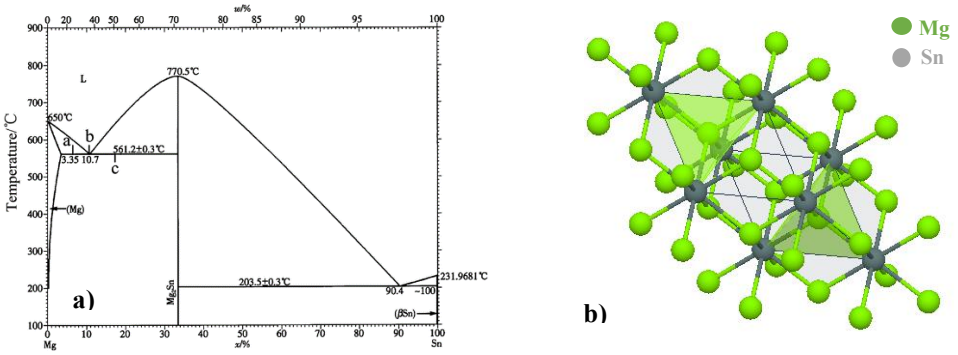

Figure 5. 1: a) Phase diagram of Mg-Sn-system. [3] There is only one single binary phase Mg_2Sn. b) The crystal structure of Mg_2Sn.

We study the alloying of Mg into multilayers of Sn using non-aqueous electrolytes by cyclic voltammetry and eQCM techniques in this work (0.5 M MACC in tetraglyme). The cycling reversibility of alloying/de-alloying of Mg with Sn and a DEMs measurement will be demonstrated. The kinetics of the alloying/de-alloying will be studied by the potential step experiment and the apparent diffusion coefficient of Mg in the Sn solid-state will be estimated.

5.2 Experimental

Chemicals, materials and electrolyte

All aqueous electrolytes were prepared by 18.2 MΩ from Milli-Q water and de-aerated with high purity argon gas for at least 15 min before use. Electrochemical measurements in 0.1 M H_2SO_4 (Spectro pure grade) were conducted in a conventional three-electrode glass-cell. A Au sheet of 1 cm^2 and RHE are used as a counter electrode and a reference electrode respectively. The electrochemical deposition at an Au working electrode was done in 10 mM $SnSO_4$ (99.999%, Aldrich) + 0.5 M H_2SO_4 electrolyte for Sn deposition;

A polycrystalline Au electrode and a Sn modified Au electrode were used as working electrodes for Mg deposition and alloying measurements. Magnesium foil was then used as a counter electrode and another one as a quasi-reference electrode. All the calcium electrochemical deposition measurements were carried out in the MBraun glovebox (H_2O < 0.5 ppm, O_2 < 0.5 ppm).

Preparation of MACC

All chemicals were purchased from Sigma-Aldrich. The Tetraglyme was distilled over sodium and stored over molecular sieves (3 Å) until the water content reaches to an amount less than 5 ppm. The water content has been determined by Coulometric Karl Fischer titration (Mettler

Toledo). $MgCl_2$ was heated overnight under vacuum at 290°C and then stored under thionyl chloride for 1 week. At low pressure the thionyl chlorid was removed completely. All materials were handled in an Argon filled glovebox. The MACC electrolyte was prepared by adding tetraglyme (20.5ml) to $MgCl_2$ (0.966g). While stirring the $AlCl_3$ (1.368g) was then added stepwise. The whole mixture was stirred overnight after addition of an equivalent (H_2O: 63 ppm) amount of MgH_2 to reduce the water content (to below 10 ppm after). For details see Hegemann et al. [5]

Cyclic Voltammogram (CV)

Electrochemical measurements in 0.5 M H_2SO_4 were carried out in a conventional three-electrode glass H-cell consisting of three compartments for fixing the working electrode, reference electrode, and counter electrode. The working electrode is placed in the central compartment and contacted with a solution in a hanging meniscus configuration. The reference electrode is placed in the compartment where it is connected to the central compartment with a Luggin capillary. The counter electrode is placed in the compartment, separated from the central compartment by a glass frit.

All electrochemical measurements were carried out using a potentiostat purchased from Pine Instruments, Inc. (model AFBPC1) in combination with home-made LabVIEW program (National Instruments GmbH, Munich, Germany) for recording the cyclic voltammograms (CVs)

DEMS Experiments

The electrolytes were investigated by mass spectrometry using the classical DEMS cell in the glovbox, in order to determine the decomposition products. The cell was already described before in details by Bondue et al. A porous spotterd Au membrane was used as a working electrode. A Mg wire was used as a counter electrode and a 1.0 M $AgNO_3$ solution in acetonitrile as a quasi-reference electrode. The working electrode compartment was separated from the counter electrode by a frit to avoid the diffusion of the products formed on the counter electrode into the working electrode compartment.

5.3 Results and discussion

5.3.1 Preparation of Sn modified Au electrode and eQCM characterization

The CV and eQCM measurements for the electrochemical deposition of Sn is shown in figure 5.2. With a concentration of 10 mM $SnSO_4$ in H_2SO_4 are two peaks (K_1 and K_2) in the cathodic direction for Sn deposition and three peaks (A_1, A_2, and A_3) in anodic direction for Sn dissolution are observed. The peak at potential -0.15 V vs. RHE describes the underpotential deposition of Sn on the gold electrode. [6] The second cathodic peak at -0.28 V vs. RHE corresponds Sn bulk deposition, which is described by the following equation:

$$Sn^{2+} + 2e^- \leftrightarrow Sn \tag{5.1}$$

A shoulder has also been found next to the A2, which belongs to a side oxidation process of Sn^{2+} to Sn^{4+}, as evidenced by charge involved without associated mass changes. The equilibrium potential of Sn^{2+} / Sn is -0.14 V and of Sn^{2+}/Sn^{4+} is +0.15 V (vs. RHE). [7] The broad peak A_3 in the anodic sweep shows the dissolution of the Sn monolayer. The calculated charge for Sn-deposition is about 52.89 mC and for Sn-dissolution is about 51.76 mC, which indicates a coulombs efficiency of 97.86 %. The m.p.e. value was calculated to be 59.36 g/e·mol for the deposition and 60.36 g/e·mol for the dissolution. (Table 5.1) This value agrees with the theoretic value of 60 g/emol, since the molar mass for Sn is 120 g/mol and the deposition is a reaction by two electrons transfer. So, the oxidation of Sn^{2+} to Sn^{4+} does not play a big role.

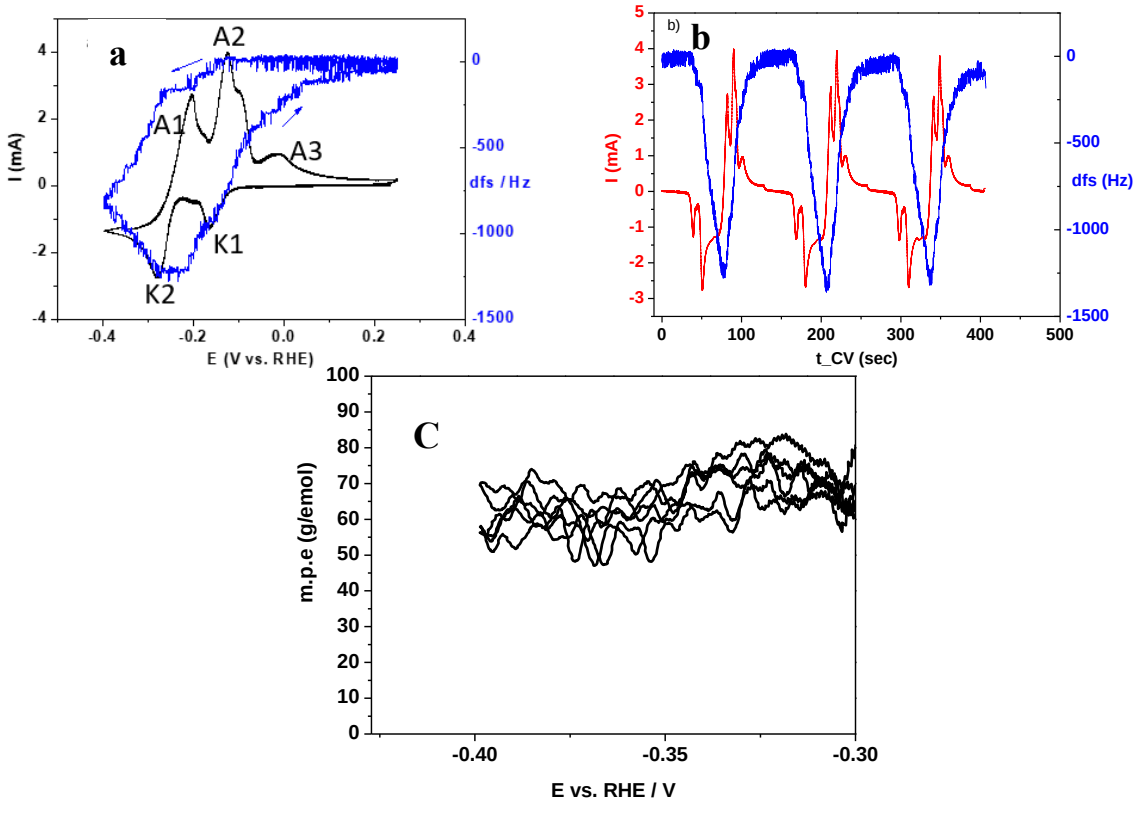

Figure 5. 2: CV and eQCM measurment for Sn-deposition in a 10 mM $SnSO_4$ in 0.5 M H_2SO_4 solution in a three electrode set up. a) CV (black) and differential frequents (blue) versus potential with 10 mV/s for Sn-deposition on an Au quartz electrode; b) Current (red) and differential frequents (blue) versus time; c) m.p.e value versus potential in the range of -0.4 V and -0.3 V, where the Sn bulk deposition occurs.

Table 5. 1: Charge, mass changes, frequency changes and m.p.e value correspond the figure 5.2 for the Sn deposition/dissolution.

	Q (mC)	**Δfs (mHz)**	**Δm (µg)**	**m.p.e (g/emol)**
Kathodic (deposition)	52.89	1.23	32,45	59,20
Anodic (dissolution)	51.76	1.22	32,38	60,36

5.3.2 Mg deposition and alloying on Sn-modified Au-Electrode in MACC/TG

In Figure 5.3 the electrochemical alloying and deposition of Mg into Sn-modified electrode is shown. The measurement started at 1.5 V vs. Mg in cathodic direction. At the potential below -0.5 V vs. Mg the cathodic current increases significantly due to magnesium bulk deposition. In the anodic sweep the current remains first negative between -0.6 V and 0 V because of the continuous bulk deposition of magnesium. Positive of the equilibrium potential the magnesium begins to be dissolved. (First anodic peak in figure 5.3) With a Sn modified electrode a cathodic current in the form of a shoulder for the magnesium alloying was observed at 0.22 V vs. Mg (which means 220 mV more positive than without Sn on the Au surface) The Mg insertion/de-insertion exhibits a reversible cycling behavior and the coulombic efficiency remains stable at 98 % – 99 % during cycling. Although the reversibility is not 100 %, the high cycling stability and the stable coulombic efficiency indicate that Sn is a good anode material for Mg batteries.

From the thermodynamic data of the Mg_2Sn compound the theoretic potential for the formation of Mg_2Sn is calculated to be 0.19 V vs. Mg/Mg^{2+} according to the following reaction equation:

$$Sn + 2Mg + 4e^- \longrightarrow Mg_2Sn \qquad (5.2)$$

The cathodic peaks shift to a more positive potential, the anodic peaks shift to more negative potential in the first few cycles and all peaks became stable at the end as shown in Figure 5.3, which means the reversibility of Mg alloying/de-alloying increased. The positive shifts of the potential which is needed for the magnesium alloying suggest that the magnesium is inserted into the host lattice of Sn. The peak at 0.85 V vs. Mg in the anodic direction describes the de-alloying magnesium. The coulombic efficiency of magnesium alloying/de-alloying is about

95 %. (The charge was integrated from the plot of i vs. t: between 0.22 V and -0.45 V for the alloying in the cathodic sweep and between 0.60 V and 1.4 V for the de-alloying in the anodic sweep) The ratio between the inserted magnesium and the deposited Sn is 0.5, which significantly less than the theoretic value of 2, which indicates 10 mV/s is a relative high sweep and not long enough for the saturation of Mg alloying. During the sweep the time for Mg de-alloying is limited, the alloyed magnesium atom could not be completely de-inserted. Otherwise, the electrolyte is decomposed at the same time as the magnesium insertion, which consuming the charge for calculation of the coulombic efficiency.

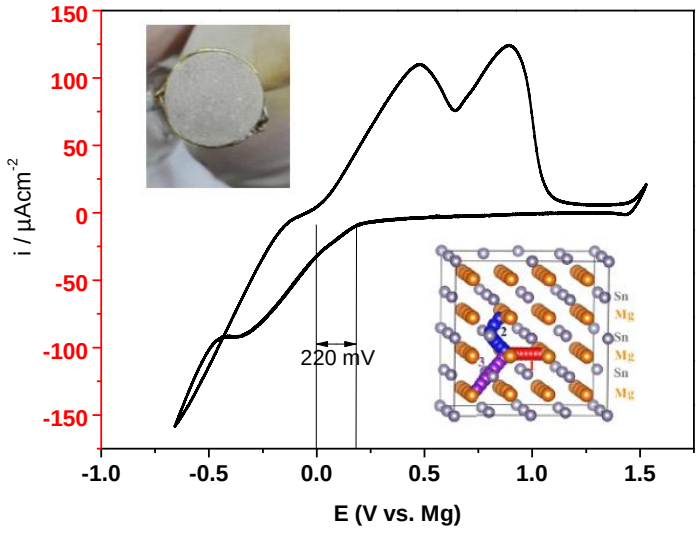

Figure 5. 3: CV for electrochemical magnesium deposition and alloying in a 0.5 M MACC/TG electrolytes in a three electrode cell with 10 mV/s. AE: Au; CE and RE: Mg. Insert: image of the Sn modified Au electrode and the structure of the binary phase Mg_2Sn.

In Figure 5.4 MSCVs for DEMS measurement of magnesium deposition and alloying into Sn modified porous Au-electrode in 0.5 M MACC/TG are shown. The experiments for magnesium alloying were investigated by various sweep rate (5 and 10 mV/s in Figure 5.4a and 1, 2, 5, and 10 mV/s in Figure 5.4b) The magnesium alloying with Sn started at 0.15 V vs. Mg with a continuous increase of the current for 5 and 10 mV/s. We propose that the alloy compound of Mg_2Sn is formed. On the pure Au electrode no shoulder for the Mg alloying is observed. (Blue curve in Fig 5.4a) In the MSCVs all the signals with m/z = 25, 26, 27 and 28 have the same shape the ionic current increases at 0.7 V vs. Mg in cathodic direction, stay at a plateau at the beginning of anodic sweep and decrease at 0.6 V vs. Mg at the end. It indicates that the ethylene was formed during the whole magnesium alloying process, which is different with the alloying on the Sb modified electrode. The ionic current increases at 0.75 V, where there is no faraday current, we assume that it might be due to a small amount of water. It might be also due to that

the magnesiation of tin underlined a multiphase mechanism involving the coexistence of c-Mg_2Sn, distorted $Mg_{2-\delta}Sn$, and Mg-doped-Sn. [8] Nguyen et al. have found also the decomposition at a very low voltage in THF based- electrolyte for magnesium alloying with Sn as a result of the XPS analysis revealed the interfacial relationship between Sn and PhMgCl. [2]

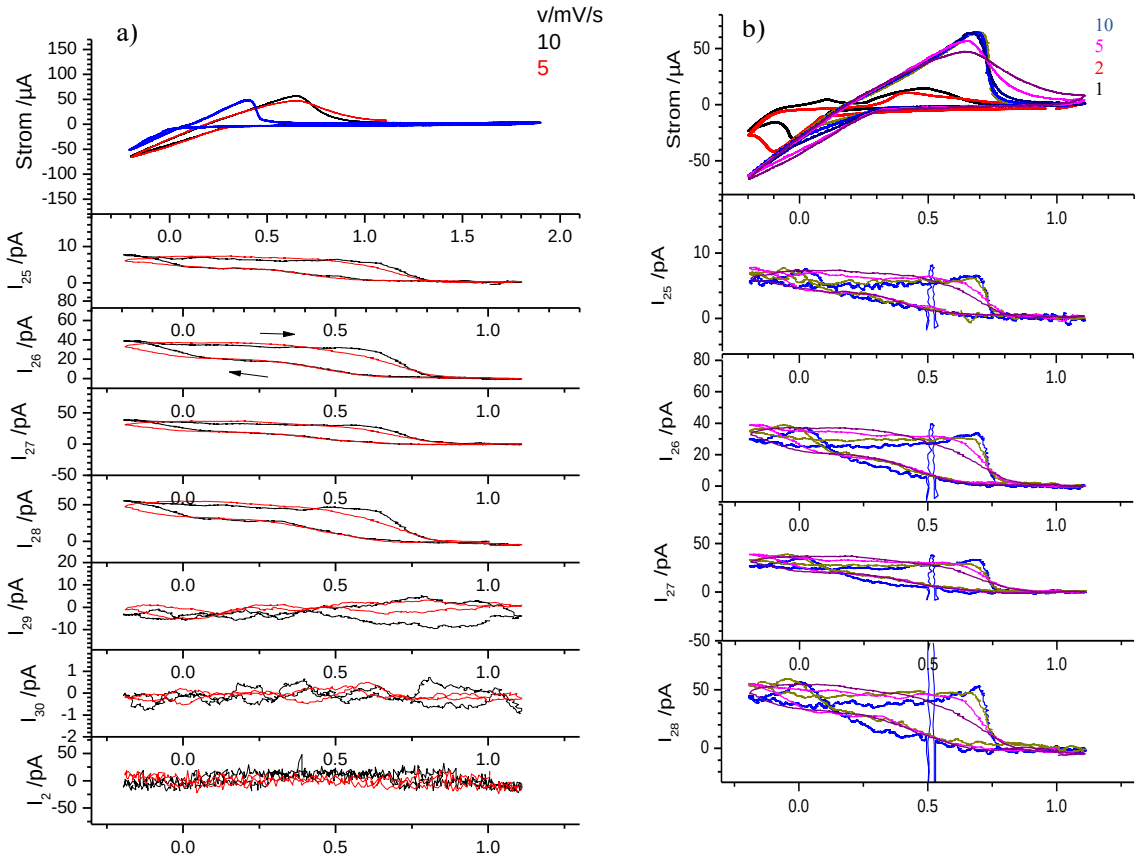

Figure 5. 4: a) MSCVs for DEMs measurement of magnesium deposition and alloying into Sn modified Au-electrode in 0.5 M MACC/TG. Blue: Magnesium deposition on pure porous Au-electrode with potentials from -0.2 V to 1.9 V. b) Magnesium alloying between -0.2 V and 1.1 V vs. Mg; RE and CE: Mg

Table 5.2 shows the comparison of the relative ratio for ethylene formation with NIST database. The relative ratio from DEMS measurement (the intensity is from rose curve with 1 mV/s in fig. 5.4b) and from the NIST database is good in agreement. It indicate that the ethylene is the main decomposition product also during the Mg alloying with Sn, which is not observed in the case of Mg alloying with Sb and Bi.

Table 5. 2: Comparison of Intensity for ethylene (rose curve) from DEMS measurement with NIST database.

m/z	25	26	27	28	29
C_2H_4 Intensity	7.63	36.27	38.09	60.75	0.9
Krel %	12.6	59.7	62.7	100	1.5
Irel C_2H_4 from NIST	12.0	62.9	32.4	100	2.4

In addition, the ethylene formation was also observed during the Mg dissolution on the pure Au electrode without Sn. There, in the MSCVs the signals for m/z = 25, 26, 27, 28 and 29 were recorded. It is assumed that the ethylene formation should be formed as a decomposition product on the surface of Au electrode. After a few amount of the magnesium dissolute into the solution the active place on the Au electrode is available for ethylene formation. [5]

5.3.3 Determination of diffusion coefficient of Mg into Sn adlayers

a) CV

The electrochemistry of alloy type electrodes of magnesium in a thin layer is complicated by slow ion migration, charge transfer, and solid-state diffusion. At relatively high scan rates the classical Randles-Sevchik equation is valid for semi-infinite diffusion [9-11]:

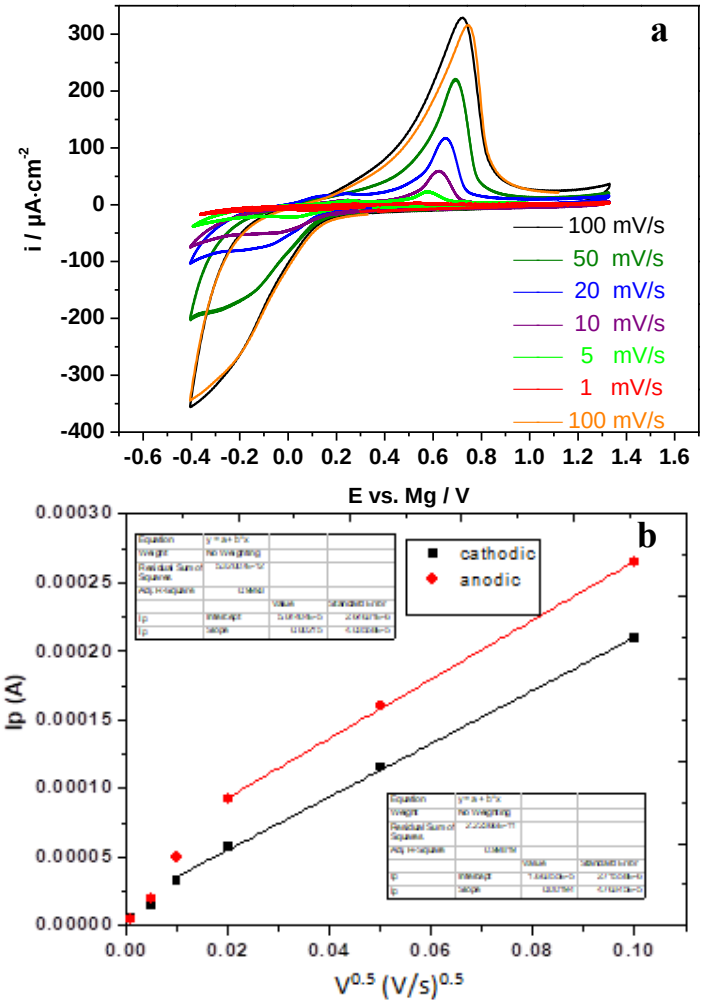

Figure 5. 5: a) Cyclic voltammograms of Mg alloying with Sn modified Au electrode in 0.5 M MACC/tetraglyme at different sweep rates from 1 to 100 mV s-1. b): Plot of ip (peak current) vs.υ1/2 (square root of scan rate). AE: Sn on Au; CE and RE: Mg. (~40 nmol cm-2 Sn on Au and Surface area was 0.785 cm2)

In this present case (semi-infinite diffusion in the solid-state), the concentration of Mg ions at the interface between the electrode and electrolyte is strongly potential dependent and the semi-infinite diffusion is only valid for relatively high sweep rates. We assume that the concentration of Mg at the surface will reach the maximal concentration (C_0) if the potential has been set to the most negative potential for Mg alloying quite before the Mg bulk deposition.

A half-cell was assembled to investigate the electrochemical performance of the magnesium alloying/de-alloying with a Sn anode and an Mg-metal counter electrode by variation of the sweep rates. The Sn adlayers (7.72 mC/cm^2) were freshly deposited which according to 40 nmol/cm^2. The Cyclic voltammograms were obtained by scan rates from 1 to 100 mV/s between -0.3 V to 1.4 V vs. Mg at room temperature. (See Figure 7.5) The peaks current increased with the increase of the sweep rates. Also, the difference between the corresponding anodic and cathodic peaks increase and the anodic peaks shift to a more positive potential with sweep rate. The anodic peak is higher and narrower than the corresponding cathodic peak. The height of peaks current is approximately proportional to $v^{0.5}$ at a relatedly high scan rate for both insertion and de-insertion. The diffusions coefficient was calculated to be 1.2×10^{-13} cm^2/s for alloying with $\alpha n_\alpha = 0.5$. (Here, the theoretical value for the concentration of Mg in Mg_2Sn is 0.012 mol/cm^3 was used) We assumed here the concentration of Mg in the Sn adlayers at the surface during the alloying/de-alloying processes is constant.

Table 5. 3: The charges for alloying/de-alloying of Sn, coulombic efficiency and the ratio between alloyed Mg and deposited Sn at different potential sweep rates.

υ (mV/s)	**Charge density (mC/cm^2) (cath.)**	**Charge density (mC/cm^2) (anod.)**	**Col. Eff. (%)**	**Ratio of Mg:Sn of insertion and (de-insertion)**
100	1.62	1.61	99.2	0.31 (0.31)
50	1.85	1.81	98.1	0.36 (0.35)
20	2.22	2.19	98.6	0.43 (0.42)
10	2.49	2.46	98.7	0.48 (0.47)
5	3.40	3.34	98.3	0.66 (0.65)
1	7.16	7.05	98.5	1.39 (1.37)
100	1.62	1.60	98.6	0.31 (0.31)

The charges for alloying/de-alloying of Sn, coulombic efficiency, and the ratio between alloyed Mg and deposited Sn at different potential sweep rates are shown in table 5.3. The charge densities of allying/de-alloying increased with the decrease of the scan rates as expected. (A control experiment at 100 mV/s recorded at the end of the experiment the CV measurements gave an identical result as for the beginning.). Thus, there is no deactivation of the electrode surface and no noticeable change in the Sb layer in the course of these cyclic voltammograms.

The ratio between the faradaic charge of anodic (de-alloying) and cathodic (alloying) gives the apparent coulombic efficiency. The coulombic efficiency remains stable at 98 % to 99 % which shows the same results to the CV in Fig. 5.4. So, the rest 1 % - 2 % was probably consumed by some side reactions such as hydrogen evolution. The ratio between the alloyed Mg and the deposited Sn gives the values from 0.31 at 100 mV/s to 1.39 at 1 mV/s. The highest value with 1.39 of Mg-Sn shows that the time is not sufficient for saturation obviously diffusion is too slow. (The scan rate of 1 mV/s is still too high)

b) Potential step

In potential step experiments, two different Sn layer thicknesses were investigated. Before each step experiments, a CV for Mg-allying/de-allying including Mg bulk deposition and dissolution was recorded. The potential was first held at 1.2 V vs. Mg (where de-insertion of Mg takes place) in the MACC electrolyte. Afterwards, the potential was stepped to a negative potential (0 V vs. Mg), at which magnesium could be inserted into the antimony layer, for different periods (10 s – 600 s), then the potential was stepped back to 1.2 V for each step with the same period of alloying where the extraction of magnesium takes place, The faradaic current does not drop down to 0 after a time depending on the insertion period. We attribute this current to some side reactions such as aluminium deposition. In figures Fig. 5.6. Fig. 5.7 the transients during alloying and de-alloying for the various alloying and de-alloying times (10s to 600 s) are shown.

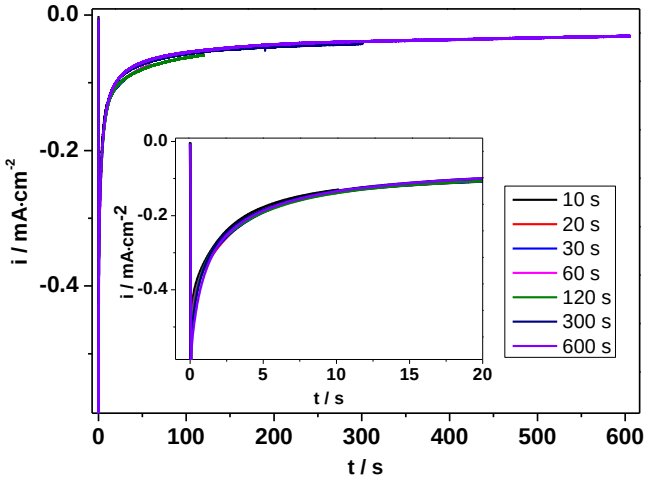

Figure 5. 6: the potential steps experiment for Mg alloying with Sn electrode out of a 0.5 M MACC/TG electrolyte at 0 V vs. Mg from 10 s to 600 s respectively. Inset: the first 20 s of the alloying. AE: Sn on Au; CE and RE: Mg. (~ 40 nmol cm^{-2} Sn on Au and Surface area was 0.785 cm^2)

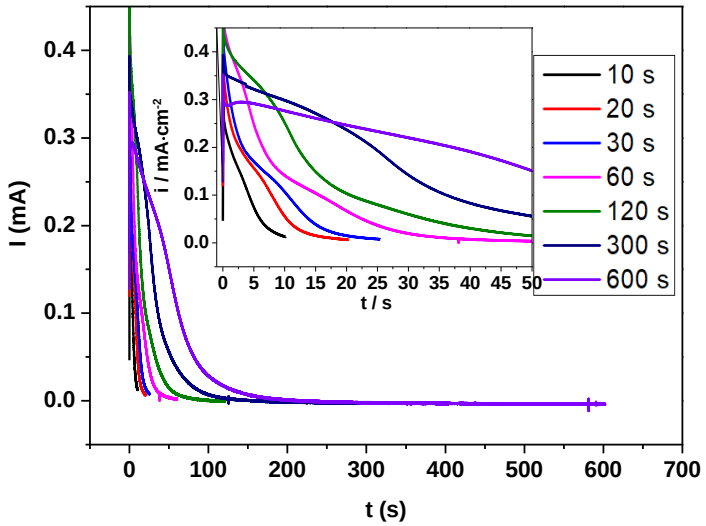

Figure 5. 7: the potential steps experiment for Mg alloying with Sn electrode out of a 0.5 M MACC/TG electrolyte at 0 V vs. Mg from 10 s to 600 s respectively. Inset: the first 50 s of the alloying. AE: Sn on Au; CE and RE: Mg. (~ 40 nmol cm^{-2} Sn on Au and Surface area was 0.785 cm^2)

It could be seen that the current for the alloying process drops directly after the double layer charging for all the periods. According to the de-alloying process the current drop directly after the double layer discharge until 30 s of the alloying. With more amount of the alloyed Mg (longer time of the alloying) there is a new shoulder appears after the double layer discharge. (From 60 s to 600 s of the alloying) For the longest time of the alloying with 600 s the current stays nearly constant at the beginning of the de-alloying and decreases slightly afterwards, indicating an initial kinetic rate limitation. The new appears shoulder may be due to the contribution of a nucleation and growth process. Then the current drop fast could be described by the Cottrell Equation and indicate a diffusion limitation.

The charge density for alloying and de-alloying of magnesium are summarized in table 5.4 together with coulombic efficiency and the ratio between the deposited Sn and the alloyed Mg. For the calculation of the charge density, the current at $t = 600\ s$ is subtracted for all step of alloying because the current does not drop to 0 after 600 s but stays nearly constant. We attribute this steady state current to the side reaction. For the de-alloying process, the current drops to 0 after 20 s for each step. As expected, the amount of alloyed Mg increases with the increase of the alloying period. The Ratio of Mg: Sn was calculated from the corrected charge of the alloying and from the charge of de-alloying which is shown in brackets. The ratio with the de-alloying period of 600 s was estimated to be 2.25, which means the Mg in the Sn adlayers is saturated only after 10 min and also indicates that a binary phase of Mg_2Sn (Mg: Sn = 2:1) was

formed during the alloying process.

Table 5. 4: Dependence of Mg alloying/de-alloying integrated charges (The steady states current at t (10 min) was subtracted for alloying) during the potential step experiments, the corresponding coulombic efficiencies, the ratio between Sn and Mg and the diffusion coefficients. (~40 nmol cm^{-2} Sn on Au and Surface area was 0.785 cm^2)

Alloying and de-alloying time	**Charge (mC/cm^2) (cath.)**	**Charge (mC/cm^2) (cath.) (corr.)**	**Charge (mC/cm^2) (anod.)**	**Ratio Mg:Sn alloying (de-alloying)**	**D ($/10^{-13} cm^2/s$) alloying (de-alloying)**	**$C\sqrt{D}$($/10^{-9}$) Alloying (de-alloying)**
10	2.07	1.38	1.56	0.18 (0.20)	0.16 (0.07)	1.52 (1.00)
20	3.38	2.76	2.83	0.36 (0.37)	0.21 (0.34)	1.74 (2.21)
30	4.38	3.46	3.98	0.45 (0.52)	0.31 (0.49)	2.11 (2.66)
60	6.82	4.98	5.61	0.65 (0.73)	0.39 (1.40)	2.37 (4.52)
120	10.85	7.18	7.27	0.93 (0.94)	0.51 (3.24)	2.71 (6.83)
300	18.52	9.34	11.48	1.21 (1.47)	0.60 (2.63)	2.94 (6.15)
600	28.48	9.97	17.38	1.29 (2.25)	0.85 (5.06)	3.50 (8.54)

A similar potential step experiment was performed for variation of the deposition potential from -0.05 V to 0.2 V instead of deposition time with the same amount of deposited Sn-adlayer (~ 40 nmol cm^{-2}) and a similar result was obtained. The transients with 5 min alloying and de-alloying are shown in Figure 5.8 and Figure 5.9. This experiment was started at 0 V for alloying and then the potential was stepped back to 1.2 V for de-alloying for ca. 300s. Afterwards the potential for alloying was changed to a more positive potential with an increment of 0.05 V. This process was repeated until the potential for alloying reach 0.2 V. Then, a control experiment at 0 V was demonstrated followed by the potential for alloying at -0.05 V at the end.

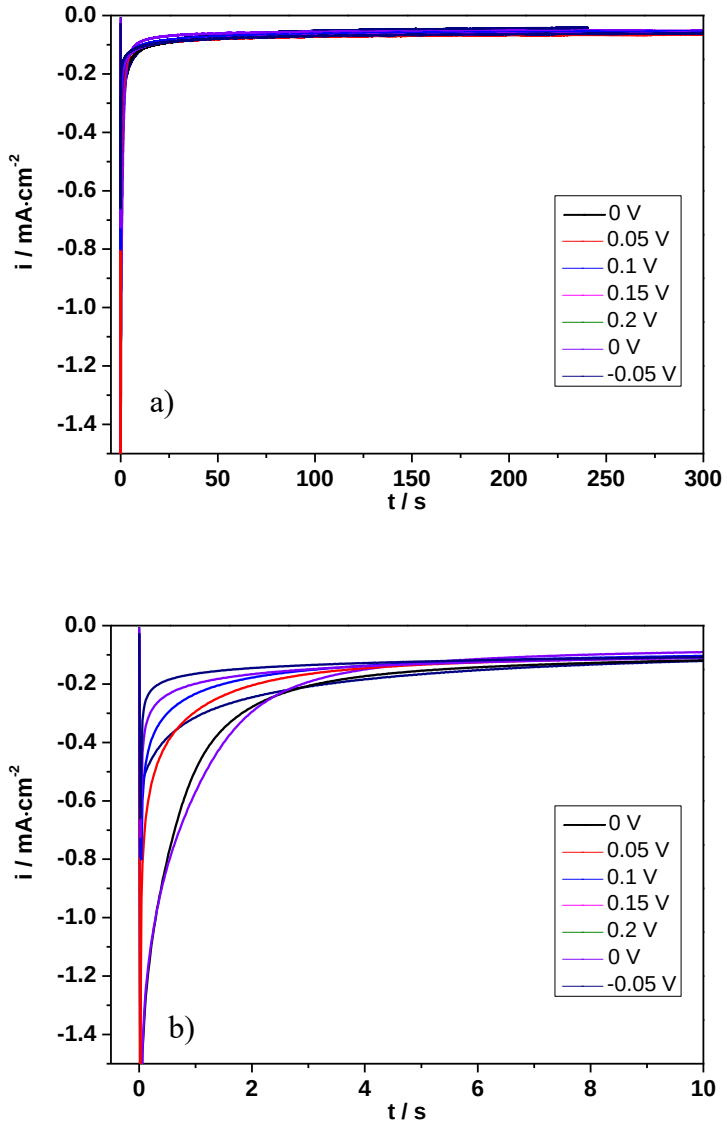

Figure 5. 8: a) the potential steps experiment for Mg alloying with Sn electrode out of a 0.5 M MACC/TG electrolyte with a period of 300 s from -0.05 V to 0.2 V vs. Mg respectively. b): the first 10 s of the alloying. AE: Sn on Au; CE and RE: Mg. (~ 40 nmol cm^{-2} Sn on Au and Surface area was 0.785 cm^2)

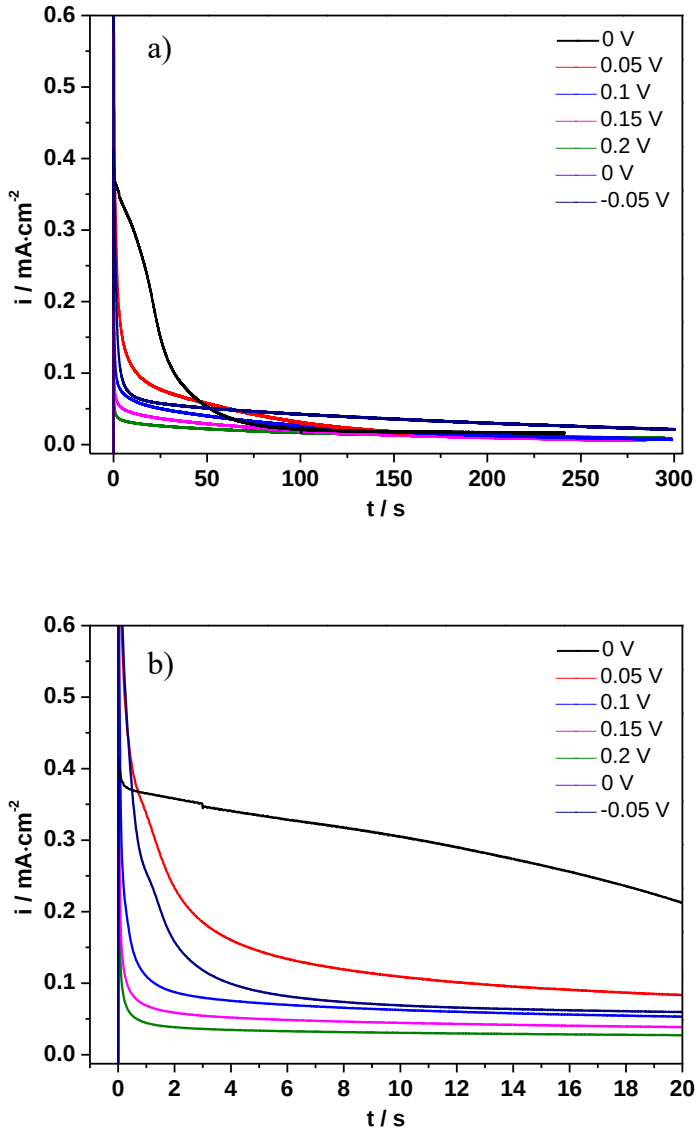

Figure 5. 9: a) the potential steps experiment for Mg de-alloying with Sn electrode out of a 0.5 M MACC/TG electrolyte at 1.2 V according to the alloying potentials from -0.05 V to 0.2 V respectively. b): the first 20 s of the de-alloying. AE: Sn on Au; CE and RE: Mg. (~ 40 nmol cm^{-2} Sn on Au and Surface area was 0.785 cm^2)

It can be seen that the current transients for alloying at 0 V and the corresponding de-allying show similar results to the transients in fig. 5.6 and 5.7. (Green curve in fig. 5.8 and 5.9) However, the current transients of the control experiment and the experiment at -0.05 V at the end are quite different because of the insufficient de-alloying of Mg. (The time for de-alloying was not enough long.)

Table 5. 5: Dependence of Mg alloying/de-alloying integrated charges at different potential, the corresponding coulombic efficiencies, the ratio between Sn and Mg, the diffusion coefficient of Mg alloying and de-alloying with Sn (Here, the saturated concentration was used) and the value of $C\sqrt{D}$ during the potential step experiments. (~40 nmol cm^{-2} Sb on Au and Surface area was 0.785 cm^2)

Potential (V vs. Mg)	**Charge (mC/cm^2) (cath.)**	**Charge (mC/cm^2) (cath.) (corr.)**	**Charge (mC/cm^2) (anod.)**	**Ratio of Mg:Sn alloying and (de-alloying)**	**D ($/10^{-13} cm^2/s$) alloying (de-alloying)**	**$C\sqrt{D}$ ($/10^{-9}$) alloying (de-alloying)**
0.00	19.16 300 s	11.28 300 s	13.17 240 s	1.46 (1.71)	1.02 (7.78)	3.83 (10.58)
0.05	15.12 300 s	8.87 300 s	9.33 158 s	1.15 (1.20)	0.77 (6.52)	3.33 (9.69)
0.10	12.60 300 s	5.61 300 s	7.27 300 s	0.70 (0.94)	0.58 (5.41)	2.89 (8.83)
0.15	10.87 300 s	3.76 300 s	5.16 285 s	0.49 (0.67)	0.35 (3.25)	2.24 (6.84)
0.20	9.65 300 s	3.20 300 s	4.68 295 s	0.41 (0.61)	0.14 (1.05)	1.42 (3.89)
-0.05	15.35 230 s	9.69 230 s	12.09 250 s	1.26 (1.56)	0.85 (5.45)	3.50 (8.85)
0.00 (control)	14.82 300 s	8.00 300 s	8.58 300 s	1.04 (1.11)	1.13 (3.31)	4.03 (6.90)

This difference could be also seen if we compare the charge density of alloying and de-alloying. The charge density for alloying and de-alloying of magnesium, and the ratio between the alloyed Mg and the deposited Sn are summarized in table 5.5. The corrected value for charge of alloying and the ratio of Mg: Sn for de-alloying are shown in brackets. The charge density for the alloying -0.05 V (9.69 mC/cm^2) and the control experiment at 0 V (8.00 mC/cm^2) is lower than the value of 0.00 V at the beginning (11.28 mC/cm^2), different from expectations. (Table 5.4) A similar change during the de-insertion is also observed. The charge density of the de-alloying at 0.05 V is much lower than the value of the corresponding alloying.

However, the charge density of alloying at 0 V (11.28 mC/cm^2) and the corresponding de-alloying (13.17 mC/cm^2), and the ratio of Mg: Sn (1.46 for alloying and 1.71 for de-alloying) show similar values as the experiment with a variation of the alloying period (300 s). (See table 5.3 and 5.4) This indicated that also the high reversibility of Mg alloying with the Sn anode and the formation of Mg_2Sn during the alloying process.

D can then be calculated from the slope as shown in Fig.5.10 and 5.12 for alloying as well as

in Fig. 5.11 and 5.13 for de-alloying where we plotted Q^2 vs t for a better comparison of the time range of the linear range with the original transients in fig.5.6 and 5.8 for alloying as well as in fig. 5.7 and 5.9 for de-alloying. The value of $C\sqrt{D}$ for both potential step experiments is also shown in table 5.3 and table 5.4, where the values calculated from the de-alloying are shown in brackets.

If we assume that the surface concentration of the Mg in the Sn adlayer at 0 V vs. Mg is equal to the maximal concentration of 0.012 nmol/cm^3 of Mg in Mg_2Sn, then the diffusion coefficient was estimated to be 0.85×10^{-13} cm^2/s for alloying and 5.06×10^{-13} cm^2/s or de-alloying corresponding to the original current transient in fig 5.6 and 5.7.(varying the time of alloying 10 s- 600 s) Also, the similar values of 1.02×10^{-13} cm^2/s and 7.78×10^{-13} cm^2/s were calculated corresponding to the original current transient in fig 5.8 and 5.9. (Varying the potentials of alloying) The estimated diffusion coefficient of Mg alloying and de-alloying with Sn at different potentials (Here, the saturated concentration was used) and the value of $C\sqrt{D}$ are also summarized in Table 5.5. So, the diffusion coefficient estimated from CV and from potential step experiment are good in agreement. These values are one order higher than the diffusion of Mg into the Sb and similar to Mg alloying with Bi, which also suggests the Sn and Bi anode are better than the Sb as alternatives for the Mg batteries.

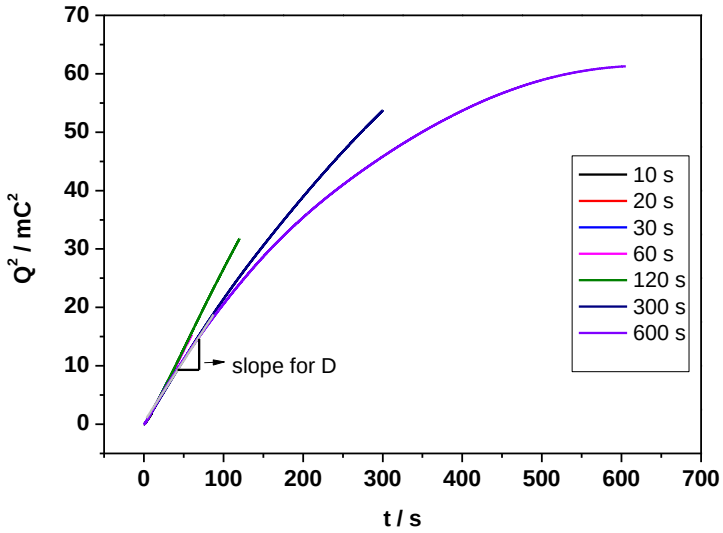

Figure 5. 10: Plot of transient Q^2 vs. t for Mg alloying at 0 V with the variation of the period from 10 s to 600 s into Sn layers. (Sn: ~40 nm/cm^2; surface area: 0.785 cm^2)

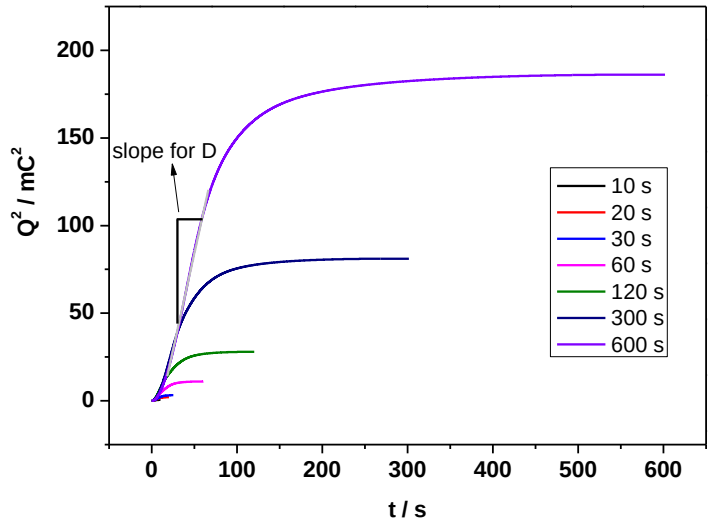

Figure 5. 11: Plot of transient Q^2 vs. t for Mg de-alloying into Sn layers at 1.2 V with the variation of the period for alloying at 0 V from 10 s to 600 s respectively. (Sn: ~40 nm/cm^2; surface area: 0.785 cm^2)

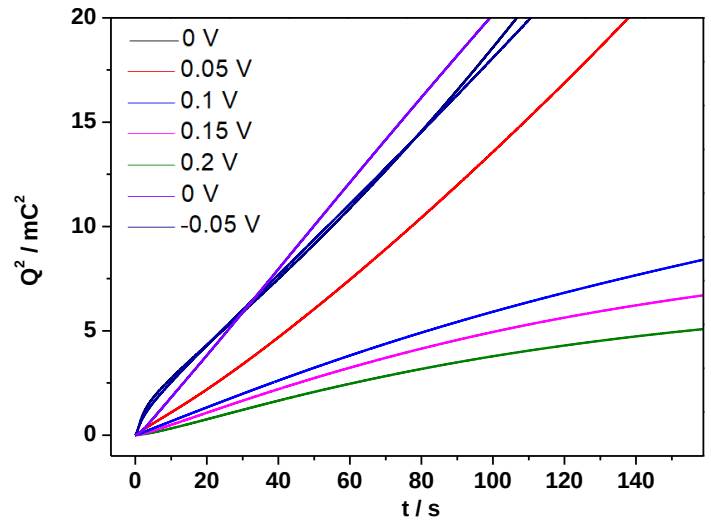

Figure 5. 12: Plot of transient Q^2 vs. t for Mg alloying at different potentials (from -0.05 V to 0.2 V) with the alloying time 5 min into Sn layers. (data from fig. 5.8) (Sn: ~40 nm/cm^2; surface area: 0.785 cm^2)

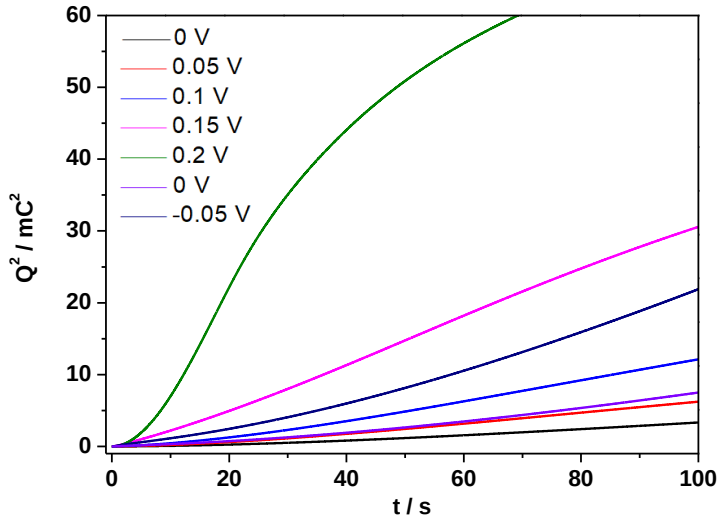

Figure 5. 13: Plot of transient Q^2 vs. t for Mg de-alloying with a Sn anode at 1.2 V corresponding to the different alloying potentials respectively (from -0.05 V to 0.2 V). (data from fig. 5.9) (Sn: ~40 nm/cm^2; surface area: 0.785 cm^2)

5.4 Conclusions

The electrochemical deposition of tin on Au was investigated in 0.5 M H_2SO_4 containing 10 mM $SnSO_4$ by cyclic voltammetry. The investigation by EQCM gives an m.p.e value around 60, which agrees with the theoretical value. Magnesium deposition and alloying on Au and Sn modified Au electrodes were investigated in 0.5 M $MgCl_2$ + 0.5 M $AlCl_3$ in tetraglyme electrolyte. Interestingly, at the Sn modified Au electrode, a cathodic peak starts at around 220 mV (vs. Mg/Mg^{2+}), which is 220 mV more positive than the onset potential of bulk deposition at the Au electrode. It is suggested that this pre-cathodic peak is related to the alloying of Mg into Sn adlayers to form Mg_2Sn alloy by the ratio of the amount of the alloyed Mg to that of the deposited Sn calculated from the corresponding peak charge close to the theoretical value of 2:1 for Mg_2Sn formation. A DEMS study has been demonstrated for the investigation of the electrolyte stability. During the alloying process of Mg with Sn no ethylene formation was observed in comparison with the Mg bulk deposition. High reversibility of Mg alloying/de-alloying has been observed in cyclic voltammetry and potential step experiments. The MACC is a complex system that during the alloying of Mg, the Al and Cl could also diffuse into the Sn-adlayers.

The kinetics of the Mg alloying/de-alloying was studied by the potential step experiment. From the current transient, a diffusion-controlled process of alloying is suggested, which the Cottrell Equation is valid. Furthermore, the diffusion coefficient of Mg into Sn multilayers was

estimated from CV to be 1.20×10^{-13} cm^2/s for alloying, and potential step experiments to be $1.02\times10^{-13} \sim 7.78\times10^{-13}$ cm^2s^{-1} respectively, which is one order of magnitude higher than the value for Mg diffusion into Sb and Bi adlayer. However, because Mg deposition is limited by the diffusion at the beginning and the Mg alloying changed the thickness by the expansion, the diffusions coefficient is an apparent value. According to the faster diffusion, high coulombic efficiency, high current density, and high reversibility the Sn anode is suggested to be a good alternative anode material for the Mg battery.

References

[1] N. Singh, T. S. Arthur, C. Ling, M. Matsui, F. Mizuno, *Chemical communications* **2013**, *49*, 149.

[2] D.-T. Nguyen, S.-W. Song, *Journal of Power Sources* **2017**, *368*, 11.

[3] H. Yaghoobnejad Asl, J. Fu, H. Kumar, S. S. Welborn, V. B. Shenoy, E. Detsi, *Chemistry of Materials* **2018**, *30*, 1815.

[4] L. R. Parent, Y. W. Cheng, P. V. Sushko, Y. Y. Shao, J. Liu, C. M. Wang, N. D. Browning, *Nano Letters* **2015**, *15*, 1177.

[5] P. Hegemann, M. Hegemann, L. Zan, H. Baltruschat, *Journal of The Electrochemical Society* **2019**, *166*, A245.

[6] V. Sudha, M. V. Sangaranarayanan, *Journal of Physical Chemistry B* **2003**, *107*, 3907.

[7] A. Collazo, R. Figueroa, X. R. Novoa, C. Perez, *Surface and Coatings Technology* **2015**, *280*, 8.

[8] F. Nacimiento, M. Cabello, C. Parez-Vicente, R. AlcÃ¡ntara, P. Lavela, G. F. Ortiz, J. Tirado, *Nanomaterials* **2018**, *8*, 501.

[9] M. Deepa, T. K. Saxena, D. P. Singh, K. N. Sood, S. A. Agnihotry, *Electrochimica Acta* **2006**, *51*, 1974.

[10] A. Kumar, R. Thomas, N. K. Karan, J. J. Saavedra-Arias, M. K. Singh, S. B. Majumder, M. S. Tomar, a. R. S. Katiyar, *Journal of Nanotechnology* **2009**.

[11] M. D. Levi, D. Aurbach, *Journal of Electroanalytical Chemistry* **1997**, *421*, 79.

Chapter 6: Magnesium Deposition and Alloying with Bi on Au Electrode

6.1 Introduction

In the past few years there has been a great deal of interest in electrodes with Bi as the anode for the rechargeable batteries. Wang et al. reported on a Bi anode in combination with glyme-based electrolyte (1.0 M $NaPF_6$ in diglyme) having a high Na storage performance.[1] The capacity of bulk Bi in 1.0 M $NaPF_6$ in diglyme achieved 400 mAh/g and still has 94.4 % of the highest capacity after 2000 cycles. The size of the Bi particles with a diameter of 15-18 μm was studied by scanning electron microscope. The intermetallic compounds formed during discharge were determined to be NaBi and Na_3Bi.

Bi-nanotubes as an anode material for Mg alloying/de-alloying showed superior cycling stability and rate performance in 0.1 M $Mg(BH_4)_2$-1.5 M $LiBH_4$-diglyme.[3] The high cyclability upon Mg alloying/extraction was attributed to the effectiveness of Bi-nanotubes in resisting the volume change. Benmayza et al. reported that the cell performance with Bi anodes for a Magnesium ion battery achieved reversible capacities of over 300 mAh/g and high coulombic efficiencies over 98%, if the cell was only cycled between 0.05 V to 0.5 V vs. Mg/Mg^{2+}. A changed surface morphology was observed during the alloying of Mg with Bi, and the amorphous layers of Bi reformed during the de-alloying process when the Mg ions diffuse into the electrolyte, and remains after completion of de-alloying. [4] Using electrodeposited Bi-CNT composite materials as magnesium battery anodes in $Mg(ClO_4)_2$/MeCN electrolyte, a high initial specific capacity of 180 mAh/g, dropped to 50 mAh/g after 3 cycles.[5] Alloying/de-alloying of Mg at electrochemically deposited Bi in $Mg(TFSI)_2$/acetonitrile solution also has been investigated. Tan et al. prepared a nanostructured Mg_3Bi_2 anode material and reported a high coulombic efficiency (99%), high reversible specific capacity (360 mAh/g) and high stability for Mg electrolytes. [6] Also, the transport properties of magnesium ions in two-phase Mg_3Bi_2-Bi electrodes have been studied. [7]

A phase diagram of Mg-Bi-system is shown in Figure 6.1. There is only a single thermodynamic stable binary phase of Mg_3Bi_2. A transition of the α-Mg_3Bi_2 to β-Mg_3Bi_2 occurs at the temperature of 703 °C. The structure of Bi metal and Mg_3Bi_2 are shown in Figure 6.2 a. In the Bi structure, the Bi atoms are connected by three covalent bonds forming wavy layers. Together with three additional bonds to atoms of the next layer, a 3 + 3 coordination for all atoms is obtained. This results in a bilayers of atoms perpendicular to the rhombohedral direction.

Between these layers the Mg ions could be inserted and then restructure to the binary phase Mg_3Bi_2. This is a Zintl-phase compound with formal charges of Mg^{2+} and Bi^{3-}. The structure is schematically shown in Figure 6.2 b. The crystal structure of Mg_3Bi_2 has two incorporates layers. One layer include tetrahedrally coordinated Mg^{2+} cations and octahedral interstitial sites $Mg_2Bi_2^{2-}$ sheets. The second layer consists of octahedrally coordinated Mg^{2+} cations and tetrahedral interstitial sites. [8]

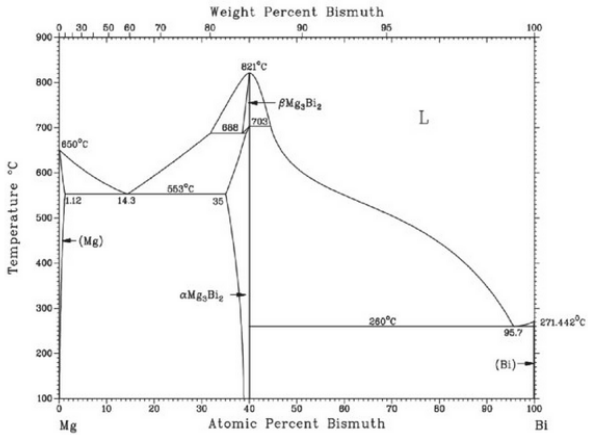

Figure 6. 1: Phase diagram of Mg-Bi-system. There is only one single binary phase Mg_3Bi_2.

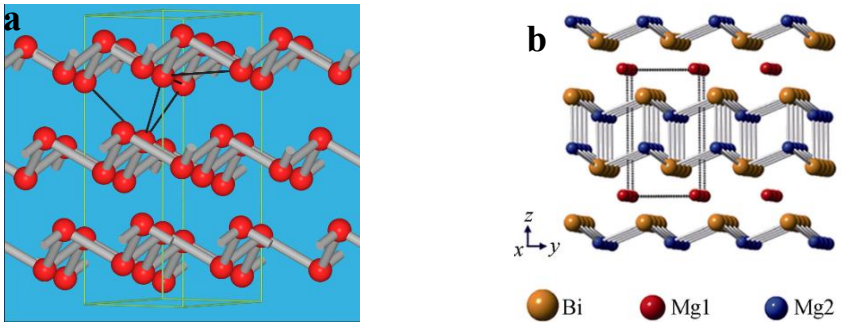

Figure 6. 2: The crystal structure of a) Bi metal: the schematic diagram of hexagonal crystal structure. The rhombohedral unit cell is shown within the crystal structure and the layers in the unit cell (space group: $R\bar{3}m$); b) Mg_3Bi_2 binary phase. [9]

Lee also reported that, the Mg_3Bi_2 is likely to be a semiconductor with relative low defect formation energies and the Mg vacancies are likely to form in this material. The migration of Mg has a lower migration barrier with 0.34 eV effecting from the spin-orbit coupling. [8]

Until now two studies of magnesium bulk deposition by scanning tunnelling microscope (STM) were reported. The solution containing Grignard salts and Mg-Al-Cl-alkyl complexes for Mg deposition was investigated by Aurbach et al. [10] Micrometric-sized, pyramid-shaped

magnesium crystals were observed from the deposition in the Grignard salt solution. In the solution containing $Mg(AlCl_2BuEt)_2$ the deposited Mg is less regular and the crystals are smaller. More recently the Mg Particles with a size of 10–30 nm and a height of 2 nm was visible on the Au(111)-surface during the bulk deposition from 0.5 M MACC/TG electrolytes. Afterwards, complete Mg dissolution was observed. [2]

We describe the electrochemical deposition of Bi on Au electrode by cyclic voltammetry, eQCM, and STM techniques. We then study the insertion of Mg into multilayers of Bi using non-aqueous electrolyte (MACC and $Mg(TFSI)_2$ in tetraglyme) by CV, DEMS, and EC-STM. The apparent diffusion coefficient of Mg in the Bi solid state will be estimated and the cycling reversibility of insertion/de-insertion will be demonstrated.

6.2 Experimental

Chemicals, materials and electrolyte

All aqueous electrolytes were prepared by 18.2 MΩ from Milli-Q water and de-aerated with high purity argon gas for at least 15 min before use. Electrochemical measurements in 0.1 M H_2SO_4 (Spectro pure grade) were implemented in a conventional three-electrode glass-cell. An Au sheet of 1 cm^2 and a RHE are used as a counter electrode and a reference electrode respectively. The electrochemical deposition at an Au working electrode was done in 0.1 mM Bi_2O_3 (99.999%, Aldrich) + 0.5 M H_2SO_4 electrolyte for Bi deposition;

A polycrystalline Au electrode and a bismuth modified Au electrode were used as working electrodes for Mg deposition and alloying measurements. Magnesium foil was then used as a counter electrode and another one as a quasi-reference electrode. All the magnesium electrochemical deposition measurements were carried out in the MBraun glovebox (H_2O < 0.5 ppm, O2 < 0.5 ppm).

Preparation of MACC

All chemicals were purchased from Sigma-Aldrich. The Tetraglyme was distilled over sodium and stored over molecular sieves (3 Å) until the water content reaches attains less than 5 ppm. The water content has been determined by Coulometric Karl Fischer titration (Mettler Toledo). $MgCl_2$ was heated overnight under vacuum at 290°C and then stored under thionyl chloride for 1 week. At low pressure the thionyl chlorid was removed completely. All materials were handled in an Argon filled glovebox. The MACC electrolyte was prepared by adding tetraglyme (20.5ml) to $MgCl_2$ (0.966g). While stirring the $AlCl_3$ (1.368g) was then added stepwise. The

whole mixture was stirred overnight after addition of an equivalent (H_2O: 63 ppm measured before the addition of MgH_2) amount of MgH_2 to reduce the water content (to below 10 ppm measured after the addition of MgH_2). For details see Hegemann et al. [2]

Cyclic Voltammogram (CV)

Electrochemical measurements of Bi deposition and Mg deposition and alloying were carried out in a conventional three-electrode glass H-cell consisting of three compartments for fixing the working electrode, reference electrode, and counter electrode. The working electrode is placed in the central compartment and contacted with a solution in a hanging meniscus configuration. The reference electrode is placed in the compartment where it is connected to the central compartment with a Luggin capillary. The counter electrode is placed in the compartment, separated from the central compartment by a glass frit.

All electrochemical measurements were carried out using a potentiostat purchased from Pine Instruments, Inc. (model AFBPC1) in combination with home-made LabVIEW program (National Instruments GmbH, Munich, Germany) for recording the cyclic voltammograms (CVs)

Preparation of Au(111) single crystal electrode

The Au(111) single crystal electrode (Mateck, Germany) with a diameter of 10 mm was used for the STM measurement. It was polished with roughness < 0.01 micron and orientation accuracy < 0.4 deg. After annealing the electrode was cooled down in pure argon (Air Liquid, 99.999%) atmosphere. All aqueous electrolytes were prepared by Milli-Q water and de-aerated with high purity argon gas for at least 15 min before use. Electrochemical measurements in 0.1 M H_2SO_4 (Spectro pure grade) were carried out in a conventional three-electrode glass H-cell consisting of three compartments. A large Au sheet (1×1 cm) was used as the counter electrode, a reversible hydrogen electrode (RHE) prepared by electrolyzing 0.1 M H_2SO_4 electrolyte was used as the reference electrode and the Au(111) was used as a working electrode.

EC-STM Measurement

All EC-STM measurements were performed with an Agilent PicoSPM and have been done in the EC-STM cell as described before. An Ag and Au wire was used as a quasi-reference electrode and a counter electrode, respectively. The reference electrode was immersed in a small

compartment filled with the same electrolyte and separated from the main compartment by a capillary. Pt/Ir (90:10) STM tips with a diameter of 0.25 cm were prepared by etching in a 2 M KOH + 4 M KSCN bath and coated with hot-melt glue. All the EC-STM measurements for Mg alloying and deposition were done in the MBraun glovebox (H_2O < 0.5 ppm, O_2 < 0.5 ppm).

6.3 Results and discussion

6.3.1 Preparation of Bi modified Au electrode

In figure 6.3 the CV and the frequency for bismuth deposition in 0.1 M Bi_2O_3 in 0.5 M H_2SO_4 solution are shown. The peaks at 0.45 V vs. RHE in both cathodic and anodic direction belong to the Bi-underpotential deposition. The bismuth bulk deposition starts at 0.25 V vs. RHE followed by an increasing current with a peak at 0.13 V vs. RHE. In the anodic sweep the bismuth dissolution gives rise to a peak at 0.4 V. The coulombic efficiency is nearly 99%. The m.p.e value is 86.7 g/emol for deposition and 74.6 g/emol for dissolution. (Table 6.1) Bismuth has a molar mass of 208.98 g/mol and during the deposition three electrons are exchanged:

$$Bi^{3+} + 3e^- \longrightarrow Bi \qquad (6.1)$$

Thus the theoretical value is 69.7 g/emol.

For magnesium alloying/de-alloying the bismuth was first deposited on the Au electrode during a potential hold of 15 min. Then the electrode was cleaned with Argon saturated water under potential control in order to remove the residue from the electrolyte. After three times changing of the water, the electrode was transferred into the glovebox under Argon atmosphere. Because of the equilibrium potential of Bi^{3+}/Bi (0.3 V vs. RHE) contact of the electrode with water and oxygen had to be avoided.

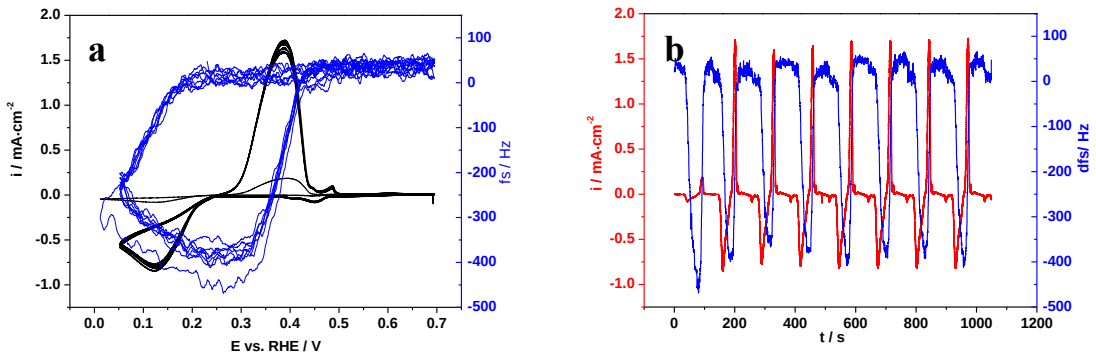

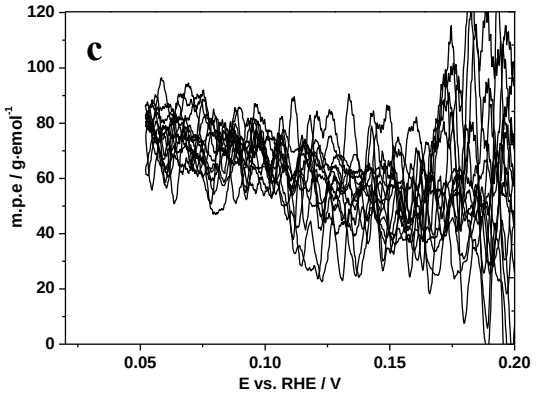

Figure 6. 3: CV and eQCM measurment for Bi-deposition in a 0.1 M Bi_2O_3 in 0.5 M H_2SO_4 solution in a three electrode set up. a) CV (black) and frequency difference (blue) versus potential with 10 mV/s for Bi-deposition on an Au quartz electrode; b) Current (red) and frequency difference (blue) versus time; c) m.p.e value versus potential in the range of 0.05 V to 0.2 V, where the Bi bulk deposition occurs.

Table 6. 1: Charge, mass changes, frequency changes and m.p.e value corresponding to the figure 7.9 for the Bi deposition/dissolution.

	Q (mC)	**dfs (Hz)**	**dm (µg)**	**m.p.e (g/emol)**
cathodic	12.9	405.7	17.4	86.7
anodic	12.2	414.3	11.6	74.6

A similar cyclic voltammogramm of Bi deposition on Au(111) in 1 mM Bi_2O_3 + 0.5 M H_2SO_4 electrolyte was obtained in the STM cell during the STM measurements as shown in Figure 6.4. Similar behaviors are observed as in the H-cell. (The potential has to be converted to that versus the reversible hydrogen electrode (RHE) using E (Pt/PtO) = 0.9 V vs. RHE.) The peak in the anodic direction with a negative current and the charge of the peak at -0.5 V vs. Pt/PtO in the cathodic direction are due to oxygen in the STM cell.

A freshly prepared Au(111) surface was employed for observing the bulk structure of Bi formed on its surface. As seen in Figure 6.5, which shows the adlayer structures of Bi deposited on Au(111) at -0.64 V vs. Pt/PtO for Bi-upd and at -0.76 V vs. Pt/PtO for Bi bulk deposition. The Bi bulk deposition shows an interesting growth on the Au(111) surface. A needle Bi bulk structure was observed along the step edges at the place with high step density. A height of 5 nm was determined by a „Local Plane Fit“. (Figure 6.6) The large height change at the bottom of figure 6.6a is due to the artefacts.

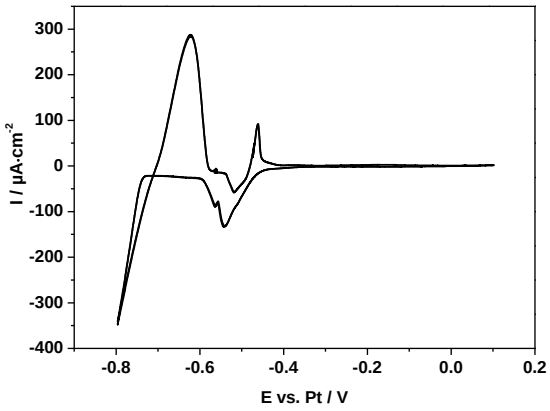

Figure 6. 4: Cyclic voltammogram of Bi deposition on Au(111) in 1 mM Bi_2O_3 + 0.5 M H_2SO_4 electrolyte in STM cell with sweep rate of 10 mV/s

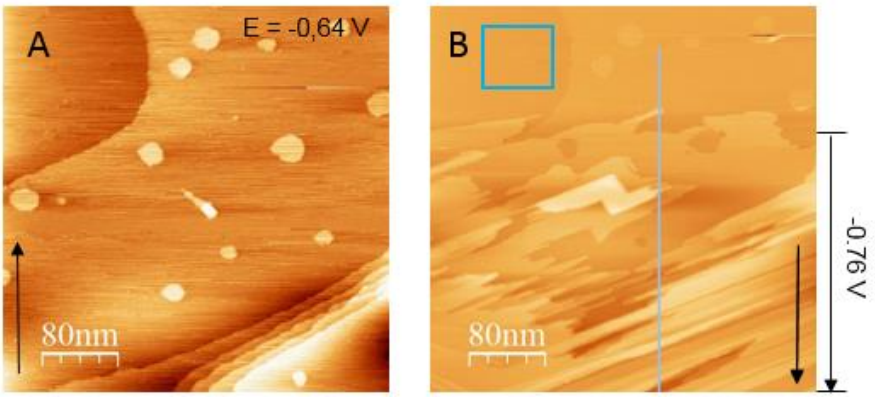

Figure 6. 5: STM images for Bi deposition in 1 mM Bi_2O_3 in 0.5 M H_2SO_4 on Au(111) surface. (A): Bi-UPD at -0.64 V vs. Pt. (B) Bi-bulk deposition between -0.64 V and -0.76 V vs. Pt. Taken from my master thesis.

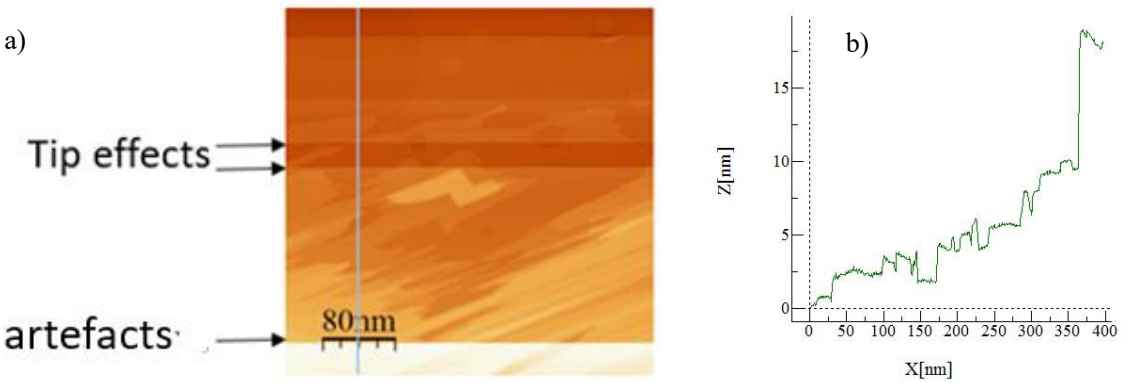

Figure 6. 6: a) the height of the Bi bulk deposition determined using a "Local Plane Fit" for background subtraction. The subtracted plane was shown with Blue Square in Figure 6.5b. b) The cross section of the image a (green line). Taken from my master thesis.

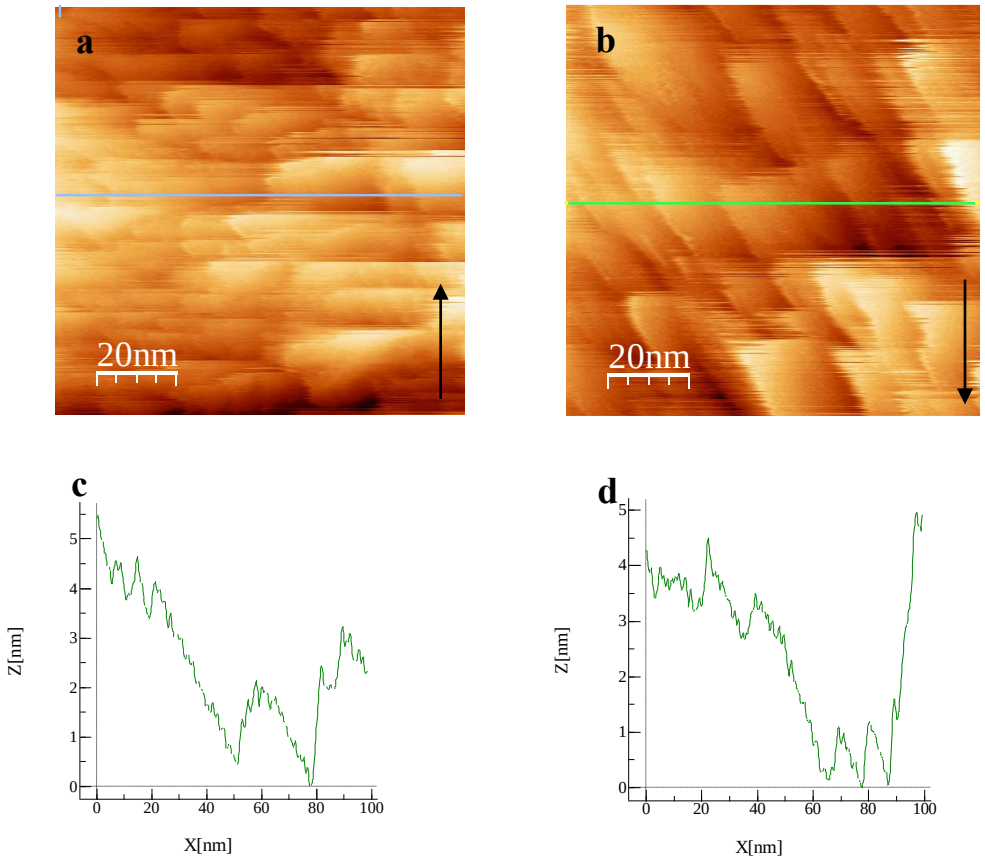

Figure 6. 7: STM images of bulk Bi on Au(111) in 0.5 M MACC/TG electrolyte after transfer into the glovebox at OCP. (The Bi was deposited from 1 mM Bi_2O_3 in 0.5 M H_2SO_4 on Au(111) surface prior to the transfer into the glovebox). (a): scan direction up; (b): scan direction down; (c): the cross section on the image a (blue horizontal line). (d): the cross section on the image b (green line).

Afterwards, the Bi-modified Au (~80 nmol/cm^2, ~12 nm) electrode has been transferred to the glovebox under inert atmosphere in order to check surface morphology by STM. Figure 6.7 a and b shows the Bi bulk structure on Au(111) surface after transport to the glovebox in the 0.5 M MACC/TG at the OCP. It is seen that the surface structure of Bi remains as flat as in the aqueous solution. (More details in my master thesis) The typical step height is about 2-5 nm.

6.3.2 Mg deposition and alloying on Bi-modified Au-Electrode in MACC/TG

The cyclic voltammogram of electrochemical deposition of bulk Bi at polycrystalline Au electrode is shown in Figure 6.8. To form a thick layer of Bi on the Au electrode, the potential was held at 0 V vs. RHE for 10 min during the cathodic going sweep. The number of moles of Bi deposited at Au electrode was calculated to be ~203 nmol/cm^2 from the integrated charge density of 46.9 mC/cm^2. Afterwards, the Bi-modified Au electrode was transferred to the glovebox under inert atmosphere where the electrochemical insertion of Mg from MACC electrolyte is examined.

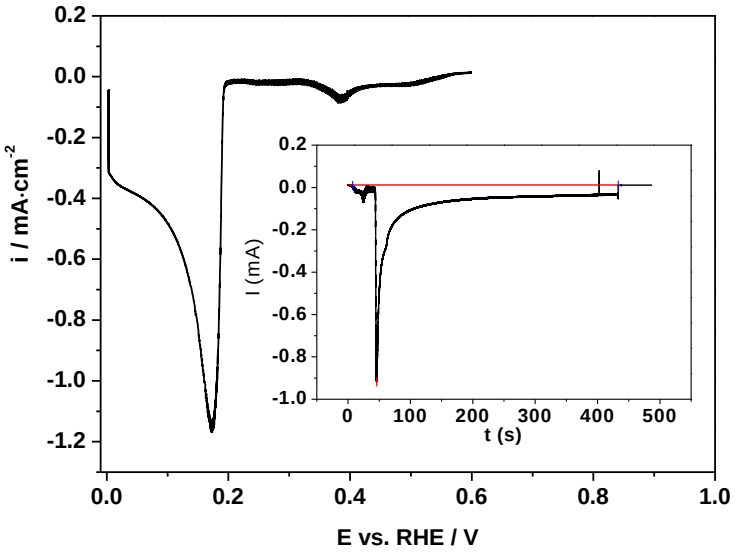

Figure 6. 8: Cyclic voltammograms of polycrystalline Au in 1 mM Bi_2O_3 + 0.5 M H_2SO_4 electrolyte at the sweep rate of 10 mV/s. Inset: current data plotted as function of time.

The Figure 6.9 shows the electrochemical magnesiation of the Bi (red) and the magnesium deposition on Au (black) with 1 mV/s. The magnesium bulk deposition occurs with 220 mV overpotential by using an Mg reference electrode. (Black curve in fig. 6.9) In comparison with the deposition on pure Au electrode the magnesium alloying process with Bi occurs already at 360 mV vs. Mg (360 mV positive) with the current increase in form of a shoulder. (Red in Figure 6.9) In the anodic sweep two peaks for the de-alloying were observed. The Mg alloying with Bi shows excellent reversibility in 0.5 M MACC/TG electrolyte and the current density is higher than the Mg alloying with Sb, although the Sb and Bi have the same crystal structure and similar chemical properties. A nearly 100 % of efficiency for Mg bulk deposition (131.3 mC/cm^2)/dissolution (130.1 mC/cm^2) and alloying (58.7 mC/cm^2)/de-alloying (58.2 mC/cm^2) is achieved. (Integration from the plot of i vs. t: between 0.36 V and -0.20 V for the alloying in the cathodic sweep and between 0.70 V and 1.6 V for the de-alloying in the anodic sweep) The ratio between the deposited bismuth and the alloyed magnesium is calculated from the charge to be 3:2. From the thermodynamic data of the formation of the Mg_3Bi_2 alloy compound, [11] the potential is calculated to be 260 mV vs. Mg, (phase diagram in Fig. 6.1) according to the following reaction equation:

$$2Bi + 3Mg + 6e^- \longrightarrow Mg_3Bi_2 \qquad (6.2)$$

Therefore, the experimental positive shift for the insertion of Mg into Bi adlayers is in agreement with the theoretical expectation. After the saturation of the host-layers, bulk deposition of Bi starts with the corresponding increase of the cathodic current. As opposed to

bulk deposition on Au, bulk deposition on the Bi modified surface occurs without nucleation overpotential. In the anodic going sweep, the bulk dissolution peak and the de-insertion peak overlap each other (see red curve). Mg de-insertion takes place at a more positive potential compared to that of bulk dissolution.

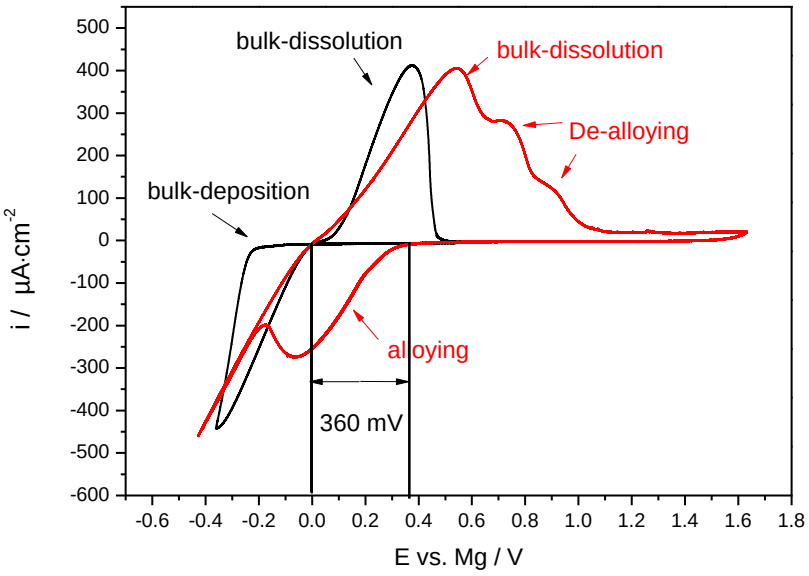

Figure 6. 9: CV for electrochemical magnesium deposition and alloying on Bi in a 0.5 M MACC/TG electrolytes in a three electrode cell with 1 mV/s. (Bi: ~203 nmol/cm^2) AE: Au and Bi modified Au; CE and RE: Mg.

A freshly deposited Bi layer (233 nmol/cm^2) on a Au(111) single crystal electrode was first prepared in an aqueous electrolyte and then transferred into the glove box for Mg deposition and alloying. In Figure 6.10 an overview of the electrochemical deposition and alloying of Mg with Bi on the Au(111)- single electrode by EC-STM measurement is shown. The recorded CVs show the same features as the CV in the glass H-cell. The current density of alloying/de-alloying decrease after the EC-STM measurements, since this electrolyte is very sensitive to water and oxygen in EC-STM cell. (dotted line in fig. 6.10)

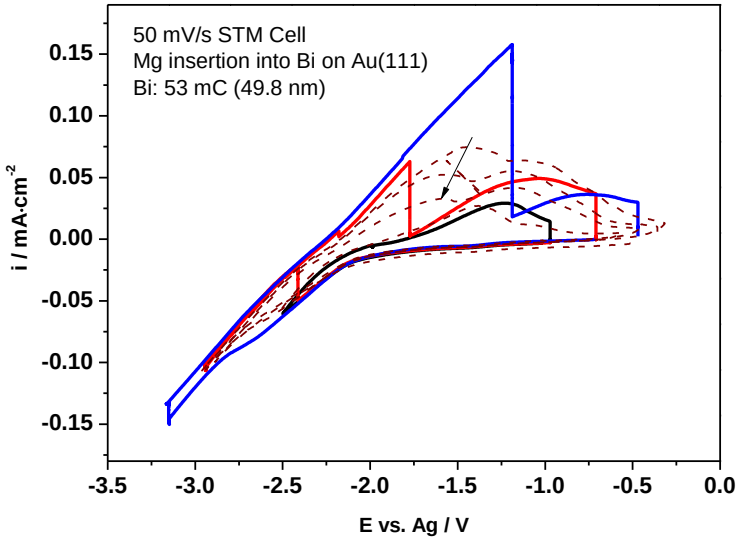

Figure 6. 10: CVs for electrochemical magnesium deposition and alloying on Bi in a 0.5 M MACC/TG electrolytes in an EC-STM cell with 50 mV/s. (Bi: ~233 nmol/cm^2) AE: Bi on Au(111); CE: Mg; RE: Ag. The curves with different colors show the sequence and the potential hold for recording the STM images in Fig. 6.11 - 6.13. Black: (1) -1.0 V (2) sweep to -2.5 V back to -2.0 V (3) -1.0 V; Red: (1) -2.42 V (2) -2.93 (3) -1.8 V (4) -0.73 V; Blue: (1) -3.14 V (2) -1.2 V (3) -0.5 V; Dotted line: recorded CVs afterwards.

The experiment starts first at OCP to check the Bi structure on Au(111) and the recorded STM image is shown in Figure 6.11 a. The Bi particles with a diameter of around 100 nm and a height of 40 nm were observed on the Au(111) electrode. A large smooth surface on the top of mountains in the 3D images (fig. 6.11 a′) is clearly seen. Afterwards, the cell and the counter electrode were switched on. After the new approach at -1.0 V, the STM images were recorded. (Fig. 6.11 b) It is seen that the surface was getting rough, which might be due to the Al deposition or some side reactions. Then the tip was retracted and the potential was swept to -2.5 V (where the Mg alloying occurs) and then back to -2.0 V (where no current flows through the cell). At this potential, the tip was approached to the surface again and the STM image was recorded. The images c and c′ show clearly that the crystalline structure of Bi disappeared during the Mg alloying process and the surface becomes rougher. The small mountains visible in Fig. 6.11c′, marked by red circles, are artefacts, possibly due to the contact of the tip with the surface. Afterwards, the potential was swept back the -1.0 V (where the Mg de-alloying occurs) with the tip still being approached the surface. (see fig. 6.11 d and d′) The Bi crystalline structure appears again during the Mg de-alloying process. At the left side in figure 6.11 d and d′ the mountains (70 nm height) with a large smooth surface on top and at the right side the Bi layers can be observed.

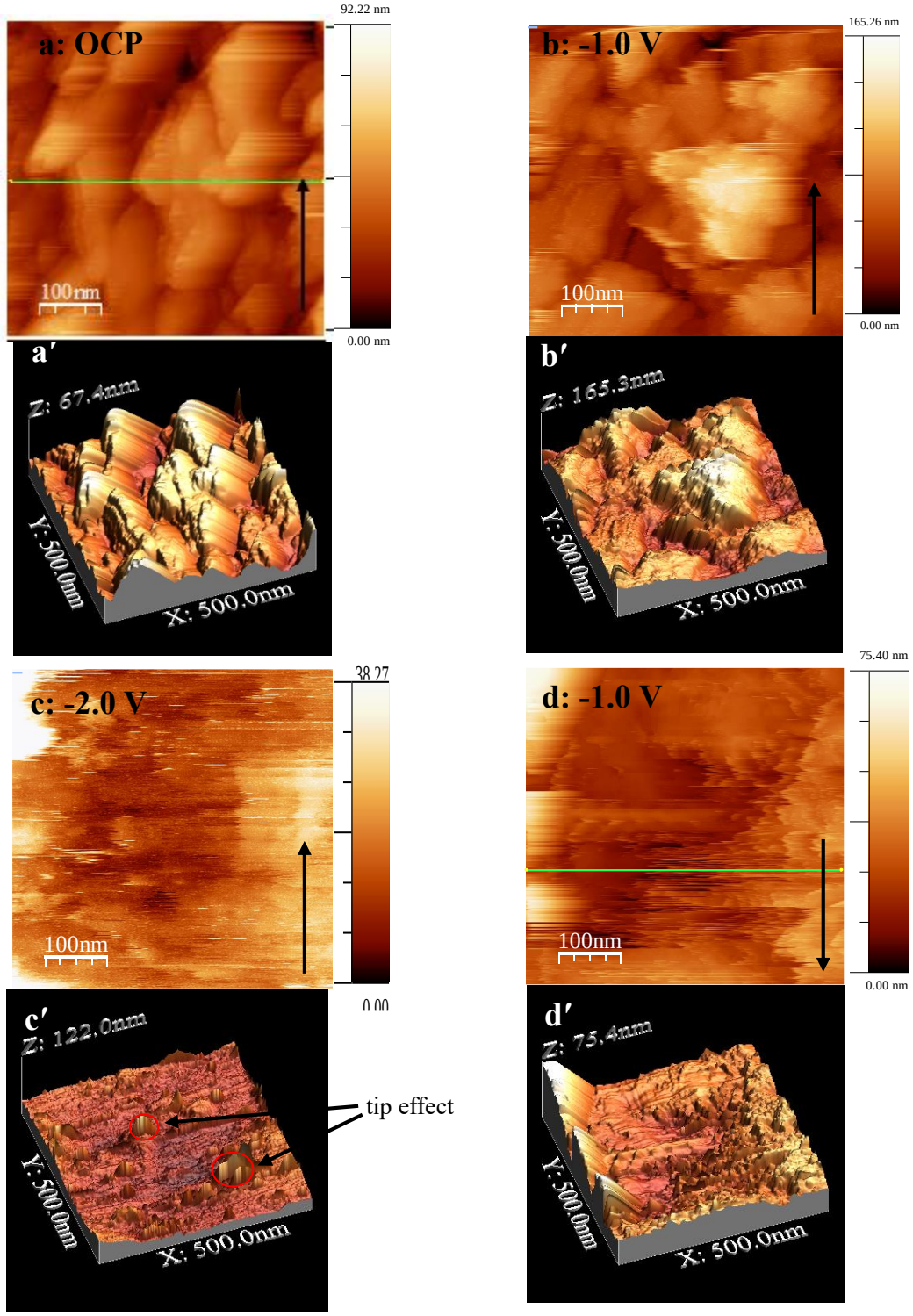

Figure 6. 11: STM images of Mg alloying at Bi modified Au(111) surface in 0.5 M MACC/TG electrolyte. (a) at open circuit potential of -0.5 V vs. Ag/AgCl, (b) potential hold at -1.0 V vs. Ag/AgCl, (c) sweep to -2.5 V and back to -2.0 V, (d) sweep back to -1.0 V vs. Ag/AgCl. a′, b′, c′, and d′ shows the corresponding 3D images, respectively. Sample bias of 50 mV, set point = 2 nA. Integral gain: 6 and proportional gain: 8. Arrows indicate scan direction.

Afterwards, th e tip potential was fixed at -1.5 V for the further measurements. A image with small surface area (zoom in) from Figure 6.11 d was first recorded and is shown Figure 6.12 a. The potential was cycled between -3.0 V and -0.7 V with the potential held at -2.4 V (Mg

alloying), -3.0 V (Mg bulk deposition), and -0.7 V (Mg dissolution and de-alloying) for recording the STM images. (Figure 6.12) The surface roughness is observed again due to the Mg alloying and the probably Al co-deposition comparing the STM images at – 2.4 V (6.12 b and b′) with the images at -1.0 V (6.12 a and a′). The spikes marked with blue square in Figure b′ are due to the disturbing tip.

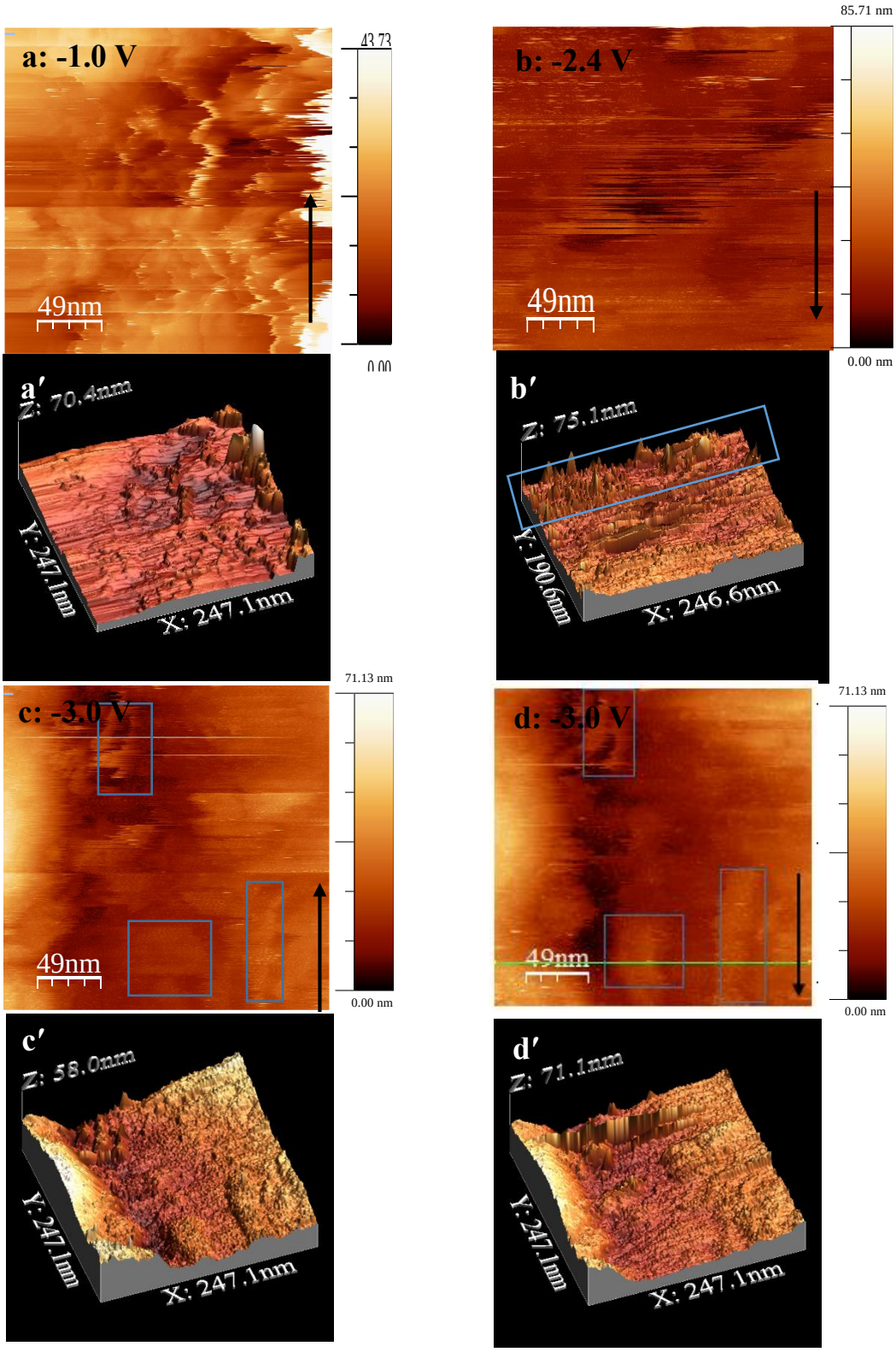

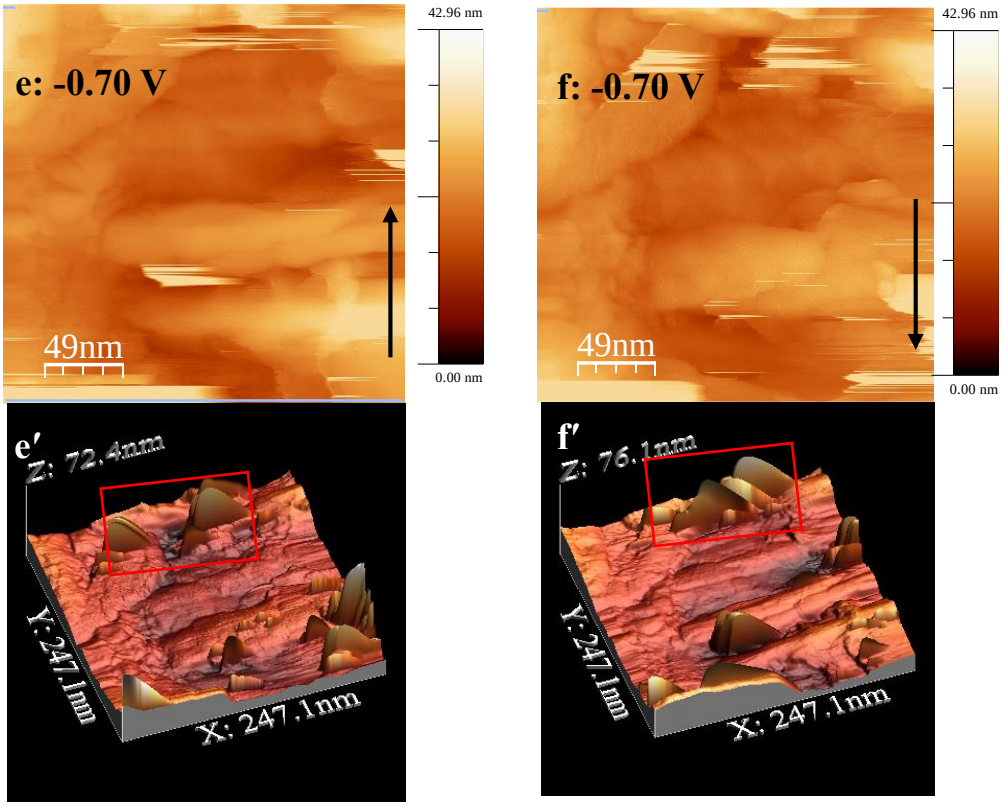

Figure 6. 12: STM images of Mg bulk deposition at Bi modified Au(111) surface in 0.5 M MACC/TG electrolyte. (a) zoom in at -1.0 V, (b) potential hold at -2.4 V, (c) and (d) potential hold -3.0 V, (e) and (f) potential hold at -0.7 V, a′, b′, c′, d′, e′ and f′ show the corresponding 3D images, respectively. Tip potential = -1.5 V, set point = 6 nA. Integral gain: 8 and proportional gain: 9. Arrows indicate scan direction.

Afterwards, the potential was held at -3.0 V in order to check the deposited bulk Mg morphology. (Figure 6.12 c and d) A large amount of the particle-like Mg and a few flaky structures of Mg were observed on the Au(111) surface. Further deposition of magnesium on its larger particles are formed at the same position marked in several blue squares as seen in Fig. 6.12 c and d. The magnesium dissolution process is shown in Fig. 6.12 e and f. Mg particles almost completely dissolve at -0.7 V and the surface changes back to be smooth. (The red marked squares in Figure e′ and f′ are artefacts caused by the tip) The STM images in Figure 6.14 a and b show Mg bulk deposition again, when the potential was directly swept to -3.0 V without a hold at -2.4 V. The images show a different position as the images in Figure 6.13 a and b. Large Mg particles with a diameter of 50 nm and a height of 30 nm can be observed during the bulk deposition. The Mg dissolution and de-alloying is shown in Figure 6.13 c, which is similar to the Fig. 6.12 e and f. But the huge crystalline Bi structure does not remain as it is seen at the beginning of the EC-STM measurements. The size of the Mg particles is larger than the Mg bulk deposition on pure

Au(111) electrode without Bi [2] and the shape of the particles is also different. (Figure 6.13 d)

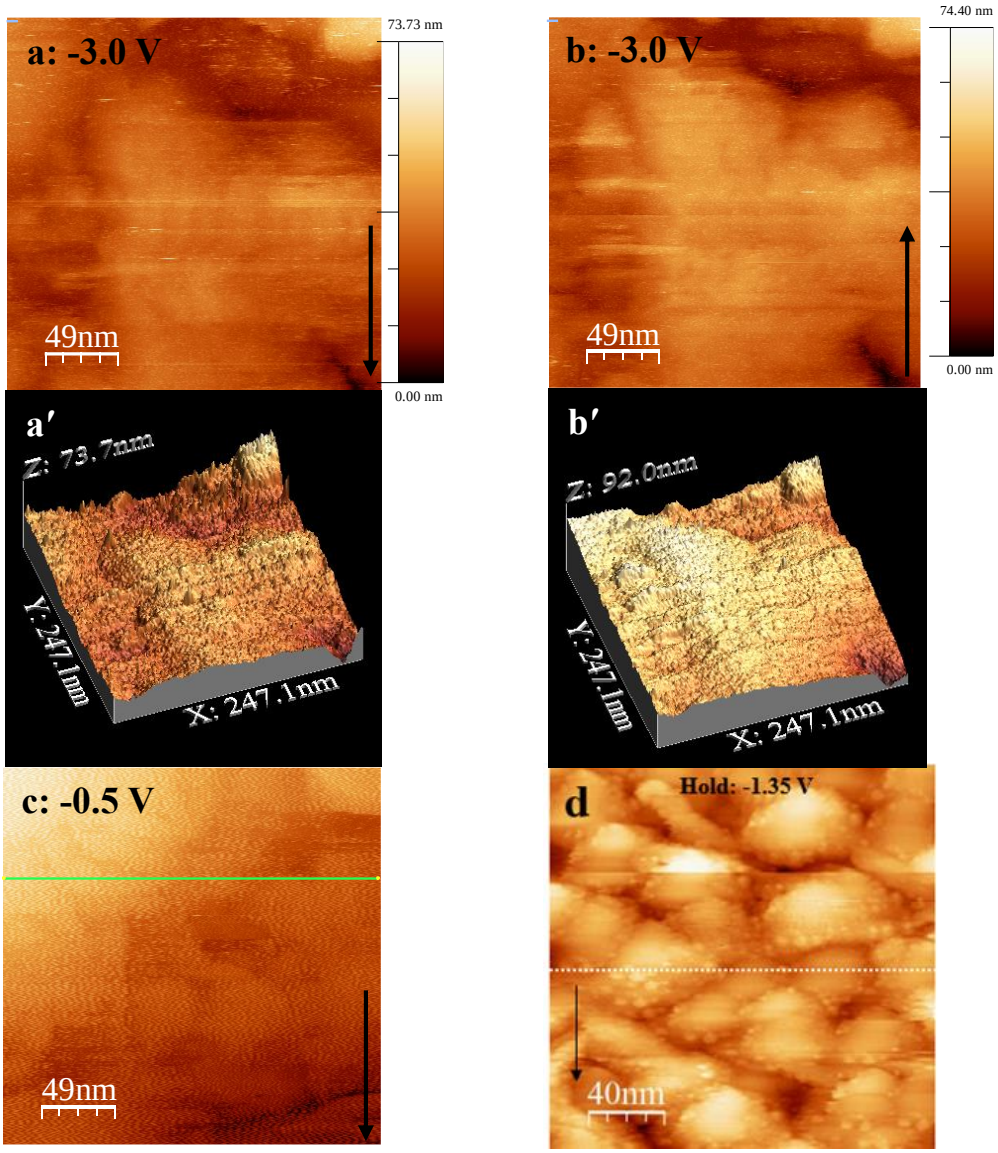

Figure 6. 13: STM images of Mg bulk deposition and dissolution at Bi modified Au(111) surface in 0.5 M MACC/TG electrolyte. (a) and (b) potential hold -3.0 V, (c) potential hold at -0.5 V, (d) Mg bulk deposition at pure Au(111) surface in 0.5 M MACC/TG electrolyte (taken from [2]). a′ and b′ show the corresponding 3D images, respectively. Tip potential = -1.5 V Sample bias of 50 mV, set point = 6 nA. Integral gain: 8 and proportional gain: 9. Arrows indicate scan direction.

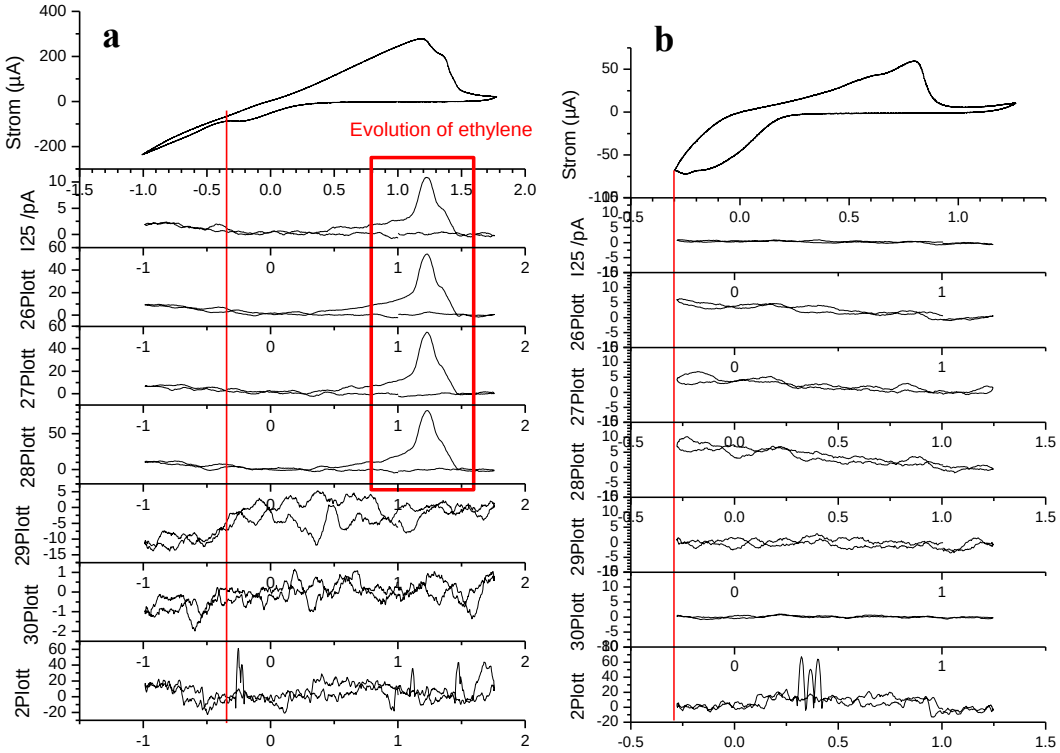

Figure 6. 14: CVs and MSCVs for DEMs measurement of magnesium deposition and alloying into Bi modified Au-electrode in 0.5 M MACC/TG with 10 mV/s. a): magnesium bulk deposition and alloying with potentials from -1.0 V to 1.7 V; b): only magnesium alloying between -0.3 V and 1.25 V vs. Mg. RE and CE: Mg. The red square shows the MS-signals for the formation of ethylene.

A DEMS measurement for investigation of the magnesium alloying/de-alloying on Bi modified electrode is shown in Figure 6.15. In order to check the influence of Bi on the decomposition of the electrolyte the CVs and MSCVs for magnesium deposition on Bi modified Au (Figure 6.15 a) and for only magnesium alloying with Bi (6.15 b) were recorded. It is seen that the ethylene is only formed during the magnesium bulk dissolution after the potential opening to -1.0 V vs. Mg. During the alloying/de-alloying of Mg with Bi no ethylene formation was observed which indicates that the electrolyte is stable within the alloying/de-alloying process between -0.3 V to 1.2 V vs. Mg/Mg^{2+}. However, so far it cannot be excluded that the maximum current density during dissolution also plays a role.

Ethylene formation had also been observed during the Mg dissolution from a pure Au electrode. There, in the MSCVs the signals for m/z = 25, 26, 27, 28 and 29 were recorded. It was assumed that ethylene formation is formed as a decomposition product on the surface of Au electrode: After some of the magnesium is dissolved into solution, some Mg-free the active sites on the Au electrode are available for ethylene formation. [2]

6.3.3 Determination of diffusion coefficient of Mg into Bi adlayers out of MACC in TG

a) CV

From cyclic voltammetry, we can estimate the diffusion coefficient from the change of peak current with varying sweep rates with the Randles-Sevcik equation (for irreversible system and semi-infinite diffusion)

$$i_p = 2.99 \times 10^5 n\sqrt{\alpha n_\alpha} A C_0 D_{Ca}^{0.5} v^{0.5} \quad (6.3)$$

where, C_0 is the concentration of Mg (theoretically, 0.035 mol cm^{-3} since the density of Mg_3Bi_2 alloy is 5.67 g/cm^3) in the solid state. Thus for diffusion controlled processes, I_p should depend linearly on $\sqrt{v}$. [12] Figure 6.16 a shows the cyclic voltammograms of a Bi modified Au electrode (~114 $nmol/cm^2$ Bi on Au) in MACC/tetraglyme at different sweep rates from 5 to 50 mV s^{-1} in the potential range of -0.3 to 1.2 V vs. Mg. A separation between the alloying and de-alloying peaks (ΔE) of around ≈ 0.25 V for the onset potential was observed, which is lower than the separation between the alloying and de-alloying with Sb (0.30 V). This indicates that the alloying/de-alloying of Mg with Bi is highly reversible and fast. It was reported that, the Mg alloying with Bi nanoparticles exhibited also a high cycling stability (more than 200 cycles). [3] An almost linear relationship between the Mg insertion and de-insertion peak currents and square root of sweep rate was obtained as shown in the inset of Fig. 6.16 b. Since the boundary conditions for of the Randles-Sevcik equation are not valid for dissolution, the diffusion coefficient is calculated from the deposition peak only. From the slopes of 9.1 mA $V^{-1/2}$ $s^{1/2}$ for alloying, we calculate a diffusion coefficient of 5.4×10^{-14} cm^2 s^{-1} for Mg alloying with $\alpha n_\alpha = 0.5$.

Table 6. 2: The charges for magnesation/demagnesation of Bi, coulombic efficiency and the ratio between alloyed Mg and deposited Bi at different potential sweep rates.

υ (mV/s)	**Charge density of alloying (mC/cm^2)**	**Charge density of de-alloying (mC/cm^2)**	**Col. Eff. (%)**	**Ratio Mg:Bi alloying (de-alloying)**
50	12.25	7.11	74	0.56 (0.32)
20	17.32	13.86	80	0.79 (0.63)
10	22.73	19.77	87	1.04 (0.90)
5	26.96	24.53	91	1.23 (1.12)

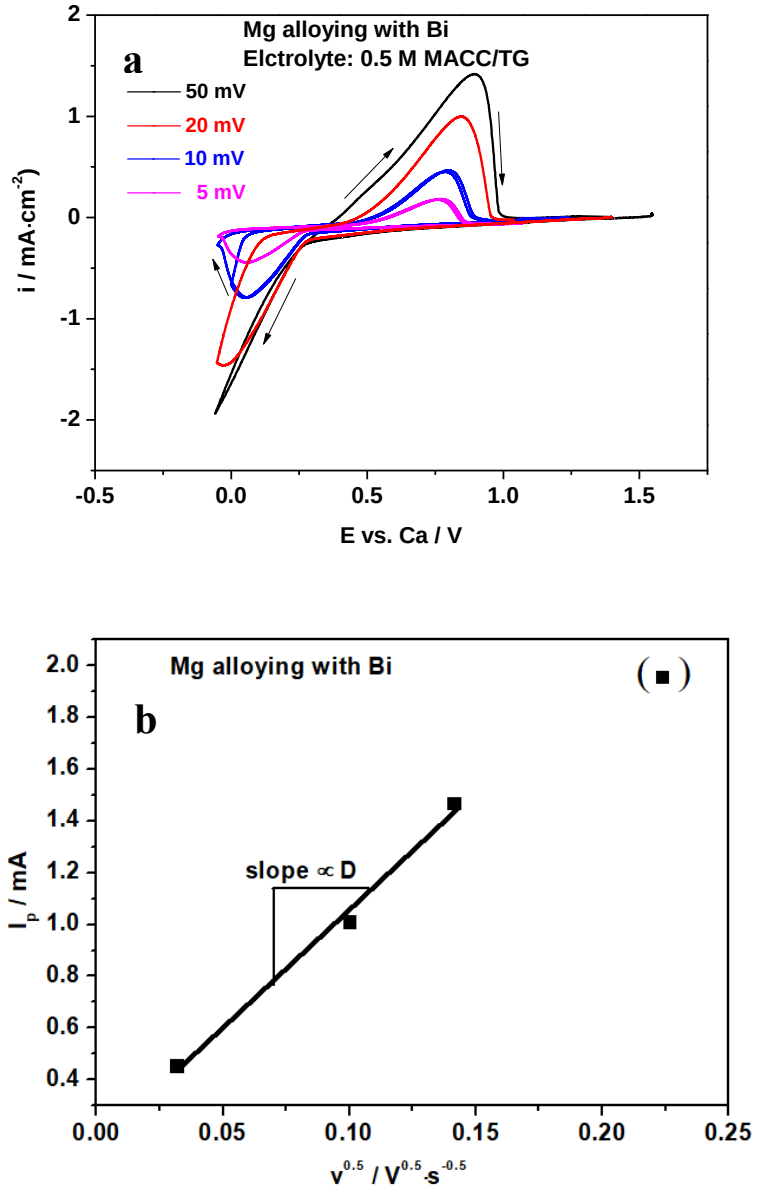

Figure 6. 15: a) Cyclic voltammograms of Mg alloying with Bi modified Au electrode in 0.5 M MACC/tetraglyme at different sweep rates from 5 to 50 mV s^{-1}. b): Plot of i_p (peaks current) vs. $\upsilon^{1/2}$ (square root of scan rate). AE: Bi on Au; CE and RE: Mg. (~114 nmol cm^{-2} Bi on Au and Surface area was 0.785 cm^2))

The charges for magnesation/demagnesation of Bi, coulombic efficiency and the ratio between alloyed Mg and deposited Bi at different potential sweep rates are shown in table 6.2. The ratio between the faradaic charge of anodic (de-alloying) and cathodic (alloying) gives the apparent coulombic efficiency. The coulombic efficiency was increasing from 74 % to 91 % with a decrease of the sweep rates from 50 mV/s to 5 mV/s. Saturation is not achieved even for 5 mV/s, as indicated by the Mg:Bi ratio.

b) Potential steps

In the following experiments, the amount of deposited Bi on Au polycrystalline is about 114 nmol/cm^2. The potential was first held at 1.0 V (where de-insertion of Mg takes place) in 0.5 M MACC/TG electrolyte for 10 min. Afterwards, the potential was stepped to several alloying potentials (from 0 to 0.3 V vs. Mg), at which magnesium could be alloyed with the Bi layer, for 5 mins. Then the potential was stepped back to 1.0 V for 5 mins where the extraction of magnesium takes place.

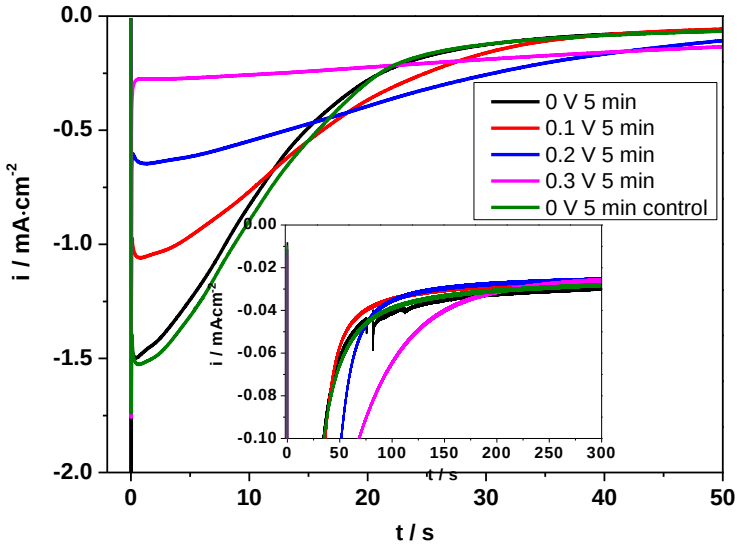

Figure 6. 16: the potential steps experiment for 5 min Mg alloying Bi bulk electrode out of a 0.5 M MACC/TG electrolyte from 0 V to 0.3 V respectively. Inset: the residual current of 20 µA after 5 min alloying. AE: Bi on Au; CE and RE: Mg. (~114 nmol/cm^2 Bi on Au and Surface area was 0.785 cm^2)

In Figure 6.17 the potential steps experiment for 5 min and 20 min Mg alloying Bi bulk electrode out of a 0.5 M MACC/TG electrolyte from 0 V to 0.2 V respectively. In the beginning, the current increased slightly for a very short time. This reductive currents at short times indicate an initial nucleation, charge transfer, and diffusion controlled process. The slight current increase is due to a nucleation and growth process for the building up of the Mg_3Bi_2 phase. In this short time, the concentration of Mg ions increased in the Bi layers at the surface, until the maximal concentration (C_0) of Mg in the new binary phase Mg_3Bi_2 was achieved. Then the current drops faster, which could be used for estimating the diffusion coefficient D with the Cottrell equation. The faradaic current didn't drops down to 0. (20 µA after 5 min insertion and 10 µA after 20 min insertion). We attributed this constant current to the Al co deposition in the

MACC electrolyte. In Figure 6.18 the potential steps experiment for Mg de-alloying electrode out of Bi bulk in 0.5 M MACC/TG electrolyte from 0 V to 0.3 V respectively are shown. In the beginning, the current increased slightly and then stayed constant at short time. This reductive currents at short times indicate an initial nucleation, charge transfer, and diffusion controlled process.

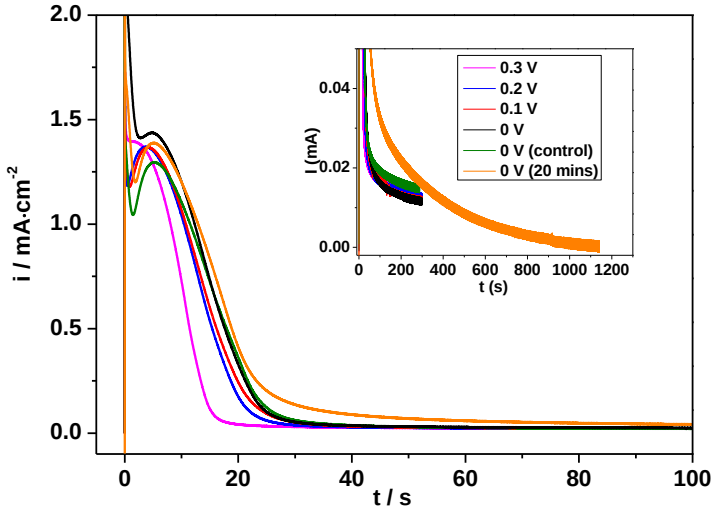

Figure 6. 17**:** Potential steps experiment for Mg de-alloying out of Bi bulk electrode in a 0.5 M MACC/TG electrolyte from 0 V to 0.3 V respectively. Inset: the current after 5 min (10 µA) and 20 min. The current drop to 0 after 20 min de-alloying. AE: Bi on Au; CE and RE: Mg. (~114 nmol cm^{-2} Bi on Au and surface area was 0.785 cm^2)

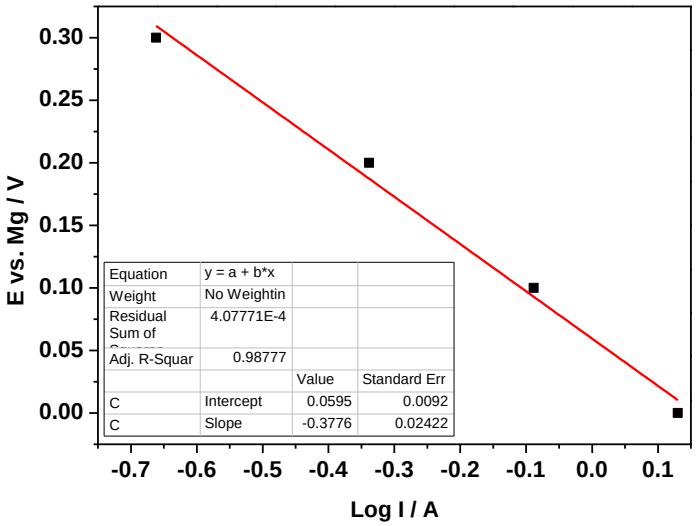

Figure 6. 18 Tafel plot of the overpotential versus the limited current for each jump potential. From the linear fitting the Tafel slop is determined to be 377 mV/decade, this value is higher than the usual value for kinetically controlled charge transfer, which is 120 mV/decade.

Table 6. 3: Dependence of Mg insertion/de-insertion integrated charges during the potential step experiments on potential of insertion, the corresponding coulombic efficiencies, the ratio between Bi and Mg and the diffusions coefficient. (~114 nmol cm^{-2} Bi on Au) (A correction of the cathodic charge density has been used for the alloying process. The current density at t = 20 min was subtracted. For de-alloying process the 0 line was used for integration)

Potential (V vs. Mg)	**Charge density (mC/cm^2) (alloying 5 min)**	**Charge density (mC/cm^2) (alloying 5 min corr.)**	**Charge density (mC/cm^2) (de-alloying)**	**Ratio of Mg:Bi alloying (corr.) (de-alloying)**
0	26.51	20.93	20.83	1.21 (1.21)
0.1	23.88	19.52	19.92	1.13 (1.15)
0.2	22.40	18.34	19.37	1.06 (1.12)
0.3	18.77	14.72	15.51	0.87 (0.92)
0 (control)	27.22	22.27	19.46	1.29 (1.13)
0 (20 min)	44.92	28.25	22.41	1.64 (1.27)

A plot of the potential versus the logarithm of the initial current is shown in Fig. 6.19. The value of Tafel slope is 377 mV/decade (this value is similar to the value of Mg alloying with Sb), much higher than the typical value of 120 mV/decade for one-electron transfer. This value of Tafel slope is equivalent to 0.32 electron transfer, which means that formally the Mg ion with 1.6 positive charged diffuse at the beginning of the alloying and appear only shortly at the interface on the Sb layers. So, the value of αn_α can be corrected to be 0.17, which should be used instead of 0.5 for the calculation of the diffusions coefficient in the Randles-Sevcik equation. With $\alpha n_\alpha = 0.17$ the diffusion coefficient was calculated to be 1.6×10^{-13} cm^2/s.

The charge density of bismuth magnesation/demagnesation, the ratio between the deposited Bi and the inserted Mg are summarized in in table 6.3. The charge density for both alloying and de-alloying increased with decreasing the alloying potentials for alloying, as expected. The charge density for 20 min (44.92 mC/cm^2) alloying without correction are much higher than for 5 min (28.25 mC/cm^2). The steady state current (~10 µA assumed for side reaction) at t = 20 min of Mg alloying at 0 V vs. has been subtracted for the each step of the Ca alloying process, which are also shown in the table 6.3. After the correction the ratio of Mg:Bi was estimated to be 1.64 at 0 V for 20 min. This value is higher than theoretical value of Mg_3Bi_2. We assumed that the Al co-deposition takes place during the alloying and the Mg bulk deposition since the

reference electrode of Mg is instable. For the alloying at 0 V a ratio of 1.21 (Mg:Bi) instead of 1.5 (theoretical value of Mg_3Bi_2) was observed, which indicated that the saturation is not achieved. This is different from the Mg alloying with Sb at 0 V, there the saturation was achieved. The reason is that the thermodynamic potential of Mg_3Bi_2 is 360 mV vs. Mg, which is more near to the 0 V than the thermodynamic potential of Mg_3Sb_2 (550 mV vs. Mg). Thus, a longer period is needed to achieve the saturation in the case of Mg alloying with Bi than Sb.

The value of D can also be calculated from the linear slope of Q^2 vs. t as shown in Fig. 6.20 for alloying and Fig. 6.21 for de-alloying with the integrated Cottrell equation, here for the C_0 we used the saturations concentration for the calculation of the diffusions coefficient.

$$Q^2 = \frac{(2zFAC_0)^2 D}{\pi} t \tag{6.4}$$

The estimated diffusion coefficients of alloying and de-alloying, and the value of $CD^{0.5}$ from potential step experiments are summarized in table 6.4.

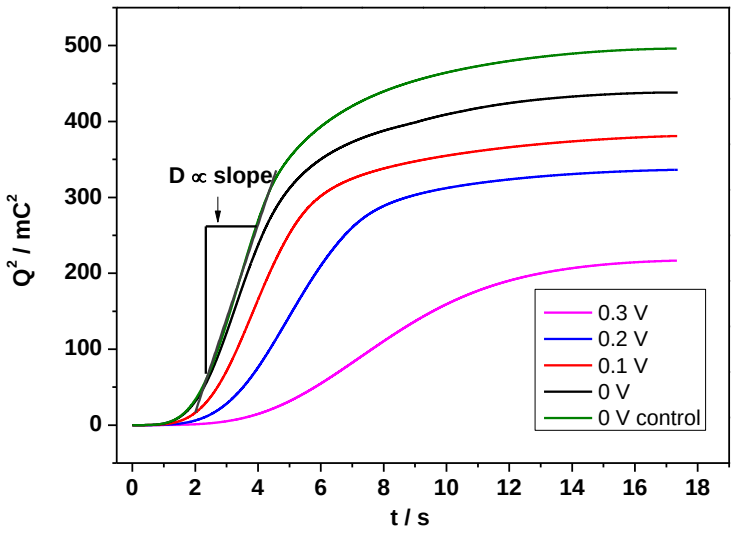

Figure 6. 19: Plot of transient Charge (Q^2 vs. t) for Mg alloying at different potentials (from 0 V to 0.3 V) with the time 5 min into Bi layers. The slope of linear area is used for calculation of the diffusions coefficient at 0 V. (Bi: ~114 nm/cm^2; surface area: 0.785 cm^2)

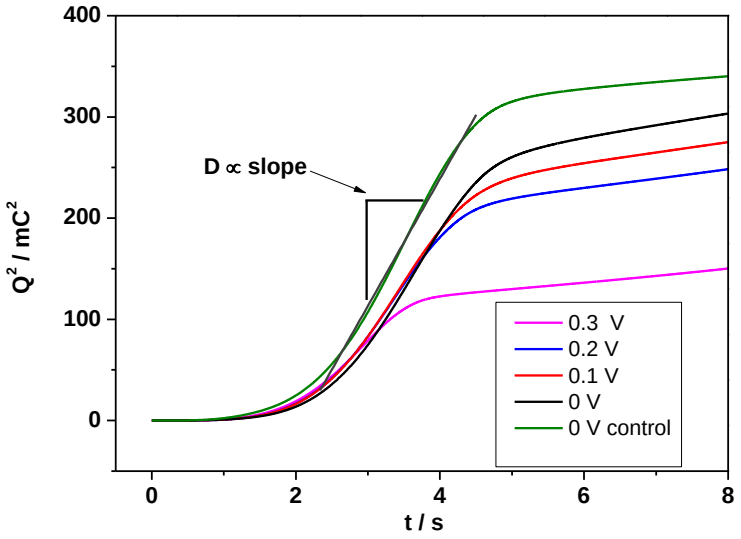

Figure 6. 20: Plot of transient Charge (Q^2 vs. t) for Mg de-alloying at 1.0 V vs. Mg corroding to the different potentials of alloying (from 0 V to 0.3 V) with the time 5 min out of Bi layers. The slope of linear area is used for calculation of the diffusions coefficient at 0 V. (Bi: ~114 nm/cm^2; surface area: 0.785 cm^2

The calculated diffusion coefficient from potential step experiments shows a value of 1.25 x 10^{-13} cm^2/s for alloying and 1.36 × 10^{-13} cm^2 s^{-1} for de-alloying at 0 V, when the saturated concentration of Mg in Bi is reached. From CV, the diffusion coefficient of Mg insertion into Bi multilayers was estimated to be 5.4×10^{-14} cm^2/s with $\alpha n_\alpha = 0.5$ and 1.6×10^{-13} cm^2/s with the experimental value for $\alpha n_\alpha = 0.17$. These values are in good agreement. This value is higher than the estimated value from GITT measurements. [13] They are one order of magnitude higher than the value obtained for the diffusion of Mg ions into Sb layers, indicating that the Mg ions diffuse faster in the Bi anode.

The pathway of Mg ions within the Bi structure has been studied by Matsui et al. using bond valence sum (BVS) mapping.[14] The Mg^{2+} ion at the tetrahedral site migrate prefer to the next tetrahedral site. This results is in agreement with the DFT calculation model for Mg^{2+}. [8] It was also suggested that the Mg^{2+} ion migrated in Bi faster than Sb, which indicated a high mobility of Mg^{2+} in the Mg_3Bi_2 phase. [7] The migration barrier of Mg^{2+} ions in the Mg_3Bi_2 phase was calculated to be 0.30 eV. [7] The estimated diffusion coefficient of Mg^{2+} ions in the Mg_3Bi_2 in this work is higher than the value in Mg_3Sb_2 layers since the migration barrier of the Mg^{2+} ions in the Mg_3Sb_2 is higher. All the results in literature and in this work on the electrochemical properties of Bi as a negative electrode suggest a good performance for rechargeable magnesium batteries.

Table 6. 4: The estimated diffusion coefficient of alloying and de-alloying, and the value of C^2D from potential step experiments

Potential for alloying (V vs. Mg)	**D alloying ($/10^{-13}$cm^2/s) (C_0 was used for all steps)**	**D de-alloying ($/10^{-13}$ cm^2/s) (C_0 was used for all steps)**	**$C\sqrt{D}$ alloying (de-alloying) ($/10^{-8}$)**
0	1.25	1.36	1.24 (1.29)
0.1	0.82	1.24	0.10 (1.23)
0.2	0.69	1.27	0.92 (1.25)
0.3	0.33	1.18	0.64 (1.20)
0 (control)	1.08	1.23	1.15 (1.23)

6.3.4 Mg deposition and alloying on Bi-modified Au-Electrode in $Mg(TFSI)_2$/TG

In this study the possibility of magnesium alloying with Bi from $Mg(TFSI)_2$ based electrolytes was tested. (Figure 6.22) It revealed that the alloying/de-alloying process of Mg with Bi exhibit coulombic efficiency of 40 % in case of 50 µV/s. (Coulombic efficiency of 20 % for Mg bulk deposition and dissolution) With adding small amount of $Mg(BH_4)_2$ the efficiency increases to 60 % and the current density is 0.165 mA/cm^2 instead of 0.065 mA/cm^2 without $Mg(BH_4)_2$. A small amount of $Mg(BH_4)_2$ adding to the electrolyte can probably remove the trace water. However the efficiency and the current density in both case of Sb and Bi do not achieve the expected value for reachable magnesium batteries. The poor performance of $Mg(TFSI)_2$ electrolytes could be due to the instability of the anion and the tetraglyme itself.

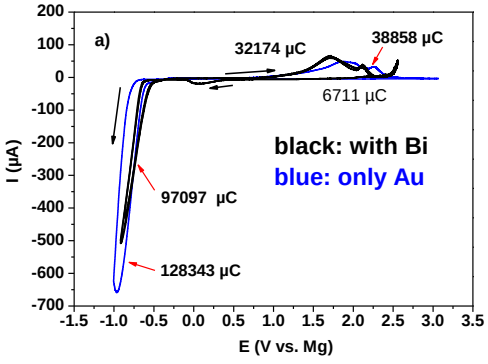

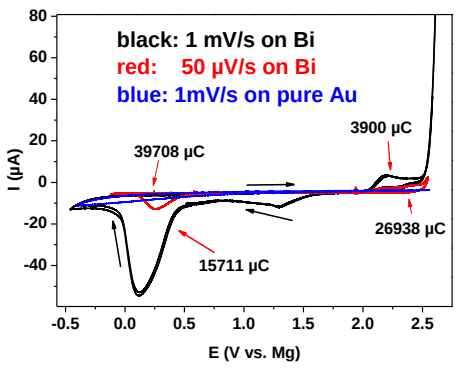

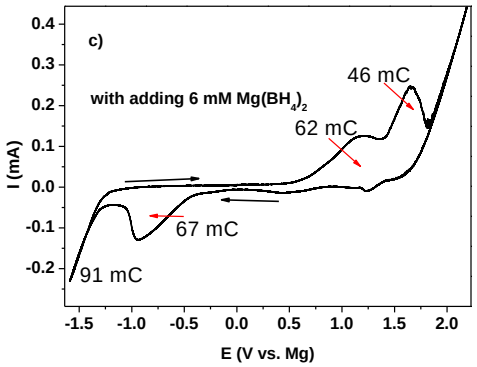

Figure 6. 21: CVs for electrochemical magnesium alloying and deposition. a): 0.5 M $Mg(TFSI)_2$ in TG on Bi (black) and on pure Au (blue) with 1 mV/s; b): 0.5 M $Mg(TFSI)_2$ in TG on Bi with 1 mV/s (black), 50 µV/s (red) and on pure Au (blue) with 1 mV/s; c) 0.5 M $Mg(TFSI)_2$ + 6 mM $Mg(BH_4)_2$ in TG on Bi. Black arrows show the direction of the scan and red arrows show peaks area related to the charge. CE and RE: Mg.

6.4 Conclusions

The electrochemical deposition of antimony on Au was first achieved in 0.5 M H_2SO_4 containing 1 mM Bi_2O_3 by cyclic voltammetry. Magnesium deposition/dissolution on Au and Bi modified Au electrodes were investigated in 1.5 M MACC/TG electrolyte. At the Bi modified Au electrode, a pre-cathodic peak started at around 360 mV (vs. Mg/Mg^{2+}), which is 360 mV more positive than the onset potential of bulk deposition at the Au electrode. It is suggested that this pre-cathodic peak is related to the alloying of Mg with Bi adlayers to form Mg_3Bi_2 alloy. The ratio of the amount of the alloyed Mg to that of the deposited Bi calculated from the corresponding peak charge is close to the theoretical value of 3:2 for Mg_3Bi_2 formation. A DEMS study has demonstrated the electrolyte stability. During the alloying process of Mg with Bi no ethylene formation was observed as opposed to the case of the Mg bulk deposition. High coulombic efficiencies, high cyclic stability, and high reversibility of Mg alloying/de-alloying with a Bi modified electrode have been observed in cyclic voltammetry and potential step experiments.

As observed by STM in MACC/tetraglyme electrolyte, the Bi bulk structure is similar to that in the aqueous solution. The Mg alloying and bulk deposition (big particles) were observed and almost all of these deposits could be dissolved reversibly. After the Mg alloying and bulk deposition the surface of the electrode was smoother and the crystalline structure of Bi does not remain as observed at the beginning.

Furthermore, the kinetics was investigated by potential steps experiments. It has been found that the alloying process was first determined by the nucleation, charge transfer, and diffusion

of Mg ions. The diffusion coefficient of Mg in Bi multilayers was estimated from CV and potential step experiments to be 1-2×10^{-13} cm^2s^{-1} respectively, which is higher than for the Mg alloying with Sb in the previous chapter. It shows a high Mg^{2+} mobility in Mg_3Bi_2 phase. This value is two orders of magnitude lower than the value for Li^+ ions from our work.

The investigation of magnesium deposition and alloying with Bi in $Mg(TFSI)_2$ based electrolyte exhibit low coulombic efficiency of 20 % for Mg deposition/dissolution and 40 % for Mg alloying/de-alloying. This value increased to 60 % with addition small amount of $Mg(BH_4)_2$. The BH_4^- ion is a relatively strong reducing agent, which enhances the electrochemical performance of the magnesium deposition and alloying process. The current density is about 0.165 mA/cm^2 for de-alloying peaks current. These findings demonstrated that the $Mg(BH_4)_2$ could be compatible with magnesium alloy type anode.

References

[1] C. Wang, Z. Xie, Z. Zhou, *APL Materials* **2019**, *7*, 040701.

[2] P. Hegemann, M. Hegemann, L. Zan, H. Baltruschat, *Journal of The Electrochemical Society* **2019**, *166*, A245.

[3] Y. Shao, M. Gu, X. Li, Z. Nie, P. Zuo, G. Li, T. Liu, J. Xiao, Y. Cheng, C. Wang, J.-G. Zhang, J. Liu, *Nano Letters* **2014**, *14*, 255.

[4] A. Benmayza, M. Ramanathan, N. Singh, F. Mizuno, J. Prakash, *Journal of the Electrochemical Society* **2015**, *162*, A1630.

[5] R. A. DiLeo, Q. Zhang, A. C. Marschilok, K. J. Takeuchi, E. S. Takeuchi, *ECS Electrochemistry Letters* **2015**, *4*, A10.

[6] Y.-H. Tan, W.-T. Yao, T. Zhang, T. Ma, L.-L. Lu, F. Zhou, H.-B. Yao, S.-H. Yu, *ACS nano* **2018**, *12*, 5856.

[7] S. C. Jung, Y.-K. Han, *The Journal of Physical Chemistry C* **2018**, *122*, 17643.

[8] Y. Lee, M. Cui, J. Choi, J. Kim, Y. Son, J. Khim, *Journal of Hazardous Materials* **2018**, *344*, 1116.

[9] T. T. Guo, X. R. Lu, R. K. Varma, C. Zhao, J. Wang, J. W. You, J. Chen, *Frontiers in Materials* **2021**, *8*, 11.

[10] **D. Aurbach**, **Y. Cohen**, **M. Moshkovich**, *Electrochemical and Solid-State Letters* **2001**, *4*, A113.

[11] A. G. Morachevskii, *Russian Journal of Applied Chemistry* **2019**, *92*, 1325.

[12] B. Markovsky, M. D. Levi, D. Aurbach, *Electrochimica Acta* **1998**, *43*, 2287.

[13] M. Ramanathan, A. Benmayza, J. Prakash, N. Singh, F. Mizuno, *Journal of The Electrochemical Society* **2016**, *163*, A477.

[14] M. Matsui, H. Kuwata, D. Mori, N. Imanishi, M. Mizuhata, *Frontiers in Chemistry* **2019**, *7*, 10.

Chapter 7: Calcium Deposition and Alloying with Sb on Au Electrode

7.1 Introduction

One of the most difficult challenges for the development of rechargeable calcium batteries is the anode. The anode materials together with the electrolytes are theoretically limited due to the low voltage and low energy density. The interfaces between the electrolytes and electrodes play a special role in reversible calcium plating and stripping. Alloys were suggested to alternative anode materials to Ca metal anode because they have a high specific capacity and low overpotential. [1] A DFT study of Ca_xM has suggested the selection of the alloy-type anode materials considering the alloying voltage, volume expansion, and specific capacity. The metals such as Si, Sb, Bi, Al, Pt, Pb, and so on were predicted to be promising inexpensive anode candidates. [1]

Calcium intercalation into graphite was first demonstrated by G. Srinivas et al., as graphite has been widely used as the anode for lithium-ion batteries. There, a high temperature hydrogenated calcium-graphite intercalation compound was investigate. It was found that only decomposition of CaC_6 took place and the hydrogenation of CaC_6 reveals a degradation of its superconducting properties. [2]The crystal structure of CaC_6 is rhombohedral and belongs to the R3m space group. [3] In 2016 Ponrouch et al. have reported that the electrochemical de-alloying of $CaSi_2$ is possible out of 0.45 M $Ca(BF_4)_2$ in PC/EC at moderate temperatures (100 °C). [4] However, the $Ca(PF_6)_2$ salt is known to be quite unstable. The DFT calculations indicated that the de-alloying of $CaSi_2$ should be observed at different voltages for different Si phases. The main particle size of $CaSi_2$ decreased from 7.3 to 2.6 µm after oxidation.

A calcium-antimony (Ca-Sb) alloy as the positive electrode in a Ca‖Sb liquid metal battery was investigated by Ouchi. [5] The OCP of the Ca-Sb electrode was tested to be around 1.1 V vs. Ca. Both alloying and de-alloying of Ca with Sb took place at a potential between 0.95 V and 0.75 V vs. Ca. The cell could be cycled with high coulombic efficiency (near 100 %). This experiment also suggested that Sb could be an alternative electrode for the rechargeable calcium batteries.

According to literature, Ca_2Sb, Ca_5Sb_3, $Ca_{11}Sb_{10}$, and $CaSb_2$ were considered for the Ca-Sb binary system. [6] Reversible Ca deposition were observed only in $Ca(BH_4)_2$/THF and $Ca[B(hfip)_4]_2$/DME electrolytes. [7, 8] [9]. In this work we study the alloying of Ca into thin layers of Sb on polycrystalline Au using non-aqueous electrolyte (1.5 M $Ca(BH_4)_2$ in THF) at room

temperature. The cycling reversibility of alloying/de-alloying will be demonstrated. During the discharge, the formation of $CaSb_2$ occurs, and the Sb structure will be then formed again during the charging process.

7.2 Experimental

Chemicals, materials and electrolyte

All aqueous electrolytes were prepared by 18.2 MΩ from Milli-Q water and de-aerated with high purity argon gas for at least 15 min before use. Electrochemical measurements in 0.1 M H_2SO_4 (Spectro pure grade) were implemented in a conventional three-electrode glass cell. Au sheet 1 cm^2 and RHE are used as a counter electrode and a reference electrode respectively. The electrochemical deposition at an Au working electrode was done in 0.25 mM Sb_2O_3 (99.999%, Aldrich) + 0.5 M H_2SO_4 electrolyte for Sb deposition;
A polycrystalline Au electrode and an antimony modified Au electrode were used as working electrodes for Mg deposition and alloying measurements. Magnesium foil was then used as a counter electrode and another one as a quasi-reference electrode. All the calcium electrochemical deposition measurements were carried out in the MBraun glovebox (H_2O < 0.5 ppm, O_2 < 0.5 ppm).

Preparation of 1.5 M $Ca(BH_4)_2$ in THF

Calcium borohydride bis (tetrahydrofuran) ($Ca(BH_4)_2 \cdot 2THF$) was purchased from Sigma-Aldrich. Extra dry tetrahydrofuran (THF, <5 ppm) was produced from the inorganic institute at the University of Bonn and stored several days over molecular sieves (4Å, Aldrich). The calcium metal (purity 99.99 %) was achieved from the project partner ZSW Ulm. The salt was first dissolved in THF overnight and a clear solution was obtained. (10 ppm) The preparation of the solution was made and all materials were stored in the MBraun glovebox (H_2O < 0.5 ppm, O_2 < 0.5 ppm).

Cyclic Voltammogram (CV)

Electrochemical measurements for Sb deposition on Au electrode and the Ca deposition including alloying were carried out in a conventional three-electrode glass H-cell consisting of three compartments for fixing the working electrode, reference electrode, and counter electrode. The working electrode is placed in the central compartment and contacted with a solution in a hanging meniscus configuration. The reference electrode is placed in the compartment where it

is connected to the central compartment with a Luggin capillary. The counter electrode is placed in the compartment, separated from the central compartment by a glass frit.

All electrochemical measurements were carried out using a potentiostat purchased from Pine Instruments, Inc. (model AFBPC1) in combination with home-made LabVIEW program (National Instruments GmbH, Munich, Germany) for recording the cyclic voltammograms (CVs)

7.3 Results and Discussion

7.3.1 Ca deposition and alloying on Sb-modified Au-Electrode in $Ca(BH_4)_2$ in THF Electrolyte

Sb was first freshly deposited on Au electrode and then transferred to the glovebox under inert atmosphere where the electrochemical alloying of Ca was started. (Modification of Au by Sb as described in previous chapter 4) Fig. 7.1 shows the comparison of electrochemical deposition and stripping behavior of Ca at a bare gold electrode and Sb-modified gold electrode in 1.5 M $Ca(BH_4)_2$ in THF. A stable CV of the calcium deposition starts on the bare poly-crystalline Au electrode has been shown in Fig 7.1 a. The calcium bulk deposition started at about -0.2 V vs. Ca/Ca^{2+} in the cathodic sweep, and in the anodic direction, a bread peak for calcium dissolution starts at -0.05 V vs. Ca/Ca^{2+}. (Fig. 7.1 a) The coulombic efficiency, which was calculated from the charge of the dissolution divided by the charge of deposition to be 97%. (The initial coulombic efficiency was 81 % in the first cycle Fig. 7.1 a) This value is higher than the literature value of 94.8 %. [7] The missing coulombic efficiency is probably due to the formation of a small amount of CaH_2, which might act as SEI allowing the high reversible calcium deposition and dissolution. [7] This coulombic efficiency is high, but still is not sufficient for use in a rechargeable battery.

The calcium deposition and dissolution at the Sb-modified gold electrode is shown in Fig 7.1 b. The black curve shows the first cycle of Ca alloying with Sb and the Ca bulk deposition, It is seen that there is a larger overpotential for Ca bulk deposition in the first cycle (similar as the first cycle without Sb shown as red curve in Figure 7.1a) than it in the stable CV (black curve in Fig 7.1a). In the cathodic direction the current was increasing slightly at 1.0 V vs. Ca/Ca^{2+}, giving rise to a shoulder which we attribute this to the alloying of Ca into the Sb-adlayer and formation of the binary phase of $CaSb_2$, according to the following equation:

$$2Sb + Ca^{2+} + 2e^{-} \rightarrow CaSb_2 \qquad (7.1)$$

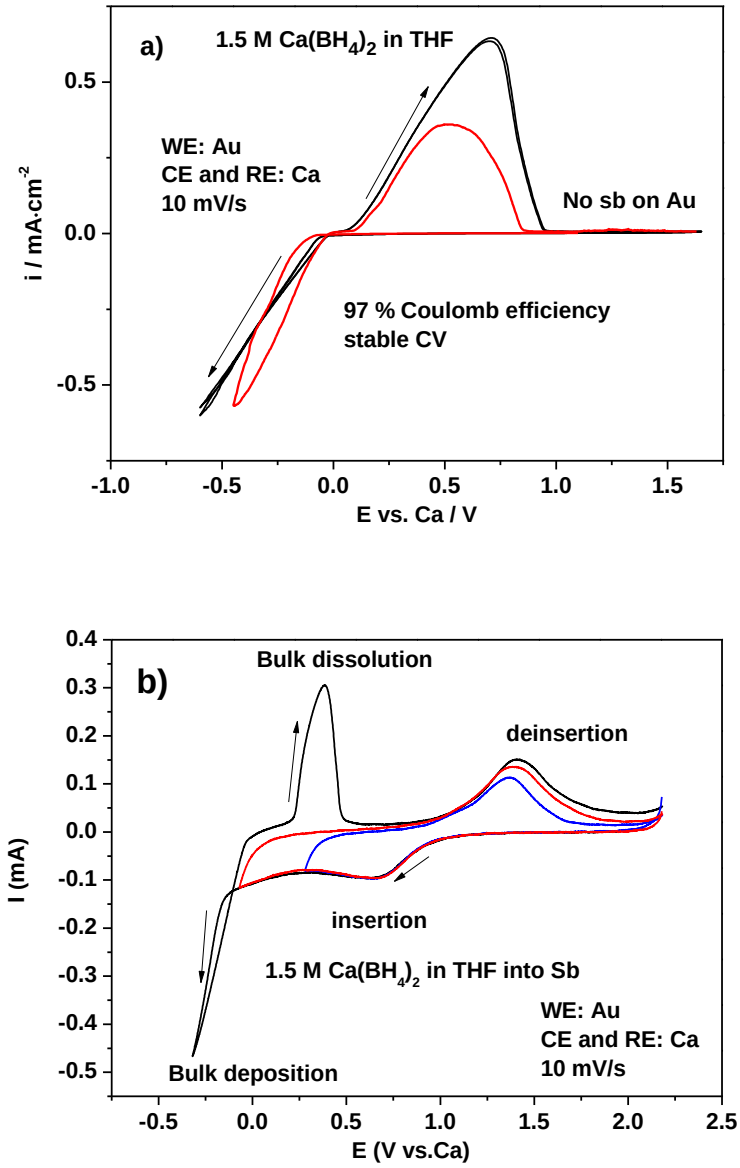

Figure 7. 1: Cyclic voltammograms of Ca deposition/dissolution at bare Au-electrode (a) and Sb modified Au-electrode (b) in 1.5 M $Ca(BH_4)_2$/THF at the sweep rate of 10 mV s^{-1}. Ca alloying/de-alloying at Sb modified electrode in the potential range of -0.5 V to 2.0 V vs. Ca/Ca^{2+}. Red curve in a shows the first cycle of Ca deposition. Red and blue curve in b show the different cathodic potential limits. (~286 nmol cm^{-2} Sb on Au and Surface area was 0.785 cm^2)

From the thermodynamic data for $CaSb_2$ alloy formation [6] $\Delta G = -225000 + 89.7T$ the calculated potential for $CaSb_2$ alloy formation at room temperature is ~ 1.05 V (vs. Ca). ($E(Ca_2Sb)$=0.54 V; $E(Ca_5Sb_3)$=0.64 V; $E(Ca_{11}Sb_{10})$=0.97 V) The experimental positive shift for the onset alloying of Ca with Sb adlayers is 1.0 V. Therefore, the experimental positive shift in the potential of Ca deposition during the alloying of Ca into Sb adlayers is in agreement with the theoretical value. In the case of the Ca plating and stripping on the pure Au electrode the

shoulder for the alloying formation was not observed. (Figure 7.1 a) In the anodic sweep a broad peak appeared in the potential range between 1.0 V and 2.0 V, we attributed this to the de-alloying of $CaSb_2$, and the Sb substrate formed again.

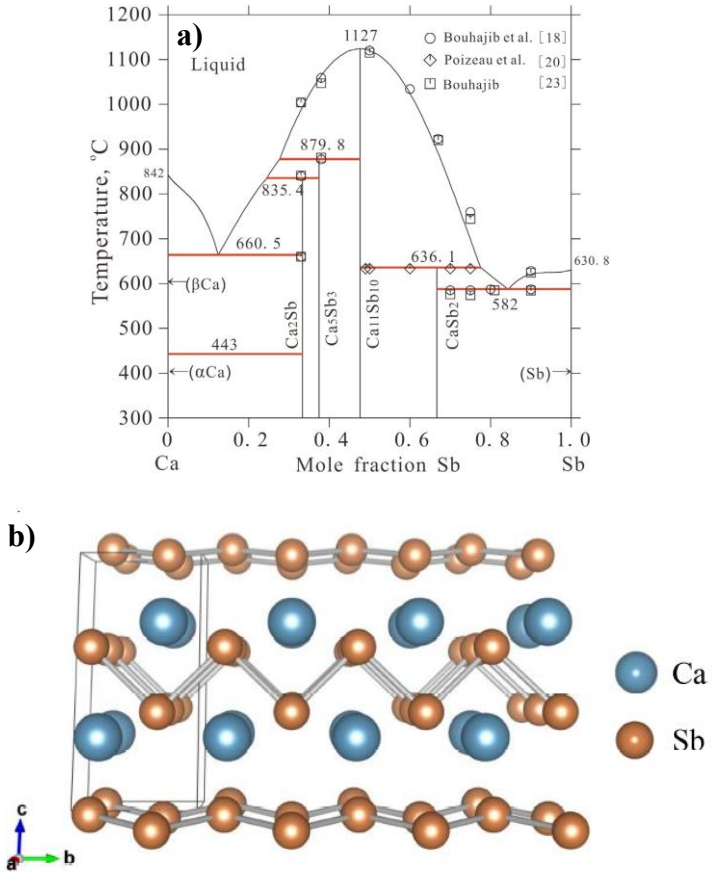

Figure 7. 2: a) Ca–Sb phase diagram. [6] and b) the crystal structure of $CaSb_2$. The $CaSb_2$ has a monoclinic structure belonging to the group $P2_1/m$. The density of $CaSb_2$ is 5.41 g/cm^3. [10]

After the saturation of the host layers, bulk deposition of Ca starts with the corresponding increase of the cathodic current, and bulk dissolution occurred at 0 V in the anodic direction. The coulombic efficiency of bulk deposition and dissolution in Fig 7.1 b was calculated to be 83 %, which is the same as the first cycle without Sb ad-layers. As opposed to bulk deposition on Au, the alloying process with Sb modified surface achieved 93 % reversibility even in the first cycle. (14.2 mC/cm^2 of the anodic peak at 1.2 V for de-alloying and 15.3 mC/cm^2 of the cathodic peak at 0.5 V for alloying in Fig 7.1b blue curve)

The amount of the deposited Sb and the inserted Ca in Sb (from the charge of the cathodic peak at 0.5 V) was calculated to be 286 nmol/cm^2 and 90 nmol/cm^2 (blue curve in Fig. 7.1b) and 180 nmol/cm^2 (red curve in Fig 7.1b) respectively according to the corresponding peak in the cyclic voltammograms. The ratio between the amount of the inserted Ca to the deposited Sb is thus 0.28 for blue curve and 0.5 for red curve (Ca:Sb). The theoretical value is 0.5 of Ca:Sb. However,

the coulombic efficiency of Ca alloying/de-alloying for the red curve in Fig. 7.1b is only 56.7 %, which could be result from the side reactions at the more negative potential between -0.05 V and 0.25 V vs. Ca. Therefore, the results from the blue curve in Fig. 7.1 b is more reliable. The $CaSb_2$ binary phase is the first thermodynamic stable compound in the Ca-Sb system. (See the phase diagram and the crystal structure in Fig 7.2) [6]

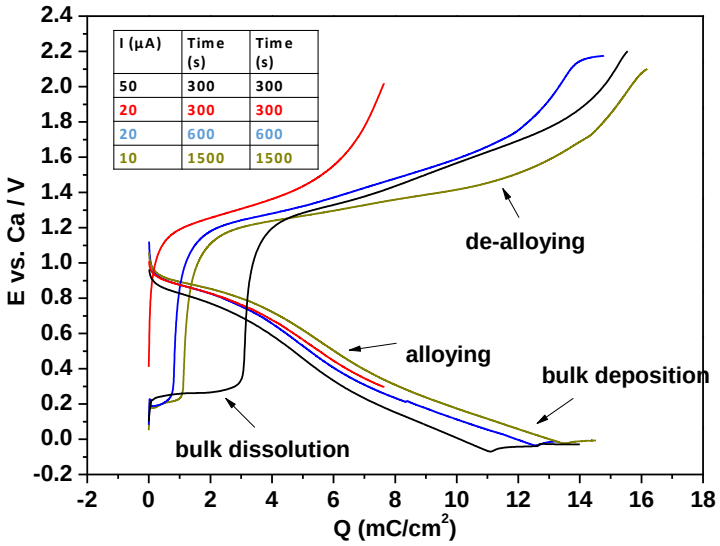

Figure 7. 3: Galvanostatic experiments of Calcium alloying and de-alloying with Sb modified Au electrode out of 1.5 M $Ca(BH_4)_2$/THF electrolyte. The applied current for each curve are shown in the figure. (~148 nmol cm^{-2} Sb on Au and Surface area was 0.785 cm^2)

Figure 7.3 shows similar results of galvanostatic experiments for calcium deposition in the same electrolyte comparing with the recorded CVs. The current (from 10 µA to 50 µA) was first applied with a negative value for Ca alloying and then with a positive value for Ca de-alloying. The Ca alloying starts at around 0.9 V and then give the shoulder until ~ -0.2 V for the Ca bulk deposition. With the positive applied current, the bulk dissolution takes place and then the Ca de-alloying occurs at about 1.3 V. The cut off potential is 2.2 V, because the Sb is slowly dissolved into the electrolyte above 2.2 V. The ratio of Ca: Sb was calculated to be 0.45 ($Ca_{0.9}Sb_2$) with 10 µA, which is similar to the theoretical value of 0.5 ($CaSb_2$)

These curves clearly show that the amount of achievable Ca alloying strongly depends on the current used. These curves also show that the currents in the CV are too high to achieve saturation. This effect is even clearer for de-alloying, which is another explanation for the low efficiency in the CVs of fig. 7.1b. It is also obvious that none of the others phases like Ca_2Sb mentioned above is formed because alloying is too slow. However, the sharper decrease of the potential at Q: 4 mC/cm^2 during alloying might indicate that this phase is formed at the surface. But diffusion of Ca into the bulk is too slow.

7.3.2 Determination of diffusion coefficient of Ca into Sb adlayers

a) CV

Figure 7.4 shows the cyclic voltammetry of calcium insertion into Sb adlayers with different sweep rates from 1 to 50 mV/s in the potential range between 0.23 V and 2.2 V vs. Ca. In this potential range, only calcium alloying takes place. (No calcium bulk deposition, comparing with Fig. 7.1b) The Sb layer was first freshly deposited on the Au polycrystalline. The amount of Sb was about 140 nmol/cm^2 (~40 mC). This experiment was starting at 50 mV/s, followed by lower sweep rates, and finally with a control experiment with 50 mV/s. The first experiment with 50 mV/s and the control experiment at the end show an identical form. Similar CVs for different sweep rates were observed. In the cathodic direction, the calcium alloying started at about 1.0 V vs. Ca for all sweep rates. The peak potential shifts to more positive values with decreasing sweep rates. This indicates that the calcium alloying into Sb adlayers is a kinetic (charge transfer) and diffusion-controlled process. In the anodic direction, the peak of calcium de-alloying is at 1.7 V vs. Ca at 50 mV/s and then shifted to less positive potential 1.5 V vs. Ca. The separation between the cathodic and anodic potentials indicates that the calcium ions diffuse slowly in the Sb adlayers.

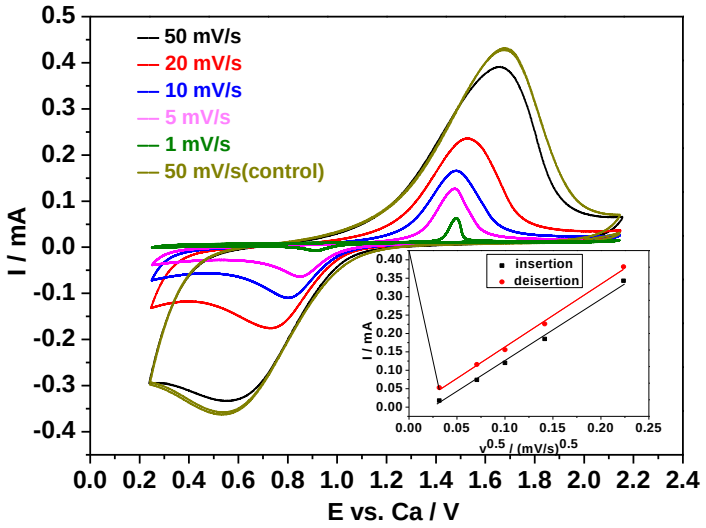

Figure 7. 4: Cyclic voltammograms of Ca alloying with Sb modified Au electrode in 1.5 M $Ca(BH_4)_2$/THF at different sweep rates from 1 to 50 mV s^{-1}. Insert: Plot of i_p (peaks current) vs. $\upsilon^{1/2}$ (square root of scan rate). AE: Sb on Au; CE and RE: Ca. (~140 nmol cm^{-2} Sb on Au and Surface area was 0.785 cm^2)

We can simply estimate the diffusion coefficient from the change of peak current with varying sweep rates assuming simple solid state diffusion as rate limiting using the Randles-Sevcik equation (for an irreversible system and semi-infinite diffusion) according to eq. (7.1) [11]:

$$I_p = 2.99 \times 10^5 n\sqrt{\alpha n_\alpha} A C_0 D_{Mg}^{0.5} v^{0.5} \quad (7.2)$$

C_0 the saturation concentration of Ca in $CaSb_2$ and drops to zero within the Sb layer (semi-infinite diffusion condition). From the slope in the insert of fig 7.4, we estimate a diffusion coefficient of 3.4×10^{-14} cm^2 s^{-1} with $\alpha n_\alpha = 0.5$ for Ca alloying.

The charges for Ca alloying and de-alloying, coulombic efficiency, and the ratio between alloyed Ca and deposited Sb at different potential sweep rates are shown in table 7.1. The ratio between the faradaic charge of anodic (de-alloying) and cathodic (alloying) gives the apparent coulombic efficiency. The amount of inserted calcium increases with decreasing the sweep rate (increasing the time of insertion). The apparent coulombic efficiency increases also with the time (92.5 % at the beginning and around 96 % at the end). We assume that the missing 6 % is due to the side reactions, such as decomposition of the solvent molecule, B and BH_3 co-deposition, and the electrolyte decomposition because of the low stability and high reactivity of the BH_4^- ion. The integrated charges of Ca alloying and de-alloying for 50 mV/s at the first step are similar to the control experiment at the end, which shows no change in the profile and no deactivation of the electrode surface. The ratio between the inserted Ca and the deposited Sb shows values from 0.22 to 0.48 for de-alloying and from 0.20 to 0.46 for de-alloying (the theoretical value is about 0.5 of $CaSb_2$).

Table 7. 1: The charges Ca alloying and de-alloying with Sb, coulombic efficient and the ratio between alloyed Ca and deposited Sb at different potential sweep rates.

υ (mV/s)	**Charge density (mC/cm^2) (cath.)**	**Charge density (mC/cm^2) (anod.)**	**Col. Eff. (%)**	**Ratio Ca:Sb alloying (de-alloying)**
50	5.94	5.50	92.5	0.22 (0.20)
20	7.94	7.49	94.3	0.29 (0.27)
10	9.02	8.47	93.9	0.33 (0.31)
5	11.84	11.25	95.1	0.44 (0.42)
1	13.08	12.57	95.9	0.48 (0.46)
50	6.11	5.82	95.2	0.23 (0.22)

b) Potential steps

In potential step experiments, the potential was first held at 1.8 V (where de-alloying of Ca with Sb takes place) in 1.5 M $Ca(BH_4)_2$/THF electrolyte. The amount of deposited Sb on Au polycrystalline is about 140 $nmol/cm^2$. Afterwards, the potential was stepped to several alloying

potentials (from 0 to 0. 8 V vs. Ca), at which calcium could be inserted into the Sb layer, for 1, 2, and 5 min. Then the potential was stepped back to 1.8 V, where the extraction of calcium takes place. In Figure 7.5 the potential step experiment of Ca alloying with Sb for 1, 2, and 5 mins out of a 1.5 M $Ca(BH_4)_2$/THF electrolyte from 0 V to 0.8 V with an increment of 0.2 V respectively are shown. Directly after the double-layer charging, the current drops nearly linearly for the first 5 s of the 5 min alloying cf. black solid line in Fig. 7.5 and then decreases more slowly until the current reaches zero. These current profiles for Ca alloying with Sb are different from those for Mg alloying with Sb. There, the current was first slightly increasing and then stayed constant at the beginning in case of the Mg alloying with Sb.

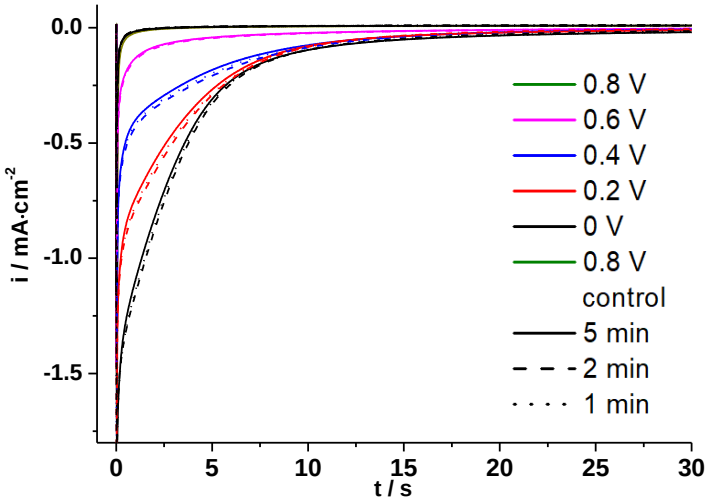

Figure 7. 5: Potential step experiment for Ca insertion from 1.5 $Ca(BH_4)_2$/THF electrolyte into Sb modified Au electrode at different potentials for 1, 2, and 5 min: The potential of insertion are from 0 V to 0.8 V vs. Ca with an increment of 0.2 V. AE: Sb on Au: CE and RE: Ca. (~140 nmol cm^{-2} Sb on Au and Surface area was 0.785 cm^2)

Figure 7.6 shows the recorded current transients for Ca de-alloying with different de-alloying times. The current transients show different shapes than those during Ca alloying. The current decreases first slowly after the double layer charging (for example the first 3 s of the red curve in fig. 7.6) and then decreases fast. Thus, the de-alloying of Ca with Sb is controlled by both charge transfer and diffusion.

The charges for alloying and de-alloying of calcium, the ratio between the alloyed Ca and the deposited Sb, and the calculated diffusion coefficient are summarized in table 7.2. The integrated charges of Ca alloying and de-alloying increase with the decrease of the alloying potential (Increase of the alloying time) as respected. The ratio between the alloyed Ca and the deposited Sb is about 0.42 for alloying at 0 V vs. Ca of 5 min. The theoretical value is 0.5 in

the case of $CaSb_2$ binary phase. The experimental value is a little less than the theoretical value because the alloying is very slow and the alloying time is not enough in comparison with the ratio (0.48) with 1 mV/s which was shown in Fig. 7.3 and Tab. 7.1. However, this value also indicated that the phase $CaSb_2$ could be formed during the alloying with Sb and the Sb layers will be reformed during the de-alloying. The coulombic efficiencies were calculated to be 91.5 % and 98.2 %, which are similar to the efficiencies estimated by CVs (95 %) in Fig. 7.3.

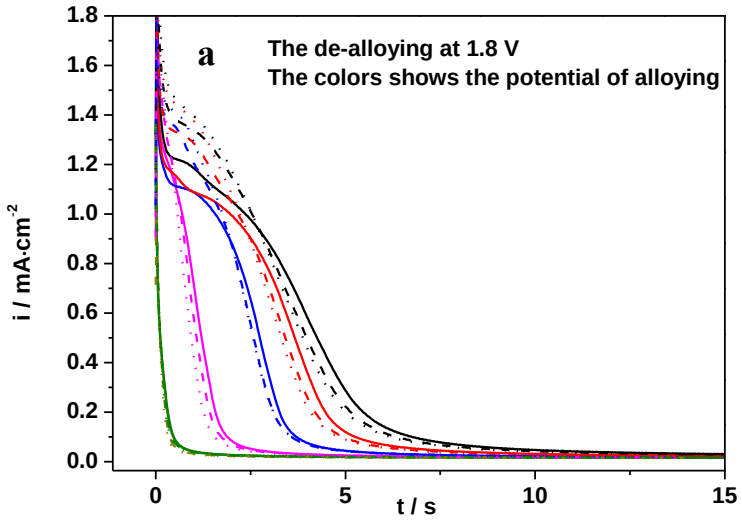

Figure 7. 6: Potential step experiment for Ca de-alloying from 1.5 $Ca(BH_4)_2$/THF electrolyte into Sb modified Au electrode at 1.8 V vs. Ca. AE: Sb on Au: CE and RE: Ca. (~140 nmol cm^{-2} Sb on Au and Surface area was 0.785 cm^2)

Here, we attribute the linear relationship between the current and the square root of time at the beginning for Ca alloying to a kinetic and diffusion controlled process, which could be explained by the following equation:

$$i = i_{CT} - \frac{2i_{CT}}{nFC_0\sqrt{\pi}\sqrt{D}} \cdot \sqrt{t} \qquad (7.3)$$

Where i is the current density, i_{CT} is the charge transfer current which is determined by the kinetic; F is faraday`s constant; z is the electron transfer number; C_0 is the saturated concentration of Ca in $CaSb_2$; t is the time; D is the diffusion coefficient of Ca.

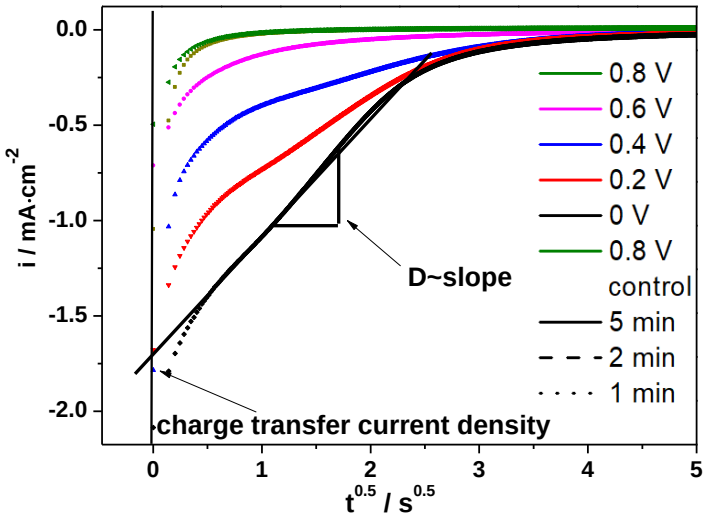

Figure 7. 7: Plot of transient current density (i vs.$\sqrt{t}$) for Ca alloying at different potentials (from 0 V to 0.8 V vs. Ca) with the time of 5 min into Sb layers. The charge transfer current density could be got from the extrapolation of the linear fitting with the axis. (Sb: ~140 nm/cm^2; surface area: 0.785 cm^2)

Table 7. 2: Dependence of Ca alloying/de-alloying integrated charges during the potential step experiments on potential of insertion, the corresponding coulombic efficiencies, the ratio between Ca and Sb , the estimated diffusion coefficient and the value of C$\sqrt{D}$.(~140 nmol cm^{-2} Sb on Au and Surface area was 0.785 cm^2) The experiment has been done first at all potentials from 0.8 V to 0 V for 1 min alloying and de-alloying and then at all potentials from 0.8 V to 0 V for 2 min alloying/de-alloying and finally at all potentials from 0.8 V to 0 V for 5 min alloying/de-alloying.

Potential (V vs. Ca)	**Charge density (mC/cm^2) alloying (de-alloying)**			**Ratio of Ca:Sb for alloying and (de-alloying)**			**D (cm^2/s) (/10^{-13}) (calculated with C$_0$)**	**C$\sqrt{D}$(/10^{-9})**
	1 min	2 min	5 min	1 min	2 min	5 min	Average of 3 different times	Average of 3 different times
0.8	0.76 (0.66)	0.82 (0.77)	2.95 (2.77)	0.03 (0.03)	0.04 (0.04)	0.11 (0.10)	0.15	2.35
0.6	2.11 (1.98)	2.65 (2.42)	4.87 (4.55)	0.08 (0.08)	0.10 (0.09)	0.18 (0.17)	0.33	3.51
0.4	4.21 (3.94)	4.97 (4.56)	7.13 (6.81)	0.16 (0.15)	0.18 (0.17)	0.26 (0.25)	0.54	4.42
0.2	5.57 (5.47)	6.37 (5.88)	9.24 (8.55)	0.21 (0.20)	0.24 (0.23)	0.34 (0.33)	0.95	5.86
0	7.26 (6.81)	8.13 (7.44)	11.4 (10.9)	0.27 (0.25)	0.30 (0.28)	0.42 (0.40)	1.30	6.85

We can estimate the diffusion coefficient from the slope of the linear part of the curve if we plot the current density versus the square root of time. Figure 7.7 shows the plot of current density versus the square root of time. The current drops linearly after the double-layer charge until the diffusion layer of the Ca ions reaches the limit thickness of the Sb-adlayers. At this time (about 4 s in Fig. 7.7) the shape of the current transient changes, which is different from the current transient within an infinite diffusion layer. There, the current drops linearly with $\sqrt{t}$ before becoming more flat due to pure diffusion limitation. Thus, the diffusion coefficient should be estimated before the changing of the current. The slope for calculation of the diffusion coefficient at 0 V is also shown in Figure 7.7 b. The charge transfer current density could be estimated by extrapolation of the linear fitting.

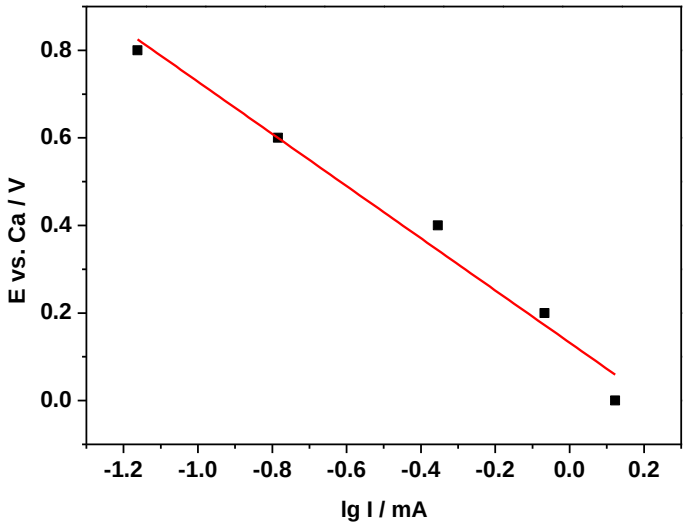

Figure 7. 8: Tafel plot of the overpotential versus the limited current for each jump potential.

In Figure 7.8 the Tafel plot of the overpotential versus the limited current is shown for each jump potential. From the linear fitting, the Tafel slop could be determined to be 352 mV/disc, this value is higher than the usual value for kinetically controlled charge transfer, which is 120mV/div. Certainly also the potential dependence of the equilibrium alloy composition plays a big role. This value of Tafel slope is equivalent to 0.34 electron transfer, which means that the Mg ion with 1.6 positive charges is transferred in the layers (together with counter ions) before the alloying and appear only shortly at the interface on the Sb layers. So, the value of αn_α can be corrected to be 0.162, which should be used instead of 0.5 for the calculation of the diffusions coefficient in the Randles-Sevcik equation. With $\alpha n_\alpha = 0.17$ the diffusion coefficient was calculated to be 1.0×10^{-13} cm^2/s. Thus, the diffusion coefficient estimated from the CVs and the potential experiment is comparable.

c) PITT-Measurement (Potentiostatic Intermittent Titration Technique)

The experiment starts by recording the OCP of this system. Then, a step composed of 30 s pulse at the potential 0.8 V vs. Ca (where the insertion of Ca takes place), followed by 30 s of relaxation with the cell switched off is applied. Afterwards, a negative potential increment of -0.1 V vs. Ca is applied on the previous potential, and the current signal is recorded for 30 s, followed by 30 s of relaxation time. The same potential increment is consecutively applied, starting from the voltage resulting from the previous step and the signal is recorded for 30 s. The potential pulses are applied until the lower limit of 0 V vs. Ca is reached, where bulk deposition of Ca starts. Each potential pulse is followed by 30 s of relaxation time. Afterwards, from 1.0 V vs. Ca positive potential increments of 0.1 V are consecutively applied to the voltage resulting from the previous step, and the signal is also recorded for 30 s. The potential pulses are repeated until the upper limit of 1.8 V is reached. Each potential pulse is followed by 30 s of relaxation time.

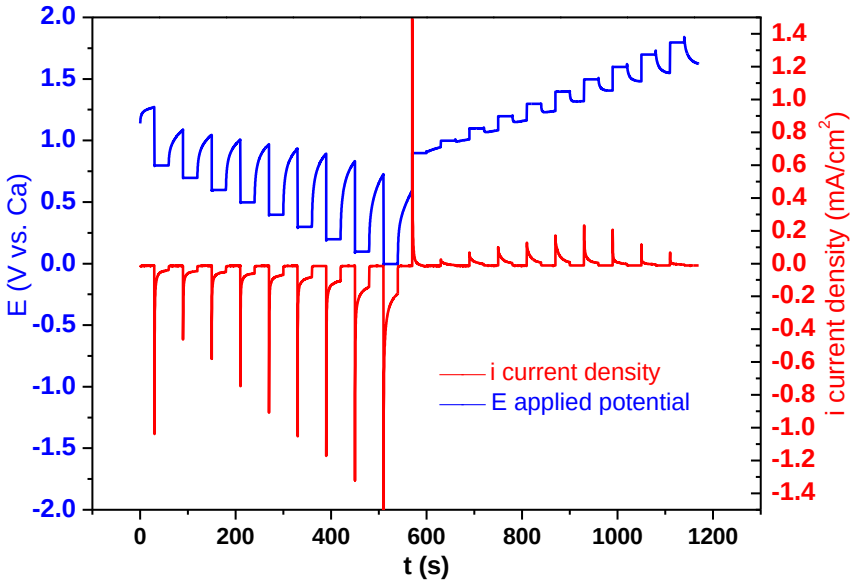

Figure 7. 9: Potentials and relative current Curve from the PITT-measurement to determine the diffusions coefficient of Ca-alloying and de-alloying with the Sb-adlayers. Potential from 0.8 V to 0 V vs. Ca for the alloying and from 1.0 V to 1.8 V for the de-alloying. (Sb: 310 nmol/cm^2; surface area: 0.785 cm^2)

During the negative potential pulses, Ca-ions are alloyed with the Sb-modified negative electrode. The reverse occurs during the positive discharging potential pulses, where the Ca-ions are de-alloyed from the negative electrode, and the corresponding current is recorded (Fig. 7.10). During each relaxation period, the cell is switched off. Then, at the beginning of each

potential pulse, a peak in the current signal is observed. Afterward, the value of the current signal decreases in an exponential like fashion.

The sum of charge density for each step of Ca alloying and de-alloying from PITT and the ratio between Ca and Sb are summarized in Table 7.4. The charge density of each step for alloying and de-alloying increased. The sum charge density for Ca alloying is 32.6 mC/cm^2 and the ratio of Ca:Sb is 0.54, which indicated the formation of $CaSb_2$ phase during the alloying process. However, the charge density of each step and the sum charge density for Ca de-alloying is much less than Ca alloying. The ratio of Ca:Sb is only 0.22 for Ca de-alloying, which is also much less than the theoretical value of 0.5. ($CaSb_2$). It is assumed that during the relaxation there is always a residual current. It means that the alloyed Ca ions is de-alloyed during the relaxation. Nevertheless, the diffusion coefficient from the Ca alloying by the PITT experiment can be determined. We plot also here Q^2 vs t for estimating the diffusion coefficient (Figure 7.11 b), since the current do not drop linearly in the plot of i vs $t^{0.5}$. (Figure 7.11 a) Obviously, there is no kinetic charge transfer limitation. The reason is that de-alloying is done at a very positive potential, where the charge transfer rate is very fast. The values of the diffusion coefficients by each step are also summarized in Table 7.4.

Table 7. 3: Dependence of Ca alloying/de-alloying integrated additive charges during the PITT experiments, the ratio between Ca and Sb, the estimated diffusion coefficient and the value of $C\sqrt{D}$ (~310 nmol cm^{-2} Sb on Au and Surface area was 0.785 cm^2)

Ca alloying					**Ca de-alloying**		
Potentials (V vs. Ca)	**Charge density (sum) (mC/cm^2)**	**Ratio Ca:Sb**	**D (/10^{-14} cm^2/s)**	**$C\sqrt{D}$(10^{-9})**	**Potentials (V vs. Ca)**	**Charge density (sum)(mC/cm^2)**	**Ratio Ca:Sb**
0.8	2.16	0.03	0.12	0.66	1.0	2.29	0.04
0.7	3.82	0.06	0.28	1.00	1.1	2.93	0.05
0.6	5.73	0.10	1.12	2.01	1.2	3.95	0.07
0.5	8.02	0.13	1.87	2.60	1.3	5.35	0.09
0.4	10.7	0.18	2.09	2.75	1.4	7.26	0.12
0.3	13.9	0.23	3.86	3.73	1.5	9.68	0.16
0.2	18.0	0.30	5.25	4.35	1.6	11.2	0.19
0.1	23.9	0.39	6.03	4.67	1.7	12.2	0.20
0	32.6	0.54	8.69	5.60	1.8	13.0	0.22

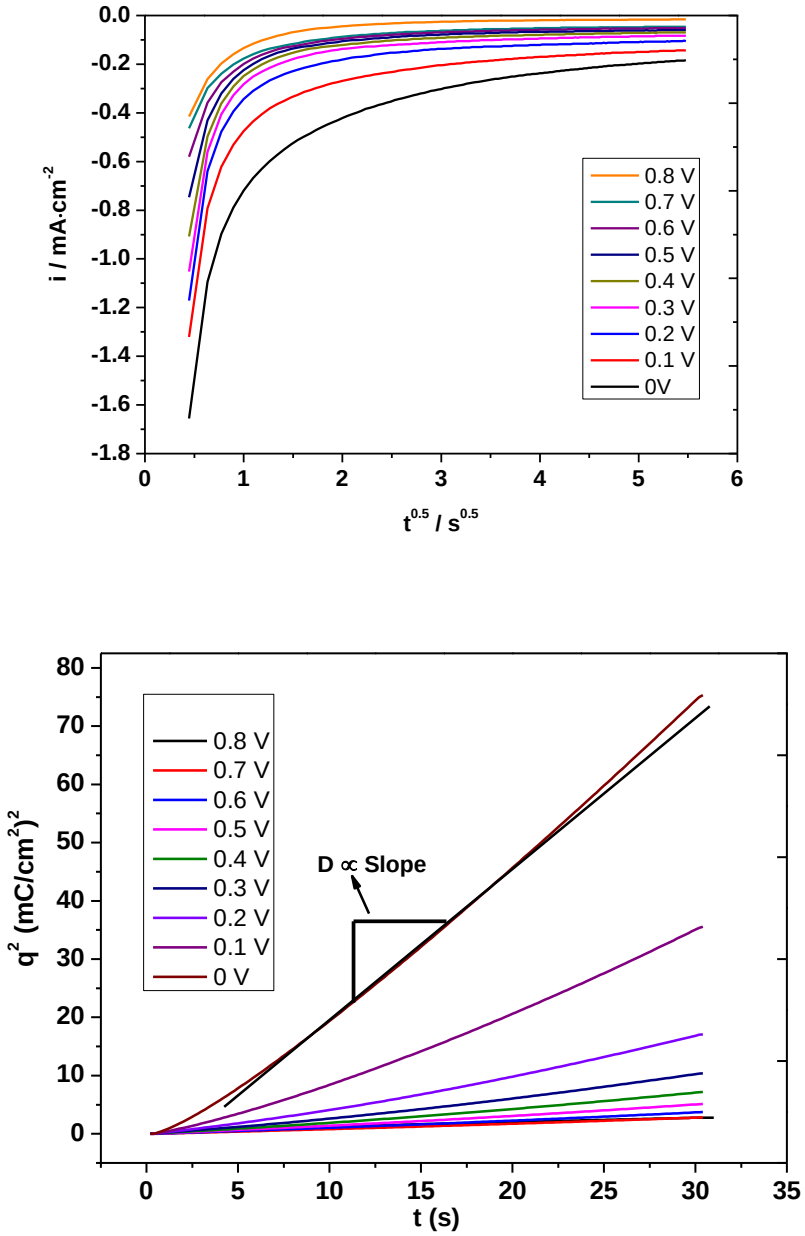

Figure 7. 10: a) Plot of the i vs. $t^{0.5}$ and b) Plot of Q^2 vs t for the Ca alloying process to calculate the diffusion coefficient. Where the signal becomes linear, the linear regression tool allows the diffusion coefficient calculation. In this figure only an example is shown for calculation of the diffusion coefficient by 0 V vs. Ca. (~310 nmol cm^{-2} Sb on Au and Surface area was 0.785 cm^2)

The diffusion coefficient determined from variation of the sweep rates from 50 to 1 mV/s of CVs were estimated to be 3.4×10^{-14} cm^2 s^{-1} with $\alpha n_\alpha = 0.5$ and 1.0×10^{-13} cm^2 s^{-1} $\alpha n_\alpha = 0.17$ for alloying in the Sb modified electrode. Assuming the concentration of calcium in the antimony layers from the experiment with different jump potentials from 0 V to 0.8 V, the calculated diffusion coefficient is from 3.93 x 10^{-14} to 1.3×10^{-13} cm^2 s^{-1} . The diffusion

coefficients estimated by PITT method show the values of 0.12×10^{-14} to 8.69×10^{-14} cm^2 s^{-1}.

The values of diffusion coefficient from PITT are similar as the estimated value from PITT measurements for Mg diffusion into porous Sb electrode in MACC/TG electrolyte and lower than the calculated value from CVs results. This discrepancy in the diffusion coefficient values may be due to the difference in the time of relaxation of Ca into electrodeposited Sb. In the cyclic voltammetry, the relaxation time after the insertion is not enough to get a stable profile with homogenous distribution of Ca in the whole layers of Sb. Consequently, during the stripping process, there is a competition between the continuous distribution of Ca especially in the deep layers and the extraction of Ca from the outer layers. In potential step experiments for 5 min was not enough to relax the Ca in the antimony layers and to obtain a constant concentration of Ca everywhere.

7.4 Conclusions

The thin antimony layer was first deposited on Au in 0.5 M H_2SO_4 containing 0.25 mM Sb_2O_3 by cyclic voltammetry. Calcium deposition/dissolution on Au and Sb modified Au electrodes were investigated in 1.5 M $Ca(BH_4)_2$ in THF electrolyte. Interestingly, at the Sb modified Au electrode, a pre-cathodic peak started at around 1.0 V (vs. Ca/Ca^{2+}), which is 1.0 V more positive than the onset potential of bulk deposition at the Au electrode. It is suggested that this pre-cathodic peak is related to the alloying of Ca with Sb adlayers to form $CaSb_2$ alloy since the ratio of the amount of the alloyed Ca to that of the deposited Sb calculated from the corresponding peak charge is close to the theoretical value of 1:2 for $CaSb_2$ formation. High coulombic efficiencies of Ca stripping/insertion have been observed in cyclic voltammetry and potential step experiments.

Furthermore, the kinetics was investigated by the potential step and PITT experiments. It has been found that the alloying process was first determined by charge transfer and diffusion of Ca ions. The diffusion coefficient of Ca in Sb multilayers was estimated from CV and potential step experiments to be $0.9\text{-}1.3\times10^{-13}$ cm^2s^{-1} respectively, which is, higher than the Mg alloying with Sb from our work in the previous chapter and in the literature. [12, 13] This value is two orders of magnitude lower than the value for Li^+ ions from our work.

References

[1] Z. Yao, V. I. Hegde, A. n. Aspuruâ€Guzik, C. Wolverton, *Advanced Energy Materials* **2019**, *9*, 1802994.

[2] G. Srinivas, C. A. Howard, N. T. Skipper, S. M. Bennington, M. Ellerby, *Physica C-Superconductivity and Its Applications* **2009**, *469*, 2000.

[3] N. Emery, C. Herold, M. d'Astuto, V. Garcia, C. Bellin, J. F. Mareche, P. Lagrange, G. Loupias, *Physical Review Letters* **2005**, *95*, 4.

[4] A. Ponrouch, C. Frontera, F. Barde, M. R. Palacin, *Nature Materials* **2016**, *15*, 169.

[5] T. Ouchi, H. Kim, X. H. Ning, D. R. Sadoway, *Journal of the Electrochemical Society* **2014**, *161*, A1898.

[6] S. Qin, S. H. Liu, C. Zhang, J. H. Xin, Y. Wang, Y. Du, *Calphad-Computer Coupling of Phase Diagrams and Thermochemistry* **2015**, *48*, 35.

[7] D. Wang, X. Gao, Y. Chen, L. Jin, C. Kuss, P. G. Bruce, *Nature Materials* **2017**, *17*, 16.

[8] A. Shyamsunder, L. E. Blanc, A. Assoud, L. F. Nazar, *ACS Energy Letters* **2019**, *4*, 2271.

[9] Z. Li, O. Fuhr, M. Fichtner, Z. Zhao-Karger, *Energy & Environmental Science* **2019**.

[10] K. Funada, A. Yamakage, N. Yamashina, H. Kageyama, *Journal of the Physical Society of Japan* **2019**, *88*, 5.

[11] A. J. Bard, L. R. Faulkner, *Electrochemical Methods: Fundamentals and Applications*, 2nd ed., John Wiley & Sons Inc., New York, Weinheim, **2001**.

[12] M. Stromme Mattsson, *Solid State Ionics* **2000**, *131*, 261.

[13] M. D. Levi, G. Salitra, B. Markovsky, H. Teller, D. Aurbach, U. Heider, L. Heider, *Journal of The Electrochemical Society* **1999**, *146*, 1279.

Chapter 8: Calcium Deposition and Alloying with Bi on Au Electrode

8 .1 Introduction

Bismuth electrodes as anode for rechargeable batteries have been of great interest in recent years. Several Mg-salts such as MACC, $Mg(TFSI)_2$, and $Mg(BH_4)_2$ in organic solvent (DG, TG, THF, MeCN, and so on…) with Bi anode have been investigated for rechargeable magnesium batteries. [1-3] [4] [5-7] All the results shown in literature and in our work demonstrate high coulombic efficiency, high reversibility and high reversibility with Bi anode. The mobility of Mg ions in the Bi electrode was calculated and estimated to be high due to the low migration barrier of 0.34 eV for Mg diffusion in Mg_3Bi_2 and the activation barrier of 1.46 eV for the reaction of Mg with Bi. [7] [6] Since the Ca ions with their less polarizing character should have a higher mobility than Mg ions, [8] the Bi anode could be an alternative for the rechargeable calcium batteries. The Ca-Bi alloy has also been studied by DFT and suggested for use as a negative electrode.

The Ca-Bi alloy has been investigated for thermal batteries by Kim et al. in 2013. [9] The operation temperature is lower by using Ca-Bi alloy at 500-700 ℃ with a molten electrolyte. It shows high reversibility with high exchange current densities of 200 mA/cm^2 between 0.8 and 1.0 V vs. Ca and sufficiently high coulombic efficiencies around 98 %. The formed intermetallic was found to be $Ca_{11}Bi_{10}$ at the electrode-electrolyte interface.

The thermodynamic properties of Ca-Bi alloys were determined by electromotive force measurements. [10] Several types of alloys such as $CaBi_2$, $Ca_{11}Bi_{10}$, and Ca_5Bi_3 are shown in the phase diagram. (Fig. 13.2) The crystal structure of $CaBi_2$ phase was first reported by Merlo and Fornasini, [11] which belongs to group Cmcm in an orthorhombic lattice. Bi atoms are arranged in two different planes in the crystal structure of $CaBi_2$: one is made by a stacking of Bi(1) square and the second is Bi(2)-Ca corrugated square net. The Ca atoms form a tetrahedral, which is centred around Bi(1) atoms. (See Fig. 13.3) This alloy was also found to be a superconductor with a transition temperature $Tc = 2.0$ K. This kind of compound with layer structure could be used as a negative electrode for the batteries. During the charge and discharge, the reversible insertion and de-insertion will take place with structural change.

There are several determining processes such as capacity, redox voltage, and diffusion rates (kinetics and thermodynamics) for the Ca alloying/de-alloying. One of the major challenges is the limited mobility of Ca^{2+} ions. A good ionic diffusion for battery electrode materials was

reported to be 10^{-12} cm^2/s. There is no reported literature direct corroding to the measurements of diffusion coefficients.

In this work, we study the alloying of Ca into multilayers of Bi on polycrystalline Au and single-crystal Au (111) using non-aqueous electrolyte (1.5 M $Ca(BH_4)_2$ in THF) at room temperature. The cycling reversibility of alloying/de-alloying will be demonstrated. During the discharge, the formation of $CaBi_2$ occurs, and the substrate structure will be then formed again during the charging process. The kinetics of the Ca ions diffusion was studied and the diffusion coefficients were estimated by cyclovoltamogramm and potential steps experiments.

8.2 Experimental

Chemicals, materials and electrolyte

All aqueous electrolytes were prepared by 18.2 MΩ from Milli-Q water and de-aerated with high purity argon gas for at least 15 min before use. Electrochemical measurements in 0.1 M H_2SO_4 (Spectro pure grade) were implemented in a conventional three-electrode glass cell. Au sheet 1 cm^2 and RHE are used as a counter electrode and a reference electrode respectively. The electrochemical deposition at an Au working electrode was done in 1 mM Bi_2O_3 (99.999%, Aldrich) + 0.5 M $HClO_4$ electrolyte for Sb deposition;

A polycrystalline Au electrode and a bismuth modified Au electrode were used as working electrodes for Mg deposition and alloying measurements. Magnesium wire was then used as a counter electrode and another one as a quasi-reference electrode. All the calcium electrochemical deposition measurements were carried out in the MBraun glovebox (H_2O < 0.5 ppm, O_2 < 0.5 ppm).

Preparation of 1.5 M $Ca(BH_4)_2$ in THF

Calcium borohydride bis (tetrahydrofuran) ($Ca(BH_4)_2 \cdot 2THF$) was purchased from Sigma-Aldrich. Extra dry tetrahydrofuran (THF, <5 ppm) was produced from the inorganic institute at the University of Bonn and stored several days over molecular sieves (4Å, Aldrich). The calcium metal (purity 99.99 %) was achieved from the project partner ZSW Ulm. The salt was first dissolved in THF overnight and a clear solution was obtained. (10 ppm) The preparation of the solution was made and all materials were stored in the MBraun glovebox (H_2O < 0.5 ppm, O_2 < 0.5 ppm).

Cyclic Voltammogram (CV)

Electrochemical measurements (Bi deposition on Au and Ca deposition including alloying) were carried out in a conventional three-electrode glass H-cell consisting of three compartments for fixing the working electrode, reference electrode, and counter electrode. The working electrode is placed in the central compartment and contacted with a solution in a hanging meniscus configuration. The reference electrode is placed in the compartment where it is connected to the central compartment with a Luggin capillary. The counter electrode is placed in the compartment, separated from the central compartment by a glass frit.

All electrochemical measurements were carried out using a potentiostat purchased from Pine Instruments, Inc. (model AFBPC1) in combination with home-made LabVIEW program (National Instruments GmbH, Munich, Germany) for recording the cyclic voltammograms (CVs)

8.3 Results and Discussion:

8.3.1 Ca deposition and alloying on Bi-modified Au-Electrode in $Ca(BH_4)_2$ in THF Electrolyte

Bi was first freshly deposited on Au electrode and then transferred to the glovebox under inert atmosphere. (Modification of Au by Bi as described in previous chapter 6) Fig. 8.1 shows the comparison of electrochemical deposition and stripping behavior of Ca at a bare gold electrode and Bi-modified gold electrode in 1.5 M $Ca(BH_4)_2$ in THF. A stable CV of the calcium deposition on the bare poly-crystalline Au electrode is shown in Fig 8.1 a. The calcium bulk deposition started at about -0.2 V vs. Ca/Ca^{2+} in the cathodic sweep, and in the anodic direction, the current is still negative in the potential range of -0.6 V to 0 V vs. Ca/Ca^{2+} and afterwards a bread peak for calcium dissolution starts at 0 V vs. Ca/Ca^{2+}. (The potential of 0 V vs. Ca has been corrected since the Ca reference electrode is varies from day to day.) (Fig.8.1 a) The coulombic efficiency, which was calculated from the charge of the deposition divide by the charge of dissolution to be 97%.

On Bi-modified gold electrode the Ca deposition occurs already 1.0 V more positive, giving rise to a shoulder we attribute this to the alloying of Ca with the Bi-adlayer and formation of binary phase $CaBi_2$ according to the following equation:

$$2Bi + Ca^{2+} + 6e^{-} \rightarrow CaBi_2 \qquad (8.1)$$

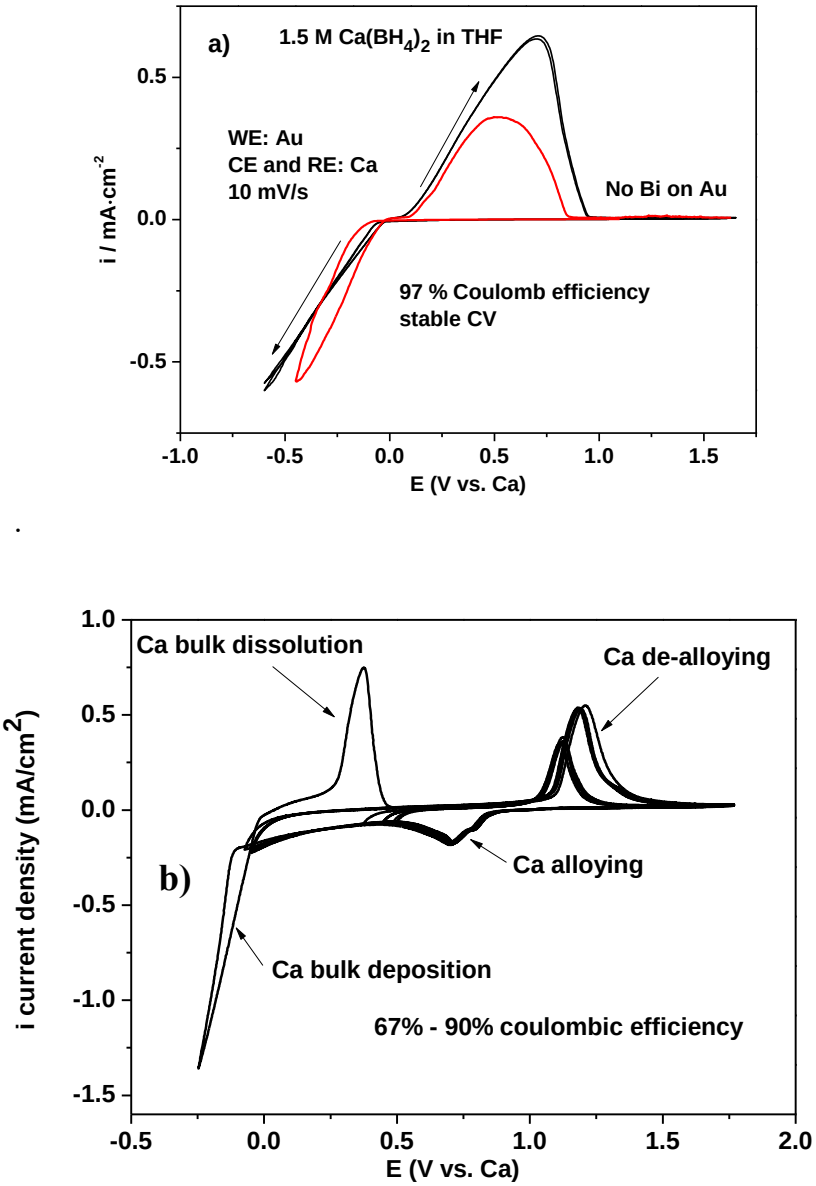

Figure 8. 1: Cyclic voltammograms of Ca deposition/dissolution at bare Au-electrode (a) and Bi modified Au-electrode (b) in 1.5 M $Ca(BH_4)_2$/THF at the sweep rate of 10 mV s^{-1}. Ca alloying/de-alloying at Bi modified electrode in the potential range of -0.8 V to 1.5 V vs. Ca/Ca^{2+}. Red curve in figure a shows the first cycle of Ca deposition. The 0 V vs. Ca in figure b was corrected by taking the value of the cross from x and y axis. WE: Au and Bi modified Au; CE and RE: Ca. (~34 nmol cm^{-2} Bi on Au and Surface area was 0.785 cm^2)

From the thermodynamic data for $CaBi_2$ alloy formation [13, 14], the calculated potential for $CaBi_2$ alloy formation at room temperature is ~ 0.95 V (vs. Ca). (Here, the enthalpy and entropy of $CaBi_2$ at 542 K and the temperature of 298 K were used for calculation.) Therefore, the experimental positive shift in the potential of Ca alloying is in agreement with the theoretical value. The phase diagram and the crystal structure are shown in Figure 8.2 and Figure 8.3 respectively.

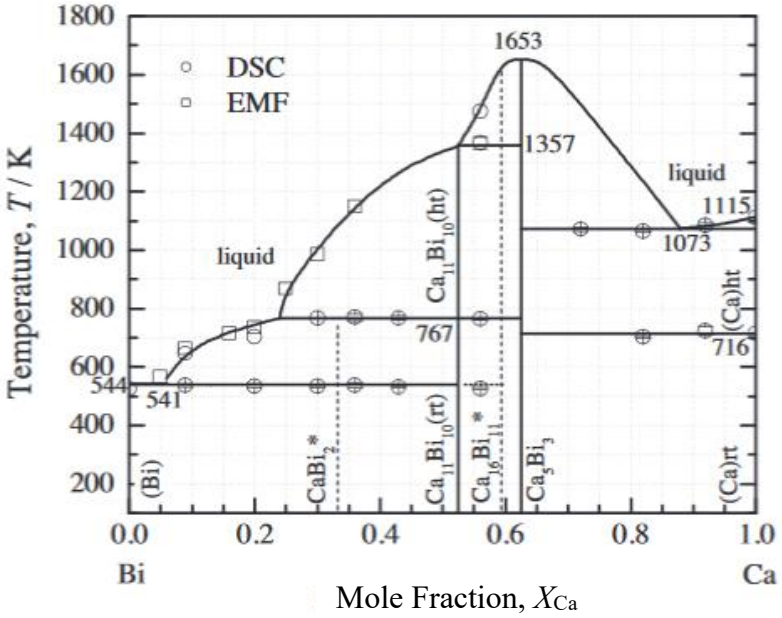

Figure 8. 2: Ca-Bi phase diagram. [10]

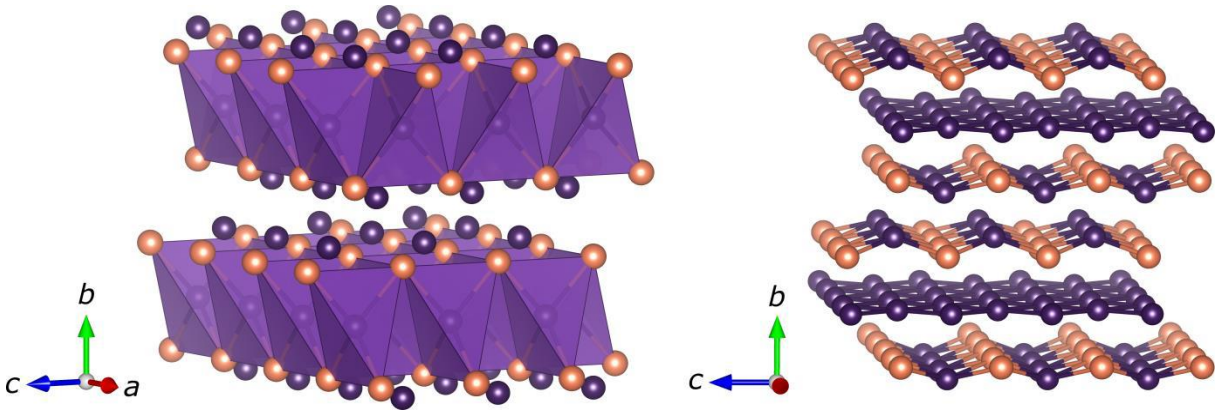

Figure 8. 3: The $CaBi_2$ crystal structure. Calcium and bismuth atoms are represented by orange and violet balls, respectively. [12]

In the anodic going sweep, the de-alloying peak occurs at 1.1 V vs. Ca when the potential was reversed at 0 V vs. Ca before the bulk deposition. When the sweeping potential was reversed at about 0.5 V vs. Ca, the de-alloying peak occurs at 1.0 V vs. Ca, which is 100 mV (less overpotential) negative than the above one. The coulombic efficiencies, calculated from the charges of Ca alloying/de-alloying, have shown the value of 90 % for reversed the sweeping potential at 0.5 V in comparison with 67 % for reversed sweeping potential at 0 V. We attribute this to the side reactions which were arising at the potential between 0 V and 0.5 V vs. Ca.

The amount of the deposited Bi and the alloyed Ca in Bi was calculated to be 34.5 and 5.28 nmol/cm^2 (from the charge of the cathodic peak between 0.5 V and 0.9 V) as well as 9.43

nmol/cm^2 (from the charge of the cathodic peak between 0 V and 0.9 V). The ratio between the amount of the alloyed Ca to the deposited Bi (Ca: Bi) is thus 0.15 for reversed sweeping potential at 0.5 V and 0.26 for reversed sweeping potential at 0 V, which is lower than the theoretical value of 0.5 for the formation of the $CaBi_2$ phase during the insertion process. The reason is that the diffusion of Ca^{2+} ions in the Bi adlayers is very slow, the alloying time here (10 mV/s) was not enough for saturation of the Ca atoms in Bi adlayers.

8.3.2 Determination of diffusion coefficient of Ca into Bi adlayers

a) CV

Fig. 8.4 shows the cyclic voltammograms of a Bi modified Au electrode (~34 nmol/cm^2 Bi on Au) in 1.5 M $Ca(BH_4)_2$/THF at different sweep rates from 50 μV/s to 10 mV/s in the potential range of 0.4 to 1.6 V vs. Ca. In the cathodic sweep, a small shoulder is observed at the potential of 0.8 V vs. Ca. (C1 in Fig. 8.4 a) Possibly this small shoulder belongs to the another phase of the Ca-Bi intermetallic compound or surface phase which is formed during the alloying of Ca with Bi at the beginning. The ratio of Ca: Bi for this shoulder calculated to be 0.125 from the charge of C1 (0.68 mC/cm^2) for 50 µV/s. So the exact phase of Ca-Bi formed in this shoulder is not clear in this case.

From cyclic voltammetry, we can simply estimate the diffusion coefficient from the change of peak current with varying sweep rates assuming simple solid-state diffusion as rate-limiting using (8.2) (the Randles-Sevcik equation for an irreversible system and semi-infinite diffusion [15]:

$$I_p = 2.99 \times 10^5 n\sqrt{\alpha n_\alpha} A C_0 D_{Ca}^{0.5} v^{0.5} \quad (8.2)$$

Here, I_p is the peak current in amps (A); n is the number of electrons transferred in the reaction ($2e^-$ for Ca^{2+}); A is the apparent surface area of the working electrode (0.785 cm^2); D_{Ca} is the diffusion coefficient of Ca (cm^2 s^{-1}) in Bi; υ is the sweep rate (V s^{-1}); C_0 is the concentration of Mg (theoretically, 0.016 mol cm^{-3}) in the solid state. For this equation to hold, it is assumed that during deposition the concentration of Ca drops to zero within the Bi layer (semi-infinite diffusion condition).

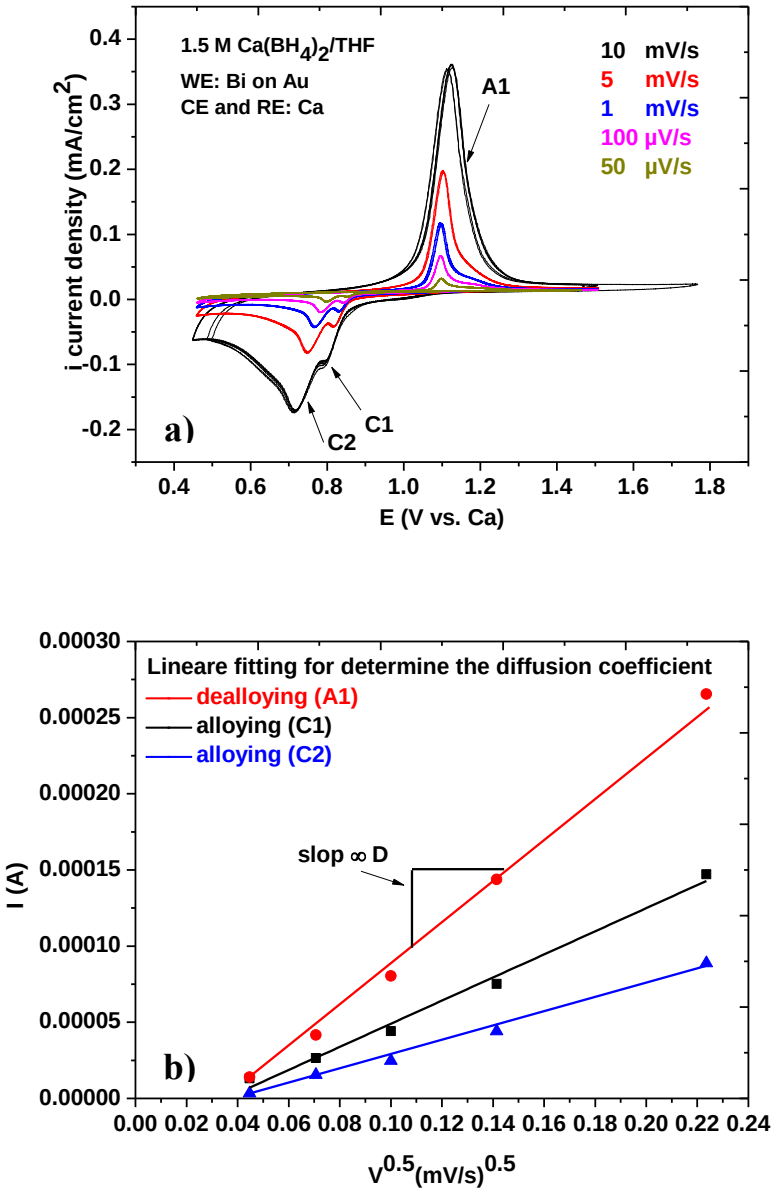

Figure 8. 4: a) Cyclic voltammograms of Ca alloying with Bi modified Au electrode in 1.5 M $Ca(BH_4)_2$/THF at different sweep rates from 50 µV/s to 1 mV/s. b): Plot of i_p (peaks current) vs. $\upsilon^{1/2}$ (square root of scan rate). The slop of the linear fitting is used for determining the diffusion coefficient. WE: Au and Bi modified Au; CE and RE: Ca. (~34 nmol cm^{-2} Bi on Au and Surface area was 0.785 cm^2)

An almost linear relationship between the Ca alloying/de-alloying peak currents and the square root of sweep rate was obtained as shown in Fig. 8.4 b. The diffusion coefficient is calculated from the deposition peak only. From the slopes, we calculate the diffusion coefficients of 3.8×10^{-14} cm^2 s^{-1} for Ca alloying with Bi with $\alpha n_\alpha = 0.5$. This value is similar to the value of Ca and Mg alloying with Sb, one order of magnitude lower than the value of Mg alloying with Bi, three orders of magnitude lower than the value obtained for the diffusion of Li^+ ions in a composite electrode. [16-19]

The charge density of Ca alloying with Bi, coulombic efficiency and the ratio between alloyed Ca and deposited Bi at different potential sweep rates are shown in table 8.1. The charge density increased with the decrease of the sweep rate. A control experiment at 10 mV/s has been recorded at the end of the experiment the CV measurements gave an identical result as for the beginning. Thus, there is no deactivation of the electrode surface and no noticeable change in the Bi layers in the course of these cyclic voltammograms. The ratio between the faradaic charge of anodic (de-alloying A1) and cathodic (alloying C1 + C2) gives the apparent coulombic efficiency. The coulombic efficiency was increasing from 90 % to 97 % with the decrease of the sweep rates from 10 mV/s to 50 µV/s. The value for 10 mV/s is lower than that for the experiment with the sweep rate of 50 µV/s because for higher sweep rates (higher than 1 mV/s), the time is not sufficient for saturation, obviously diffusion is too slow. The ratio between Ca and Bi for the sweep rate of 10 µV/s is 0.44 (theoretical value 0.5 for $CaBi_2$).

Table 8. 1: Dependence of Ca alloying/de-alloying with Bi modified electrode integrated charges densities on the potential sweep rate, the corresponding coulombic efficiencies, and the ratio of Ca:Bi. (~34 nmol/cm^2 Bi on Au and Surface area was 0.785 cm^2)

υ (mV/s)	**Charge (mC/cm^2) (alloying)**	**Charge (mC/cm^2) (de-alloying)**	**Col. Eff. (%)**	**Ratio Ca:Bi**
10	1.08	0.97	90	0.16
5	1.40	1.27	91	0.21
1	1.76	1.64	93	0.28
0.1	2.29	2.15	94	0.35
0.05	2.87	2.78	97	0.44
10	1.21	1.16	96	0.18

The cyclic voltammograms of Ca alloying/de-alloying with a Bi modified Au electrode in the same electrolyte at different sweep rates from 50 µV/s to 10 mV/s in the potential range of 0 to 1.6 V vs. Ca was also recorded after the potential step experiment described below. It could be seen that an additional anodic peak (A 2 in Fig. 8.5) appears at 1.4 V vs. Ca for sweep rates from 5 mV/s to 50 µV/s and in the control CV with 10 mV/s. This peak is obviously not related to the shoulder C1, as obvious from a comparison with fig.8.4. We assume that the second peak is visible because of a surface structure change. After repeated Ca alloying and de-alloying in the potential step experiment, the surface morphology of Bi might change, as observed for the Bi structure on the Au (111) single electrode after Mg alloying and de-alloying (see STM measurement in Chapter 6). Also, the appearance of the peak A2 might be due to the larger potential limits than before potential step experiment.

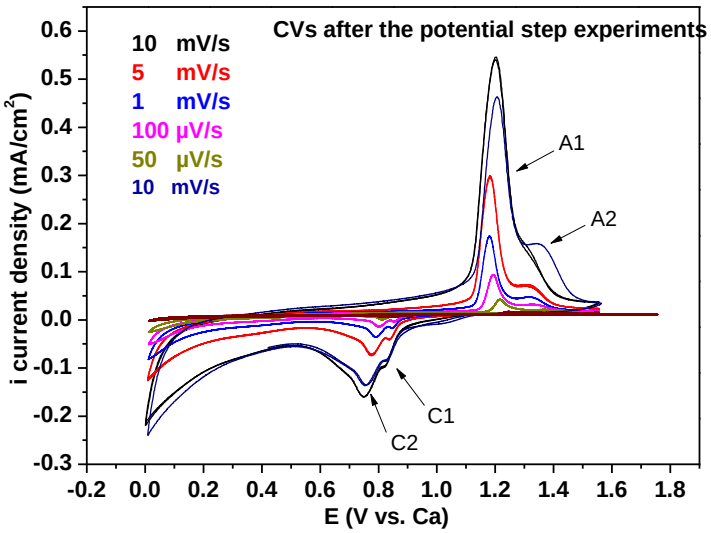

Figure 8. 5: The cyclic voltammograms of Ca alloying/de-alloying with a Bi modified Au electrode in the same electrolyte at different sweep rates from 50 μV/s to 10 mV/s in the potential range of 0 to 1.6 V vs. Ca (0.4 V to 1.6 V before the potential step experiment) after the potential step experiment. (~34 nmol cm^{-2} Bi on Au and Surface area was 0.785 cm^2)

Table 8. 2: Dependence of Ca alloying/de-alloying with Bi modified electrode integrated charges densities on the potential sweep rate, the corresponding coulombic efficiencies, and the ratio of Ca:Bi for the CVs after the potential step experiments. (~34 nmol/cm^2 Bi on Au and Surface area was 0.785 cm^2)

υ (mV/s)	**Charge (mC/cm^2) (alloying)**	**Charge (mC/cm^2) (de-alloying)**	**Col. Eff. (%)**	**Ratio of Ca:Bi (alloying)**	**Ratio of Ca:Bi (de-alloying)**
10	1.79	1.46	82	0.26	0.22
5	2.25	1.85	82	0.34	0.28
1	2.59	2.10	81	0.39	0.33
0.1	3.11	2.61	84	0.47	0.39
0.05	3.78	3.23	85	0.58	0.51
10	1.87	1.61	86	0.29	0.26

The charges density of Ca alloying with Bi, coulombic efficiency and the ratio between alloyed Ca and deposited Bi at different potential sweep rates are shown in table 8.2. The charge density for both alloying and de-alloying increased with the decrease of the sweep rate. The coulombic efficiencies were calculated to be 81 % to 86 % which is less than observed for the experiments of fig 8.4 prior to the potential step experiments. These integrated charges have been estimated from the cathodic peak C1 and C2 between 0 V and 1.2 V vs. Ca. The coulombic efficiencies at different sweep rates which are shown in table 8.1 were calculated between 0.4 V and 1.2 V vs. Ca. It is seen that there is a large cathodic current between 0 V and 0.4 V vs. Ca for each sweep rate. We assume that this large current is due to the continually alloying of Ca and also

due to some side reaction, which results in a lower coulombic efficiency. Also, the ratio between the alloyed Ca and the deposited Bi at 50 μV/s in table 8.2 is 0.58, which is higher than the theoretical value of 0.5 for $CaBi_2$ for the same reason as above mentioned. The ratio calculated from de-alloying is nearly 0.51, which means that the Ca is saturated in the Bi layers for low sweep rates. For higher sweep rates, the time is not sufficient for saturation, obviously diffusion is too slow. (E = 0.799 V vs. Ca for $Ca_{11}Bi_{10}$, E=0.723 V vs. Ca for Ca_5Bi_3 for T=873 K)

b) Potential step

In potential step experiments, the potential was first held at 1.5 V vs. Ca in 1.5 M $Ca(BH_4)_2$/THF , where de-alloying of Ca with a high reaction rate takes place in order to be sure that there is no Ca left in the Bi layer. Afterwards, the potential was stepped to the potential (from 0 V to 0.9 V vs. Ca), at which calcium could be alloyed with the bismuth layer, for different periods (2 min and 10 min), then the potential was stepped back to 1.5 V for 2 or 10 min where the extraction of calcium takes place, respectively.

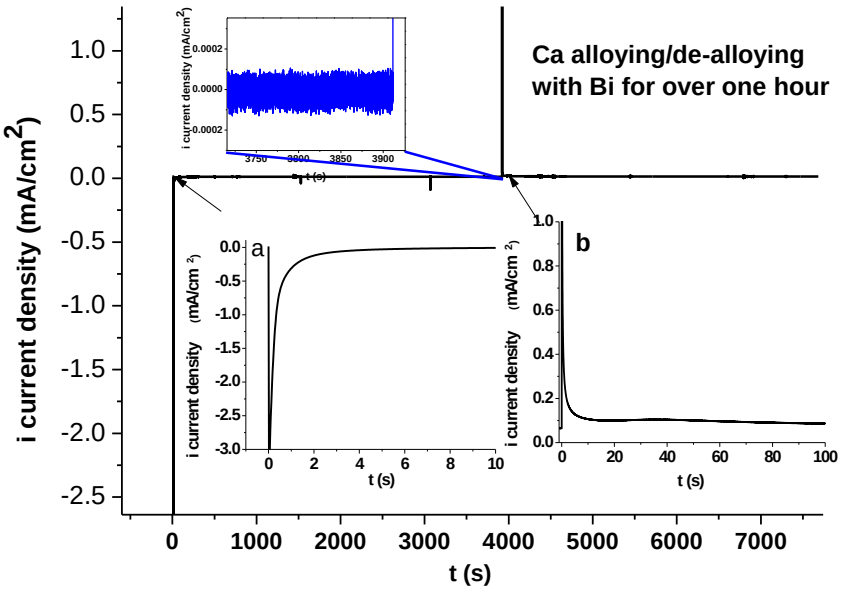

Figure 8. 6: Potential step experiment for Ca alloying and de-alloying from 1.5 M $Ca(BH_4)_2$/THF electrolyte into Bi modified Au electrode at 0 V and 1.5 V respectively. Alloying and de-alloying of Ca for over one hour. Insert: a) the first 10 s of alloying; b) the first 100 s of de-alloying. (~34 nmol cm^{-2} Bi on Au and Surface area was 0.785 cm^2)

Figure 8.6 shows comparison of the transients during alloying and de-alloying for one hour. The first 20 s of Ca alloying and de-alloying with Bi are shown in insert of Figure 8.6. It can be seen that the current drops directly after the double-layer charging for alloying and discharge for de-alloying. The faradaic current drops down to nearly 0 at the end of the alloying process,

which indicated that the Bi ad-layers were saturated by the Ca atoms. The amount of the deposited Bi and the alloyed Ca in Bi (from the charge of the cathodic current) was calculated to be 16 and 34 nmol/cm^2 respectively according to the corresponding current transient in Fig. 8.6. The ratio between the amount of the alloyed Ca to the deposited Bi is thus ~0.48 (Ca: Bi), which also indicates the formation of the above-mentioned $CaBi_2$ phase during the insertion process according to the structure model [12] shown in Fig. 8.3.

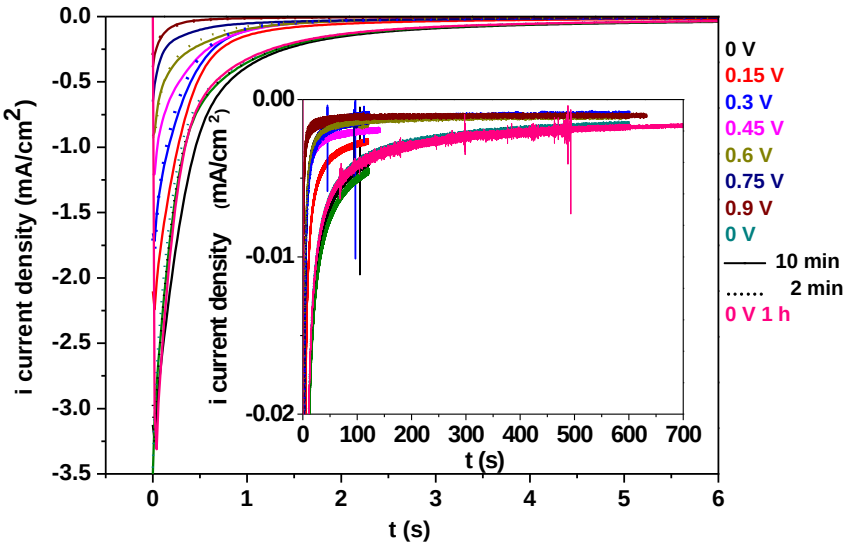

Figure 8. 7: Potential step experiment for Ca alloying from 1.5 M $Ca(BH_4)_2$ /THF electrolyte into Bi modified Au electrode at different potentials respectively. Each potentials is held for 2 min (straight line) and 10 min (dotted line). Insert: the current density of each potential hold with alloying time until 120 s and 600 s. (~34 nmol cm^{-2} Bi on Au and Surface area was 0.785 cm^2)

Figure 8. 7 shows the potential step experiment for Ca alloying and de-alloying from 1.5 M $Ca(BH_4)_2$/THF electrolyte into Bi modified Au electrode at different potentials respectively. (0 V to 0.9 V vs. Ca) Each potential was held for 2 min (dash line in Fig. 8.7) and 10 min (solid line in Fig. 8. 7) for Ca alloying. The current transient has a similar shape as in Fig. 8.6.

Fig. 8.8 shows the current transients during de-alloying of Bi after each potential step. After the initial double layer charging, a slight current increase may be due to some contribution of a nucleation and growth process. Then the current for de-alloying nearly stays constant for few seconds, indicating an initial both kinetic and diffusion rate limitation. Only after alloying at the lowest potential and for the longer alloying time of 10 min. notably a slightly increasing current with a faint indication of nucleation. The current drops to 0 after de-alloying of 10 min, which indicates that all of the alloyed Ca atoms left the Bi-layer. Thus there would be no

residual Ca atoms in the Bi ad-layers for the next potential step. In this case, the diffusion coefficient could be estimated for each potential step.

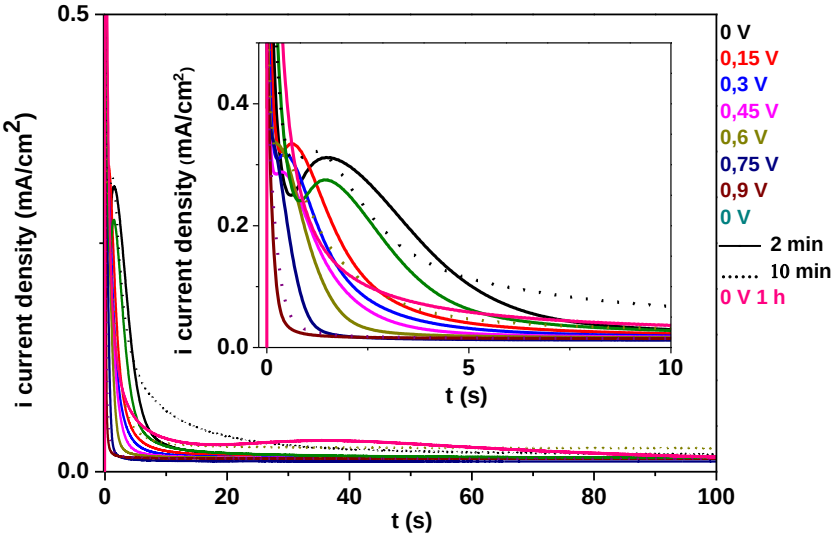

Figure 8. 8: Potential step experiment for Ca de-alloying from 1.5 M $Ca(BH_4)_2$ /THF electrolyte into Bi modified Au electrode at different potentials respectively. Each potentials held for 2 min (solid line) and 10 min (dot line). Insert: the current density of each potential hold with de-alloying time until 120 s and 600 s. (~34 nmol cm^{-2} Bi on Au and Surface area was 0.785 cm^2)

The charges of Ca alloying/de-alloying, the ratio between the alloyed Ca, and the deposited Bi and columbic efficiency are summarized in table 8.3. It can be seen that the ratio between alloyed Ca and deposited Bi is from 0.03 to 0.35 for 2 min alloying and from 0.02 to 0.32 for 2 min de-alloying. (The theoretical value of $CaBi_2$ is 0.5) It means that the Ca atoms are not saturated in Bi ad-layers with 2 min alloying. The ratio for the alloying and de-alloying of 10 min shows both nearly 0.5 at 0 V vs. Ca, which indicates again that the $CaBi_2$ is the product during the Ca alloying in the Bi ad-layers.

Here, we attribute the linear relationship between the current and square root of the time at the beginning (cf. Fig. 8.9) for Ca alloying to a kinetic and diffusion controlled process, which could be explained by the following equation:

$$i = i_{CT} - \frac{2i_{CT}}{nFC_0\sqrt{\pi}\sqrt{D}} \cdot \sqrt{t} \tag{7.3}$$

Where i is the current density, i_{CT} is the charge transfer current which is determined by the kinetic; F is faraday`s constant; n is the electron transfer number; C_0 is the saturated concentration of Ca in $CaBi_2$; t is the time; D is the diffusion coefficient of Ca. The diffusion coefficient can be estimated from the slope of the linear region if we plot the current density

versus the square root of time. Figure 8.9 shows the plot of current density versus the square root of alloying time. The slop of linear area for calculation of the diffusions coefficient at 0 V is shown. The charge transfer current density was estimated by extraction of the linear fitting.

Table 8. 3: Dependence of Ca alloying/de-alloying integrated charges during the potential step experiments on potential of alloying, the corresponding coulombic efficiencies, the ratio between Bi and Ca, the estimated diffusion coefficient and the value of $C\sqrt{D}$. (~34nmol cm^{-2} Bi on Au and Surface area was 0.785 cm^2)

E (V vs. Ca)	**Q (mC/cm^2) (cath. 2min**	**Q (mC/cm^2) (cath.) 10min**	**Q (mC/cm^2) (anod.) 2 min**	**Q (mC/cm^2) (anod.) 10 min**	**Ratio (Ca:Bi) alloying (de-alloying) 2 min**	**Ratio (Ca:Bi) alloying (de-alloying) 10 min**	**D ($/10^{-13}$ cm^2/s) alloying (de-alloying) 2min**	**$C\sqrt{D}$ ($/10^{-9}$) Alloying (de-alloying) 2min**	**D ($/10^{-13}$ cm^2/s) alloying (de-alloying) 10 min**	**$C\sqrt{D}$ ($/10^{-9}$) Alloying (de-alloying) 10 min**
0	2.28	2.88	2.13	2.82	0.35 (0.32)	0.44	2.2 (0.59)	8.4 (4.2)	1.9 (0.52)	7.8 (4.1)
0.15	1.86	-	1.49	-	0.28 (0.22)	-	2.0 (0.35)	8.0 (3.3)	-	-
0.3	1.28	2.11	1.22	2.05	0.20 (0.19)	0.32 (0.31)	1.2 (0.31)	6.2 (3.2)	1.1 (0.26)	5.9 (2.9)
0.45	1.04	-	1.02	-	0.16 (0.15)	-	0.55 (0.28)	4.2 (3.0)	-	-
0.6	0.74	1.15	0.50	1.07	0.11 (0.08)	0.18 (0.16)	0.29 (0.20)	3.1 (2.5)	0.17 (0.15)	2.3 (2.2)
0.75	0.22	-	0.16	-	0.03 (0.02)	-	0.25 (0.17)	2.8 (2.3)	-	-
0	2.15	2.75	2.08	2.68	0.33 (0.32)	0.42	2.4 (0.52)	8.8 (4.1)	2.0 (0.58)	8.0 (4.3)
0 (1 h)		3.15 (1 h)		3.13 (1 h)		0.48 (0.48) (1h)	1.0	5.7		

The value of D can also be calculated from the linear slope of Q^2 vs. t as shown in Fig. 8.10 for de-alloying with the integrated Cottrell equation, since the de-alloying is controlled by nucleation, charge transfer and diffusion. (Q^2 vs. t for alloying has also been plotted, but no linear region is observed.) Here for the C_0 we used the saturations concentration for the calculation of the diffusions coefficient. The estimated diffusion coefficients of alloying and de-alloying, and the value of $C\sqrt{D}$ from potential step experiments are also summarized in table 8.3.

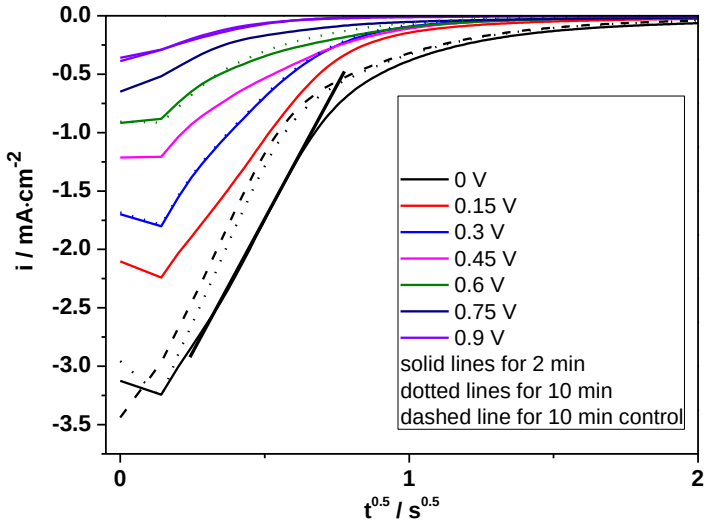

Figure 8. 9: Plot of transient current density (i vs.$\sqrt{t}$) for Ca alloying at different potentials (from 0 V to 0.9 V vs. Ca) with the time of 2 and 10 min into Bi layers. The slope of linear region for calculation of the diffusions coefficient at 0 V, the charge transfer current density is obtained from the intersection of the linear fitting with the axis. (Bi: ~34 nmol/cm^2; surface area: 0.785 cm^2)

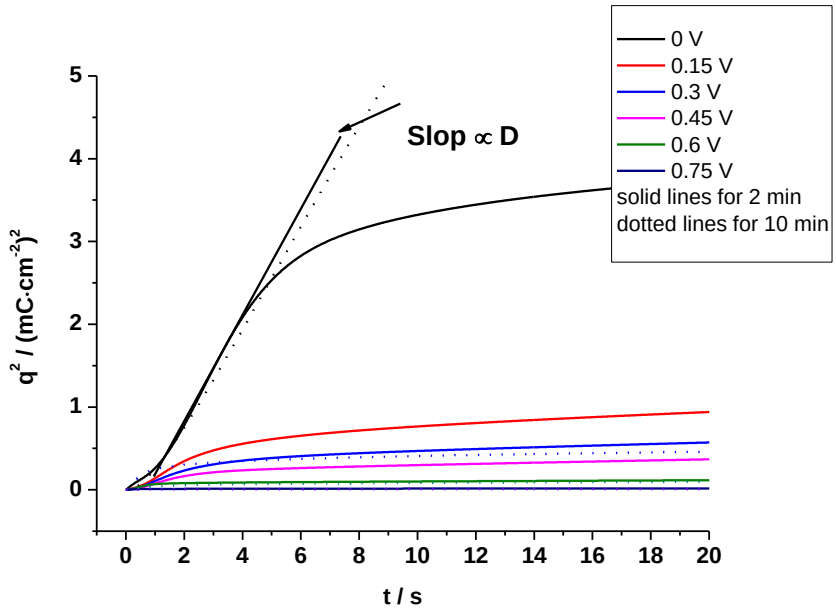

Figure 8. 10: Plot of Q^2 vs. t for Ca de-alloying with the time of 2 and 10 min. The slope of linear region for calculation of the diffusions coefficient at 0 V. (Bi: ~34 nmol/cm^2; surface area: 0.785 cm^2)

The calculated diffusion coefficients of 0.3×10^{-13} – 2.4×10^{-13} for alloying and 1.68×10^{-14} – 5.90×10^{-14} for de-alloying from the slope of linear region in Figure 8.9 and in Figure 8.10 by potential step experiment are summarized in table 8.4. (Here, the theoretical concentration of Ca in $CaBi_2$ was used.) The diffusion coefficient of de-alloying is lower than alloying, because

the Ca ions diffuse during the alloying easily into the Bi, which has a layer structure. However, during the de-alloying the structure has changed to the phase of $CaBi_2$. This structure needs to be broken before the Ca ions diffuse out of the layers into the electrolyte. Since after 10 min of alloying the system does not reach an equilibrium, so the equilibrium concentration of Ca in $CaBi_2$ at the applied potential for alloying is not known. In this case, the value of $C\sqrt{D}$ is calculated for comparison of alloying with different potentials and shown also in table 8.3.

In Figure 8.11 the Tafel plot of the overpotential versus the limited current is shown for each jump potential. The value of Tafel slope is 896 mV/decade, much higher than the typical value of 120 mV/decade for one-electron transfer. This value of Tafel slope is equivalent $\alpha n_\alpha = 0.07$ and therefore, for an assumed α of 0.5 to 0.1, to the transfer of only 0.5 to 0.1 elementary charges. The Ca^{2+} ions are likely to initially diffuse in between those layers before a phase transition to the Zintl phase is taking place. Using the above value of $\alpha n_\alpha = 0.07$ instead of 0.5 for the calculation of the diffusions coefficient in the Randles-Sevcik equation. We obtain D = 2.7×10^{-13} cm^2/s.

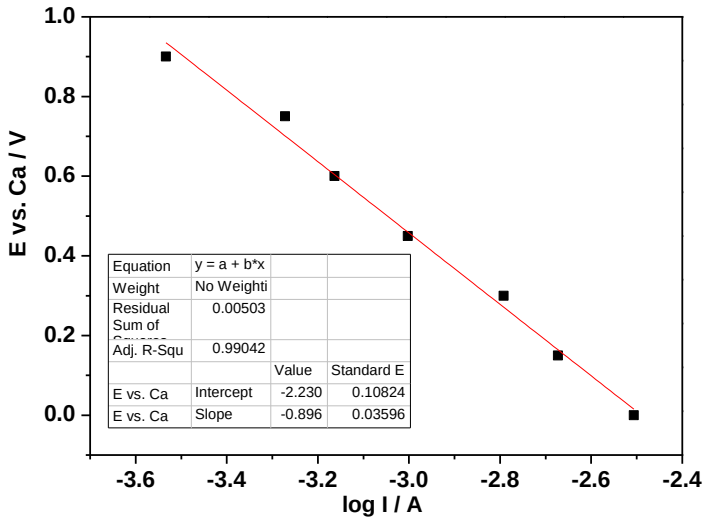

Figure 8. 11: Tafel plot of Ca alloying with Bi after the double layer charging.

The diffusion coefficient calculated from the variation of the sweep rates in CV (fig. 8.4) were estimated to be 3.8×10^{-14} cm^2 s^{-1} with $\alpha n_\alpha = 0.5$ and 2.7×10^{-13} cm^2/s $\alpha n_\alpha = 0.07$ for alloying, and from potential step experiments to be $1\text{-}2.4\times10^{-13}$ cm^2/s depending on the calcium content in the Bi modified electrode assuming the concentration of calcium in the bismuth layers (0.018 mol/cm^3 in $CaBi_2$). These values are similar to the value of Ca diffusion into Sb layers and higher than the estimated value from measurements for Mg diffusion into Bi electrode in

magnesium organohaloaluminate electrolyte in this work. Furthermore, it has to be taken into account that the estimated apparent diffusion coefficients which we have determined is the diffusion in the bulk of the homogenous material. Also, the incorporation of Ca into the Bi layer leads to an expansion and changing thickness. In the cyclic voltammetry, the relaxation time after the alloying is not enough to get a stable profile with homogenous distribution of Ca in the whole layers of Bi. Consequently, during the stripping process, there is a competition between the continuous distribution of Ca especially in the deep layers and the extraction of Ca from the outer layers.

8.4 Conclusions

The thin bismuth layer was first deposited on Au in 0.5 M H_2SO_4 containing 1 mM Bi_2O_3 by cyclic voltammetry. Calcium deposition/dissolution on Au and Bi modified Au electrodes were investigated in 1.5 M $Ca(BH_4)_2$ in THF electrolyte. On the Bi modified Au electrode, a pre-cathodic peak started at around 0.95 V (vs. Ca/Ca^{2+}), which is 0.95 V more positive than the onset potential of bulk deposition at the Au electrode. This peak is related to the alloying of Ca with Bi adlayers to form $CaBi_2$ alloy, as indicated by the ratio of the amount of the alloyed Ca to that of the deposited Bi calculated from the corresponding peak charge which is close to the theoretical value of 1:2 for $CaBi_2$ formation. High coulombic efficiency (97 %) of Ca stripping/alloying have been observed in cyclic voltammetry and potential step experiments.
Furthermore, the rate of alloying was investigated by CVs and the potential steps experiments. It has been found that the alloying process is determined by charge transfer kinetics and diffusion. During the alloying process, on additional anodic peak was observed due to the change of surface morphology, which indicated that the structure is changed after the Ca alloying. The diffusion coefficient of Ca in Bi multilayers was estimated from CVs to be 2.7×10^{-13} cm^2/s for alloying, and from potential step experiments to be 2.4×10^{-13} cm^2s^{-1} for the alloying at 0 V vs. Ca respectively, which are, twice as high as the diffusion coefficient of Ca alloying with Sb from this work in the previous chapter. These values are one order higher than Mg alloying with Sb and Bi and are two orders of magnitude lower than the value for Li^+ ions with Sb from this work.

References

[1] D. Wang, X. Gao, Y. Chen, L. Jin, C. Kuss, P. G. Bruce, *Nature Materials* **2017**, *17*, 16.

[2] Y. Shao, M. Gu, X. Li, Z. Nie, P. Zuo, G. Li, T. Liu, J. Xiao, Y. Cheng, C. Wang, J.-G. Zhang, J. Liu, *Nano Letters* **2014**, *14*, 255.

[3] A. Benmayza, M. Ramanathan, N. Singh, F. Mizuno, J. Prakash, *Journal of the Electrochemical Society* **2015**, *162*, A1630.

[4] R. A. DiLeo, Q. Zhang, A. C. Marschilok, K. J. Takeuchi, E. S. Takeuchi, *ECS Electrochemistry Letters* **2015**, *4*, A10.

[5] Y.-H. Tan, W.-T. Yao, T. Zhang, T. Ma, L.-L. Lu, F. Zhou, H.-B. Yao, S.-H. Yu, *ACS nano* **2018**, *12*, 5856.

[6] S. C. Jung, Y.-K. Han, *The Journal of Physical Chemistry C* **2018**, *122*, 17643.

[7] Y. Lee, M. Cui, J. Choi, J. Kim, Y. Son, J. Khim, *Journal of Hazardous Materials* **2018**, *344*, 1116.

[8] M. E. Arroyo-de Dompablo, A. Ponrouch, P. Johansson, M. R. PalacÃn, *Chemical Reviews* **2019**.

[9] H. Kim, D. A. Boysen, T. Ouchi, D. R. Sadoway, *Journal of Power Sources* **2013**, *241*, 239.

[10] H. Kim, D. A. Boysen, D. J. Bradwell, B. C. Chung, K. Jiang, A. A. Tomaszowska, K. L. Wang, W. F. Wei, D. R. Sadoway, *Electrochimica Acta* **2012**, *60*, 154.

[11] F. Merlo, M. L. Fornasini, *Materials Research Bulletin* **1994**, *29*, 149.

[12] M. J. Winiarski, B. Wiendlocha, S. Golab, S. K. Kushwaha, P. Wisniewski, D. Kaczorowski, J. D. Thompson, R. J. Cava, T. Klimczuk, *Physical Chemistry Chemical Physics* **2016**, *18*, 21737.

[13] H.-D. Lim, K.-Y. Park, H. Gwon, J. Hong, H. Kim, K. Kang, *Chemical Communications* **2012**, *48*, 8374.

[14] A. A. Nayeb-Hashemi, J. B. Clark, *Bulletin of Alloy Phase Diagrams* **1984**, *5*.

[15] A. J. Bard, L. R. Faulkner, *Electrochemical Methods: Fundamentals and Applications*, 2nd ed., John Wiley & Sons Inc., New York, Weinheim, **2001**.

[16] M. Deepa, T. K. Saxena, D. P. Singh, K. N. Sood, S. A. Agnihotry, *Electrochimica Acta* **2006**, *51*, 1974.

[17] G. Leftheriotis, S. Papaefthimiou, P. Yianoulis, *Solid State Ionics* **2007**, *178*, 259.

[18] M. Stromme Mattsson, *Solid State Ionics* **2000**, *131*, 261.

[19] M. Mao, T. Gao, S. Hou, F. Wang, J. Chen, Z. Wei, X. Fan, X. Ji, J. Ma, C. Wang, *Nano letters* **2019**, *19*, 6665.

9. Summery and outlook

In this thesis, the electrochemical properties of Li, Mg, and Ca deposition and dissolution on pure Au and Pt electrode as well as their alloying and de-alloying with Sb, Sn, and Bi modified Au electrodes have been discussed. The main results are summarized in Tables 9.1 and 9.2.

Table 9. 1: Main results of Metal (Li, Mg and Ca) deposition and dissolution in aprotic electrolytes for rechargeable metal batteries.

	Mg deposition	**Mg deposition**	**Mg deposition**	**Ca deposition**	**Li deposition**
Electrolytes	0.5 M MACC TG	1.0 M $Mg(BH_4)_2$ + 0.5 M $MgCl_2$ TG	0.5 M $Mg(TFSI)_2$ TG	1.5 M $Ca(BH_4)_2$ THF	3 M LiTFSI DMSO
Overpotential	-0.05 V vs. Mg	-0.10 V vs. Mg	-0.8 V vs. Mg	-0.20 V vs. Ca	-0.10 V vs. Li
Reversible Potential	-2.4 V vs. Ag/Ag^+	-2.4 V vs. Ag/Ag^+	n.d.	-2.75 V vs. Ag/Ag^+	-3.5 V vs. Ag/Ag^+
Anodic stability	2.7 V vs. Mg	1.5 V vs. Mg	3.0 V vs. Mg	2.3 V vs. Ca	4 V vs. Li
Coulombic efficiency	99%	97%	25%	98%	99%
Electrolyte stability	Decomposes [1]	n.d.	Decomposes [2]	n.d.	Decompose

Good electrochemical properties and high columbic efficiency (99 %) of Li deposition and dissolution was observed in 3M LiTFSI/DMSO on Au electrode. For 1 M solution on Au electrode and for 1M and 3M solution on Pt electrode the coulombic efficiency is lower. The decomposition of the specific lithium salt (LiTFSI) and the DMSO-molecule is the main reason and demonstrated by using DEMS. The oxidative stability of this electrolyte is found to be around 4 V. The Li-Au and Li-Pt alloy formation was observed.

For the magnesium deposition, the electrolytes of MACC/TG and $Mg(BH_4)_2$/TG have high reversibility and coulombic efficiency. However, they have a very limited electrochemical window. The $Mg(TFSI)_2$-based electrolyte, which has a wider electrochemical window than MACC and $Mg(BH_4)_2$ in TG, shows however very low electrochemical properties (low coulombic efficiency and high overpotential) due to the less stability of $TFSI^-$ ion and the decomposition of electrolytes.

Many electrolyte systems with varying Ca salts and organic solvents have been studied for Ca deposition and dissolution. Most of Ca salts are not commercially available and their solubility is quite low in the organic solvent. No reversible Ca deposition or alloying were observed in most Ca^{2+} containing electrolytes except $Ca(BH_4)_2$/THF and $Ca[B(hfip)_4]_2$ in DME (up to 98 %

coulombic efficiency). However, the electrochemical window of these electrolytes is quite low.

Table 9. 2: Main results of Metal (Li, Mg and Ca) alloying and de-alloying with Sb, Sn, and Bi as a negative electrode in aprotic electrolytes for rechargeable metal batteries.

	Mg Alloying with Sb	**Mg Alloying with Sb**	**Mg Alloying with Sn**	**Mg Alloying with Bi**	**Ca Alloying with Sb**	**Ca Alloying with Sn**	**Ca Alloying with Bi**	**Li Alloying with Sb**
Electrolyte	0.5 M MACC TG	1.0 M $Mg(BH_4)_2$ + 0.5 M $MgCl_2$ TG	0.5 M MACC TG	0.5 M MACC TG	1.5 M $Ca(BH_4)_2$ THF	1.5 M $Ca(BH_4)_2$ THF	1.5 M $Ca(BH_4)_2$ THF	2 M LiTFSI PC/EC
Onset potential of alloying	320 mV vs. Mg	400 mV vs. Mg	220 mV vs. Mg	360 mV vs. Mg	900 mV vs. Ca	840 mV vs. Ca	950 mV vs. Ca	700 mV vs. Li
Coulombic Efficiency	99%	97%	99%	99%	98%	60%	90%	99%
Formed alloy	Mg_3Sb_2	Mg_3Sb_2	Mg_2Sn	Mg_3Bi_2	$CaSb_2$	$CaSn_3$	$CaBi_2$	Li_3Sb and Li_2Sb
Kinetics of alloying	Type I	Type I	Type II	Type III	Type I	Type II	Type III	Type III
Charge transfer current (mA/cm^2)	0.60 at 0 V vs. Mg	0.12 at 0 V vs. Mg	n.d.	1.5 at 0 V vs. Mg	1.7 at 0 V vs. Ca	n.d.	3.4 at 0 V vs. Ca	n.d.
Diffusion coefficient (cm^2/s)	4-7 $\times10^{-14}$	3-4 $\times10^{-14}$	4-8 $\times10^{-13}$	1-4 $\times10^{-14}$	0.9-1 $\times10^{-13}$	3-5 $\times10^{-14}$	2-3 $\times10^{-13}$	4-6 $\times10^{-12}$

Magnesium alloying and de-alloying with Sb, Sn, and Bi modified Au electrodes were investigated in 0.5 M $MgCl_2$ + 0.5 M $AlCl_3$ in tetraglyme electrolyte. Interestingly, at the metal (Sb, Sn, and Bi) modified Au electrodes, pre-cathodic peaks which are more positive than the onset potential of bulk deposition were observed; they are related to the alloying of Mg into these metals thin adlayers to form Mg_3M_2 (for M = Sb and Bi) and the Mg_2Sn alloy. High coulombic efficiencies and high reversibility of Mg alloying/de-alloying have been observed in cyclic voltammetry and potential step experiments. No formation of ethylene was observed by DEMS measurements during the alloying and de-alloying with Sb, and Bi as opposed to the deposition on pure Au electrode. Ethylene formation for Mg alloying with Sn as well as the deposition on pure Au were observed. Calcium alloying and de-alloying with Sb, and Bi modified Au electrodes show high coulombic efficiencies and high reversibility in 1.5 M $Ca(BH_4)_2$ electrolyte. The electrochemical performance of Ca alloying/de-alloying with Sn is poor. In some experiments, the current density decreases very fast even in the second cycle in this system. The CaM_2 (for M = Sb and Bi) and $CaSn_3$ alloy formation is in accordance with

the calculation of the ratio between alloyed Ca and the deposited metals (Sb, Sn, and Bi) at the corresponding positive onset potential.

The kinetics of the alloying process of Mg and Ca with Sb, Sn and Bi was studied by potential step experiments and PITT measurements. Three completely different behaviors were observed.

I. The metal alloying is controlled first by the nucleation and charge transfer after the double-layer charging and then by the diffusion (for Mg alloying with Sb and Bi in MACC/TG); or first by the charge transfer after the double-layer charging and then by the diffusion (for Mg alloying with Sb in $Mg(BH_4)_2$/TG). The obvious consecutive occurrence of charge transfer and diffusion control shows that the charge transfer rate is independent of the concentration of inserted Mg in the alloy. A plot of Q^2 vs. t is used for estimating the diffusion coefficient.

II. The other behavior was controlled simultaneously by both charge transfer and diffusion. The current drops directly after the double-layer charge. This shows, that the concentration of the alloyed metal has an influence on the rate of charge transfer, e.g. because it influences the number of surface sites available for the alloying. A plot of i vs. $t^{0.5}$ is used for estimating the diffusion coefficient and, by extrapolation to t=0, the pure kinetic current. (for Ca alloying with Sb and Bi in $Ca(BH4)_2$/THF)

III. The metal alloying is only diffusion-determined process. The current drops directly after the double-layer charge. A plot of Q^2 vs. t is used for estimating the diffusion coefficient. (for Mg alloying in MACC/TG and Ca alloying in $Ca(BH_4)_2$/THF with Sn)

The charge transfer current (reaction rate) of Mg alloying at 0 V vs. Mg changes as follows: Bi (MACC/TG)> Sb (MACC/TG) >Sb ($Mg(BH_4)_2$/TG). The reaction rate of Ca alloying with Bi is twice as high as with Sb at 0 V vs. Ca. The diffusion coefficients were estimated to be 4-7×10^{-14} cm^2/s for Mg alloying with Sb and 1-4×10^{-14} cm^2/s for Mg alloying with Bi, which are one magnitude less than the diffusion coefficient 4-8×10^{-13} cm^2/s for Mg alloying Sn. These values suggest that Sn is an alternative anode better than Sb and Bi for rechargeable magnesium batteries. The diffusion coefficients of Ca alloying were estimated to be 0.9-1×10^{-13} cm^2/s for Ca alloying with Sb and 2-3×10^{-13} cm^2/s for Ca alloying with Bi, which is one magnitude higher than the diffusion coefficient of 3×10^{-14} cm^2/s for Ca alloying with Sn. It suggest that Sb and Bi are better than Sn as the negative electrode for rechargeable calcium batteries. In addition, a STM measurement for the Mg alloying with Bi has been studied. The Bi bulk shows similar crystalline structure before (in aqueous solution) and after (in organic solution) transfer into the

glovebox. After the Mg alloying/de-alloying the surface of Bi is smoother and the crystalline structure disappears. Furthermore, the diffusion rate of divalent cations (Mg and Ca) is less than the diffusion rate of Li in the Sb adlayers.

However, the following problems of kinetics for alloying and de-alloying need to be more studied. In this work, an incorporation of Mg or Ca alloying with Sb, Sn, and Bi leads to a surface expansion and changing the thickness. The diffusion coefficients obtained from the de-alloying transients are not same as the alloying. In case of Mg alloying/de-alloying with Sb, Sn, and Bi in MACC/TG electrolyte and the Ca alloying with Sb, there is still residual current after long period of the alloying in the potential step experiment due to the side reactions. Also, in the PITT measurement the de-alloying charge is much less than the alloying one.

The development of electrolytes for rechargeable calcium batteries is still the main challenge. The electrolytes, which are suitable for reversible Ca-plating and stripping, all contain boron based compounds. It might be a good idea of adding boron based compounds for further development of electrolytes. Otherwise, CaH_2 and CaF_2 were observed during the Ca deposition. Due to the high reactivity of Ca metal the alloying-type anodes (Sb, Sn, and Bi), which have been investigated in this work, are still promising to be a good choice. Sb and Bi are suggested to be better than Sn due to the high diffusion rate. The mechanism of the Ca deposition needs to be further studied and a better characterization of electrodes needs to be done.

The intensive research of rechargeable magnesium batteries is based on their high theoretical volumetric capacity and non-dendrite formation, which are the issues for lithium-ion batteries. However, the commercialized rechargeable magnesium batteries have not yet been produced due to the problems with both the electrodes and the electrolytes. The passivation of the electrode is still one of the largest problems in the development of new anode materials. From a view of literature, graphite [3] or other carbon-based [4] compounds are not suitable for the intercalation of Mg ions, unlikely lithium-ion-batteries. The oxides of titanium [5] and vanadium [6] suffer low rate capability and low coulombic efficiency. A SnSb alloy [7] [8] and a SbBi alloy [9] have already been reported and show good rate capability and cyclic stability. We report that the Sb only could be also used as a negative electrode for rechargeable magnesium batteries. Tin exhibits a specific capacity of 900 $mAhg^{-1}$, which suggest that the theoretical capacity could be practically achieved [10], and could be a good choice for the anode material because Mg alloying with Sn has a higher diffusion coefficient than with Sb and Bi, which is estimated from this work. The best electrochemical behavior is observed from bismuth-based anode materials in the literature [11, 12] [13] and in this work. The diffusion coefficient of Mg alloying with Bi from this work is similar to the value in the literature [14]. Furthermore, the alloying-type anode has

more possibility to be compatible with the high voltage cathode. However, the volume expansion, fast capacity fading, and low diffusion rate still need to be further studied. The ether-based solvents are still the choices for the development of electrolytes. In addition, the Mg^{2+} conducting layer has also been studied and reported by Ban et al. [15] Due to those contributions, it is proposed that possible commercialized rechargeable magnesium batteries could be made in the near future.

References

[1] P. Hegemann, M. Hegemann, L. Zan, H. Baltruschat, *Journal of The Electrochemical Society* **2019**, *166*, A245.

[2] I. Shterenberg, M. Salama, H. D. Yoo, Y. Gofer, J.-B. Park, Y.-K. Sun, D. Aurbach, *Journal of the Electrochemical Society* **2015**, *162*, A7118.

[3] P. Novak, J. Desilvestro, *Journal of the Electrochemical Society* **1993**, *140*, 140.

[4] G. A. Elia, I. Hasa, J. Hassoun, *Electrochimica Acta* **2016**, *191*, 516.

[5] Q. L. Wu, T. Tran, W. Q. Lu, J. Wu, *Journal of Power Sources* **2014**, *258*, 39.

[6] Q. Zhang, A. M. Bruck, D. C. Bock, J. Li, V. Sarbada, R. Hull, E. A. Stach, K. J. Takeuchi, E. S. Takeuchi, A. C. Marschilok, *Physical Chemistry Chemical Physics* **2017**, *19*, 14160.

[7] Y. W. Cheng, R. M. Stolley, K. S. Han, Y. Y. Shao, B. W. Arey, N. M. Washton, K. T. Mueller, M. L. Helm, V. L. Sprenkle, J. Liu, G. S. Li, *Physical Chemistry Chemical Physics* **2015**, *17*, 13307.

[8] L. R. Parent, Y. W. Cheng, P. V. Sushko, Y. Y. Shao, J. Liu, C. M. Wang, N. D. Browning, *Nano Letters* **2015**, *15*, 1177.

[9] T. S. Arthur, N. Singh, M. Matsui, *Electrochemistry Communications* **2012**, *16*, 103.

[10] N. Singh, T. S. Arthur, C. Ling, M. Matsui, F. Mizuno, *Chemical communications* **2013**, *49*, 149.

[11] Y. Shao, M. Gu, X. Li, Z. Nie, P. Zuo, G. Li, T. Liu, J. Xiao, Y. Cheng, C. Wang, J.-G. Zhang, J. Liu, *Nano Letters* **2014**, *14*, 255.

[12] F. Murgia, UniversitÃ© Montpellier **2016**.

[13] Z. Liu, J. Lee, G. Xiang, H. F. J. Glass, E. N. Keyzer, S. n. E. Dutton, C. P. Grey, *Chemical Communications* **2017**, *53*, 743.

[14] W. Wang, L. Liu, P.-F. Wang, T.-T. Zuo, Y.-X. Yin, N. Wu, J.-M. Zhou, Y. Wei, Y.-G. Guo, *Chemical communications* **2018**, *54*, 1714.

[15] S.-B. Son, T. Gao, S. P. Harvey, K. X. Steirer, A. Stokes, A. Norman, C. Wang, A. Cresce, K. Xu, C. Ban, *Nature Chemistry* **2018**, *10*, 532.

A Appendix

A1: Mg deposition and alloying on Sb-modified Au-Electrode in $Mg(BH_4)_2$-based electrolyte in TG

Figure A1.1 shows CVs for magnesium deposition and alloying onto Sb with varying the sweep rate in 1.0 M $Mg(BH_4)_2$ + 0.5 M $MgCl_2$ in TG electrolytes. The magnesium alloying process occurs at 0.70 V vs. Mg with 50 mV/s and shifts more negative with decrease of the scan rate. (0.30 V vs. Mg with 1 mV/s) The magnesium bulk deposition starts at 0 V vs. Mg on pure Au electrode (Figure A 1.1a) and was also observed with the sweep rate of 1, 2 and 5 mV/s on the Sb-modified electrolyte (brown, dark yellow, and rose curves in Figure A 1.1b), because the alloying process is very slow, the bulk deposition only occurs after the Sb-adlayer is saturated with Mg atoms. In the anodic sweep the peak potential of de-alloying shifts from 1.2 V with 50 mV/s to 1.0 V with 1 mV/s. It is also seen that the Mg bulk dissolution was observed at 0.3 V with 1, 2 and 5 mV/s.

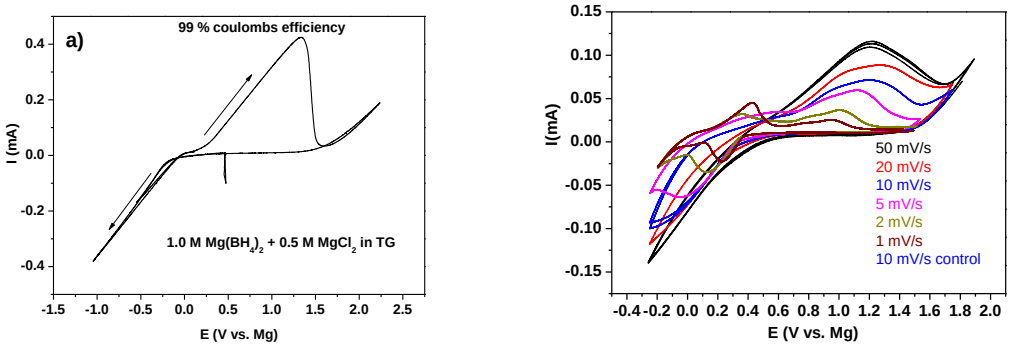

Figure A1. 1: CVs for electrochemical magnesium deposition (a) and alloying on Sb (b) in a 1.0 M $Mg(BH_4)_2$ + 0.5 M $MgCl_2$ in TG electrolytes in a three electrode cell with 10 mV/s. AE: Au and Sb modified Au; CE and RE: Mg.

In this measurement, high concentration (1.5 M Mg^{2+}) was used and $MgCl_2$ was added into the electrolyte in order to enhance the electrochemical performance of the Mg alloying/de-alloying. The increased concentration accelerates the deposition kinetics. The coulombic efficiency decreases to 30 % and the current density is about 0.03 mA/cm^2 with 10 mA/s, if the concentration decreases to 0.2 M. (Here is about 0.13 mA/cm^2 with an electrode surface of 0.785 cm^2, blue curve in Figure A 1.1b) Furthermore without addition of $MgCl_2$ is the coulombic efficiency drop to 90 % instead of close 100% with $MgCl_2$ for Mg-deposition. The $Mg(BH_4)_2$-based electrolyte has the advantage that no Al deposition occurs and no "conditioning" process is needed which is important and necessary for a fresh prepared MACC

electrolyte. However the anodic stability (up to 1.5 V vs. Mg) is lower than MACC electrolyte (2.8 V vs. Mg). The charge of Mg alloying with 1 mV/s is 9.24 mC/cm^2 (47.8 nmol/cm^2 integrated from the alloying peak between 0.10 V and 0.4 V in the cathodic sweep) and the charge of de-alloying is 9.18 mC/cm^2 (47.5 nmol/cm^2) integrated from the de-alloying peak between 0.10 V and 0.4 V in the anodic sweep 0.6 V and 1.4 V. (0 was token as the base line for integration of alloying and de-alloying). So, the ratio between Mg and Sb is 1.36 for alloying and 1.35 for de-alloying.

we can simply estimate the diffusion coefficient from the change of peak current with varying sweep rates assuming simple solid state diffusion as rate limiting using the Randles-Sevcik equation (for an irreversible system and semi-infinite diffusion) according to eq. (A 1.1) [1]:

$$I_p = 2.99 \times 10^5 n\sqrt{\alpha n_\alpha} A C_0 D_{Mg}^{0.5} v^{0.5}$$

From the slope for alloying and de-alloying in the fig. A 1.2, we estimate a diffusion coefficient of 6.8×10^{-15} cm^2 s^{-1} with $\alpha n_\alpha = 0.5$ for Mg alloying. The peak current of alloying with high sweep rate (20 and 50 mV/s) is not visible. Thus, only the peak current of alloying with low sweep rate has been took for calculating the diffusion coefficient.

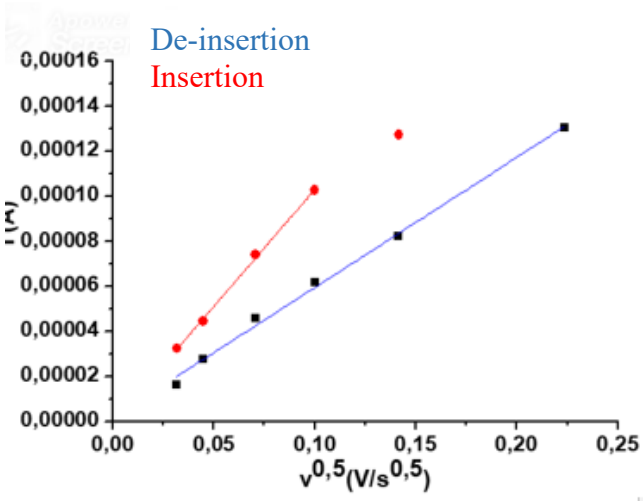

Figure A1. 2: Plot of i_p (peaks current) vs. $\upsilon^{1/2}$ (square root of scan rate).

In potential step experiments, the potential was first held at 1.3 V (where de-alloying of Mg with Sb takes place) in 1.0 M $Mg(BH_4)_2$ + 0.5 M $MgCl_2$ electrolyte. The amount of deposited Sb on Au polycrystalline is about 35.2 nmol/cm^2. Afterwards, the potential was stepped to alloying potential 0.1 V vs. Mg, at which Mg could be alloying with the Sb layer, for 1, 2 and 5 min, followed by the de-alloying at 1.3 V for 1, 2 and 5 min, respectively. Afterwards, the

experiment was repeated for Mg alloying at other potentials (from 0.2 V to 0.4 V)/de-alloying (1.3 V) for 1, 2 and 5 min followed by the experiment at 0 V for alloying as well as 1.3 V for de-alloying for 1, 2 and 5 min. Finally a control experiment at 0.1 V of alloying/de-alloying for 5 min followed by the alloying of one hour at 0.1 V has been done. In Figure A1.3 the potential steps experiment of Mg alloying with Sb for 1, 2, and 5 mins from 0 V to 0.4 V are shown. The current stay constant after the double- layer charge and then decrease until the current reaches zero, which indicate that the Mg alloying is controlled by charge transfer at the beginning and then by the diffusion. This is different as the current transient observed in the MACC/TG electrolyte. There, the current increases slightly due to the nucleation, which is not observed here. Figure A1.4 show the recorded current transients for Mg de-alloying with different de-alloying time (1, 2, and 5 min respectively). The current transients for each step for 1, 2, and 5 min show the similar form with the same time of Mg alloying. The current drop directly after the double layer charge.

The charges for alloying and de-alloying of Mg, the ratio between the alloyed Mg and the deposited Sb, and the calculated diffusion coefficient are summarized in table A1.1. The integrated charges of Mg alloying and de-alloying increased with the decrease of the alloying potential (Increase of the alloying time) as respected. The ratio between the alloyed Mg and the deposited Sb is about 1.52 for 1h alloying at 0.1 V vs. Mg. This value indicated that the phase Mg_3Sb_2 (Mg:Sb = 1.52) could be formed during the alloying with Sb.

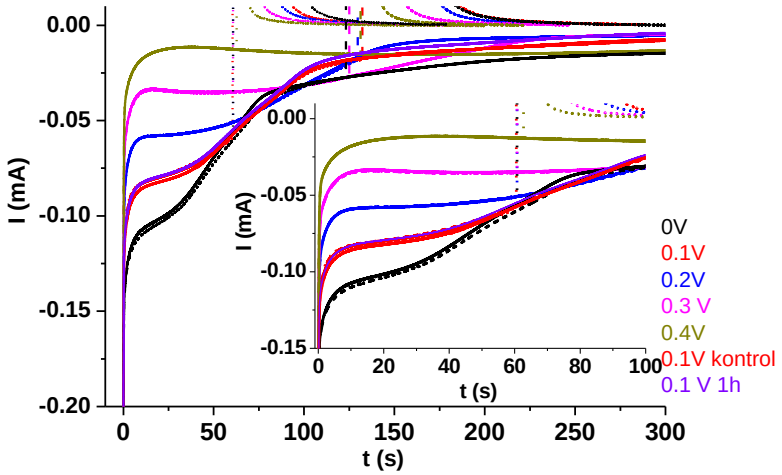

Figure A1. 3: Potential step experiment for Ca insertion from 1.5 $Mg(BH_4)_2$+0.5 M $MgCl_2$ in TG electrolyte into Sb modified Au electrode at different potentials respectively. Insertion for 1, 2, and 5 min. Insert: the first 100 s of the insertion. The potential of insertion are from 0 V to 0.4 V vs. Mg. AE: Sb on Au: CE and RE: Mg. (~35 nmol cm^{-2} Sb on Au and Surface area was 0.785 cm^2)

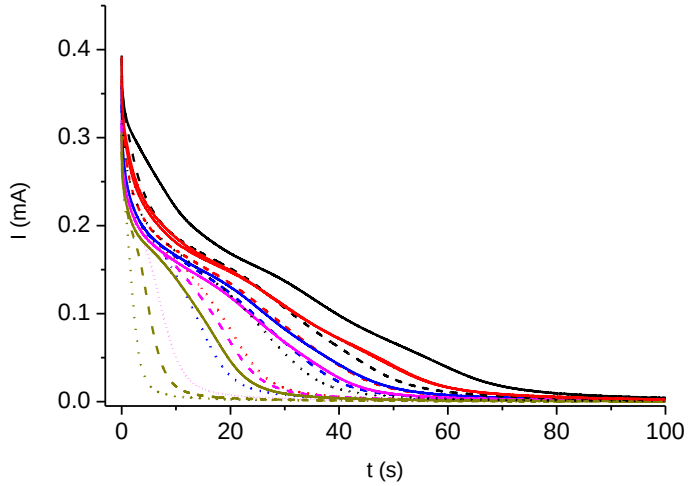

Figure A1. 4: Potential step experiment for Ca insertion from 1.5 $Mg(BH_4)_2$+0.5 M $MgCl_2$ in TG electrolyte into Sb modified Au electrode at different potentials respectively. Insertion for 1, 2, and 5 min. The potential of de-insertion are from 1.3 V vs. Mg. AE: Sb on Au: CE and RE: Mg. (~35 nmol cm^{-2} Sb on Au and Surface area was 0.785 cm^2)

The value of D can also be calculated from the linear slope of Q^2 vs. t as shown in Fig. A1.5 for alloying and Fig. A1.6 for de-alloying with the integrated Cottrell equation, here for the C_0 we used the saturations concentration for the calculation of the diffusions coefficient.

$$Q^2 = \frac{(2zFAC_0)^2 D}{\pi} t$$

The estimated diffusion coefficients of alloying and de-alloying from potential step experiments are also summarized in table A1.1. The value of Tafel slope is 443 mV/decade (this value is similar to the value of Mg alloying with Sb), much higher than the typical value of 120 mV/decade for one-electron transfer. (see Fig. A1.7) This value of Tafel slope is equivalent to 0.27 electron transfer. With $\alpha n_\alpha = 0.137$ the diffusion coefficient was calculated to be 2.43×10^{-14} cm^2/s. Thus, the diffusion coefficient of Mg into Sb in 1.5 M $Mg(BH_4)_2$ + 0.5 M $MgCl_2$ in TG electrolyte is $2\text{-}5\times10^{-14}$ cm^2/s, which is in the same range to $4\text{-}7\times10^{-14}$ cm^2/s determined in 0.5 M MACC/TG from CV and potential step experiment. The only difference between these two electrolytes is the appearance of Al ion in the MACC/TG system, which result in a different value of diffusion coefficient.

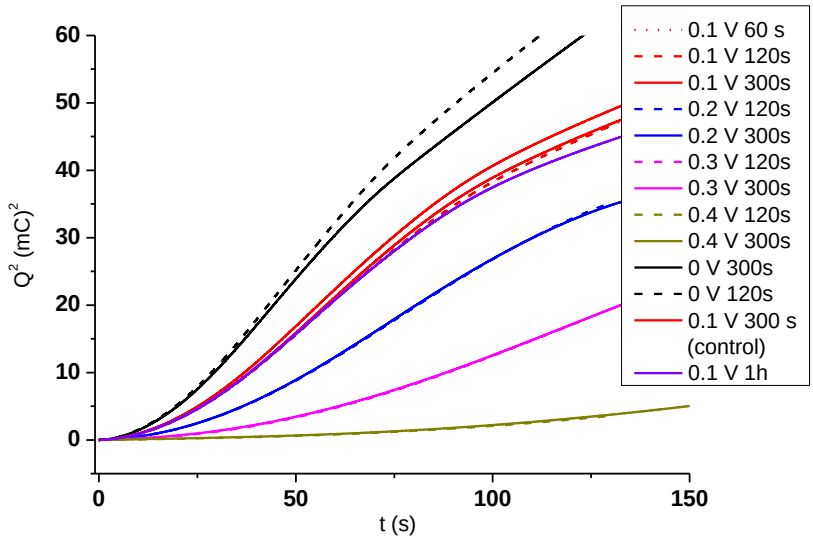

Figure A1. 5: Plot of transient Charge (Q^2 vs. t) for Mg alloying at different potentials (from 0 V to 0.4 V) into Mg layers. The slope of linear area is used for calculation of the diffusions coefficient at 0 V. (~35 nmol/cm^2; surface area: 0.785 cm^2)

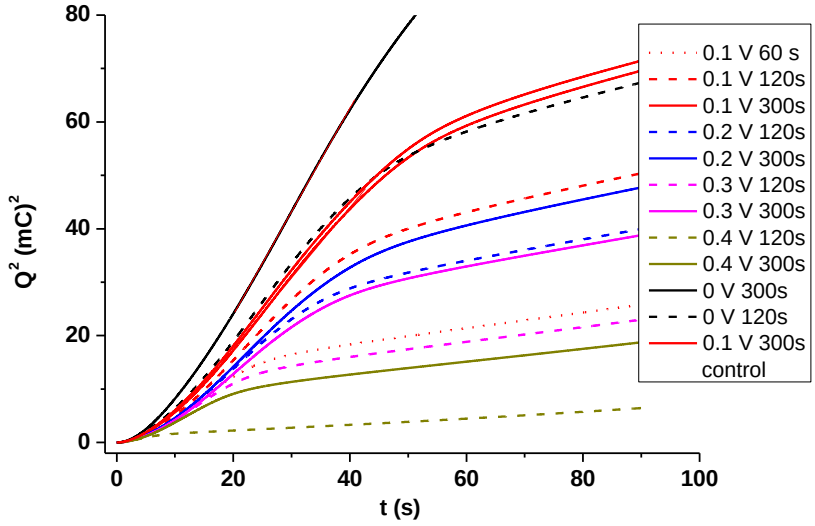

Figure A1. 6: Plot of transient Charge (Q^2 vs. t) for Mg De-alloying. (~35 nmol/cm^2; surface area: 0.785 cm^2)

Table A1. 1: Dependence of Mg insertion (black) /de-insertion (red) integrated charges (mC/cm^2) during the potential step experiments on potential of insertion, the ratio between Sb and Mg (bleu) and the diffusions coefficient of alloying and (de-alloying) (green, cm^2/s). (~35 nmol cm^{-2} Sb on Au and Surface area was 0.785 cm^2)

Time of insertion(s)	**0 V**	**0.1 V**	**0.1 V (control)**	**0.2 V**	**0.3 V**	**0.4 V**
60	5.56/5.43 0.81	4,50/4.06 0.65		3.42/3.29 0.50	2.36/2.22 0.35	1.22/1.12 0.18
120	7.93/7.72 1.15	6.60/6.33 0.96		5.52/5.40 0.81	4.01/3.92 0.59	1.63/1.57 0.24
300	9.44/9.15 1.38 2.85 (3.38)	8.26/8.14 1.21 2.19 (3.22)	8.17/8.12 1.21 2.03 (2.58)	6.18/5.96 0.90 1.83 (2.16)	5.52/5.48 0.81 1.03 (1.07)	3.53/3.48 0.52
3600 (1 h)		10.30 1.52 3.42 (4.55)				

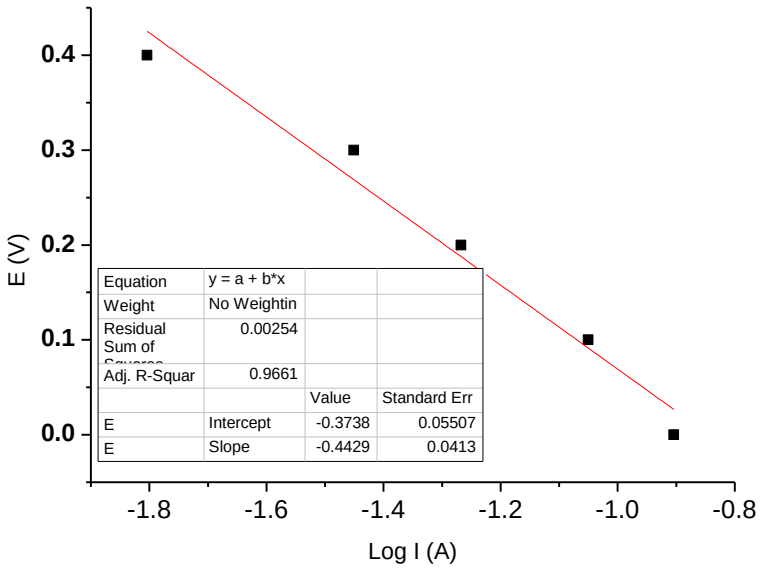

Figure A1. 7: Tafel plot of the overpotential versus the limited current for each jump potential. From the linear fitting the Tafel slop is determined to be 443 mV/decade, this value is higher than the usual value for kinetically controlled charge transfer, which is 120 mV/decade.

A 2: Mg deposition and alloying on Sb modified Au-Electrode in $Mg(TFSI)_2$-based electrolyte in TG

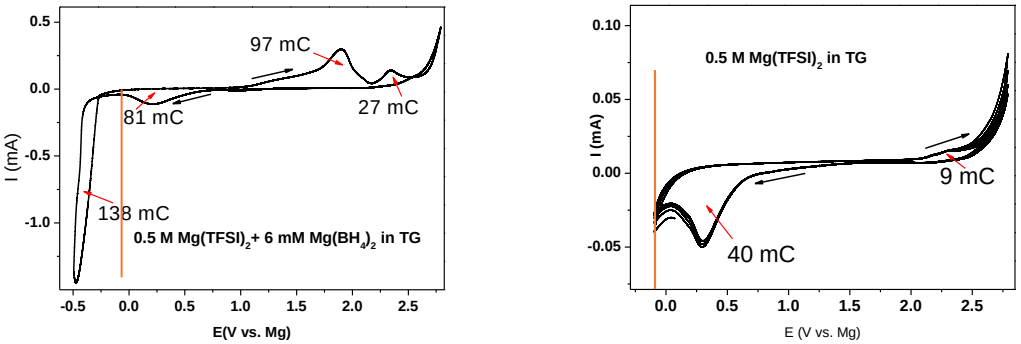

Figure A2. 1: CVs for electrochemical magnesium alloying and deposition on Sb in a three electrode cell with 10 mV/s. left): 0.5 M $Mg(TFSI)_2$ + 6 mM $Mg(BH_4)_2$ in TG; right: 0.5 M $Mg(TFSI)_2$ in TG. AE: Sb modified Au; CE and RE: Mg. Black arrows show the direction of the scan and red arrows show peaks area related to the charge.

The electrochemical deposition of magnesium in $Mg(TFSI)_2$/TG shows very low current density and very high overpotential. So we try to enhance the electrochemical performance by using the Sb and Bi alloy compounds with Mg as anode materials. Figure A 2.1 shows the magnesium alloying and deposition onto Sb-modified Au electrode. It could be seen that with the addition of 6 mM $Mg(BH_4)_2$ the coulombic efficiency for the magnesiation of Sb increase to 33 % in comparison with 22 % without $Mg(BH_4)_2$. The CVs for magnesium alloying and deposition with Bi have been shown in Figure A 2.1.

A 3: EC-STM measurement for Mg deposition and alloying on Bi-modified Au-Electrode in MACC/TG (150 nmol/cm^2 Bi)

A freshly deposited Bi layer (120 nmol/cm^2) on a Au(111) single crystal electrode was first prepared in an aqueous electrolyte and then transferred into the glove box for Mg deposition and alloying. Figure A3.1 shows the CV for Mg deposition and alloying on Bi-modified Au (111)-electrode in 0.5 M MACC/TG in a EC-STM cell. The current transient in EC-STM cell shows similar shape to the CV recorded in H-cell. The negative current at -0.5 V vs. Ag is due to the oxygen in the Glovebox.

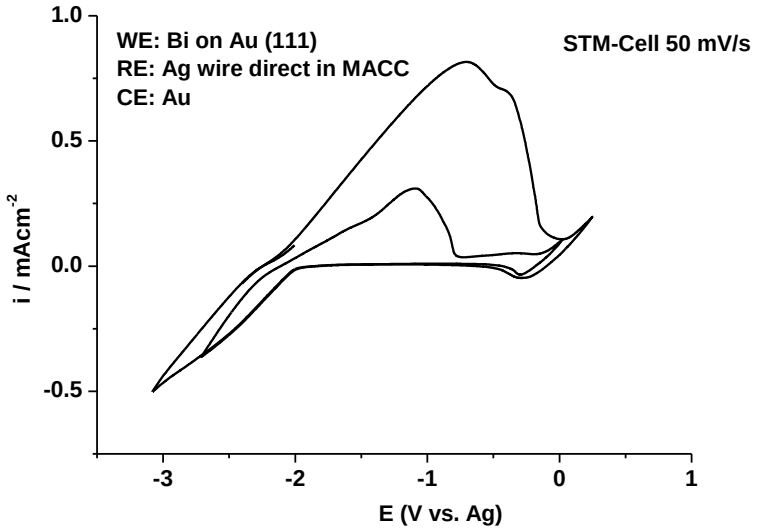

Figure A3. 1: CV for Mg deposition and alloying with Bi on Au(111) electrode in 0.5 M MACC/TG in a EC-STM cell.

In Figure A 3.2 STM images for the electrochemical deposition and alloying of Mg with Bi on the Au(111)- single electrode by EC-STM measurement are shown. The experiment starts at OCP and recorded the STM image, then the potential was swept to -3.0 V vs. Ag for Mg bulk deposition followed by sweeping back to -1.0 V vs. Ag for Mg dissolution and recorded the STM images.

The Bi particles were clearly observed on the Au(111) electrode at OCP and a large smooth surface on the top of mountains in the 3D images (fig. A 3.2 a and a′) is seen. It is seen that in fig. A3.2 b the surface was getting rough, which might be due to the Al deposition or some side reactions. Then the tip was retracted and the potential was swept to -3.0 V (where the Mg deposition occurs) and then back to -1.0 V (where the Mg dissolution occurs.) The images c and d show clearly that the crystalline structure of Bi disappeared after the Mg deposition/dissolution (as well as their alloying/de-alloying) process. It shows same results which is shown in Fig 6.11-6.13 with the amount of Bi 233 nmol/cm^2.

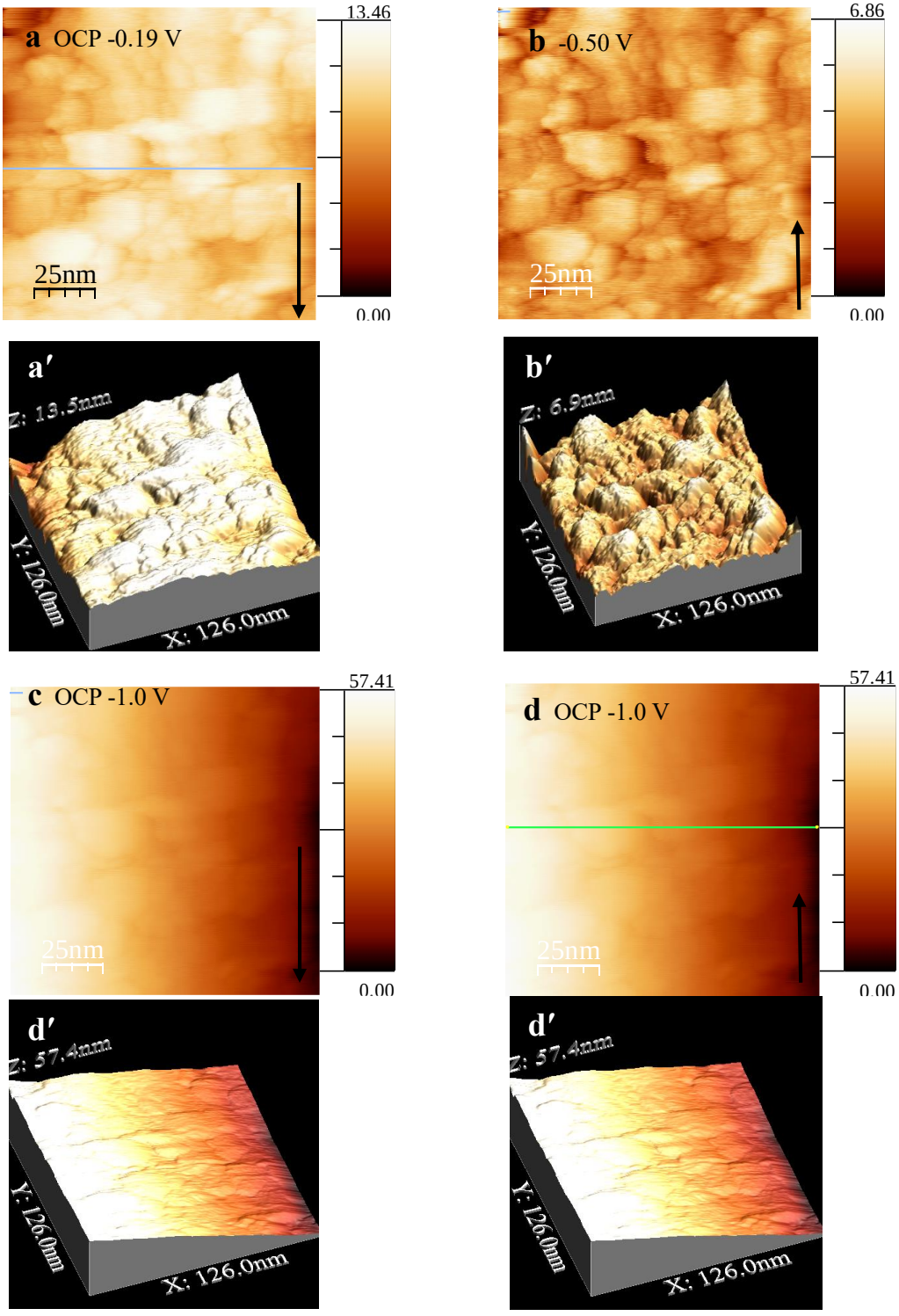

Figure A3. 2: STM images of Mg alloying at Bi modified Au(111) surface in 0.5 M MACC/TG electrolyte. (a) at open circuit potential of -0.5 V vs. Ag/AgCl, (b) potential hold at -1.0 V vs. Ag/AgCl (new approach), (c) and (d) sweep to -3.0 V and back to -1.0 V. a′, b′, c′, and d′ show the corresponding 3D images, respectively. Sample bias of 50 mV, set point = 2 nA. Integral gain: 6 and proportional gain: 8. Arrows indicate scan direction.

A 4: Calcium alloying in Sn-modified Electrode in $Ca(TFSI)_2$ + TG based Electrolyte

No reversible Ca bulk deposition/dissolution in $Ca(TFSI)_2$/TG was observed because of very high overpotential and the low stability of TFSI- ion. Here, the Sb modified Au electrode was used to check the Ca alloying/de-alloying in this electrolyte. In Figure A 4.1 the CVs for Ca alloying with Sb in 0.5 M $Ca(TFSI)_2$/TG with sweep rate of 10 mV/s between -1.0 V and 2.5 V were shown. In the cathodic sweep the current decrease at 0.5 V, which might be due to the Ca alloying with Sb. However, no peak for the Ca de-alloying in the anodic sweep is observed. The current decrease very fast even at the second cycles due to the decomposition of $TFSI^-$ ion, which was observed for the Mg deposition. [2] Furthermore, a complex formed from the TG molecule and the $TFSI^-$ anion deactivate the electrode. [3] A additive of 0.1 M $Ca(BH_4)_2$ in the electrolyte has no influence of the electrochemical performance of Ca alloying/de-alloying in 0.5 M $Ca(TFSI)_2$/TG electrolyte.

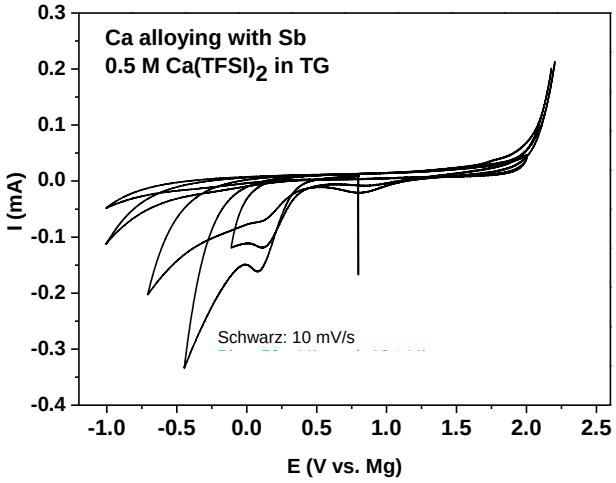

Figure A4. 1: Cyclovoltamogramm of Ca alloying with Sb in 0.5 M $Ca(TFSI)_2$/TG with 10 mV/s and 50 mV/s. AE: Au; CE and RE: Ca.

A 5: Ca deposition and alloying on Sn-modified Au-Electrode in 1.5 M $Ca(BH_4)_2$/THF

In Figure A5.1 the electrochemical alloying and deposition of Ca into Sn-modified (~170 nmol/cm^2) electrode with 50 mV/s is shown. The measurement started at -1.5 V vs. Ag/Ag^+ in cathodic direction. At the potential below -2.80 V vs. Ag/Ag^+ the cathodic current increases significantly due to Ca bulk deposition. With a Sn modified electrode a cathodic current in the form of a shoulder for the magnesium alloying was observed at about -1.95 V vs. Ag/Ag^+ (which means 800 mV more positive than without Sn on the Au surface) The coulombic efficiency for Ca bulk deposition/dissolution is 95% and for the Ca alloying/de-alloying is 60 %. We attribute that the low coulombic efficiency is due to the side reactions. From the thermodynamic data of

the $CaSn_3$ compound the theoretic potential for the formation of $CaSn_3$ is calculated to be 900 mV vs. Ca/Ca^{2+} according to the following reaction equation:

$$3Sn + Ca + 2e^- \longrightarrow CaSn_3 \qquad \text{(eq. A5.1)}$$

The ratio between the alloyed Ca and the deposited Sn is 0.07, which significantly less than the theoretic value of 0.33, which indicates 50 mV/s is a relative high sweep and not long enough for the saturation of Mg alloying. Otherwise, the electrolyte is decomposed at the same time as the Ca alloying, which consuming the charge for calculation of the coulombic efficiency.

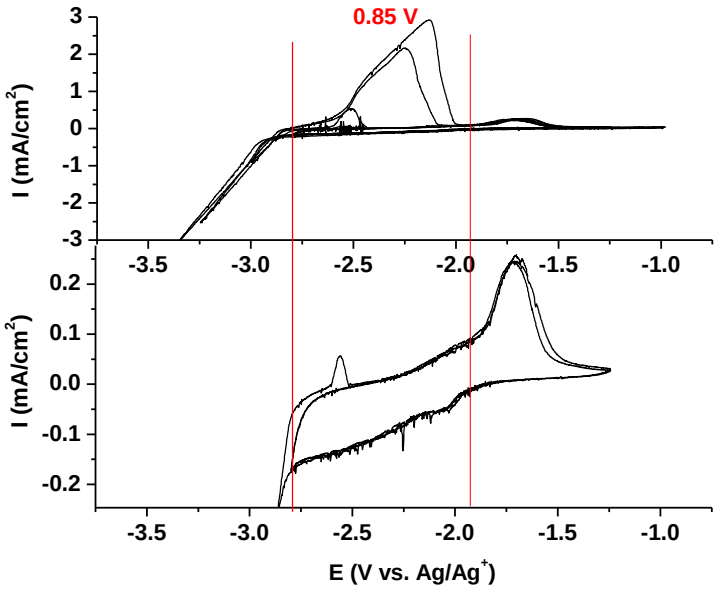

Figure A5. 1: CVs for electrochemical calcium deposition and alloying in a 1.5 M $Ca(BH_4)_2$/THF electrolytes in a three electrode cell with 50 mV/s. AE: Sn on Au; CE: Mg. RE: 0.1 M $AgNO_3$ in MeCN. (~170 nmol/cm^2)

The diffusion coefficient can be estimated by using Randles-Sevchik equation for irreversible and semi-infinite diffusion. The deposited Sn is about ~170 nmol/cm^2. The Cyclic voltammograms were obtained by scan rates from 5 to 50 mV/s between -2.85 V to 1.75 V vs. Ag/Ag^+ at room temperature. (See Figure A 5.2a) The height of peaks current is approximately proportional to $v^{0.5}$ at a relatedly high scan rate for both alloying and de-alloying. (Figure A 5.2b)The diffusions coefficient was calculated to be 4.4×10^{-14} cm^2/s for alloying with αn_α = 0.5. (Here, the theoretical value for the concentration of Ca in $CaSn_3$ is 0.015 mol/cm^3 was used)

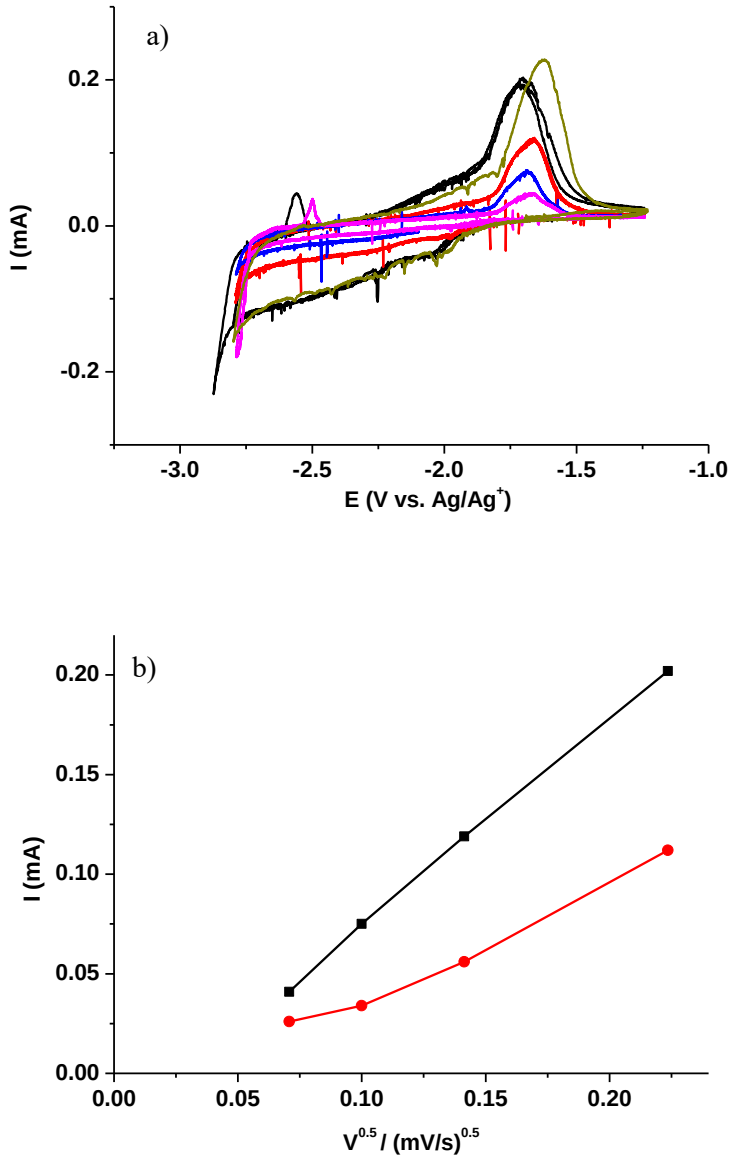

Figure A5. 2: a) Cyclic voltammograms of Ca alloying with Sn modified Au electrode in 1.5 M $Ca(BH_4)_2$/THF at different sweep rates from 5 to 50 mV s^{-1}. b): Plot of i_p (peak current) vs. $\upsilon^{1/2}$ (square root of scan rate). AE: Sn on Au; CE: Mg; RE: 0.1 M $AgNO_3$ in MeCN. (~170 nmol cm^{-2} Sn on Au and Surface area was 0.785 cm^2)

Then the diffusion coefficient was estimated by potential step experiment. In figures Fig. A 5.3a. Fig. A 5.3b the transients during alloying and de-alloying for the various potential from 0 V to 0.25 V of alloying for 5 min are shown. It could be seen that the current for the alloying process drops directly after the double layer charging for all the periods.

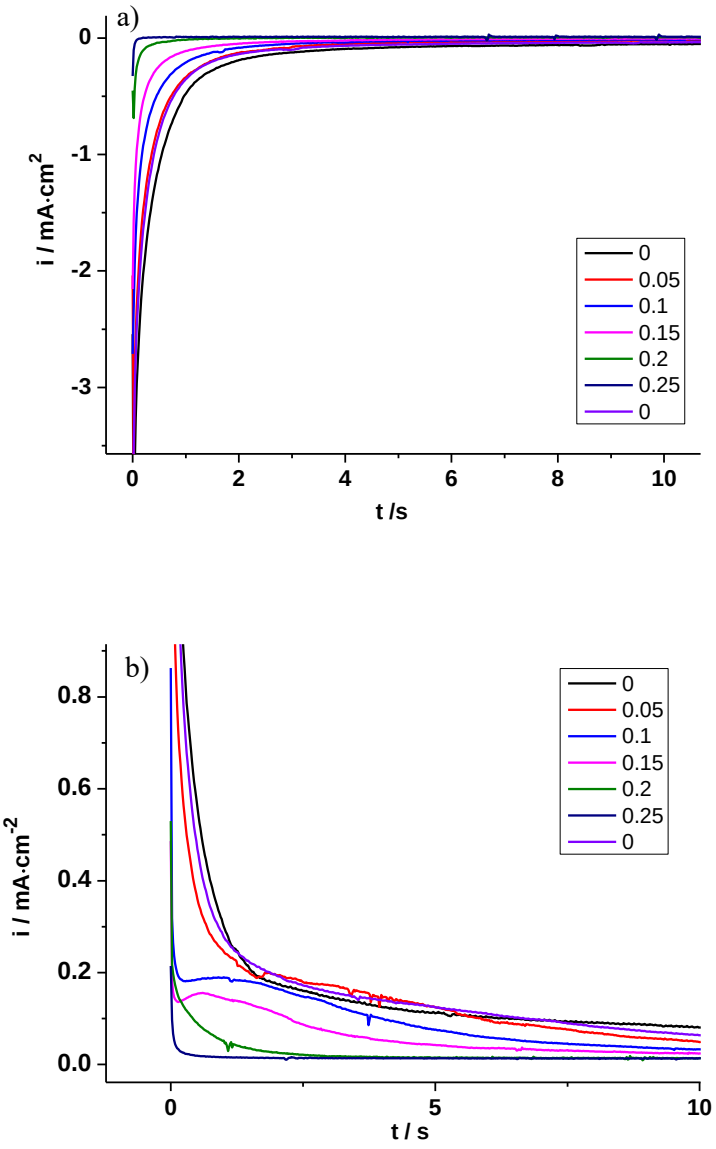

Figure A5. 3: the potential steps experiment for a) Ca alloying and b) Ca de-alloying with Sn electrode out of a 1.5 M $Ca(BH_4)_2$/THF electrolyte at 0 V to 0.25 V respectively. AE: Sn on Au; CE: Mg; RE: 0.1 M $AgNO_3$ in MeCN. (~ 170 nmol cm^{-2} Sn on Au and Surface area was 0.785 cm^2)

The charge density for alloying and de-alloying of Ca with Sn are summarized in table A 5.1 together with coulombic efficiency, the ratio between the deposited Sn and the alloyed Ca, and the estimated diffusion coefficient. D can then be calculated from the slope as shown in Fig. A5.4 for alloying where we plotted Q^2 vs t for a better comparison of the time range of the linear range with the original transients in fig. A 5.3. The estimated diffusion coefficient is 3-5×10^{-14} cm^2/s.

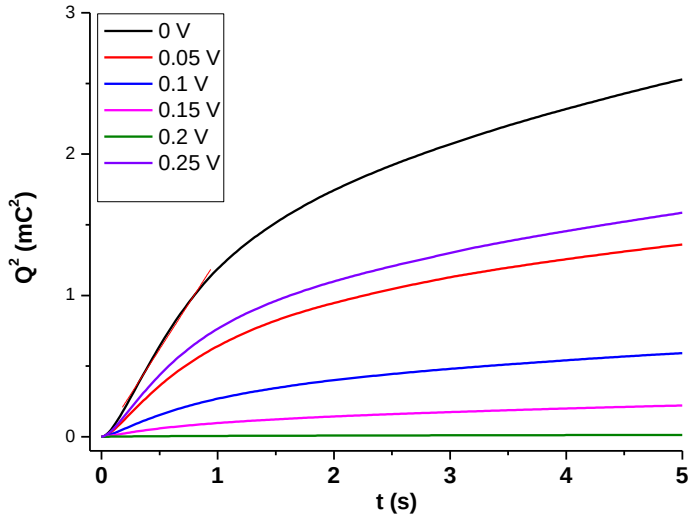

Figure A5. 4: Plot of transient Q^2 vs. t for Ca alloying at different potentials (from 0 V to 0.25 V) with the alloying time 5 min into Sn layers. (Sn: ~170 nm/cm^2; surface area: 0.785 cm^2)

Table A5. 1: Dependence of Ca alloying/de-alloying integrated charges (The steady states current at t (5 min) was subtracted for alloying) during the potential step experiments, the corresponding coulombic efficiencies, the ratio between Sn and Mg and the diffusion coefficients. (~170 nmol cm^{-2} Sb on Au and Surface area was 0.785 cm^2)

Potential (V vs. Mg)	**Charge (mC/cm^2) (cath.5min) (corr. value)**	**Charge (mC/cm^2) (anod. 5 min)**	**Ratio of Mg:Sb for alloying and [de-alloying] of 10 min**	**D (/10^{-13}cm^2/s) Alloying**
0	11.6 (4.06)	2.96	0.12 [0.09]	4.81
0.05	5.97 (2.36)	1.98	0.07 [0.76]	3.24
0.1	3.93 (1.77)	1.15	0.05 [0.03]	2.17
0.15	2.65 (1.09)	0.70	0.03 [0.02]	0.99
0.2	n.d.	n.d.	n.d.	n.d.
0.25	n.d.	n.d.	n.d.	n.d.
0 (control)	8.27 (3.23)	2.19	0.10 (0.07)	1.31

References

[1] A. J. Bard, L. R. Faulkner, *Electrochemical Methods: Fundamentals and Applications*, 2nd ed., John Wiley & Sons Inc., New York, Weinheim, **2001**.

[2] R. Jay, A. W. Tomich, J. Zhang, Y. Zhao, A. D. Gorostiza, V. Lavallo, J. Guo, *ACS Applied Materials & Interfaces* **2019**, *11*, 11414−11420.

[3] P. Hegemann, M. Hegemann, L. Zan, H. Baltruschat, *Journal of The Electrochemical Society* **2019**, *166*, A245.